Thermo-visco-elastic modelling of photovoltaic laminates: Advanced shear-lag theory and model order reduction techniques

Ojo Saheed Olalekan

Thermo-visco-elastic modelling of photovoltaic laminates

Advanced Shear-Lag Theory and Model Order Reduction Techniques

Thesis for the degree of Doctor of Philosophy
XXVIII Cycle (2013-2016)
Doctorate

Dottorato di Ricerca in Ingegneria delle Strutture
Politecnico di Torino

March 2016

Dottorato di Ricerca in Ingegneria delle Strutture

Tutor: Prof. Marco Paggi
Coordinator: Prof. Giuseppe Lacidogna

Department of Structural Engineering,
Politecnico di Torino,
C.so Duca Degli Abruzzi 24
10129 Torino, Italy.

Contents

Summary

During lamination, residual thermo-mechanical stresses are induced in the encapsulated solar cells composing photovoltaic (PV) modules. Depending on the material and geometrical configuration of the layers of the laminate, this residual stress field can be beneficial since it may lead to a compressive stress state in Silicon and therefore crack closure effects in the presence of cracks, with a recovery of electrical conductivity in cracked solar cells. It is therefore important to investigate the distribution of thermo-mechanical stresses within the PV laminate with a view to optimizing the coupling between the electrical response and elastic deformation in the operation of PV modules. A promising approach proposed in the present thesis regards the prediction of residual stresses in composite laminates by using a shear-lag theory to model the epoxy-vinil-acetate polymeric layers, accounting for their thermo-visco-elastic response. Moreover, it will be shown that thermomechanical formulations for stress analysis of a PV laminate lead to a system of higher order ordinary differential equations or partial differential equations in which the exact solutions may be impossible to be determined in closed form and hence numerical schemes become desirable. However, the computational cost associated with the implementation of the numerical scheme may be significantly expensive. Therefore, a method to reduce the computational complexity is expected to be very important. To this aim, Model Order Reduction (MOR) techniques are applied hierarchically, first to the thermal system of a PV module in service, and then extended to coupled thermo-mechanical

problems. A combination of proper orthogonal decomposition (POD) and discrete empirical interpolation method (DEIM) with a modified formulation is proposed for the first-order thermal equations of photovoltaic system during service and a new coupled second-order Krylov based formulation is developed for model order reduction of the coupled thermo-mechanical model of the photovoltaic module. The results of these reduction schemes show a huge computational gain in the reduced system solutions and a high accuracy of the reduced system outputs.

Sommario

Durante la laminazione, sollecitazioni termomeccaniche residue nascono nelle celle solari che compongono i moduli fotovoltaici. A seconda della configurazione del materiale e della geometrica degli strati del laminato, questo campo di tensione residuo può essere vantaggioso in quanto può portare ad uno stato sollecitazione di compressione nel Silicio inducendo effetti di richiusura nelle fessure, con un recupero della conducibilità elettrica nelle celle solari fessurate. È quindi importante indagare la distribuzione delle sollecitazioni termo-meccaniche all'interno del laminato al fine di ottimizzare l'accoppiamento tra la risposta elettrica e la deformazione elastica nel funzionamento dei moduli fotovoltaici. In questa tesi si propone un promettente approccio per la previsione delle tensioni residue mediante la teoria shear-lag per la modellazione degli strati di materiale polimerico incapsulante, considerando il suo comportamento termo-visco-elastico. Inoltre, la formulazione del problema termo-meccanico per l'analisi delle tensioni nel modulo fotovoltaico porta ad un sistema di equazioni differenziali ordinarie o alle derivate parziali di non agevole soluzione in forma chiusa. Per ridurre al minimo la complessità computazionale del modello di calcolo associato alla soluzione numerica, si propongono tecniche di Model Order Reduction applicate in modo gerarchico, innanzitutto al sistema di equazioni dovute al problema termico, successivamente estese al problema termo-meccanico accoppiato. Una combinazione del metodo del proper orthogonal decomposition (POD) e del

discrete empirical interpolation method (DEIM) con una formulazione modificata viene proposto per la soluzione delle equazioni termiche differenziali del primo ordine per prevedere la risposta del modulo fotovoltaico in condizioni di servizio, ed una formulazione originale accoppiata del secondo ordine basata sul metodo di Krylov per la riduzione del modello termomeccanico accoppiato. I risultati di questi algoritmi di riduzione portano ad un guadagno computazionale enorme grazie ai modelli ridotti, seppure preservando una notevole accuratezza.

Dedication

This PhD thesis is dedicated to my late father, Barrister Muslihudeen Olawale Imran.

Acknowledgement

This thesis was prepared as a result of research carried out at the department of Structural and Geotechnical Engineering, Politecnico di Torino under the supervision of Prof. Giuseppe Lacidogna and Prof. Marco Paggi.

Special thanks to my tutor Prof. Marco Paggi whom without this thesis would have been inconceivable. His purposeful tutelage on structural mechanics greatly assist in the execution of this task. My profound appreciation to Prof. Stefano Grivet-Talocia for introducing me to model order reduction techniques and advanced numerical procedures. Indeed, I have benefited from his wealth of experience.

I want to express my sincere gratitude to my wonderful mum, Fausat who has contributed immensely to my success throughout my career. The sacrifice and immense support of my lovely wife, Taofikat is highly acknowledged. My lovely sons Abdul Hakam and Muadh are acknowledged for their motivational and friendly activities. Finally, I am grateful for the unflinching support of my siblings throughout the course of my academic endeavours. Glory be to Allah.

CHAPTER 1

INTRODUCTION

1.1 Motivation

The necessity to reduce CO_2 emission has shifted the focus for global energy supply to renewable energy sources [1]. By reducing the production cost, increasing the module efficiency and improving the service lifetime of the module, the cost per KWh of PV power can be reduced [2]. Lifetime indicator (warranties) given by module manufacturer over the years has reached 25 years due to improved reliability studies which date back to early commercial production in the 1980s (see Figure 1.1).

To address the thermomechanical induced failure of photovoltaic (PV) modules, standard test like thermal cycling, hail and mechanical test are employed in order to imitate field service conditions for the modules [2]. Research studies have shown that silicon cells are under compressive stresses up to 76 MPa due to thermal cycling [3, 12]. On this basis, thermomechanical characteristics of the PV module during production and service can be determined and service life of the PV can be improved in turn.

Some of the critical issues relating to lifetime service of PV module are microcracking and fatigue degradation which can be present in case of repeated mechanical loading. These have been widely reported to affect the performance of

silicon cells [3, 4, 8, 10]. Due to mechanical and thermal loads which induce mechanical stresses in the encapsulated solar cells, photovoltaic modules may experience electrical power loss during service [4, 5]. The presence of different materials composing the layers of photovoltaic modules further complicates the distribution of stresses which in turn affects the phenomenon of crack propagation in the silicon solar cells. This is particularly the case when the module is cooled down in the laminator as shown in Figure 1.4 from a high temperature, which is the stress-free condition during the production stage, to the ambient temperature leading to a build-up of residual stresses after lamination due to the thermo-elastic mismatch between the materials composing the layers of a PV module. Depending on the thicknesses and on the thermo-mechanical properties of the layers composing the photovoltaic module, compressive stresses in silicon may lead to a crack closure state, which is positively influencing the recovery of electrical conductivity in the cracked regions [3]. This coupling between the electrical response and the elastic deformation in the presence of cracking is an important concept which can be used to improve the lifetime of silicon solar cells. On the other hand, high stress concentrations might arise in critical points of the laminates, promoting layers delamination after exposing the module to the environment, causing thermoelastic deformation which may induce failure of the busbars connecting solar cells, due to an increase in the gap between cells, as experimentally and numerically studied in [6, 4]. Moreover, cyclic thermoelastic stresses are responsible for crack growth in silicon cells and a power-loss of the PV system in time. In all of these cases, it is important to accurately compute the temperature distribution in the plane of the solar cells [10], but also the temperature in the various layers [8] for the study of fully coupled thermomechanical problems. Similarly, the computation of thermal stresses and thermo-elastic displacements is of paramount importance both during the production process, and during the operating conditions of the module. Several research studies on thermo-elastic

lamination theory within the last few years have been dedicated to the distribution of stresses inside the laminate with a uniform temperature profile [11, 13, 14, 15] while other studies focused on modelling the behaviour of a PV module during thermal cycling and have shown that Silicon cells are under compressive stresses up to 76 MPa [12]. In view of the interaction between various fields (elastic, thermal and electric) that characterize a typical photovoltaic system as illustrated in Figure 1.3, a multiphysics approach has been proven to be very attractive [7].

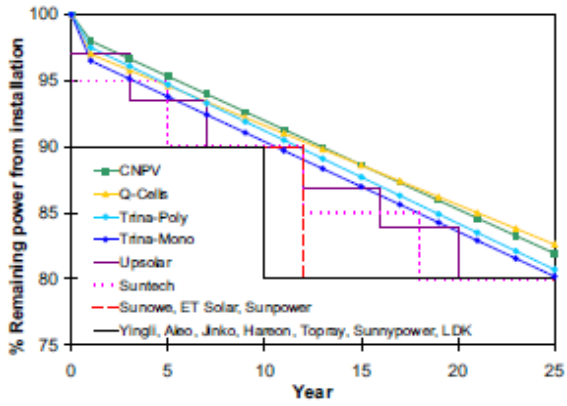

Figure 1.1 Comparison among warranty specifics declared by various producers of PV modules [5].

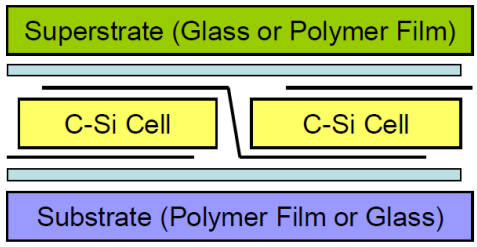

Figure 1.2. Cross-section of a PV module.

A photovoltaic (PV) system usually consists of an array of PV modules (e.g. 10), and each module contains several solar silicon cells (e.g. 60 or 70 in commercial modules) as shown in Figure 1.5. Each module is a layered composite such that the silicon cells are sandwiched between the different layers (see Figure 1.2 for a schematic representation of a module cross-section). So far, semi-analytical and numerical solutions [6, 4] for the assessment of the change in the gap between solar cells have been proposed by assuming a uniform temperature field across the module, which is an assumption holding for stationary conditions. In reality, temperature contour plots obtained from finite element thermal analysis [9] show that there is a temperature gradient across each layer, with the regions near the frame being significantly cooler, while the temperature distribution across the cells in the centre of the module is found to be quite uniform.

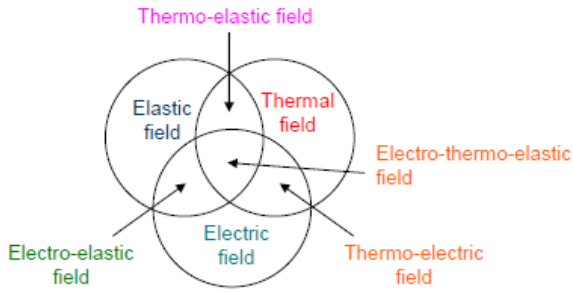

Figure 1.3 Interplay among the elastic, the thermal and the electric fields in PV modules [5].

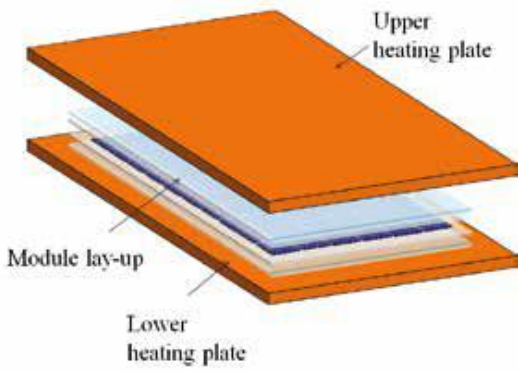

Figure 1.4 Representation of a symmetrical laminator for PV module production [101].

In addition, existence of cracks in the silicon cells may induce a localized temperature increment (hot spots) in the region near the cracks due to a localized electrical resistance [7]. Moreover, transient regimes, such as those taking place in accelerated environmental tests within climate chambers, or under operating conditions, have only marginally been investigated due to the inherent complexity related to the very different thicknesses of the layers composing a PV module. In such cases, accurate predictions require the solution of large systems of equations resulting from the finite element or finite difference approximation of the partial differential equations governing the problem of heat conduction and thermomechanical deformation. Suitable techniques for reducing the computational requirements for such simulations are therefore highly desirable.

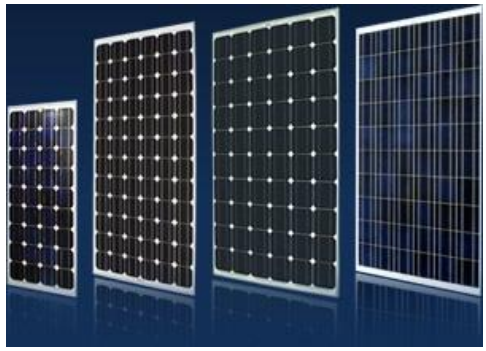

Figure 1.5 Real PV modules of different sizes.

Model order reduction (MOR) is a numerical procedure that is performed to find a low order approximation of the original high order model with the main objective of obtaining best approximation of the output of the original system. In other words, the purpose of MOR is to minimize the error between the outputs of the original system and the reduced-order model as illustrated in Fig. 1.6 [78]. One of the most significant gain of MOR scheme is the decrease in runtime of repeated simulations. With respect to thermomechanical simulations of PV modules, model formulations lead to derivation of systems of higher order ordinary differential equations or higher order partial differential equations in which the exact solution is either too complex to be derived or it is not feasible at all. On the other hand, implementing suitable numerical solutions for the system equations with many degrees of freedom may be computationally expensive to accomplish or may give rise to significant errors in the final result due to inherent errors in the numerical scheme. By performing model order reduction of the system equations based on minimization of some predefined error functions and deleting less important states and using an input function $u(t)$ (see Fig. 1.6) to train the system, it is possible to match some parameters of the original and reduced systems. In case of repeated simulations, the reduced-order model can be excited with desirable input signals to determine the system response.

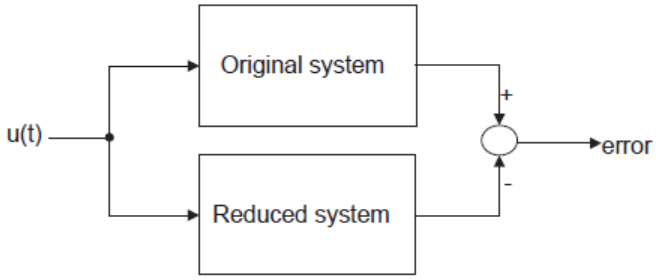

Figure 1.6. Order reduction by minimization of the difference of the outputs [78].

Early model reduction methodologies in structural fields are based on mode superposition methods [104] or its variant such as mode acceleration method [104, 105]. In these methods, small number of free vibration modes is used to represent the system dynamics with reduced number of generalized degrees of freedom. However due to some computational limitations associated with these methods, other efficient methods such as Krylov subspace methods have been proposed. These methods approximates a large system with many degrees of freedom with a small system with fewer degrees of freedom and similar input-output behaviour. The method proposed in this work for reduction of second-order thermomechanical system is based on the Krylov subspace method and a review of the variants of this method is discussed in detail in Chapter 3.

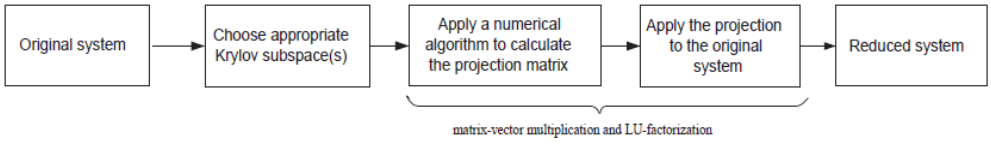

Figure 1.7. Main steps of Krylov subspace method [78].

1.2 Outline of the thesis

In the next Chapter, a brief discussion on current Silicon collar cell technology is presented. The focus is mainly on single crystalline and multicrystalline Silicon solar cell technology as it constitutes the major share of the production market. Layer-by-layer material composition and properties of PV module are presented and finally, recent developments in reliability studies of PV modules are highlighted.

Fundamental theory of isotropic linear thermoelasticity is presented in Chapter 3 with specific focus on linear elasticity and linear viscoelasticity. A major review of methods to estimate the behaviour of viscoelastic materials is expatiated. This is followed by detailed discussion on theory of thermomechanics based on small displacement principle. Method of derivation of equilibrium equations for plates using Kirchhoff's theory are shown.

Since equilibrium equations for thermomechanical models leads to derivation of system of differential equations, Chapter 4 is focused on a review of method for solution of system of linear partial differential equations. Exact solution methods for homogeneous and non-homogeneous initial and boundary value problems are presented. Discussed in detail is the numerical solution by method of implicit finite difference for first order and second order system and a special treatise on non-uniform finite difference method is mentioned in brief. Techniques for finite difference discretization at the boundary for structural system are also emphasized. Finally, a review of the fundamentals of model order reduction techniques for first-order and second-order systems is presented.

In Chapter 5 a detail formulation for coupled thermomechanical shear-lag model is developed. Following the 2D derivation is an extension to 3D formulation for

comprehensive stress analysis of the PV module. Results of residual stresses are for 2D and 3D cases are provided with detailed analysis.

Chapter 6 is focused on model order reduction application to thermomechanical models for PV modules and a step-by-step application is offered for thermal system with a first-order formulation and extended to coupled second-order thermomechanical model developed in chapter 5 with a newly proposed coupled second-order structure-preserving formulation. Numerical examples are presented showing the suitability of the order reduction schemes for PV systems.

Chapter 7 is the concluding part of this work where general discussions about the developed shear-lag models for PV systems are presented and promising applications of proposed model order reduction techniques to PV systems are highlighted. Further developments and recommendations for improvement on current models are also mentioned.

CHAPTER 2

PHOTOVOLTAIC MODULES: MATERIALS AND PRODUCTION

2.1 Introduction

A photovoltaic module is a unit comprising several PV cells which is intended to generate direct current (DC) electrical power from semi-conductors under illumination of photons from un-concentrated sunlight [17, 18]. Two categories of technology commonly used for the manufacturing of PV cells are crystalline Silicon and thin films as illustrated in Figure 2.2. Crystalline Silicon are manufactured either as a single or multicrystalline wafers or ribbons which was reported in 2001 to account for almost 90% of worldwide production [17] (see Fig. 2.1).

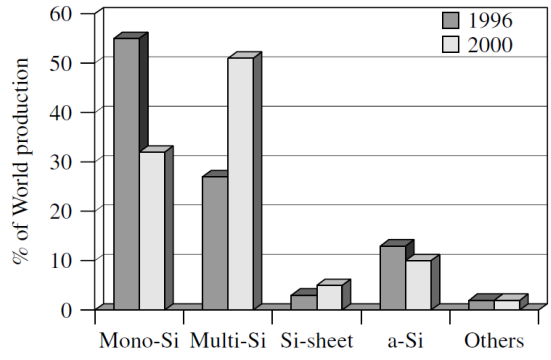

Figure 2.1. PV market distribution by technology [17].

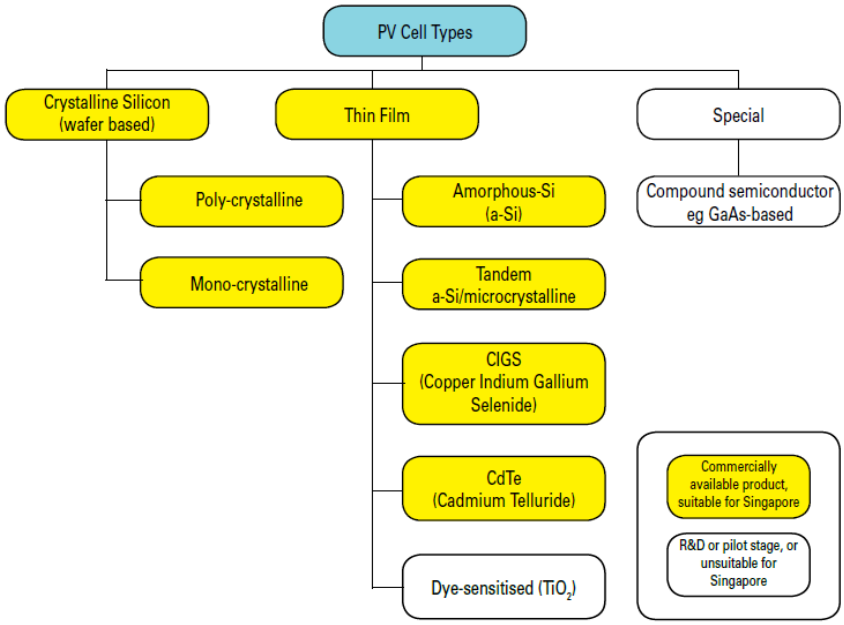

Figure 2.2. PV technology.

2.2 Production of photovoltaic modules

Production of Silicon starts with carbothermic reduction of silicates in an electric arc furnace, a process where metallurgical grade silicon (MG-Si) reacts with HCl to form a range of chlorosilanes, including tri-chlorosilane (TCS). A detail representation of the production stages is illustrated in Fig. 2.3 [19].

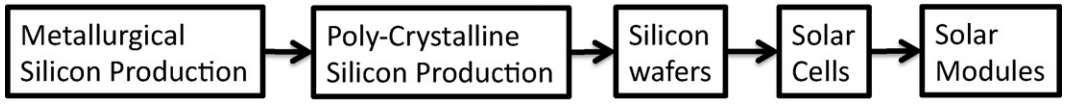

Figure 2.3. Supply chain for solar cell modules.

By passing TCS over high purity silicon starter rods in a bed reactor, TCS is heated to 1150 ^{0}C through electrical resistive heating and the gas decomposes according to the chemical equation:

$$2HSiCl_3 \rightarrow Si + 2HCl + SiCl_4$$

This process results in the deposition of a solar grade Silicon (SOG-Si) on the silico rods which can be used to produce high quality solar cells. The next step entails production of thin Silicon wafers which are typically of $200 - 300$ µm size thickness. The Silicon wafers are then treated with chemicals to enhance optical and electrical properties after which the Silicon is doped with phosphorous or boron to produce the p-n junction for the supply and extraction of electrons in the conduction bands. To reduce reflection losses at the front surface, the Silicon is coated with anti-reflection layers which trap incident light within the cell. Finally, front and back electrical contacts are added to complete the production process [19, 22].

2.2.1 Lamination

The components needed for the encapsulation of the Silicon cell are [20]:

- Superstrates: Glass / polymeric layer (PGT)
- Encapsulant: Poly (ethylene-co-vinyl acetate) or EVA
- Substrates: Backfoils (or Backsheet)
- Edge seals

The encapsulation process takes place in a high performance vacuum laminator where the laminate as configured in Fig. 1.2 is heated up to a temperature of about 150 ^{0} C for about 30 minutes. Typically there are two stages involved in the encapsulation process: The lamination process to bond the different layers together

which occurs at a temperature of 110 – 120 ^{0}C and curing process to enable cross-linking of the EVA polymer and this occurs at a temperature of about 140 – 150 ^{0}C. These processes can be actualized as a single step in the laminator (fast cure) or double step, lamination in the laminator and curing in the oven (slow cure). It should be noted that the lamination process depends on numerous variables such as temperature (heating plate, membrane and temperature rates), the time (insertion time, time on pins, time on plate, curing time and cooling time) and the pressure (upper and lower chamber as well as the pressure application rates) [20, 21, 23]. Systematic research (experimental and simulation) to optimise the process to obtain the fastest cycle time which guarantees high quality process are continuously being performed.

2.3 Material composition and properties

A typical PV module is designed as a stack of materials with different geometrical, thermal, mechanical and electrical properties. This design configuration is indeed responsible for the complicated nature of thermomechanical simulation of PV modules. Investigations to enhance material performance and consequently reliability of PV modules are continuously being undertaken. In this section, a layer-by-layer composition of the module is discussed and the properties of different materials which compose the module are highlighted.

2.3.1 Crystalline Silicon (C-Si)

A standard Silicon cell is made up of 150 – 350 nm deep diffusion layer of phosphorous or boron doped Silicon, a passivation layer of Silicon nitride (anti-reflective coating) of about 80 nm thickness, a metallization grid of 15 – 25 μm thick H-like pattern silver paste at the front (divided into two device elements namely contact busbars and contact fingers) for efficient carrier transport, a 25 – 50 μm thick metallization of aluminium at the back (contact pads) to enhance

mechanical contact and collect current from the metallized area and a front surface of 2 – 15 µm high randomly distributed pyramids to increase photon transmission into the Silicon absorber [2, 23].

Crystalline Silicon cells are made into standard sizes of $125\ \text{mm} \times 125\ \text{mm}$ or $156\ \text{mm} \times 156\ \text{mm}$ pseudo-square or full-squared (see Fig. 2.4). Crystalline silicon investigated in this work is oriented in the crystallographic direction of < 100 > i.e. the edges of the Silicon cells are parallel to the [100] direction. As cubic symmetry holds in this direction, it follows that:

$$\mathrm{E}_{<100>} = \mathrm{E}_{<010>} = \mathrm{E}_{<001>} = \mathrm{E}_x = \mathrm{E}_y = \mathrm{E}_z$$

To complete the parameter requirements for thermomechanical simulation, thermal properties such as density, thermal conductivity as well as specific heat capacity of the Silicon cells have to be specified. Table 2.1 shows in details material properties for the Silicon cells considered in this study.

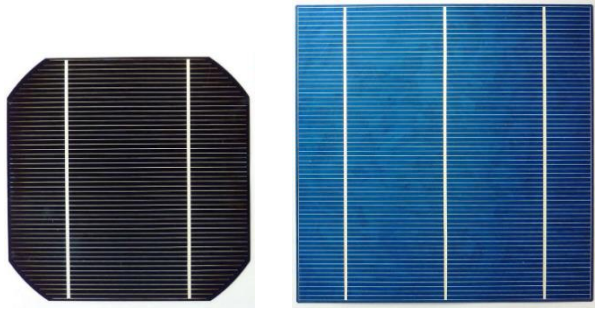

Figure 2.4. Crystalline Silicon cell as a finished product.

2.3.2 Interconnectors

These are highly conductive solder coated ribbon strips along the length of the cell which extended part is soldered to the back of a neighbouring cell to enable current transfer from the front of one cell to the back of a neighbouring cell in series connections [24, 25]. The size of a typical ribbon for Silicon cell is 130 μm thick and 2 mm wide while the solder coating has thickness of 20 μm. Infra-red soldering method is used to attach the interconnect to the solar cell, a process which may induce high thermomechanical stresses in the module and in turn accelerate fatigue failure. Alternatively, a well-controlled laser soldering technology may be used which delivers heat fast, and efficiently on a small area of the solder interconnection with minimum physical contact with the crystalline silicon [25].

2.3.3 Glass

The general criteria for selection of glass superstrate include low iron content, high transmittance, tempered, toughened, pre-stressed, plain or textured [2, 20, 26]. Typically, the standard size for a float glass for solar application is 4 mm and the glass is designed to provide mechanical rigidity, optical transparency, impact resistance (hail), electrical insulation and outdoor weatherability [2]. To modify performance for specific needs, some glass superstrate are supplied with anti-reflective and corrosion retarded coatings [27]. In general for thermomechanical simulations, mechanical and thermal properties of glass are essentially required parameters. Glass properties considered in this study are enumerated in Table 2.1.

2.3.4 Encapsulant

This is the adhesive material that provides chemical and physical bond between different layers of the PV module. The use of EVA encapsulant has been field-proven over 20 years due to its favourable optical, physical electrical, mechanical

and thermal properties. EVA is a viscoelastic material which transform from viscous material at high temperature in the laminator to elastomeric material after lamination [2, 6, 28]. Like other viscoelastic materials, EVA properties have strong dependence on time and temperature during lamination. This is confirmed from experimental studies [2] which results are shown in Fig. 2.5.

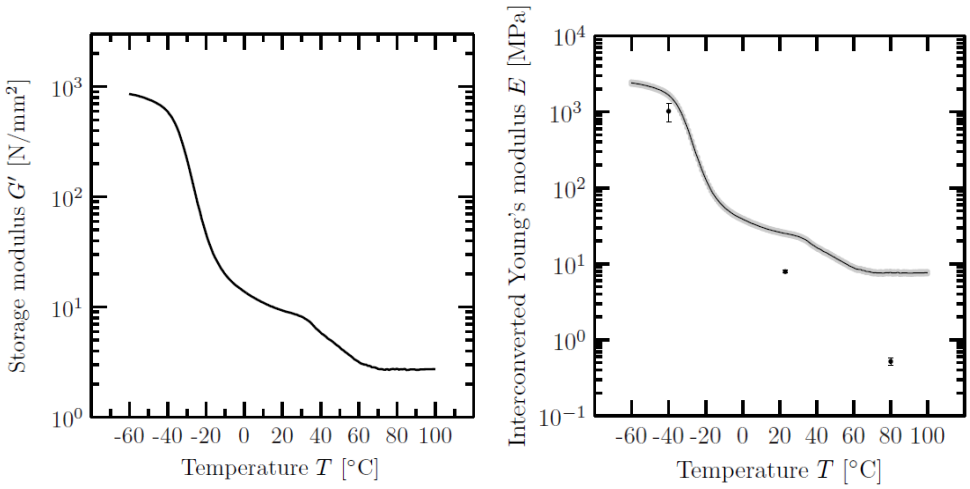

Figure 2.5 Temperature dependence of Storage modulus and Young's modulus of EVA [2].

To accurately determine and model the temperature dependent properties of EVA, uniaxial relaxation tests have to be performed and then traditionally interpreted by using rheological models à la Maxwell. A detail study of the procedures to obtain the properties of EVA using classical Maxwell model has been presented in [2]. Other efficient methods to determine viscoelastic material properties has also been proposed in [28, 29, 30, 31]. In this study, we have implemented proposed models as described in [2, 28, 31] for thermomechanical simulations using the shear-lag theory. An overview of the different modelling and identification procedures used in this study for determination of material viscoelastic properties is discussed

within the framework of linear viscoelasticity in the next chapter. Geometrical and thermal properties of EVA are detailed in Table 2.1.

Other examples of non-EVA encapsulant are PVB, silicones, ionomer, TPU e.t.c. The requirements of a good encapsulant include but not limited to high density breakdown, high volume resistivity, high adhesion strength, mechanically strong and resistant to break, low moisture absorption, high resistant to ultraviolet light, resistant to moisture induced delamination. Some of the functions of an encapsulant are electrical and physical insulation for the solar cell, mechanical support and physical support against environmental degradation [20].

2.3.5 Backsheet

This is the outermost layer on the rear side of the PV module to protect the solar cell and the encapsulant from environmental degradation while acting as an electrical insulator [32, 33]. Backsheet are multi-layered polymeric materials with different compositions such as TPT-primed (Tedlar/ PET /Tedlar), TPE (Tedlar/ PET /EVA) or PVF (polyvinyl fluoride) [20]. For the shear-lag model described in the work, mechanical and thermal properties of the backsheet are reported in table 2.1.

Table 2.1. Material properties of PV module.

Layer	Thickness (mm)	Elastic modulus (MPa)	Coefficient of thermal expansion	Poisson's ratio	Thermal conductivity (W/ m K)	Density (Kg/ m^3)	Specific heat capacity (J/ Kg K)
Glass	4	73000	8×10^{-6}	0.23	1.8	3000	500
EVA	0.5	Viscoelastic	2.7×10^{-4}	0.35	0.35	960	2090
Silicon cell	0.166	130000	2.49×10^{-6}	0.28	148	2330	677
Backsheet	0.1	2800	5.04×10^{-5}	0.4	237	2700	900

2.4 Reliability and durability of photovoltaic modules

After the installation of a solar panel on site, some challenges arise during service which affect the long term performance of the panel. Key criteria to measure reliability of solar panels for long term service are efficiency with which sunlight is converted into power and how this relationship changes with time [34]. Common challenges encountered in long term service of the module may include corrosion due to harsh environment (including moisture and heat), interconnect cracking and failure due to poorly specified material and processes and poor lamination quality, cell cracks due to wind storm, hot spot due to current mismatch or voltage mismatch which arises from shading of the connected solar cells (see Fig. 2.6). Long term service of the module are affected by these problems which effects range from increase resistance at the solar cell, reduction of current flow and loss of efficiency, delamination, micro-cracking and power loss [35].

Of particular importance in the reliability assessment of PV module are failures which occur at the end of working lifetime (wear-out failures). Common failures in this category are delamination of encapsulant and/or loss of elastic properties, cell part isolation and discolouration of the laminate encapsulant which may lead to power loss of 10% in the mean [36]. To eliminate these problem requires careful selection of adhesive and primers which are stable to UV and moisture, control of raw materials and processes and most importantly, module testing.

Standard tests to predict and possibly improve reliability of the module during service may include environmental stress test, mechanical load test, humidity freeze test, accelerated aging test, hotspot endurance test, thermal cyclic test and glass breakage test [35, 36]. These standard physical tests are usually expensive to perform, hence the need for simulation strategy to complement physical experiments for efficient reliability assessment.

Numerical approaches to reliability assessment of PV module is increasingly being adopted as reported in [7, 10, 37, 38]. Particularly promising is a multi-physics approach which treats the coupling between various fields governing the behaviour of PV module in service (see Fig. 1.3).

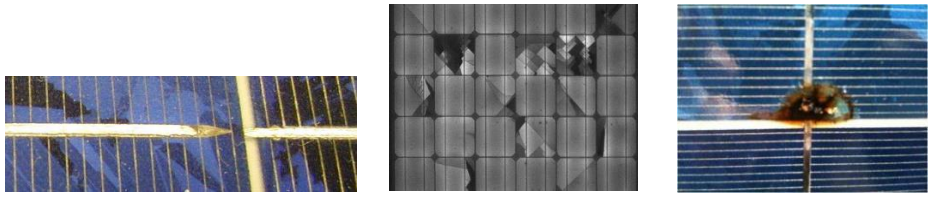

(a) (b) (c)

Figure 2.6 (a) Corrosion of cell interconnects or soldering joints (b) Crack solar cell (c) Solar cell hotspot.

CHAPTER 3

THERMO-VISCOELASTICITY OF COMPOSITE LAMINATES

3.1 Introduction

Most composite laminate structures are composed of various types of materials representing different layers. Reliability and life of such structures depends on the internal microstructural characteristics of the materials as well as on the structural design parameters. In thermomechanics of solids, conservation principles e.g., equations of continuity, motion and energy (thermodynamics) are frequently invoked in form of differential equations which express balance of conserved quantities over differential volume elements. To produce a well posed problem that can be solved by standard mathematical methods requires additional equations which constitute mathematical description of individual material response or behaviour. Such equations which are called constitutive equations are available for a whole group of material behaviours such elastic, viscoelastic, plastic and so on. With regards to thermomechanics of PV laminates, elastic and viscoelastic material behaviours have been identified to ideally represent the system response of the layers of the PV module during lamination. In line with these realities, a review of thermomechanical theories of solids with elastic and viscoelastic material behaviour is presented in this chapter.

3.2 Linear thermo-elasticity of an isotropic solid

The governing equations for isotropic thermoelastic solid in a steady state are:

- Equilibrium equations:

$$\frac{\partial \sigma_{ij}}{\partial x_j} + X_j = 0 \qquad i,j = 1,2,3 \tag{3.1}$$

where σ_{ij} is the stress tensor, X_j is the force vector and x_j is the vector of coordinates.

- Thermoelastic constitutive (stress-strain) relations:

$$\sigma_{ij} = \lambda e_{kk}\delta_{ij} + 2Ge_{ij} - \beta\delta_{ij}\theta \tag{3.2}$$

where

$$\lambda = \frac{Ev}{(1+v)(1-2v)}, \qquad G = \frac{E}{2(1+v)}, \qquad \beta = \frac{E\alpha}{2(1+v)}, \qquad \theta = T - T_o$$

e_{ij} is the strain tensor, δ_{ij} is the Kronecker's delta, E is the elastic modulus and v is the Poisson's ratio. T is the body temperature, T_o is the reference temperature and α is the coefficient of thermal expansion.

Eq. (3.2) can be expressed in strain-stress form as:

$$e_{ij} = \frac{1+v}{E}\sigma_{ij} - \frac{v}{E}\sigma_{\mu\mu}\delta_{ij} + \alpha\theta\delta_{ij} \tag{3.3}$$

- The small displacement strain-displacement relations:

$$e_{ij} = \frac{1}{2}\left(u_{i,j} + u_{j,i}\right) \tag{3.4}$$

And the compatibility equations must be satisfied.

The temperature distribution θ can be determined from the energy conservation equation:

$$\frac{dU}{dt} = T\frac{\partial S}{\partial t} + \frac{1}{\rho}\sigma_{ij}V_{ij} \tag{3.5}$$

where U is the internal energy, S is the entropy and

$$V_{ij} = \frac{1}{2}\left(\frac{\partial v_i}{\partial x_j} + \frac{\partial v_j}{\partial x_i}\right) \tag{3.6}$$

is the rate of deformation tensor where v_i is the velocity vector.

From the equation above i.e. from Eqs. (3.5) and (3.6), the thermal energy balance equation can be derived as:

$$\frac{\partial H}{\partial t} + \theta\beta_{ij}\frac{\partial e_{ij}}{\partial t} = \nabla.(k\nabla\theta) + r \tag{3.7}$$

where H is the enthalpy, β_{ij} is the experimentally determined numerical coefficient and r is the rate of internal energy generation.

By solving Eq. (3.7) subject to suitable initial and boundary conditions, the temperature field in the body can be determined. For steady state conditions in a medium of constant conductivity without internal heat generation, the harmonic function

$$\nabla^2\theta = 0 \tag{3.8}$$

has to be solved.

In uncoupled thermoelastic theory, the mechanical terms in the energy and heat equations are neglected so that heat conduction and thermoelastic problem can be handled separately.

By substituting the generalized thermoelastic constitutive equations Eq. (3.2) and strain-displacement relations Eq. (3.4) into Eq. (3.1), the generalized Navier's equation can be derived:

$$Gu_{i,\mu\mu} + (\lambda + G)u_{\mu,\mu i} + X_i - \beta\theta_{,i} = 0 \tag{3.9}$$

Equation (3.9) is the generalized thermomechanical equilibrium equation which together with the energy equation and the stress-strain constitutive relations constitute a set of relations to determine the unknown displacements u_i, stresses σ_{ij} and the temperature field θ. This system is complete and yields unique solution under suitable boundary conditions and resulting strain satisfies the compatibility conditions.

3.3 Isotropic linear visco-elastic model

Viscoelasticity is a time-dependent mechanical response to loading exhibited by mostly polymeric materials. In other words, viscoelasticity combines time independent elastic behaviour and time dependent viscous behaviour, hence the linear viscoelastic constitutive relation

$$\sigma = C\epsilon + \eta\frac{d\epsilon}{dt} \tag{3.10}$$

in which the first term describes the elastic behaviour while the second term describes the viscous behaviour. This relation is referred in the literature to as Voigt model. This model fails to describe the phenomenon of stress relaxation mathematically described as $G(t) = {}^{\sigma(t)}/_{\mathrm{e}}$ or creep described as $J(t) = {}^{\mathrm{e}(t)}/_{\sigma}$ where $G(t)$ and $J(t)$ are, respectively, the time dependent stress relaxation modulus and creep compliance. To account for these viscoelastic behaviours, Boltzmann proposed the superposition principle to compute the stress-strain

response of a viscoelastic solid subjected to an arbitrary loading history. He proposed for an applied stress $\sigma(t)$, strain as [106]:

$$\mathrm{e}_{ij} = \int_{-\infty}^{t} J_{ijkl}(t-\tau)\frac{\partial \sigma_{kl}}{\partial \tau}d\tau \tag{3.11}$$

And for applied strain $e(t)$, stress as

$$\sigma_{ij} = \int_{-\infty}^{t} G_{ijkl}(t-\tau)\frac{\partial \mathrm{e}_{kl}}{\partial \tau}d\tau \tag{3.12}$$

where G_{ijkl} and J_{ijkl} are the experimentally determined tensorial relaxation modulus and creep compliance function.

For an isotropic solid, Eq. (3.12) can be decomposed into deviatoric and the volumetric part such that the constitutive relations is formulated in terms of the shear relaxation modulus $G(t)$ and bulk relaxation modulus $K(t)$. Given that assumption of linearity holds for polymeric materials up to small strains in the range of few percent, the constitutive relation for isotropic linear viscoelasticity is given as [2, 39]:

$$\boldsymbol{\sigma} = \int_{-\infty}^{t} G(t-\tau)\dot{\mathbf{e}}(\tau)d\tau + K\mathrm{tr}(\mathbf{e}(t)) \tag{3.13}$$

or

$$\boldsymbol{\sigma} = \boldsymbol{s}(t) + \boldsymbol{p}(t) \tag{3.14}$$

where $\boldsymbol{s}(t) = \int_{-\infty}^{t} G(t-\tau)\dot{\mathbf{e}}(\tau)d\tau$, $\boldsymbol{p}(t) = K\mathrm{tr}(\mathbf{e}(t))$

It is noted that the relations above are generalization of the Maxwell material and indeed the integral equation can be defined as a generalized Maxwell model by making $G(t)$ to assume the Prony series form:

$$G(t) = G_{\infty} + \sum_{i=1}^{N} G_i \exp\frac{-t}{\lambda_i} \tag{3.15}$$

or alternatively

$$G(t) = G\left(\mu_0 + \sum_{i=1}^{N} \mu_i \exp\frac{-t}{\lambda_i}\right) \tag{3.16a}$$

where G is the instantaneous modulus i.e. $G(t=0)$. At $t=0$,

$$G(t=0) = G_\infty + \sum_{i=1}^{N} G_i \tag{3.16b}$$

and it is remarked from Eq. (3.16a) that:

$$\mu_0 + \sum_{i=1}^{N} \mu_i = 1$$

where G_i and λ_i represent, respectively, shear relaxation modulus and relaxation times for each Maxwell's arm. N is the number of Maxwell arms taken into account in the approximation and G_∞ is the long term shear modulus once the material is totally relaxed at an infinite time.

The integral representation of $\boldsymbol{s}(t)$ in Eq. (3.14) can be simplified by dividing the integral into [39]:

$$\int_{-\infty}^{t}(.) = \int_{-\infty}^{0-}(.) + \int_{-0}^{0+}(.) + \int_{0+}^{t}(.)$$

Given that material is undisturbed until a time identified as zero, the first term is zero and the result of this separation applied to $\boldsymbol{s}$ in Eq. (3.14) gives:

$$\boldsymbol{s}(t) = 2G(t)\mathbf{e}_0 + 2\int_0^t G(t-\tau)\dot{\mathbf{e}}(\tau)d\tau \tag{3.17}$$

where the first term is a jump associated with $\mathbf{e}_0$ at time $t=0$ and the second term covers the subsequent strain history.

By substituting Eq. (3.16) into Eq. (3.17), we obtain:

$$\boldsymbol{s}(t) = 2G\left[\mu_0\mathbf{e}(t) + \sum_{i=1}^{N}\mu_i \exp\frac{-t}{\lambda_i}\left(\mathbf{e}_0 + \int_0^t \exp^{\frac{t}{\lambda_i}}\dot{\mathbf{e}}(\tau)d\tau\right)\right] \tag{3.18}$$

According to [31, 39], the integral in Eq. (3.18) can be numerically evaluated as:

$$\int_0^t (.) = \int_0^{t_n} (.) + \int_{t_n}^t (.)$$

By defining integral variables as:

$$\mathbf{i}^i(t) = \int_0^t \exp^{\frac{\tau}{\tau_i}}\dot{\mathbf{e}}(\tau)d\tau \tag{3.19}$$

and with the above separation, Eq. (3.19) becomes:

$$\mathbf{i}^i(t) = \mathbf{i}^i(t_n) + \int_{t_n}^t \exp^{\frac{t}{\lambda_i}}\dot{\mathbf{e}}(\tau)d\tau \tag{3.20}$$

Let $\mathbf{h}^i(t) = \exp^{\frac{t}{\lambda_i}}\mathbf{i}^i(t)$ (3.21)

$\mathbf{h}^i$ at time t_{n+1} can now be written as:

$$\mathbf{h}_{n+1}{}^i = \exp^{\left(\frac{-\Delta t}{\lambda_i}\right)}\mathbf{h}_n{}^i + \Delta\mathbf{h}^i \tag{3.22}$$

It is remarked that $\mathbf{h}_0{}^i = \mathbf{e}_0$ from Eq. (3.18), and:

$$\Delta\mathbf{h}^i = \int_{t_n}^{t_{n+1}} \exp^{-\left(\frac{t_{n+1}-\tau}{\lambda_i}\right)}\dot{\mathbf{e}}(\tau)d\tau \tag{3.23}$$

By approximating the strain rate $\dot{\mathbf{e}}(\tau)$ as constant over each time increment t_n to t, we get:

$$\dot{\mathbf{e}}(\tau) = \frac{\mathbf{e}_{n+1}-\mathbf{e}_n}{\Delta \mathrm{t}} \tag{3.24}$$

where $\mathbf{e}_n$ denotes strain at time t_n and $\Delta \mathrm{t} = t_{n+1} - t_n$.

With this approximation, Eq. (3.23) becomes:

$$\Delta \mathbf{h}^i = \frac{1}{\Delta t}\int_{t_n}^{t_{n+1}} \exp^{-\left(\frac{t_{n+1}-\tau}{\lambda_i}\right)} (\mathbf{e}_{n+1} - \mathbf{e}_n) d\tau \tag{3.25}$$

The integral in Eq. (3.25) can now be directly evaluated to obtain:

$$\Delta \mathbf{h}^i = \frac{\lambda_i}{\Delta t}\left[1 - \exp^{-\left(\frac{\Delta t}{\lambda_i}\right)}\right](\mathbf{e}_{n+1} - \mathbf{e}_n) = \Delta h^i (\mathbf{e}_{n+1} - \mathbf{e}_n) \tag{3.26}$$

where $\Delta h^i = \frac{\lambda_i}{\Delta t}\left[1 - \exp^{-\left(\frac{\Delta t}{\lambda_i}\right)}\right]$

This approximation has the advantage of being doubly asymptotically accurate as it produces stable results for small time steps and large time steps and also gives smooth transitions under variable time steps.

The constitutive relation (3.18) now takes the form:

$$\boldsymbol{s}_{n+1} = 2G\left[\mu_0 \mathbf{e}_{n+1} + \sum_{i=1}^{N} \mu_i \, \mathbf{h}_{n+1}{}^i\right] \tag{3.27}$$

By substituting $\mathbf{h}_{n+1}{}^i$ into Eq. (3.27) and differentiating, we can determine the stress increment at time t_{n+1} as:

$$\frac{\partial \boldsymbol{s}_{n+1}}{\partial \mathbf{e}_{n+1}} = 2G\left[\mu_0 + \sum_{i=1}^{N} \mu_i \, \Delta h^i(\Delta t)\right] = 2G_{visc} \tag{3.28}$$

where G_{visc} is the equivalent shear relaxation modulus for the evaluation of EVA properties in the PV laminate.

3.3.1 Estimation of relaxation parameters

It is shown in Eq. (3.28) that relaxation parameters μ_i and λ_i are needed to estimate the equivalent shear relaxation modulus for evaluation of viscoelastic properties. This section highlights procedures to obtain experimentally, the relaxation parameters for accurate modelling of EVA properties.

The procedure to obtain these parameters are mainly [2]:

a. Determination of tensile relaxation modulus and creep compliance at different constant temperatures.
b. Time-temperature superposition of relaxation and creep functions.
c. Interconversion of tensile data to shear relaxation modulus.
d. Fitting generalized Maxwell model to a mastercurve.

Eitner [2] carried out a tensile test on laminated EVA to determine the tensile relaxation moduli and tensile creep compliance at different constant temperatures. The results indicate strong dependence of EVA properties on the temperature as shown in Fig. 3.1.

Performing the tensile tests to obtain the relaxation modulus $E(t)$ and creep compliance $J(t)$, interconversion between different deformation modes is deemed necessary to determine the shear relaxation modulus $G(t)$ which can then be fitted to the generalized Maxwell model in Eq. (3.16). To achieve this, elastic-viscoelastic correspondence principle is applied using the Laplace transform on the stress-strain constitutive relations in order to express the applied stress during uniaxial tests in terms of the shear modulus. The transformed constitutive relations is given as:

$$\bar{\sigma}_{11}(s) = 2s\bar{G}(s)(\bar{\mathrm{e}}_{11}(s) - \bar{\mathrm{e}}_{22}(s)) \tag{3.29}$$

which can now be inverse transformed to obtain an expression for the unknown $G(t)$ as:

$$\sigma_{11}(t) = 2G(t)\big(\mathrm{e}_{11}(0) - \mathrm{e}_{22}(0)\big) + 2\int_0^t G(\tau)\frac{d\big(\mathrm{e}_{11}(t-\tau) - \mathrm{e}_{22}(t-\tau)\big)}{d\tau}d\tau \tag{3.30}$$

where σ_{11}, e_{11} and e_{22} are known from the relaxation and creep tests. To solve Eq. (3.30), a recursive interconversion procedure is applied by using numerical interconversion formulas from which G is calculated from discrete test data. This

procedure which is explained in details in [2] produces the shear relaxation modulus G within the range of numerical errors.

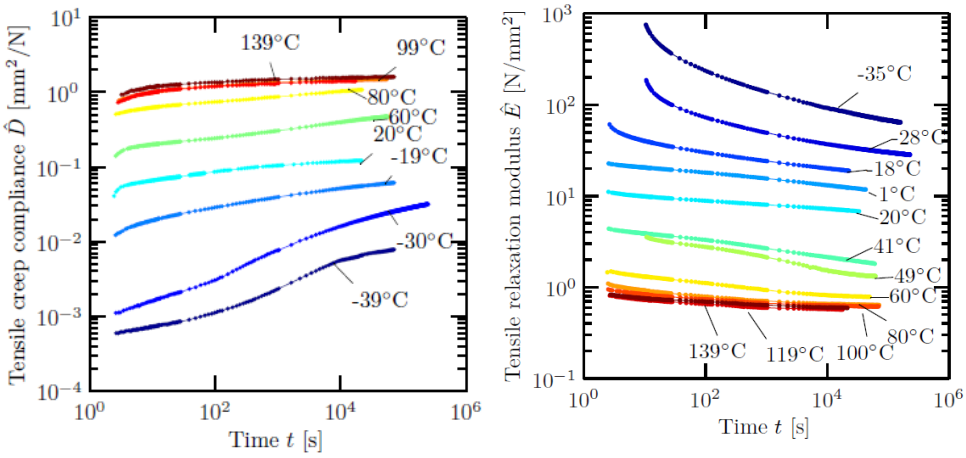

(a) (b)

Figure 3.1 (a) Tensile relaxation moduli for laminated EVA at constant temperatures (b) Tensile creep compliance for laminated EVA at constant temperatures [2].

As an example, Fig. 3.2 shows interconverted G for relaxation and creep tests at 60℃ and 39℃ respectively.

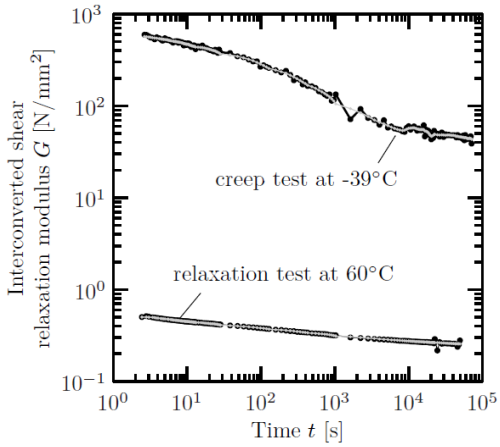

Figure 3.2 Interconversion of two different experiments via recurrence formula (black) and regularized formulation (grey) [2].

To account for the strong sensitivity of EVA to temperature, a time-temperature superposition can be applied. This procedure involves shifting the relaxation curves along the logarithmic time axis to another curve from a slightly different temperature which results in the overlapping of both curves. The new curve now covers a larger time domain at the constant (reference) temperature of the unshifted curve. This procedure can be applied to several relaxation curves to create a relaxation curve known as a mastercurve which covers a time domain which cannot be practically included in one experiment.

Typically, for 2 isothermal curves at T_{ref} and T_1, a modulus value is selected at different times and the modulus value $E(t, T_1)$ at T_1 is then shifted to T_{ref} according to the relation:

$$E(t, T_1) = E\left({}^{t}/_{\alpha_{T_{\mathrm{ref}}}(T_1)}, T_{\mathrm{ref}}\right) = E(t_{\mathrm{red}}, T_{\mathrm{ref}}) \tag{3.31}$$

where $\alpha_{T_{\mathrm{ref}}}(T_1)$ is the shift factor, a material property which indicates how far the relaxation curve at T_1 has to be shifted to overlap the curve at T_{ref} and t_{red} is the reduced time representing the shifted time scale. The relationship between t_{red} and $\alpha_{T_{\mathrm{ref}}}(T_1)$ is expressed as:

$$t_{\mathrm{red}} = \xi(t) = \int_0^t \frac{1}{\alpha_{T_{\mathrm{ref}}}(T(\tau))} d\tau \tag{3.32}$$

To implement the reduced time into viscoelastic constitutive relation, a derivation of temperature-dependent viscoelastic constitutive relation is expressed as [40]:

$$\sigma(t, T(t)) = \int_0^t E(\xi(t) - \xi(\tau), T_{\mathrm{ref}}) \dot{\mathrm{e}}(\tau) d\tau \tag{3.33}$$

The shift factor $\alpha_{T_{\mathrm{ref}}}(T)$ is needed to estimate $\xi(t)$ in Eq. (3.33) and this can be achieved by using empirical models in the literature. For example, to approximate the shift factor as a function of temperature, respectively, below the glass transition temperature T_{G} and for temperatures between $T_{\mathrm{G}} - 10$ and $T_{\mathrm{G}} + 100$, the Arrhenius model and the Williams-Landel-Ferry (WLF) model are widely used and are expressed as:

$$\log_{10} \alpha_{T_{\mathrm{ref}}}(T) = \frac{E_A}{2.303R}\left(\frac{1}{T} - \frac{1}{T_{\mathrm{ref}}}\right) \tag{3.34}$$

$$\log_{10} \alpha_{T_{\mathrm{ref}}}(T) = \frac{-C_1(T - T_{\mathrm{ref}})}{C_2 + T - T_{\mathrm{ref}}} \tag{3.35}$$

where E_A and R are the activation energy and the universal gas constant while C_1 and C_2 are fit parameters from the shift factor versus temperature curve. Fig. 3.3 shows the mastercure and shift factor values of EVA at a reference temperature of -20℃.

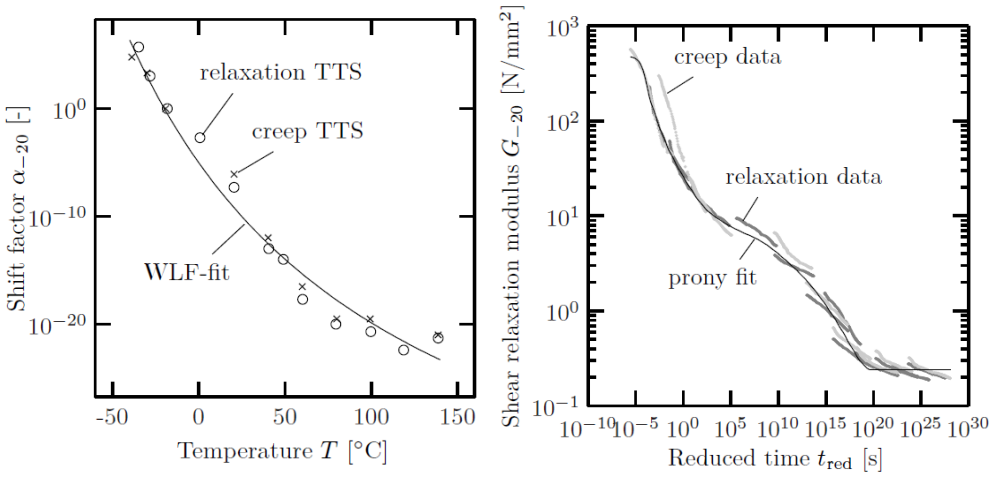

(a) (b)

Figure 3.3 (a) Values of α_{-20} from time-temperature superposition of EVA (b) Mastercurve and Prony fit of shear modulus G of EVA using interconverted data from relaxation and creep experiments and then shifted with WLF equation.

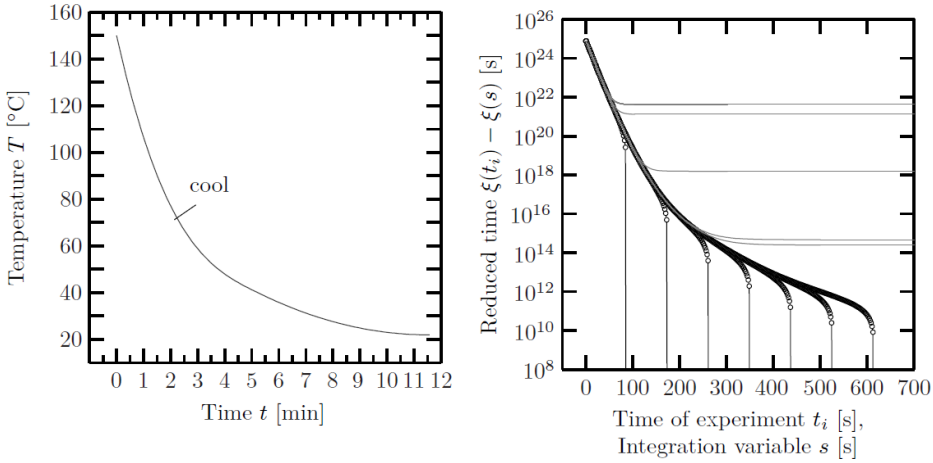

(a) (b)

Figure 3.4 (a) Time-temperature curve of cooling stage of lamination (b) Reduced times calculated from time-temperature curve of the cooling stage of lamination.

The mastercurve in Fig. 3.3b is fitted with Maxwell's arm to cover reduced time domain up to 10^{22}. The Maxwell relaxation parameters for the viscoelastic material model for EVA is presented in Table 3.1.

To determine the number of Maxwell arms that is needed to satisfactory estimate the shear relaxation modulus, the range of the reduced times that can be crossed during lamination of the PV module should be inspected using the temperature-dependent viscoelastic constitutive relation in Eq. (3.33) from which the argument $\xi(t) - \xi(\tau)$ for the relaxation modulus can be computed for a number of experimental times $t_i < t$.

Table 3.1: Parameters for viscoelastic material model for EVA with 26 Maxwell arms determine in [2].

Maxwell parameters		
	λ_i	G_i
0		0.24
1	10^{-3}	90
2	10^{-2}	40
3	10^{-1}	19
4	10^{-0}	11
5	10^{1}	7
6	10^{2}	4
7	10^{3}	2.5
8	10^{4}	1.4
9	10^{5}	1
10	10^{6}	0.8

Maxwell parameters		
	λ_i	G_i
11	10^7	0.6
12	10^8	0.7
13	10^9	0.8
	λ_i	G_i
14	10^{10}	0.8
15	10^{11}	0.7
16	10^{12}	0.6
17	10^{13}	0.56
18	10^{14}	0.48
19	10^{15}	0.5
20	10^{16}	0.3
21	10^{17}	0.25
22	10^{18}	0.12
23	10^{19}	0.07
24	10^{20}	0.03
25	10^{21}	0.02
26	10^{22}	0.02

By considering the time-temperature curve shown in Fig. 3.4a during the cooling of the laminate, the calculated reduced times is shown in Fig. 3.4b.

3.3.2 Visco-elastic model based on fractional calculus

Model fitting using the Prony series involves a lot of parameters to satisfactorily evaluate the relaxation modulus of EVA within the range of application of PV

modules. A Prony series of up to 32 and 100 Maxwell arms were used in [2, 41] to satisfactorily model the behaviour of encapsulant in PV module. In addition, the numerical procedure for the identification of these parameters is a tedious task as described in the previous section. To overcome these drawbacks, Paggi et al [28], based on the work of Di Paola [29, 30], proposed a rheological model to accurately estimate the relaxation modulus of EVA. The constitutive material relation is derived based on fractional calculus using a two parameter element consisting of a fractional dashpot to model the viscoelastic properties of the encapsulant. The fractional model is obtained by replacing the first order derivative in the constitutive equation $\sigma = \eta \frac{d\epsilon}{dt}$ with the derivative of order $\alpha \in (0, 1)$ [42]. Using the simplest fractional element known as Scott-Blair element, the constitutive relation for the fractional model is:

$$\sigma(t) = a \frac{d^{\alpha}\epsilon}{dt^{\alpha}} \quad \alpha \in (0, 1) \tag{3.36}$$

The relaxation modulus $E(t)$ assumes the power law of the form:

$$E(t) = a \frac{t^{-\alpha}}{\Gamma(1-\alpha)} \tag{3.37}$$

a (with SI unit of Pa s^{α}) has the mechanical meaning from stiffness ($\alpha = 0$) to viscosity ($\alpha = 1$). Time t is measured in seconds.

Based on the results of uniaxial relaxation tests carried out in [2], the fractional model is applied to obtain a fit to evaluate the coefficients of nonlinear regression functions at different temperatures using a least square estimate [19]. The efficiency of the fractional model is seen from Fig. 3.5 for the relaxation of EVA as it is noted the fractional model fits well with the experimental data. It is also notable to point out that this formulation has the advantage over Prony series to involve only two parameters (a and α) to model the viscoelastic behaviour of the EVA accurately. Table 3.2 shows the identified parameters for the fractional model to fit experimental uniaxial relaxation tests at different temperatures.

To obtain the relaxation modulus $E(t)$ of the EVA during cooling using the fractional model, fitted parameters identified in Table 3.2 are plotted against a change in temperature with respect to the reference temperature to determine a and α as functions of temperature change. Due to modification in the material microstructure of EVA at $\Delta T \sim 84\,℃$, two different correlations are used to accurately fit the experimental data. The correlations for a and α in Fig. 3.6 are mathematically represented as ($T_{\mathrm{ref}} = -20℃$):

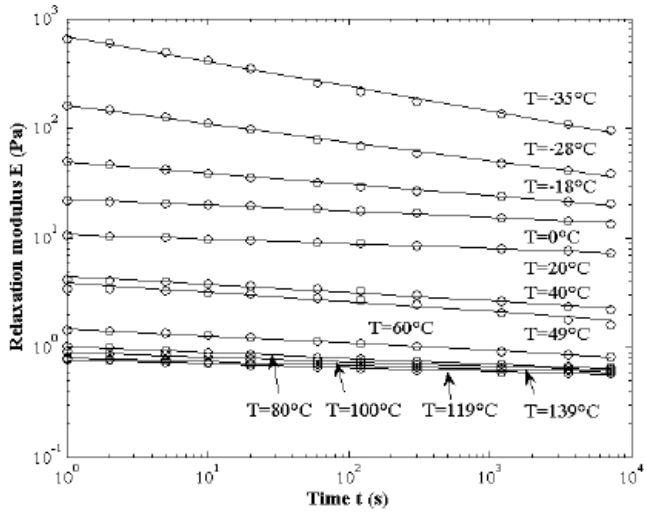

Figure. 3.5 Relaxation modulus vs. time for EVA specimens at different temperatures: experimental data (in circles) and fractional model (continuous lines) [28].

Table 3.2: Identified parameters for the fractional model to fit experimental uniaxial relaxation tests at different temperatures [28].

Temperature (℃)	α	a (Pa s$^{\alpha}$)	Mean absolute percentage error (%)
-35	0.22600	814.7	3.728
-28	0.16810	182.7	2.702
-18	0.10150	52.63	1.823
0	0.05566	23.55	1.851
20	0.04227	11.04	0.3044
40	0.07417	4.668	2.977
49	0.08634	4.116	5.467
60	0.06542	1.544	0.9898
80	0.05117	1.049	1.110
100	0.04179	0.9276	0.8064
119	0.03610	0.7965	0.9627
139	0.03311	0.8228	0.3811

$$\alpha = \begin{cases} -6.5 \times 10^{-7}\Delta T^3 + 1 \times 10^{-4}\Delta T^2 - 0.0093\Delta T + 0.225 & \Delta T \leq 84\ ℃ \\ -1.2 \times 10^{-7}\Delta T^3 + 5.4 \times 10^{-5}\Delta T^2 - 0.0083\Delta T + 0.474 & \Delta T > 84\ ℃ \end{cases} \quad (3.38a)$$

$$a = \begin{cases} 733.5 \exp -0.26\Delta T + 81.2 \exp -0.04\Delta T & \Delta T \leq 84\ ℃ \\ 6.5 \times 10^{6} \exp -0.17\Delta T + 1.7 \exp -0.004\Delta T & \Delta T > 84\ ℃ \end{cases} \quad (3.38b)$$

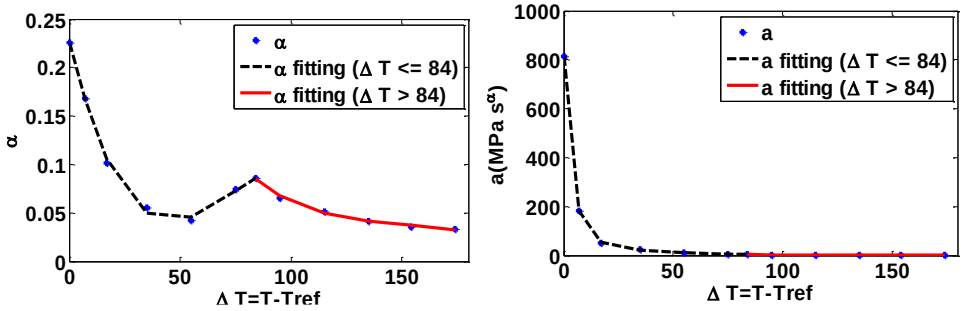

Figure. 3.6 Correlations for α and a as a function of the change of temperature. T_{ref} corresponds to -20°C.

With the mathematical correlations in Eq. (3.38), values of α and a can be determined at any temperature which can now be used in Eq. (3.37) to estimate $E(t)$.

3.4 Thermo-mechanical stress analysis of composite laminates

A significant advantage offered by composite laminates is that their properties can be designed; layer-by-layer, to meet specific field applications. During production and service, laminates are widely known to experience high stress gradients at the interface near the free edges which may cause delamination and high stresses in the layers [14-15, 43-44]. The first step in predicting the mechanical response of a laminate is by developing the stress-strain relations of the laminate structure and a good approach at achieving this is by using the beam theory as presented in [45-50].

In classical plate theory, small deflection of plates is based on Kirchhoff's hypothesis which states as follows:

a. The middle plane remains unstrained (see Fig. 3.7).

b. The normal strain ε_{zz} in the z direction is small enough to be neglected and the normal stress σ_{zz} is small compared σ_{11} and σ_{22} so that it can be neglected in the stress-strain relations.
c. The normal to the middle plane before bending remains normal to this plane after bending. This implies that out-of-plane shear strains are small and can be neglected.

These assumptions can be expressed mathematically as:

$$\varepsilon_{zz} = \frac{\partial w}{\partial z} = 0 \tag{3.39a}$$

$$\varepsilon_{11} = \frac{\partial u_1}{\partial x_1} = \frac{1}{E}(\sigma_{11} - v\sigma_{22}) \tag{3.39b}$$

$$\varepsilon_{22} = \frac{\partial u_2}{\partial x_1} = \frac{1}{E}(\sigma_{22} - v\sigma_{11}) \tag{3.39c}$$

$$\varepsilon_{1z} = \frac{1}{2}\left(\frac{\partial u_1}{\partial z} + \frac{\partial w}{\partial x_1}\right) \approx 0 \tag{3.40a}$$

$$\varepsilon_{2z} = \frac{1}{2}\left(\frac{\partial u_2}{\partial z} + \frac{\partial w}{\partial x_2}\right) \approx 0 \tag{3.40b}$$

$$\varepsilon_{12} = \varepsilon_{21} = \frac{1}{2}\left(\frac{\partial u_1}{\partial x_2} + \frac{\partial u_2}{\partial x_1}\right) \tag{3.40c}$$

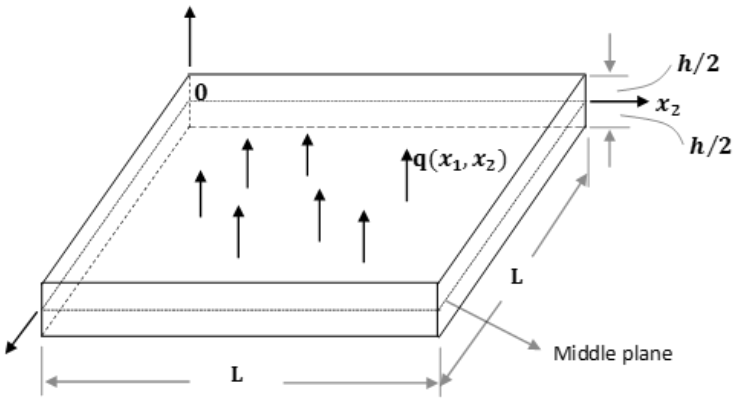

Figure 3.7 A stressed plate showing the middle plane.

It is noted from Eq. (3.39a) that the plate deflection w is a function of x_1 and x_2. By integrating Eqs. (3.40a) and (3.40b) with respect to z, we get:

$$u_1 = -z\frac{\partial w}{\partial x_1} + g_1(x_1, x_2) \tag{3.41a}$$

$$u_2 = -z\frac{\partial w}{\partial x_2} + g_2(x_1, x_2) \tag{3.41b}$$

where g_1 and g_2 are mid-plane displacements which are negligible according Kirchhoff's assumption. Therefore, Eq. (3.41) becomes:

$$u_1 = -z\frac{\partial w}{\partial x_1} \tag{3.42a}$$

$$u_2 = -z\frac{\partial w}{\partial x_2} \tag{3.42b}$$

With respect to Eq. (3.42), the relations for strains in Eqs. (3.39) and (3.40) can now be expressed as:

$$\varepsilon_{11} = -z\frac{\partial^2 w}{\partial {x_1}^2} = \frac{1}{E}(\sigma_{11} - v\sigma_{22}) \tag{3.43a}$$

$$\varepsilon_{22} = -z\frac{\partial^2 w}{\partial {x_2}^2} = \frac{1}{E}(\sigma_{22} - v\sigma_{11}) \tag{3.43b}$$

$$\varepsilon_{12} = \varepsilon_{21} = -z\frac{\partial^2 w}{\partial x_1 \partial x_2} = \frac{\sigma_{12}}{2G} \tag{3.43c}$$

From Eq. (3.43), the stresses are then functions of w as follows:

$$\sigma_{11} = -\frac{Ez}{1-v^2}\left(\frac{\partial^2 w}{\partial {x_1}^2} + v\frac{\partial^2 w}{\partial {x_2}^2}\right) \tag{3.44a}$$

$$\sigma_{22} = -\frac{Ez}{1-v^2}\left(\frac{\partial^2 w}{\partial {x_2}^2} + v\frac{\partial^2 w}{\partial {x_1}^2}\right) \tag{3.44b}$$

$$\sigma_{12} = -\frac{Ez}{1+v}\frac{\partial^2 w}{\partial x_1 \partial x_2} \tag{3.44c}$$

By considering the differential element $\mathrm{d}x_1\mathrm{d}x_2\mathrm{d}z$ in Fig. 3.8, the equilibrium equations for this differential element are:

$$\sum F_{x_1} = 0 \tag{3.45a}$$

$$\sum F_{x_2} = 0 \tag{3.45b}$$

$$\sum F_z = 0 \tag{3.45c}$$

By neglecting body forces, the equilibrium equations yield:

$$\frac{\partial \sigma_1}{\partial x_1} + \frac{\partial \sigma_{12}}{\partial x_2} + \frac{\partial \sigma_{z1}}{\partial z} = 0 \tag{3.46a}$$

$$\frac{\partial \sigma_{12}}{\partial x_1} + \frac{\partial \sigma_2}{\partial x_2} + \frac{\partial \sigma_{z2}}{\partial z} = 0 \tag{3.46b}$$

$$\frac{\partial \sigma_{1z}}{\partial x_1} + \frac{\partial \sigma_{2z}}{\partial x_2} + \frac{\partial \sigma_{zz}}{\partial z} = 0 \tag{3.46c}$$

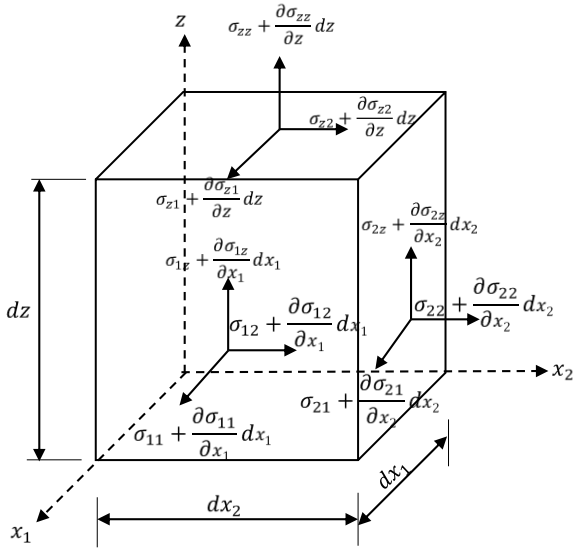

Figure 3.8. A differential element subject to internal stresses.

The boundary conditions to solve the equilibrium equations are specified as follows:

$$\sigma_{1z} = 0, \qquad \sigma_{2z} = 0, \qquad \sigma_{zz} = q \qquad \text{at } z = \frac{h}{2} = c \tag{3.47a}$$

$$\sigma_{1z} = 0, \qquad \sigma_{2z} = 0, \qquad \sigma_{zz} = 0 \qquad \text{at } z = -\frac{h}{2} = -c \tag{3.47b}$$

where q is the applied load at the upper part of the plate.

Integrating Eq. (3.46) with respect to z gives:

$$\sigma_{1z} = \frac{E}{2(1-\nu^2)}\left(z^2 - \frac{h^2}{4}\right)\frac{\partial w}{\partial x_1}\nabla^2 w \tag{3.48a}$$

$$\sigma_{2z} = \frac{E}{2(1-\nu^2)}\left(z^2 - \frac{h^2}{4}\right)\frac{\partial w}{\partial x_2}\nabla^2 w \tag{3.48b}$$

$$\sigma_{zz} = -\frac{E}{2(1-v^2)}\left(\frac{h^3}{12} + \frac{h^2 z}{4} - \frac{z^3}{3}\right)\nabla^4 w \tag{3.48c}$$

where $\nabla^2 w = \frac{\partial^2 w}{\partial {x_1}^2} + \frac{\partial^2 w}{\partial {x_2}^2}$ and $\nabla^4 w = \frac{\partial^4 w}{\partial {x_1}^4} + 2\frac{\partial^4 w}{\partial {x_2}^2 \partial {x_1}^2} + \frac{\partial^4 w}{\partial {x_2}^4}$

By applying the boundary condition at $z = \frac{h}{2}$ to Eq. (3.48c),

$$q = -\frac{Eh^3}{12(1-v^2)}\nabla^4 w \tag{3.49}$$

The axial force, shear force and moment resultants N, Q, M are defined as:

$$N_i = \int_{-c}^{c} \sigma_i \, dz \tag{3.50a}$$

$$M_i = \int_{-c}^{c} \sigma_i \, z dz \tag{3.50b}$$

$$Q_j = \int_{-c}^{c} \sigma_{jz} \, dz \tag{3.50c}$$

for $i = 1, 2, 6$ and $j = 1, 2$

With respect to stress relations in Eq. (3.44), the $i = 1, 2, 6$ indices in the resultant equations (3.50) correspond to $i = 11, 22, 12$. Thus, $N_6 = N_{12}$ and $M_6 = M_{12}$ are, respectively, the twisting force and twisting moment. Substituting Eqs. (3.44) and (3.48) into Eq. (3.50), the relations for the resultants are expressed as:

$$M_1 = -\frac{Eh^3}{12(1-v^2)}\left(\frac{\partial^2 w}{\partial {x_1}^2} + v\frac{\partial^2 w}{\partial {x_2}^2}\right) \tag{3.51a}$$

$$M_2 = -\frac{Eh^3}{12(1-v^2)}\left(v\frac{\partial^2 w}{\partial {x_1}^2} + \frac{\partial^2 w}{\partial {x_2}^2}\right) \tag{3.51b}$$

$$M_6 = -\frac{Eh^3}{12(1-v^2)}(1-v)\frac{\partial^2 w}{\partial x_1 \partial x_2} \tag{3.51c}$$

$$Q_1 = -\frac{Eh^3}{12(1-v^2)}\frac{\partial w}{\partial x_1}\nabla^2 w \tag{3.51d}$$

$$Q_2 = -\frac{Eh^3}{12(1-v^2)}\frac{\partial w}{\partial x_2}\nabla^2 w \tag{3.51e}$$

Substituting Eqs. (3.51d) and (3.51e) into Eq. (3.48) while noting that thickness $h = 2c$ and moment of inertia $I = \frac{h^3}{12}$, σ_{1z}, σ_{2z} and σ_{zz} are now expressed as:

$$\sigma_{1z} = \frac{Q_1}{2I}(c^2 - z^2) \tag{3.52a}$$

$$\sigma_{2z} = \frac{Q_2}{2I}(c^2 - z^2) \tag{3.52b}$$

$$\sigma_{zz} = \frac{q}{6I}(2c^3 + 3c^2 z - z^3) \tag{3.52c}$$

The expression for axial stresses can be rewritten as:

$$\sigma_i = \frac{N_i}{h} + \frac{M_i}{I}z \qquad (\text{for } i = 1, 2, 6) \tag{3.53}$$

By substituting Eqs. (3.52) and (3.53) into the equilibrium equation (3.46), the following differential relations are obtained:

$$\frac{\partial N_1}{\partial x_1} + \frac{\partial N_6}{\partial x_2} = 0 \tag{3.54a}$$

$$\frac{\partial N_2}{\partial x_2} + \frac{\partial N_6}{\partial x_1} = 0 \tag{3.54b}$$

$$\frac{\partial M_1}{\partial x_1} + \frac{\partial M_6}{\partial x_2} - Q_1 = 0 \tag{3.54c}$$

$$\frac{\partial M_2}{\partial x_2} + \frac{\partial M_6}{\partial x_1} - Q_2 = 0 \tag{3.54d}$$

$$\frac{\partial Q_1}{\partial x_1} + \frac{\partial Q_2}{\partial x_2} + q = 0 \tag{3.54e}$$

The set of partial differential equations in (3.54) can be solved by substituting for the constitutive relations in Eq. (3.51) to obtain the displacement w and it derivatives and in turn determine the stress and strain distribution in the plate.

CHAPTER 4

MODEL ORDER REDUCTION APPLIED TO LINEAR SYSTEM OF DIFFERENTIAL EQUATIONS

4.1 Introduction

Modelling of many physical systems involves derivation of differential equations with many dependent variables and more than one independent variables. Typically in the case of structural and thermo-mechanical models, formulation of general equilibrium equations leads to derivation of higher order differential equations with many dependent variables with respect to time and space. This is even more complicated in the case of composite laminates which may be composed of many real or numerical layers with each layer governed by a system of partial differential equations and this eventually leads to a system comprising of many differential equations. Exact solution, although rare, may be obtained for some of the system equations by imposing special conditions but most commonly numerical solutions are sought to compute the solution of variables which ideally and realistically represent the physical system. To this end, exact and numerical solutions are implemented in this work and specifically, the finite difference (FD) method has been used to obtain numerical solutions of the derived system equations. In this

chapter, a review of methods for the solution of system of differential equations and discrete dynamical system is presented. In order to minimize the computational complexity of the numerical solutions, model order reduction techniques are often necessary. Basic techniques in the literature to reduce linear state-space systems are discussed in details and recent advances in reduction of second order systems are highlighted.

4.2 Exact solution of first-order linear system of differential equations

A first order system of differential equation is of the form:

$$\frac{\mathrm{d}x_1}{\mathrm{d}t} = f_1(t, g_1, x_1, x_2, \dots\dots, x_n)$$

$$\frac{\mathrm{d}x_2}{\mathrm{d}t} = f_2(t, g_2, x_1, x_2, \dots\dots, x_n)$$

$$\vdots \qquad \vdots \qquad \vdots \qquad \vdots \qquad \vdots$$

$$\frac{\mathrm{d}x_n}{\mathrm{d}t} = f_n(t, g_n, x_1, x_2, \dots\dots, x_n) \tag{4.1}$$

Equation (4.1) is a first order linear system of differential equations of the functions $f_1, f_2, \dots., f_n$ which are linear in the dependent variables $x_1, x_2, \dots., x_n$. If the functions $g_1, g_2, \dots., g_n$ are zero, then Eq. (4.1) is called homogeneous system of differential equations. Otherwise, the system is non-homogeneous. System Eq. (4.1) can be written in matrix form:

$$\frac{\mathrm{d}\boldsymbol{X}}{\mathrm{d}t} = \boldsymbol{AX} + \boldsymbol{G}(t) \tag{4.2}$$

where $\boldsymbol{X}$ is the vector of all unknown dependent variables, $\boldsymbol{A}$ is the coefficient matrix and $\boldsymbol{G}$ is the vector of non-homogeneous terms. For homogeneous system, $\boldsymbol{G} = \boldsymbol{0}$ and Eq. (4.2) reduces to:

$$\frac{\mathrm{d}\boldsymbol{X}}{\mathrm{d}t} = \boldsymbol{AX} \tag{4.3}$$

To determine which solution of Eq. (4.2) or (4.3), a set of initial conditions are specified at a point in the system, say t_0 so that Eq. (4.2) or (4.3) becomes an initial value problem (IVP). The solution of this system is a vector defined on the interval $\boldsymbol{I}$ whose entries are differentiable functions satisfying Eq. (4.2) or (4.3) on the interval $\boldsymbol{I}$ with column matrix given by:

$$\boldsymbol{X} = \begin{bmatrix} x_1(t) \\ x_2(t) \\ \vdots \\ x_n(t) \end{bmatrix}$$

For the system described by Eqs. (4.2) and (4.3), if the coefficient function entries in matrix $\boldsymbol{A}$ and the non-homogeneous term $\boldsymbol{G}$ are each continuous in an interval around $t = t_0$, then the system

$$\frac{\mathrm{d}\boldsymbol{X}}{\mathrm{d}t} = \boldsymbol{AX} + \boldsymbol{G}$$

with the initial conditions $x_1(t_0) = b_1, \ldots\ldots x_n(t_0) = b_n$ has a unique solution $(x_1, x_2, \ldots\ldots, x_n)$ in some interval around $t = t_0$. This is called the existence-uniqueness theorem.

Finding a solution of this system requires the determination of the eigenvalues and eigenvectors of $n \times n$ matrix $\boldsymbol{A}$. The eigenvalue λ and the eigenvector $\boldsymbol{\eta}$ of $\boldsymbol{A}$ are defined by the expression:

$$\boldsymbol{A\eta} = \lambda\boldsymbol{\eta} \tag{4.4}$$

If Eq. (4.4) is rewritten as:

$$(\boldsymbol{A} - \lambda\boldsymbol{I})\boldsymbol{\eta} = \boldsymbol{0} \tag{4.5}$$

Equation (4.5) is a system of homogeneous linear equations in which the eigenvectors $\boldsymbol{\eta}$ are the values which characterise non-zero solution of the system. This implies that the eigenvalue λ of matrix $\boldsymbol{A}$ are the values for which:

$$\det(\boldsymbol{A} - \lambda I) = \boldsymbol{0}$$

Eq. (4.5) is an n-th degree polynomial called the characteristic polynomial of matrix $\boldsymbol{A}$. The idea behind this eigenvalue procedure is that:

if $\boldsymbol{v} = \begin{bmatrix} c_1 \\ c_2 \\ \vdots \\ c_n \end{bmatrix}$ is an eigenvector of $\boldsymbol{A}$ with an eigenvalue λ, then $\boldsymbol{X} = \begin{bmatrix} c_1 \\ c_2 \\ \vdots \\ c_n \end{bmatrix} e^{\lambda t}$ is solution to Eq. (4.3).

Therefore, if $\boldsymbol{A}$ has n linearly independent eigenvectors $\boldsymbol{v}_1, \ldots\ldots, \boldsymbol{v}_n$ with eigenvalues $\lambda_1, \ldots\ldots, \lambda_n$, then the general solution to the matrix differential system (4.3) are given by:

$$\boldsymbol{X} = \mathrm{C}_1 \boldsymbol{v}_1 e^{\lambda_1 t} + \mathrm{C}_2 \boldsymbol{v}_2 e^{\lambda_2 t} + \cdots + \mathrm{C}_n \boldsymbol{v}_n e^{\lambda_n t}$$

where $\mathrm{C}_1, \ldots\ldots, \mathrm{C}_n$ are arbitrary constants.

This remark allows us to solve all homogeneous system of linear differential equations whose coefficient matrix $\boldsymbol{A}$ is diagonalizable with $\boldsymbol{A} = \boldsymbol{P}^{-1}\boldsymbol{D}\boldsymbol{P}$ where the diagonal elements of $\boldsymbol{D}$ are $\lambda_1, \ldots\ldots, \lambda_n$ and the columns of $\boldsymbol{P}$ are the vectors $\boldsymbol{v}_1, \ldots\ldots, \boldsymbol{v}_n$. It is noted that determining the eigenvalues of $\boldsymbol{A}$ may present some possibilities:

(a) $\boldsymbol{A}$ has distinct real eigenvalues
(b) $\boldsymbol{A}$ has complex conjugate eigenvalues
(c) $\boldsymbol{A}$ has a repeated real eigenvalue.

If, for example, the number of linearly independent eigenvectors $n = 2$, then for case (a):

$$\boldsymbol{X} = \mathrm{C}_1\boldsymbol{v}_1 e^{\lambda_1 t} + \mathrm{C}_2\boldsymbol{v}_2 e^{\lambda_2 t}$$

In case (b), matrix $\boldsymbol{A}$ has complex conjugate eigenvalues $\lambda = \lambda_1 \pm \mu_1 i$ and by implication, a complex conjugate eigenvectors $\boldsymbol{v} = \boldsymbol{a} \pm \boldsymbol{b}i$, then the homogeneous system (4.3) has a real-valued general solution:

$$\boldsymbol{X} = \mathrm{C}_1 e^{\lambda_1 t}(\boldsymbol{a}\cos\mu_1 t - \boldsymbol{b}\sin\mu_1 t) + \mathrm{C}_2 e^{\lambda_1 t}(\boldsymbol{a}\sin\mu_1 t + \boldsymbol{b}\cos\mu_1 t)$$

In case (c) where matrix $\boldsymbol{A}$ has a repeated real eigenvalues λ, there are 2 sub-cases:

- λ has two linearly independent eigenvectors $\boldsymbol{v}_1$ and $\boldsymbol{v}_2$, then the system has a general solution:

$$\boldsymbol{X} = \mathrm{C}_1\boldsymbol{v}_1\boldsymbol{e}^{\lambda t} + \mathrm{C}_2\boldsymbol{v}_2\boldsymbol{e}^{\lambda t}$$

- λ has only one linearly dependent eigenvectors $\boldsymbol{v}_1$, then the system has a general solution:

$$\boldsymbol{X} = \mathrm{C}_1\boldsymbol{v}_1\boldsymbol{e}^{\lambda t} + \mathrm{C}_2\left(\boldsymbol{v}_1 t\boldsymbol{e}^{\lambda t} + \boldsymbol{\varphi}\boldsymbol{e}^{\lambda t}\right)$$

where the vector $\boldsymbol{\varphi}$ is any solution of non-homogeneous linear system of equations:

$$(\boldsymbol{A} - \lambda\boldsymbol{I})\boldsymbol{\varphi} = \boldsymbol{v}_1$$

4.2.1 General solution to non-homogeneous system of linear differential equations

Based on the method of variation of parameters, if the homogeneous part of Eq. (4.2) is assumed to have a fundamental set of solutions $\boldsymbol{X}_1, \ldots\ldots, \boldsymbol{X}_n$, then the general solution is given by:

$$\boldsymbol{X} = \mathrm{C}_1 \begin{bmatrix} x_{11} \\ x_{21} \\ \vdots \\ x_{n1} \end{bmatrix} + \mathrm{C}_2 \begin{bmatrix} x_{12} \\ x_{22} \\ \vdots \\ x_{n2} \end{bmatrix} + \cdots + \mathrm{C}_n \begin{bmatrix} x_{1n} \\ x_{2n} \\ \vdots \\ x_{nn} \end{bmatrix} = \boldsymbol{\Psi}(\mathrm{t})\mathbf{C}$$

where $\mathbf{C}$ is $n \times 1$ vector containing of all the arbitrary constants $\mathrm{C}_1, \ldots\ldots, \mathrm{C}_n$ and $\boldsymbol{\Psi}(\mathrm{t})$ is an $n \times n$ matrix whose columns consist of entries of the solution vector of the homogeneous system $\frac{\mathrm{d}\boldsymbol{X}}{\mathrm{d}t} = \boldsymbol{AX}$. Matrix $\boldsymbol{\Psi}(\mathrm{t})$ is called the fundamental matrix of the system. Substitution of $\boldsymbol{X} = \boldsymbol{\Psi}(\mathrm{t})\mathbf{C}$ into $\frac{\mathrm{d}\boldsymbol{X}}{\mathrm{d}t} = \boldsymbol{AX}$ yields:

$$\frac{\mathrm{d}\boldsymbol{\Psi}(\mathrm{t})}{\mathrm{d}t} = \boldsymbol{A}\boldsymbol{\Psi}(\mathrm{t}) \tag{4.6}$$

If we assume the particular solution of the non-homogeneous system (4.2) is expressed as:

$$\boldsymbol{X}_p = \boldsymbol{\Psi}(\mathrm{t})\mathbf{Q}(\mathrm{t}) \tag{4.7}$$

where $\mathbf{Q}(\mathrm{t}) = \begin{bmatrix} q_1(t) \\ q_2(t) \\ \vdots \\ q_n(t) \end{bmatrix}$

By differentiating$\boldsymbol{X}_p$ and substituting into Eq. (4.2), we get:

$$\mathbf{Q}(\mathrm{t})\frac{\mathrm{d}\boldsymbol{\Psi}(\mathrm{t})}{\mathrm{d}t} + \boldsymbol{\Psi}(\mathrm{t})\frac{\mathrm{d}\mathbf{Q}(\mathrm{t})}{\mathrm{d}t} = \boldsymbol{A}\boldsymbol{\Psi}(\mathrm{t})\mathbf{Q}(\mathrm{t}) + \boldsymbol{G}(\mathrm{t}) \tag{4.8}$$

By substituting Eq. (4.6) into (4.8),

$$\boldsymbol{\Psi}(\mathrm{t})\frac{\mathrm{d}\mathbf{Q}(\mathrm{t})}{\mathrm{d}t} = \boldsymbol{G}(\mathrm{t}) \tag{4.9}$$

Solving for $\mathbf{Q}(\mathrm{t})$ in Eq. (4.9) gives:

$$\mathbf{Q}(\mathrm{t}) = \int \boldsymbol{\Psi}(\mathrm{t})^{-1}\boldsymbol{G}(t)\mathrm{dt} \tag{4.10}$$

Therefore, the particular solution of the non-homogeneous system (4.2) is:

$$\boldsymbol{X}_p = \boldsymbol{\Psi}(\mathrm{t}) \int \boldsymbol{\Psi}(\mathrm{t})^{-1} \boldsymbol{G}(t)\mathrm{dt}$$

(4.11)

So the general solution of the non-homogeneous system (4.2) is expressed as:

$$\boldsymbol{X} = \boldsymbol{\Psi}(\mathrm{t})\mathbf{C} + \boldsymbol{\Psi}(\mathrm{t}) \int \boldsymbol{\Psi}(\mathrm{t})^{-1} \boldsymbol{G}(t)\mathrm{dt}$$

(4.12)

4.3 Solution of higher-order differential equations

Given an n-th order linear differential equation of the form:

$$a_n x^{(n)} + a_{n-1} x^{(n-1)} + a_{n-2} x^{(n-2)} + \cdots + a_2 x'' + a_1 x' + a_0 x = g(t)$$

(4.13)

By making the substitutions $y_1 = x, y_2 = x', y_3 = x'', \ldots, y_n = x^{(n-1)}$, and ${y_n}' = x^{(n)}$, Eq. (4.13) can be reduced to a system of first order differential equations of the form:

$${y_1}' = y_2$$

$${y_2}' = y_3$$

$$\vdots \qquad \vdots$$

$${y_{(n-1)}}' = y_n$$

$${y_n}' = -\frac{a_0}{a_n} y_1 - \frac{a_1}{a_n} y_2 - \cdots - \frac{a_{n-1}}{a_n} y_n - \frac{g(t)}{a_n}$$

(4.14)

With the linear system of first order differential equations (4.14), a solution can be obtained as described in Sec. 4.1. If we have a linear system of higher order differential equations, it is remarked that this technique can also be used to reduce

the system to a system of first order differential equations and solutions obtained as described for first order systems.

4.4 The boundary value problems

The system described in the previous section is an initial value problem (IVP) because it has conditions or value of the solution variables specified at one time t_0. In the case of boundary value problem (BVP), values of the solution variables are specified at different spatial points such that a complete solution of the system can be obtained. For example, a BVP for a second order system may be expressed as:

$$\frac{\mathrm{d}^2\boldsymbol{X}}{\mathrm{d}t^2} + \boldsymbol{D}\frac{\mathrm{d}\boldsymbol{X}}{\mathrm{d}t} + \boldsymbol{A}\boldsymbol{X} = \boldsymbol{G}(t) \tag{4.15a}$$

$$\boldsymbol{X}(t_0) = \boldsymbol{X}_0 \qquad \boldsymbol{X}(t_1) = \boldsymbol{X}_1 \tag{4.15b}$$

A BVP such as Eq. (4.15) is homogeneous if, in addition to $\boldsymbol{G}(t) = 0$, the values of the solution at the boundaries are also zero i.e., $\boldsymbol{X}(t_0) = \boldsymbol{0}$, $\boldsymbol{X}(t_1) = \boldsymbol{0}$. Otherwise, the system is non-homogeneous. To solve a BVP requires the same technique like IVP except that BVP is more complicated since, depending on the values of the solution variables at the boundaries, a BVP may have an infinite solution or no solution.

4.5 The finite difference method

Modelling of many physical systems in engineering usually leads to a system of partial differential equations (PDEs) with more than one independent variable, or higher order ordinary differential equations (ODEs) with a variable coefficient matrix. Such a situation may arise due to the boundary conditions of the system, geometry of the problem or dynamics of the system. To obtain a solution, a numerical approach which involves approximating the solution variables at discrete points in the system is required. There are many standard numerical

procedures available to obtain the numerical solution of the system and of these procedures, the finite difference (FD) method has been identified in this work for the solution of a system of differential equations.

4.5.1 Formulae for the approximation of derivatives

Given a small value of grid spacing $h > 0$, the d-th order derivative satisfies the equation:

$$\frac{h^d}{d!}F^{(d)}(t) = \sum_{i_{min}}^{i_{max}} C_i\, F(t + ih) + \mathcal{O}(h^{d+p}) \tag{4.16}$$

for some choice of extreme indices i_{min} and i_{max} and for some choice of coefficients C_i. The integer order of error $p > 0$ may be selected as desired. The approximations are obtained by neglecting the error terms indicated by the $\mathcal{O}$ notation. The order of error is seen from formal expansion as Taylor's series about the value of t:

$$F(t + h) = F(t) + hF'(t) + \frac{h^2}{2!}F''(t) + \cdots = \sum_{n=0}^{\infty}\frac{h^n}{n!}F^{(n)}(t) \tag{4.17}$$

and

$$F(t - h) = F(t) - hF'(t) + \frac{h^2}{2!}F''(t) + \cdots = \sum_{n=0}^{\infty}(-1)^n\frac{h^n}{n!}F^{(n)}(t) \tag{4.18}$$

where $F^{(n)}(t)$ denotes the n-th derivative of F. By subtracting $F(t)$ from both sides of Eqs. (4.17) and (4.18) on one hand and subtracting Eq. (4.18) from Eq. (4.17) on the other hand, the first derivative finite difference formulae for forward difference, backward difference and centred difference are, respectively, given as:

$$F'(t) = \frac{F(t+h)-F(t)}{h} + \mathcal{O}(h) \tag{4.19a}$$

$$F'(t) = \frac{F(t)-F(t-h)}{h} + \mathcal{O}(h) \tag{4.19b}$$

$$F'(t) = \frac{F(t+h)-F(t-h)}{2h} + \mathcal{O}(h^2) \quad (4.19a)$$

The forward difference and backward difference formula have first order approximation error $\mathcal{O}(h)$ while the centred difference have second order approximation error. Higher order approximations can be obtained by using more terms in the Taylor's series. Higher order derivatives can be derived in a similar manner to first derivative. In Tables 4.1, 4.2 and 4.3, the coefficients of finite difference formulae for up to fourth derivatives are reported.

Table. 4.1: Coefficients for centred divided FD scheme

Derivative	**Accuracy**	**Points**						
		-3	-2	-1	0	1	2	3
1	2			$-1/2$	0	$1/2$		
	4		$1/2$	$-2/3$	0	$2/3$	$-1/2$	
2	2			1	-2	1		
	4		$-1/12$	$4/3$	$-5/2$	$4/3$	$-1/12$	
3	2		$-1/2$	1	0	-1	$1/2$	
	4	$1/8$	-1	$13/8$	0	$-13/8$	1	$-1/8$
4	2		1	-4	6	-4	1	
	4	$-1/6$	2	$-13/2$	$28/3$	$-13/2$	2	$-1/6$

Table. 4.2: Coefficients for forward divided FD scheme

Derivative	**Accuracy order**	**Points**					
		0	**1**	**2**	**3**	**4**	**5**
1	1	-1	1				
	2	$-3/2$	2	$-1/2$			
2	1	1	-2	1			
	2	2	-5	4	-1		
3	1	-1	3	-3	1		
	2	$-5/2$	9	-12	7	$-3/2$	
4	1	1	-4	6	-4	1	
	2	3	-14	26	-24	11	-2

Table. 4.3: Coefficients for backward divided FD scheme

Derivative	**Accuracy order**	**Points**					
		0	**-1**	**-2**	**-3**	**-4**	**-5**
1	1	1	-1				
	2	$3/2$	-2	$1/2$			
2	1	1	-2	1			
	2	2	-5	4	-1		
3	1	1	-3	3	-1		
	2	$5/2$	-9	12	-7	$3/2$	
4	1	1	-4	6	-4	1	
	2	3	-14	26	-24	11	-2

Given the coefficients of finite difference formulae, an approximation of second order mixed derivative using centred divided FD method is obtained as follows:

$$F_{,xy} = \frac{F_{,x}(y+h_y) - F_{,x}(y-h_y)}{2h_y} + \mathcal{O}(h^2) \quad (4.20)$$

$$F_{,x}(y+h_y) = \frac{F(x+h_x,y+h_y) - F(x-h_x,y+h_y)}{2h_x} + \mathcal{O}(h^2) \quad (4.21a)$$

$$F_{,x}(y-h_y) = \frac{F(x+h_x,y-h_y) - F(x-h_x,y-h_y)}{2h_x} + \mathcal{O}(h^2) \quad (4.21b)$$

where the subscript after the comma denotes a derivative with respect to the corresponding variable. Substituting Eq. (4.21) into (4.20), we get:

$$F_{,xy} = \frac{F(x+h_x,y+h_y) - F(x-h_x,y+h_y) - F(x+h_x,y-h_y) + F(x-h_x,y-h_y)}{4h_x h_y} + \mathcal{O}(h^2) \quad (4.22)$$

Using a similar procedure, the formulae for forward divided FD and backward divided FD are:

$$F_{,xy} = \frac{F(x+h_x,y+h_y) - F(x,y+h_y) - F(x+h_x,y) + F(x,y)}{h_x h_y} + \mathcal{O}(h) \quad (4.23)$$

$$F_{,xy} = \frac{F(x,y) - F(x-h_x,y) - F(x,y-h_y) + F(x-h_x,y-h_y)}{h_x h_y} + \mathcal{O}(h) \quad (4.24)$$

The procedure can be routinely repeated to obtain the formulae for higher order mixed derivatives.

4.5.2 Relationship between finite difference method and Lagrange polynomials

An alternative to deriving the finite difference weights from the Taylor's series is to differentiate Lagrange polynomials given as:

$$l_j(\xi) = \prod_{i=0, i\neq j}^{n} \frac{\xi - x_i}{x_j - x_i} \quad (4.25)$$

where, for a 3-point stencil, the interpolation points are:

$x_0 = x - h, \qquad x_1 = x, \qquad x_2 = x + h.$

The quadratic polynomial $P_2(x)$ interpolating $F(x)$ at these points is given as:

$$P_2(x) = \sum_{j=0}^{2} F(x_j) l_j(x) \tag{4.26}$$

Differentiating Eq. (4.26), we get:

$$P_{2,x}(x) = \sum_{j=0}^{2} F(x_j) l_{j,x}(x) \tag{4.27}$$

The finite difference approximation of $F_{,x_1}$ at the mid-point $x = x_1$ is:

$$F_{,x}(x_1) = l_{0,x}(x_1)F(x_0) + l_{1,x}(x_1)F(x_1) + l_{2,x}(x_1)F(x_2) + \mathcal{O}(h^2) \tag{4.28}$$

By evaluating the derivatives of the 3 Lagrange polynomials at x_1 gives the same weights for centred difference formula for first derivative with second order accuracy as shown in Table 4.1. To obtain higher order derivatives or higher order approximations, higher order polynomials are needed to estimate the weights of the derivatives using a stencil that covers more points around the point of interest.

4.5.3 Finite difference method applied to a non-uniform grid

The significance of the Lagrange polynomials is that the procedure to obtain the weights for the derivative of mesh points with uniform spacing can be easily extended to mesh points with non-uniform spacing. Accordingly, the second and fourth derivatives of the points in Fig. 4.1 are shown in Table 4.4 (see Appendix **B**).

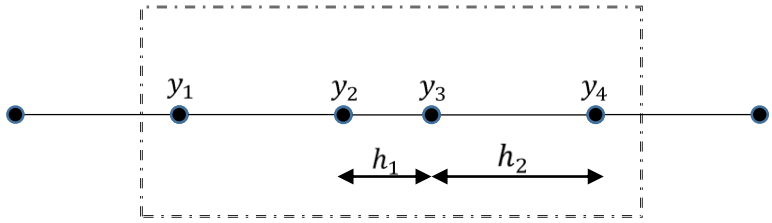

Figure 4.1. Nodes along longitudinal axis with non-uniform mesh size.

Table 4.4: Finite difference weights for derivatives at nodes with non-uniform mesh size.

Derivative	Points	y_1	y_2	y_3	y_4
4	-2	$\frac{4r(2+r)(1+r)}{s_1}$	$\frac{12r(1+r)}{s_1}$	$\frac{24r}{s_1}$	$\frac{24}{s_1}$
	-1	$\frac{-12r(3+r)(1+r)}{s_1}$	$\frac{-24r(3+r)}{s_1}$	$\frac{-24(3+r)}{s_1}$	$\frac{-4r(3+r)(r^2+3r+2)}{s_1}$
	0	$\frac{12r(3+r)(2+r)}{s_1}$	$\frac{12(3+r)(2+r)}{s_1}$	$\frac{12(3+r)(2+r)}{s_1}$	$\frac{12r(3+r)(2+r)}{s_1}$
	1	$\frac{-4r(3+r)(r^2+3r+2}{s_1}$	$\frac{-24(3+r)}{s_1}$	$\frac{-24r(3+r)}{s_1}$	$\frac{-12r(3+r)(1+r)}{s_1}$
	2	$\frac{24}{s_1}$	$\frac{24r}{s_1}$	$\frac{12r(1+r)}{s_1}$	$\frac{4r(2+r)(1+r)}{s_1}$
2	-1		$\frac{2r}{s_2}$	$\frac{2}{s_2}$	
	0		$\frac{2(1+r)}{s_2}$	$\frac{2(1+r)}{s_2}$	
	1		$\frac{2}{s_2}$	$\frac{2r}{s_2}$	

where the variables r, s_1 and s_2 are given by:

$$r = \frac{h_1}{h_2},\ s_1 = r(3+r)(2+r)(1+r){h_2}^4,\ s_2 = r(1+r){h_2}^2 .$$

4.5.4 Finite difference discretization of boundary conditions for structural systems

Application of finite difference approximations at a point of the boundary or near the boundary of a domain is cumbersome as points outside the physical domain are involved. It is admitted therefore, that the differential equation remains valid outside the domain.

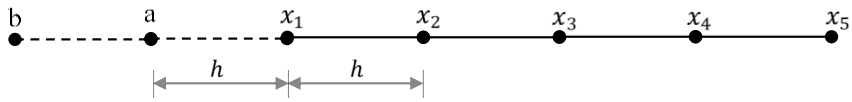

Figure 4.2. 1D structural beam with uniform mesh size.

With respect to a 1D simple structural beam as shown in Fig. 4.2, three basic boundary conditions at an end point, say x_1 are identified, namely:

(a) Simply supported end: vertical deflection w and moments are zero at point x_1. Mathematically,
$w(x_1) = 0, \qquad w_{,xx}(x_1) = 0$

(b) Fixed or clamped end: vertical deflection w and rotation vanish at point x_1. Mathematically, $w(x_1) = 0, \qquad w_{,x}(x_1) = 0$

(c) Free end: point x_1 is free from any external load and the bending moment and shearing force vanish at this point. Mathematically,
$w_{,xx}(x_1) = 0, \quad w_{,xxx}(x_1) = 0$

Considering that points a and b are outside the domain, the centred difference approximations for derivatives of the deflection w at point x_1 gives:

$$w(a) = w(x_2) - 2h\, w_{,x}(x_1) \tag{4.29a}$$

$$w(a) = 2\, w(x_1) - w(x_2) + h^2\, w_{,xx}(x_1) \tag{4.29b}$$

$$w(b) = 2\, w(a) - 2\, w(x_2) + w(x_3) - 2\, h^3\, w_{,xxx}(x_1) \tag{4.29c}$$

So depending on the boundary condition of interest, an estimate for the unknowns of the points outside the domain (also known as phantom nodes) can be obtained. For example, with a fixed end at point x_1, $w_{,x}(x_1) = 0$ and Eq. (4.29a) becomes:

$$w(a) = w(x_2) \tag{4.30}$$

Also, for a fixed end at point x_1, the fourth derivative at point x_2 is obtained as:

$$h^4\, w_{,xxxx}(x_2) = 7\, w(x_2) - 4\, w(x_3) + w(x_4) \tag{4.31}$$

The same approach can be used to obtain estimates for displacement of points at the end points or near the end points for a simply supported end or for a free end at point x_1. Accordingly, for a simply supported end at point x_1, $w(x_1) = 0$ and $w_{,xx}(x_1) = 0$, so that Eq. (4.29b) becomes:

$$w(a) = -w(x_2) \tag{4.32}$$

And the fourth derivative approximation at point x_2 is now given as:

$$h^4\, w_{,xxxx}(x_2) = 5\, w(x_2) - 4\, w(x_3) + w(x_4) \tag{4.33}$$

As for a free end at point x_1, Eqs. (4.29b) and (4.29c) become:

$$w(a) = 2\, w(x_1) - w(x_2) \tag{4.34a}$$

$$w(b) = 4\, w(x_1) - 4\, w(x_2) + w(x_3) \tag{4.34b}$$

And by substitution of Eq. (4.34) into the centred difference formula for fourth derivative of the deflection $w(x_1)$ at point x_1, we get:

$$h^4\, w_{,xxxx}(x_1) = 2\, w(x_1) - 4\, w(x_2) + 2\, w(x_3) \tag{4.35}$$

The fourth derivative at point x_2 is then given as:

$$h^4\, w_{,xxxx}(x_2) = -2\, w(x_1) + 5\, w(x_2) - 4\, w(x_3) + w(x_4) \tag{4.36}$$

4.5.5 Alternative approach to the discretization of the boundary conditions

The procedure described in Sec. 4.5.4 consider external points for the discretization at the boundary. In some cases, due to poor boundary treatment, this can give rise to large errors in the results. An alternative approach proposed in [51] uses the Taylor's series expansion of the derivatives at the boundary using a desired number of terms to get the best approximation. For example, to get the best approximation for fourth derivative of the deflection at point x_2 in terms of $w(x_1)$, $w(x_2)$, $w(x_3)$ and $w(x_4)$, Taylor series expansion is considered as:

$$\begin{Bmatrix} w(x_1) \\ w(x_2) \\ w(x_3) \\ w(x_4) \\ w_{,x}(x_1) \end{Bmatrix} = \begin{bmatrix} 1 & -h & h^2/2 & -h^3/6 & h^4/24 \\ 1 & 0 & 0 & 0 & 0 \\ 1 & h & h^2/2 & h^3/6 & h^4/24 \\ 1 & 2h & 4h^2/2 & 8h^3/6 & 16h^4/24 \\ 0 & 1 & -h & h^2/2 & -h^3/6 \end{bmatrix} \begin{Bmatrix} w(x_2) \\ w_{,x}(x_2) \\ w_{,xx}(x_2) \\ w_{,xxx}(x_2) \\ w_{,xxxx}(x_2) \end{Bmatrix} \quad (4.37)$$

By multiplying the first equation in the matrix Eq. (4.37) by A, the second by B, the third by C, the fourth by D and the last by hE and adding all the five equations together, we get:

$$Aw(x_1) + Bw(x_2) + Cw(x_3) + Dw(x_4) + hEw_{,x}(x_1) = (A + B + C + D)\, w(x_2) + (-A + C + 2D + E)\ hw_{,x}(x_2) + (A + C + 4D - 2E)\ \frac{h^2}{2}\, w_{,xx}(x_2) + (-A + C + 8D + 3E)\ \frac{h^3}{6}\, w_{,xxx}(x_2) + (A + C + 16D - 4E)\ \frac{h^4}{24}\, w_{,xxxx}(x_2) + \cdots \quad (4.38)$$

If the right hand side of Eq. (4.38) is the best approximation of $w_{,xxxx}(x_2)$, then the coefficients of $w(x_2)$, $w_{,x}(x_2)$, $w_{,xx}(x_2)$, $w_{,xx}(x_2)$ must be zero and the coefficient of $w_{,xxxx}(x_2)$ must be unit. Therefore,

$$\begin{bmatrix} 1 & 1 & 1 & 1 & 0 \\ -1 & 0 & 1 & 2 & 1 \\ 1 & 0 & 1 & 4 & -2 \\ -1 & 0 & 1 & 8 & 3 \\ 1 & 0 & 1 & 16 & -4 \end{bmatrix} \begin{Bmatrix} A \\ B \\ C \\ D \\ E \end{Bmatrix} = \frac{24}{h^4} \begin{Bmatrix} 0 \\ 0 \\ 0 \\ 0 \\ 1 \end{Bmatrix}$$

(4.39)

By solving Eq. (4.39):

$A = -\frac{22}{3h^4}$, $B = \frac{12}{h^4}$, $C = -\frac{6}{h^4}$, $D = \frac{4}{3h^4}$, $E = -\frac{4}{h^4}$.

The fourth derivative approximation for *w* at point x_2 is now given as:

$$w_{,xxxx}(x_2) = \frac{1}{h^4}\left(-4h\, w_{,x} - \frac{22}{3}\, w(x_1) + 12\, w(x_2) - 6\, w(x_3) + \frac{4}{3}\, w(x_4)\right)$$

(4.40)

For a fixed condition at point x_1 , $w(x_1) = w_{,x}(x_1) = 0$ so that the fourth derivative at point x_2 now becomes:

$$w_{,xxxx}(x_2) = \frac{1}{h^4}\left(12\, w(x_2) - 6\, w(x_3) + \frac{4}{3}\, w(x_4)\right)$$

(4.41)

By using a similar procedure for a simply supported beam, the approximation gives:

$$w_{,xxxx}(x_2) = \frac{1}{11h^4}\left(12h^2\, w_{,xx} - 24\, w(x_1) + 60\, w(x_2) - 48\, w(x_3) + 12\, w(x_4)\right)$$

(4.42)

As $w(x_1) = w_{,xx}(x_1) = 0$ for simply supported end, Eq. (4.42) becomes:

$$w_{,xxxx}(x_2) = \frac{1}{11h^4}\left(60\, w(x_2) - 48\, w(x_3) + 12\, w(x_4)\right) \qquad (4.43)$$

For a free end, fourth derivative at points x_1 and x_2 gives:

$$w_{,xxxx}(x_1) = \frac{1}{7h^4}\left(12\, w(x_1) - 24\, w(x_2) + 12\, w(x_3)\right) \quad (4.44a)$$

$$w_{,xxxx}(x_2) = \frac{1}{11h^4}\left(-24w(x_1) + 60\, w(x_2) - 48\, w(x_3) + 12\, w(x_4)\right) \quad (4.44b)$$

The approach is general and can be used in ODEs or PDEs with any type of boundary conditions.

4.6 Solution of a system of partial differential equations using the finite difference method

As noted in the previous sections, modelling of many physical systems leads to derivation of system of PDEs or higher order ODEs whose exact solutions are too complex to be obtained in closed form. As the finite difference scheme has been identified in this work, methods to obtain numerical solution of first order and second order systems are highlighted in this section. Since most higher order differential equations that occur in applications can be converted into first order or second order system, finite difference solutions of first order and second order system and specifically, implicit finite difference schemes which has been identified in this work are discussed in the sub-sections below.

4.6.1 Implicit time integration for first-order linear systems (backward Euler)

Given an example of a system represented by a parabolic PDE as:

$$\dot{u} = c u_{,xx} \quad (4.45)$$

where the dotted variable represents a derivative with respect to time and a subscripted variable denotes a derivative with respect to space. An approximation of Eq. (4.45) at time t_{j+1} using backward difference formula for $\dot{u}$ and centred difference formula for $u_{,xx}$ gives:

$$\frac{u_{i,j+1}-u_{i,j}}{\Delta t} = \frac{c}{h^2}\left(u_{i+1,j+1} - 2\,u_{i,j+1} + u_{i-1,j+1}\right) \tag{4.46}$$

where Δt is the time step.

Eq. (4.46) can be rewritten as:

$$u_{i,j} = -\bar{r}u_{i+1,j+1} + (1+2\bar{r})u_{i,j+1} - \bar{r}u_{i-1,j+1} \tag{4.47}$$

where $\bar{r} = \frac{c\Delta t}{h^2}$

Using matrix notation, Eq. (4.47) is rewritten as:

$$\boldsymbol{B}\mathbf{u}_{j+1} = \mathbf{u}_j + \bar{r}\mathbf{b}_{j+1} \tag{4.48}$$

where $\mathbf{b}_{j+1}$ is the boundary condition vector at time t_{j+1}.

$$\boldsymbol{B} = \begin{bmatrix} 1+2\bar{r} & -\bar{r} & & & & \\ -\bar{r} & 1+2\bar{r} & -\bar{r} & & & \\ & \ddots & \ddots & \ddots & & \\ & & -\bar{r} & 1+2\bar{r} & -\bar{r} & \\ & & & -\bar{r} & 1+2\bar{r} & \end{bmatrix}$$

Eq. (4.48) ensures that the solution variables at time t_{j+1} is obtained using the previous solution and the predetermined boundary values at the current time.

4.6.2 Modified Euler method for the solution of first-order linear system

An obvious shortcoming of the Euler method is that it makes the approximation based on information at the beginning of the time interval only. This problem is eliminated by the use of the so called improved Euler method otherwise known as modified Euler method. This method considers the function at the beginning and the end of each time step and take the average of the two. This is illustrated mathematically:

Given $\dot{\mathrm{u}} = f(t, \mathrm{u})$ (4.49)

The formula for the modified Euler method is expressed as:

$$\mathbf{u}_{j+1} = \mathbf{u}_j + \frac{\Delta t}{2}\left(\boldsymbol{f}\left(t_j, \mathbf{u}_j\right) + \boldsymbol{f}\left(t_{j+1}, \mathbf{u}_{j+1}\right)\right) \tag{4.50}$$

By applying the formula (4.50) to Eq. (4.45), we get:

$$\mathbf{u}_{j+1} = \boldsymbol{B_1}^{-1}\left(\boldsymbol{B_2}\mathbf{u}_j + \bar{h}\boldsymbol{b}_1\right) \tag{4.51}$$

$$\boldsymbol{B_1} = \begin{bmatrix} 1+2\bar{h} & -\bar{h} & & & \\ -\bar{h} & 1+2\bar{h} & -\bar{h} & & \\ & \ddots & \ddots & \ddots & \\ & & -\bar{h} & 1+2\bar{h} & -\bar{h} \\ & & & -\bar{h} & 1+2\bar{h} \end{bmatrix}$$

$$B_2 = \begin{bmatrix} \left(2\bar{h}-1\right) & \bar{h} & & & \\ \bar{h} & \left(2\bar{h}-1\right) & \bar{h} & & \\ & \ddots & \ddots & \ddots & \\ & & \bar{h} & \left(2\bar{h}-1\right) & \bar{h} \\ & & & \bar{h} & \left(2\bar{h}-1\right) \end{bmatrix}$$

where $\bar{h} = \frac{c\Delta t}{2h^2}$, $\boldsymbol{b}_1 = \bar{\mathbf{b}}_j + \bar{\mathbf{b}}_{j+1}$.

$\bar{\mathbf{b}}_{j+1}$ and $\bar{\mathbf{b}}_j$ are the boundary conditions at time t_{j+1} and t_j respectively.

4.6.3 Newmark algorithm for time integration of second-order linear systems

Given a second order ODE of the form:

$$\mathbf{M}\ddot{\mathbf{u}}_t + \mathbf{C}\dot{\mathbf{u}}_t + \mathbf{K}\mathbf{u}_t = \mathbf{F}_t \tag{4.52}$$

where **M, C** and **K** are the mass matrix, damping matrix and stiffness matrix.

From Taylor's series, we can obtain expansion for $\mathbf{u}_t$ and $\dot{\mathbf{u}}_t$:

$$\mathbf{u}_t = \mathbf{u}_{t-\Delta t} + \Delta t\dot{\mathbf{u}}_{t-\Delta t} + \frac{\Delta t^2}{2}\ddot{\mathbf{u}}_{t-\Delta t} + \frac{\Delta t^3}{6}\dddot{\mathbf{u}}_{t-\Delta t} + \cdots \tag{4.53}$$

$$\dot{\mathbf{u}}_t = \dot{\mathbf{u}}_{t-\Delta t} + \Delta t\ddot{\mathbf{u}}_{t-\Delta t} + \frac{\Delta t^2}{2}\dddot{\mathbf{u}}_{t-\Delta t} + \cdots \tag{4.54}$$

These equations can be truncated and expressed in the following form:

$$\mathbf{u}_t = \mathbf{u}_{t-\Delta t} + \Delta t\dot{\mathbf{u}}_{t-\Delta t} + \frac{\Delta t^2}{2}\ddot{\mathbf{u}}_{t-\Delta t} + \beta\Delta t^3\dddot{\mathbf{u}} \tag{4.55}$$

$$\dot{\mathbf{u}}_t = \dot{\mathbf{u}}_{t-\Delta t} + \Delta t\ddot{\mathbf{u}}_{t-\Delta t} + \gamma\Delta t^2\dddot{\mathbf{u}} \tag{4.56}$$

Assuming the acceleration is linear within the time step, then:

$$\dddot{\mathbf{u}} = \frac{\ddot{\mathbf{u}}_t - \ddot{\mathbf{u}}_{t-\Delta t}}{\Delta t} \tag{4.57}$$

By substituting Eq. (4.57) into Eqs. (4.55) and (4.56), we get:

$$\mathbf{u}_t = \mathbf{u}_{t-\Delta t} + \Delta t\dot{\mathbf{u}}_{t-\Delta t} + (\frac{1}{2} - \beta)\Delta t^2\ddot{\mathbf{u}}_{t-\Delta t} + \beta\Delta t^2\ddot{\mathbf{u}}_t \tag{4.58}$$

$$\dot{\mathbf{u}}_t = \dot{\mathbf{u}}_{t-\Delta t} + (1-\gamma)\,\Delta t\ddot{\mathbf{u}}_{t-\Delta t} + \gamma\Delta t\ddot{\mathbf{u}}_t \tag{4.59}$$

These are the standard Newmark approximation of displacement $\mathbf{u}_t$ and velocity $\dot{\mathbf{u}}_t$. We can write from Eqs. (4.55) and (4.56):

$$\ddot{\mathbf{u}}_t = b_1(\mathbf{u}_t - \mathbf{u}_{t-\Delta t}) + b_2\dot{\mathbf{u}}_{t-\Delta t} + b_3\ddot{\mathbf{u}}_{t-\Delta t} \tag{4.60}$$

$$\dot{\mathbf{u}}_t = b_4(\mathbf{u}_t - \mathbf{u}_{t-\Delta t}) + b_5\dot{\mathbf{u}}_{t-\Delta t} + b_6\ddot{\mathbf{u}}_{t-\Delta t} \quad (4.61)$$

where b_1 to b_6 are constants specified as:

$b_1 = \frac{1}{\beta\Delta t^2}$, $b_2 = \frac{1}{\beta\Delta t}$, $b_3 = \beta - \frac{1}{2}$,

$b_4 = \gamma\Delta t b_1$, $b_5 = 1 - \gamma\Delta t b_2$, $b_6 = \Delta t(1 + \gamma b_3 - \gamma)$.

By substituting Eqs. (4.60) and (4.61) for $\ddot{\mathbf{u}}_t$ and $\dot{\mathbf{u}}_t$ into Eq. (4.52), we get:

$$\underbrace{(b_1\mathbf{M} + b_4\mathbf{C} + \mathbf{K})}_{\bar{\mathbf{K}}}\mathbf{u}_t = \underbrace{\mathbf{F}_t + \mathbf{M}(b_1\mathbf{u}_{t-\Delta t} - b_2\dot{\mathbf{u}}_{t-\Delta t} - b_3\ddot{\mathbf{u}}_{t-\Delta t}) + \mathbf{C}(b_4\mathbf{u}_{t-\Delta t} - b_5\dot{\mathbf{u}}_{t-\Delta t} - b_6\ddot{\mathbf{u}}_{t-\Delta t})}_{\bar{\mathbf{F}}_t}$$

$$\bar{\mathbf{K}}\mathbf{u}_t = \bar{\mathbf{F}}_t \quad (4.62)$$

$\bar{\mathbf{K}}$ and $\bar{\mathbf{F}}_t$ are the effective stiffness matrix and the effective load vector.

The algorithm for the implementation of Newmark's solution is shown in Algorithm 4.1.

Algorithm 4.1 (**Newmark**)

I. **Initial calculation**

a. Form a static stiffness matrix **K**, mass matrix **M**, and damping matrix **C**
b. Specify the integration parameters β and γ. $\gamma \geq 0.50 \quad \beta \geq 0.25(0.5 + \gamma)^2$
c. Calculate the integration constants

$b_1 = \frac{1}{\beta\Delta t^2}$, $b_2 = \frac{1}{\beta\Delta t}$, $b_3 = \beta - \frac{1}{2}$, $b_4 = \gamma\Delta t b_1$

$b_5 = 1 - \gamma\Delta t b_2$, $b_6 = \Delta t(1 + \gamma b_3 - \gamma)$

d. Form the effective stiffness matrix

$$\bar{\mathbf{K}} = b_1\mathbf{M} + b_4\mathbf{C} + \mathbf{K}$$

e. Triangularize the effective stiffness matrix $\bar{\mathbf{K}} = \mathbf{LDL}^T$

f. Specify initial conditions $\mathbf{u}_0$, $\dot{\mathbf{u}}_0$ and $\ddot{\mathbf{u}}_0$

II. **Each time step**

a. Calculate the effective load vector

$$\bar{\mathbf{F}}_t = \mathbf{F}_t + \mathbf{M}(b_1\mathbf{u}_{t-\Delta t} - b_2\dot{\mathbf{u}}_{t-\Delta t} - b_3\ddot{\mathbf{u}}_{t-\Delta t}) + \mathbf{C}(b_4\mathbf{u}_{t-\Delta t} - b_5\dot{\mathbf{u}}_{t-\Delta t} - b_6\ddot{\mathbf{u}}_{t-\Delta t})$$

b. Solve for node displacement vector $\mathbf{u}_t$ at time **t** from $\bar{\mathbf{K}}\mathbf{u}_t = \bar{\mathbf{F}}_t$

$\mathbf{LDL}^T\mathbf{u}_t = \bar{\mathbf{F}}_t$ forward and back substitution only

$\mathbf{L}^T\mathbf{u}_t = \{\boldsymbol{y}\}$, $\mathbf{D}\{\boldsymbol{y}\} = \{\boldsymbol{z}\}$

$\mathbf{L}\{\boldsymbol{z}\} = \bar{\mathbf{F}}_t$ obtain $\{\boldsymbol{z}\}$ by forward substitution

$\mathbf{D}\{\boldsymbol{y}\} = \{\boldsymbol{z}\}$ obtain $\{\boldsymbol{y}\}$ by diagonal scaling

$\mathbf{L}^T\mathbf{u}_t = \{\boldsymbol{y}\}$ obtain $\mathbf{u}_t$ by backward substitution

c. Calculate node velocity and acceleration at time **t**

$$\ddot{\mathbf{u}}_t = b_1(\mathbf{u}_t - \mathbf{u}_{t-\Delta t}) + b_2\dot{\mathbf{u}}_{t-\Delta t} + b_3\ddot{\mathbf{u}}_{t-\Delta t}$$

$$\dot{\mathbf{u}}_t = b_4(\mathbf{u}_t - \mathbf{u}_{t-\Delta t}) + b_5\dot{\mathbf{u}}_{t-\Delta t} + b_6\ddot{\mathbf{u}}_{t-\Delta t}$$

d. Go to step II (a) with $t = t + \Delta t$

4.6.4 Stability of the Newmark method

For a vanishing damping, Newmark's method is conditionally stable if

$$\gamma \geq \frac{1}{2} \text{ and } \beta \leq \frac{1}{2} \text{ and } \Delta t \leq \frac{1}{\omega_{max}\sqrt{\frac{\gamma}{2} - \beta}}$$

where ω_{max} is the maximum frequency in the structural system. Newmark's is unconditionally stable if

$$2\beta \geq \gamma \geq \frac{1}{2}$$

However, if γ is greater than half, errors are introduced which are associated with numerical damping and period elongation.

Other similar methods in the Newmark family include Hilber, Hughes and Taylor's α method [86] and Wilson method [84, 85].

4.7 Introduction to model order reduction

The formulation of higher order system of differential equations for modelling composite laminates has been established in Chapter 3. Due to restrictions in numerical algorithm and digital computers, solving a high order model is associated with high computational time and poses a risk of computational errors in the result, hence the need for Model Order Reduction (MOR). MOR is a mature field when applied to linear systems, and several excellent books on the subject are available [52–55]. Many techniques are available for linear order reduction, including Krylov subspace projection based on orthogonal Arnoldi [56–57] or biorthogonal Lanczos [58] processes, principal components analysis and balanced truncation [59, 67-69], Hankel norm approximation [60], and singular value decomposition (SVD) based methods, which include Proper Orthogonal Decomposition (POD) in its many variants [61]. Many extensions to nonlinear system are also available, see e.g. [62–66], which combine system projection or truncation with suitable approximations of the nonlinear terms. While MOR has been widely applied in the fields of electric circuit and interconnect modelling [90–95] and Micro-Electro-Mechanical System (MEMS) [87–89], applications in structural models have received much less attention [102 – 103].

Choosing a particular MOR technique that is suitable for a particular system depends on several factors, such as type of system (linear or nonlinear), number and structure (order) of equations to be solved for and, in case of nonlinear systems, the degree of nonlinearity. In the case of PV module, derived formulations for thermal and mechanical system may either lead to first-order system, second-order system or coupled second-order system of differential equations. The general state-space approach is based on first order system and the procedure can be extended to reduction of second order or coupled second order systems but due to computational restraints and the need to preserve the system structure, second order based model order reduction schemes has been proposed in [70–72]. A brief review of the reduction methods based on first order and second order systems is presented in the sequel.

4.8 Model order reduction of first order systems

The state-space description of a system using the classical MOR is expressed as:

$$\begin{cases} \dot{\boldsymbol{x}}(t) = \boldsymbol{A}\boldsymbol{x}(t) + \boldsymbol{B}i(t), \\ \boldsymbol{y}(t) = \boldsymbol{C}\boldsymbol{x}(t) + \boldsymbol{D}i(t), \end{cases} \tag{4.63}$$

with $\boldsymbol{A} \in \mathbb{R}^{N\times N}$, $\boldsymbol{B} \in \mathbb{R}^{N\times P}$, $\boldsymbol{C} \in \mathbb{R}^{P\times N}$ and $\boldsymbol{D} \in \mathbb{R}^{P\times P}$, and obtain a reduced order model

$$\begin{cases} \dot{\boldsymbol{x}}_q(t) = \boldsymbol{A}_q\boldsymbol{x}_q(t) + \boldsymbol{B}_q i(t), \\ \boldsymbol{y}(t) = \boldsymbol{C}_q\boldsymbol{x}_q(t) + \boldsymbol{D}_q i(t), \end{cases} \tag{4.64}$$

with $\boldsymbol{A}_q \in \mathbb{R}^{q\times q}$, $\boldsymbol{B}_q \in \mathbb{R}^{q\times P}$, $\boldsymbol{C}_q \in \mathbb{R}^{P\times q}$ and $\boldsymbol{D}_q \in \mathbb{R}^{P\times P}$, subject to the fundamental conditions:

- The order of the reduced system must be less than the original system i.e., $q \ll N$;

- The transfer matrix of the reduced system $\boldsymbol{H}_q(s)$ must be close in some sense to the original transfer matrix $\boldsymbol{H}(s)$ i.e., $\boldsymbol{H}_q(s) \approx \boldsymbol{H}(s)$.

It is noted from Eqs. (4.63) and (4.64) that $\boldsymbol{D} = \boldsymbol{D}_q$, so this term does not affect the system complexity. Therefore, this term is dropped from the system equations by setting $\boldsymbol{D} = \boldsymbol{D}_q = \boldsymbol{0}$. The transfer matrices for system (4.63) and (4.64) are expressed as:

$$\begin{cases} \boldsymbol{H}(s) = \boldsymbol{C}(s\mathbb{I} - \boldsymbol{A})^{-1}\boldsymbol{B} \\ \boldsymbol{H}_q(s) = \boldsymbol{C}_q\left(s\mathbb{I} - \boldsymbol{A}_q\right)^{-1}\boldsymbol{B}_q \end{cases} \tag{4.65}$$

The state-space representation in Eq. (4.64) form the basis on which all the order reduction schemes are derived. In the sequel, some order reduction schemes for first order systems are highlighted. It is noted here that the techniques mentioned here are by no means exhaustive but represent fundamental approaches to reduce linear systems.

4.8.1 Moment matching

The moments or block moments [73, 74] of $\boldsymbol{H}(s)$ are defined as the matrix coefficients $\boldsymbol{M}_k \in \mathbb{R}^{P\times P}$ of the Taylor expansion $\boldsymbol{H}(s)$ around $s = 0$:

$$\boldsymbol{H}(s) = \boldsymbol{M}_0 + \boldsymbol{M}_1 s + \boldsymbol{M}_2 s^2 + \cdots \tag{4.65}$$

where the coefficients are related to the derivatives of the transfer matrix at $s = 0$,

$$\boldsymbol{M}_k = \frac{1}{k!}\frac{d^k \boldsymbol{H}(s)}{ds^k}\Big|_{s=0} \tag{4.67}$$

Based on Laplace transform property, the time-domain representation of the moment holds,

$$\boldsymbol{M}_k = \frac{(-1)^k}{k!}\int_{0^-}^{\infty} t^k\, \boldsymbol{h}(t)dt \tag{4.68}$$

where $\boldsymbol{h}(t) = \mathcal{L}^{-1}\{\boldsymbol{H}(s)\}$

An efficient way to obtain the approximation of the local behaviour of $\boldsymbol{H}(s)$ around $s = 0$ is to retain q terms in the polynomial [75]

$$\boldsymbol{H}(s) \approx \sum_{k=0}^{q-1} \boldsymbol{M}_k s^k \tag{4.69}$$

By constraining the first q moments of $\boldsymbol{H}_q(s)$ to be identical to the corresponding moments of $\boldsymbol{H}(s)$, a reduced model can be obtained. By rewriting Eq. (4.64) as:

$$\begin{cases} \boldsymbol{x}(t) = \boldsymbol{\Lambda}\dot{\boldsymbol{x}}(t) + \boldsymbol{R}i(t), \\ \boldsymbol{y}(t) = \boldsymbol{C}\boldsymbol{x}(t), \end{cases} \tag{4.70}$$

with $\boldsymbol{D} = \boldsymbol{0}$, $\boldsymbol{\Lambda} = \boldsymbol{A}^{-1}$ and $\boldsymbol{R} = -\boldsymbol{A}^{-1}\boldsymbol{B}$, it is obvious that

$$\boldsymbol{H}(s) = \boldsymbol{C}(\mathbb{I} - s\boldsymbol{\Lambda})^{-1}\boldsymbol{R} \tag{4.71}$$

The Taylor expansion of Eq. (4.71) at $s = 0$ gives:

$$\boldsymbol{H}(s) = \boldsymbol{C}\left(\sum_{k=0}^{\infty} s^k\, \boldsymbol{\Lambda}^k\right)\boldsymbol{R} = \sum_{k=0}^{\infty}[\boldsymbol{C}\boldsymbol{\Lambda}^k\boldsymbol{R}]s^k \tag{4.72}$$

From Eqs. (4.66) and (4.72), it can be seen that the moment of Eq. (4.68) is:

$$\boldsymbol{M}_k = \boldsymbol{C}\boldsymbol{\Lambda}^k\boldsymbol{R} = \boldsymbol{C}\boldsymbol{N}_k \tag{4.73}$$

with $\boldsymbol{N}_k = \boldsymbol{\Lambda}^k\boldsymbol{R} = \boldsymbol{\Lambda}\boldsymbol{N}_{k-1}$.

Equation (4.73), with the expression for $\boldsymbol{N}_k$ can be exploited to calculate the moments iteratively. The reduced order approximation $\boldsymbol{H}_q(s)$ can be computed by matching moments described by Eq. (4.73) to some prescribed order q and this can achieved by applying the so-called Pade approximation of $\boldsymbol{H}(s)$ or the method Asymptotic Waveform Evaluation (AWE) described in [75].

4.8.2 Complex frequency hopping (CPH)

Instead of performing Taylor expansion at only $s = 0$ and match q moments at this frequency as for moment matching, multiple frequencies s_v called "hops" can be selected, and match small number q_v of moments $\boldsymbol{M}_{v,k}$ at each of these frequencies. This is called complex frequency hopping. This provides more accuracy control which is distributed over the frequency band of interest. Moments evaluation at arbitrary frequencies $s = s_v$ follows from the approach for moment matching at a single frequency. By defining

$\boldsymbol{\Lambda}_v = (\boldsymbol{A} - s_v\mathbb{I})^{-1}$ and $\boldsymbol{R}_v = -(\boldsymbol{A} - s_v\mathbb{I})^{-1}\boldsymbol{B}$

the transfer function is derived from Eq. (4.65), as:

$$\begin{aligned}
&\boldsymbol{H}(s) = \boldsymbol{C}(s\mathbb{I} - \boldsymbol{A})^{-1}\boldsymbol{B} \\
&= \boldsymbol{C}[(s - s_v)\mathbb{I} - (\boldsymbol{A} - s_v\mathbb{I})]^{-1}\boldsymbol{B} \\
&= \boldsymbol{C}\left[\boldsymbol{\Lambda}_v{}^{-1}\left((s - s_v)\boldsymbol{\Lambda}_v - \mathbb{I}\right)\right]^{-1}\boldsymbol{B} \\
&= \boldsymbol{C}[\mathbb{I} - (s - s_v)\boldsymbol{\Lambda}_v]^{-1}\boldsymbol{R}_v \\
&= \boldsymbol{M}_{v,0} + \boldsymbol{M}_{v,1}(s - s_v) + \boldsymbol{M}_{v,2}(s - s_v)^2 + \cdots
\end{aligned} \tag{4.74}$$

whose moments at $s = s_v$ are expressed as:

$$\boldsymbol{M}_{v,k} = \frac{1}{k!}\frac{d^k\boldsymbol{H}(s)}{ds^k}\Big|_{s=s_v} = \boldsymbol{C}\boldsymbol{\Lambda}_v{}^k\boldsymbol{R}_v \tag{4.75}$$

With Eq. (4.75), moment matching at any arbitrary frequency point can be achieved by applying the AWE procedure in [75].

4.8.3 Projection method by Krylov subspaces

Methods of explicit moment matching and CPH are characterised by major difficulties in the calculation of the transfer function moments and limited to low orders q which makes this method to be unreliable. An alternative and more reliable approach is by projection of the system equations onto a low-dimensional (Krylov) subspaces generated by appropriate basis vectors as illustrated in Fig. 1.7. The basic steps in the method of projection are [75]:

(a) Introduce a change of coordinates through a low-dimensional subspace $\boldsymbol{V}_q \in \mathbb{R}^{N\times q}$ spanned by $q \ll N$ linearly independent vectors. Mathematically,

$$\boldsymbol{x} = \boldsymbol{V}_q \boldsymbol{x}_q = \sum_{k=1}^{q} \boldsymbol{v}_k x_k$$

(b) Projection of the state-space equations by using another full column rank matrix $\boldsymbol{W}_q \in \mathbb{R}^{N\times q}$ that is biorthogonal to $\boldsymbol{V}_q$ such that $\boldsymbol{W}_q{}^T \boldsymbol{V}_q = \mathbb{I}$.

By premultiplying first part of Eq. (4.63) by $\boldsymbol{W}_q{}^T$, we get:

$$\begin{cases} \dot{\boldsymbol{x}}_q(t) = \boldsymbol{W}_q{}^T \boldsymbol{A}\boldsymbol{V}_q \boldsymbol{x}(t) + \boldsymbol{W}_q{}^T \boldsymbol{B} i(t), \\ \boldsymbol{y}(t) = \boldsymbol{C}\boldsymbol{V}_q \boldsymbol{x}_q(t) + \boldsymbol{D} i(t), \end{cases} \tag{4.76}$$

Equation (4.76) can be compared to Eq. (4.64) by defining the reduced order state space matrices as:

$$\boldsymbol{A}_q = \boldsymbol{W}_q{}^T \boldsymbol{A}\boldsymbol{V}_q \,,\ \boldsymbol{B}_q = \boldsymbol{W}_q{}^T \boldsymbol{B} \,,\ \boldsymbol{C}_q = \boldsymbol{C}\boldsymbol{V}_q \,,\ \boldsymbol{D}_q = \boldsymbol{D} \,.$$

To match the moments of the reduced order system to the original system, the projection matrices $\boldsymbol{V}_q$, $\boldsymbol{W}_q$ are constructed with basis of order q Krylov subspaces defined by

$$\mathcal{K}_q(\boldsymbol{A},\boldsymbol{B}) = \text{span}\{\boldsymbol{B},\boldsymbol{AB},\boldsymbol{A}^2\boldsymbol{B},\dots,\boldsymbol{A}^{q-1}\boldsymbol{B}\} \quad (4.77)$$

A particular case where $\boldsymbol{W}_q = \boldsymbol{V}_q$, with ${\boldsymbol{V}_q}^T\boldsymbol{V}_q = \mathbb{I}$ is called the Galerkin projection otherwise known as one-sided Krylov method [70]. A numerically stable way to compute an orthogonal matrix whose columns form a basis of the Krylov subspace is by using the Arnoldi algorithm. The purpose of the Arnoldi process it to compute a block matrix with orthogonal columns at the time in an iteration loop and orthogonalize it with the already computed block matrices. The basic block Arnoldi algorithm is presented in Algorithm 4.2:

Algorithm 4.2 (**Block Arnoldi scheme**)

Input: matrix $\boldsymbol{\Lambda}$ and vector $\boldsymbol{R}$, dimension of Krylov subspace q_1

Compute QR factorization $\boldsymbol{R} = \boldsymbol{Q}_1\boldsymbol{X}$

For $k = 1, 2, \dots\dots, q_1 - 1$ **do**

$\boldsymbol{U} = \boldsymbol{\Lambda}\boldsymbol{Q}_k$**;**
for $j = 1, \dots,\ k$ **do**
$\boldsymbol{H}_{j,k} = {\boldsymbol{Q}_j}^T\boldsymbol{U}$
$\boldsymbol{U} \leftarrow \boldsymbol{U} - \boldsymbol{H}_{j,k}\boldsymbol{Q}_j$
end for

compute QR factorization $\boldsymbol{U} = \boldsymbol{Q}_{k+1}\boldsymbol{H}_{k+1,k}$

end for

return $\boldsymbol{V}_q = (\boldsymbol{Q}_1, \dots\dots, \boldsymbol{Q}_{q1})$

The output of this algorithm guarantees that:

$\mathrm{im}(\boldsymbol{V}_q) = \mathcal{K}_q(\boldsymbol{A}, \boldsymbol{B})$ with $\boldsymbol{V}_q{}^T \boldsymbol{V}_q = \mathbb{I}$

For improved accuracy, numerical stability and preserve passivity of the system, other methods which are based on Krylov subspace projection are available as discussed in [75]. Examples are Passive Reduced Order Interconnect Macromodeling Algorithm (PRIMA), Multipoint moment matching and implicit moment matching. Although the Krylov method provides means to reduce large-scale systems, some difficulties may arise when the number of input/output ports P becomes very large [75].

4.8.4 Proper orthogonal decomposition (POD)

Proper orthogonal decomposition (POD) builds on the fact that a good candidate for a projection matrix should provide an accurate representation of the subspace where the system states evolve during normal operation. In this regard, a full simulation of the system can be performed using some training input function $i(t)$ and computes a set of states $\boldsymbol{x}_k = \boldsymbol{x}(t_k)$ at some time points t_k, for $k = 1, \dots, m$. The computed vectors at the time points represent snapshots of the system dynamic states. By collecting these vectors in a matrix,

$$\boldsymbol{X}_m = (\boldsymbol{x}_1, \dots, \boldsymbol{x}_k) \tag{4.78}$$

a good projection matrix for reduction of the system states can be built. Matrix $\boldsymbol{X}_K$ can be orthogonalized by using a singular value decomposition (SVD):

$$\boldsymbol{X}_m \approx \boldsymbol{U}_q \boldsymbol{\Sigma}_q \boldsymbol{V}_q{}^T \tag{4.79}$$

where only $q \leq m$ singular values are retained based on a choice of suitable threshold. The span of the orthogonal columns of $\boldsymbol{U}_q$ approximately characterised

the image of $\boldsymbol{X}_m$. Thus, $\boldsymbol{U}_q$ serves as the projection matrix for the state-space system [75].

4.9 Model order reduction of second-order systems

The second order model considered here is given in the form:

$$\mathbf{M}\ddot{\boldsymbol{z}} + \mathbf{D}\dot{\boldsymbol{z}} + \mathbf{K}\mathbf{z} = \boldsymbol{G}i(t) \tag{4.80a}$$

$$\boldsymbol{y}(t) = \boldsymbol{L}\boldsymbol{z}(t) \tag{4.80b}$$

with $\boldsymbol{M}, \boldsymbol{D}, \boldsymbol{K} \in \mathbb{R}^{\mathrm{N}\times N}$ $\boldsymbol{B} \in \mathbb{R}^{\mathrm{N}\times n}$ $\boldsymbol{L} \in \mathbb{R}^{n\times N}$ $\boldsymbol{z} \in \mathbb{R}^{\mathrm{N}\times 1}$ $n \ll N$

The procedure described in Sec. 4.7 can also be extended for reduction of second-order systems by converting the system (4.80) to first-order system as described in Sec. 4.2 and then perform an order reduction as for a regular state-space system. However, two major problems are associated with this approach which are (i) inability to preserve the second-order structure of the system and (ii) high computational cost associated with solving system equations with increased order i.e., $2 \times \mathrm{N}$ system of first order equations. The second-order Krylov method which was first proposed in [76] and further investigated in [77] provides a good means to eliminate these problems. Equivalently, model (4.80) can rewritten as:

$$\mathbf{E}\dot{\boldsymbol{x}} = \boldsymbol{A}\boldsymbol{x} + \bar{\boldsymbol{B}}i(t) \tag{4.81a}$$

$$\boldsymbol{y}(t) = \bar{\boldsymbol{L}}\boldsymbol{x}(t) \tag{4.81b}$$

where

$$\mathbf{E} = \begin{bmatrix} \mathbb{I} & \mathbf{0} \\ \mathbf{0} & \boldsymbol{M} \end{bmatrix}, \quad \boldsymbol{A} = \begin{bmatrix} \mathbf{0} & \mathbb{I} \\ -\boldsymbol{K} & -\boldsymbol{D} \end{bmatrix}, \quad \bar{\boldsymbol{B}} = \begin{bmatrix} \mathbf{0} \\ \boldsymbol{G} \end{bmatrix}, \quad \boldsymbol{x} = \begin{bmatrix} \boldsymbol{z} \\ \dot{\boldsymbol{z}} \end{bmatrix}, \quad \bar{\boldsymbol{L}} = [\boldsymbol{L} \quad \mathbf{0}] .$$

The ith moment around $s = 0$ for the state-space system Eq. (4.81) is defined as;

$$\boldsymbol{m}_i = \bar{\boldsymbol{L}}(\boldsymbol{A}^{-1}\boldsymbol{E})^{\boldsymbol{i}}\boldsymbol{A}^{-1}\bar{\boldsymbol{B}},\ \ i = 0, 1, \ldots \tag{4.82}$$

By substituting for the matrices $\boldsymbol{A}$, $\boldsymbol{E}$, $\bar{\boldsymbol{B}}$ and $\bar{\boldsymbol{L}}$ into Eq. (4.82), we get:

$$\boldsymbol{m}_i = [\boldsymbol{L} \quad \boldsymbol{0}]\left(\begin{bmatrix} \boldsymbol{0} & \mathbb{I} \\ -\boldsymbol{K} & -\boldsymbol{D} \end{bmatrix}^{-1}\begin{bmatrix} \mathbb{I} & \boldsymbol{0} \\ \boldsymbol{0} & \boldsymbol{M} \end{bmatrix}\right)^{\boldsymbol{i}}\begin{bmatrix} \boldsymbol{0} & \mathbb{I} \\ -\boldsymbol{K} & -\boldsymbol{D} \end{bmatrix}^{-1}\begin{bmatrix} \boldsymbol{0} \\ \boldsymbol{G} \end{bmatrix} \tag{4.83a}$$

$$\boldsymbol{m}_i = [\boldsymbol{L} \quad \boldsymbol{0}]\begin{bmatrix} -\boldsymbol{K}^{-1}\boldsymbol{D} & -\boldsymbol{K}^{-1}\boldsymbol{M} \\ \mathbb{I} & \boldsymbol{0} \end{bmatrix}^{\boldsymbol{i}}\begin{bmatrix} -\boldsymbol{K}^{-1}\boldsymbol{G} \\ \boldsymbol{0} \end{bmatrix} \tag{4.83b}$$

The second-order Krylov subspace provides means to calculate these moments by recursive procedure. A second-order Krylov subspace is defined by [70–72]:

$$\mathcal{K}_{q1}(\boldsymbol{A}_1, \boldsymbol{A}_2, \bar{\boldsymbol{G}}) = \text{span}\left\{\mathbf{p}_0,\ \mathbf{p}_1, \ldots\ldots, \mathbf{p}_{q1-1,}\right\} \tag{4.84}$$

where

$$\begin{cases} \mathbf{p}_0 = \boldsymbol{b}_1, \quad \mathbf{p}_1 = \boldsymbol{A}_1\bar{\boldsymbol{G}} \\ \mathbf{p}_i = \boldsymbol{A}_1\mathbf{p}_{i-1} + \boldsymbol{A}_2\mathbf{p}_{i-2} \end{cases} \tag{4.85}$$

$$\boldsymbol{A}_1 = -\boldsymbol{K}^{-1}\boldsymbol{D}\ ,\ \boldsymbol{A}_2 = -\boldsymbol{K}^{-1}\boldsymbol{M}\ ,\ \bar{\boldsymbol{G}} = -\boldsymbol{K}^{-1}\boldsymbol{G}\ .$$

With respect Eq. (4.84), the so-called input and output second-order Krylov subspaces for system (4.80) are, respectively, $\mathcal{K}_{q_1}(-\boldsymbol{K}^{-1}\boldsymbol{D}, -\boldsymbol{M}^{-1}\boldsymbol{D}, -\boldsymbol{K}^{-1}\boldsymbol{G})$ and $\mathcal{K}_{q_1}(-\boldsymbol{K}^{-T}\boldsymbol{D}^T, -\boldsymbol{K}^{-T}\boldsymbol{M}^T, -\boldsymbol{K}^{-T}\boldsymbol{L})$. These Krylov subspaces can be used to find the projection matrices $\boldsymbol{V}_r$, $\boldsymbol{W}_r$ that can be applied directly to the second-order system (4.80). A change of coordinate may be considered for the original system as:

$$\boldsymbol{z} = \boldsymbol{V}_r\boldsymbol{z}_r\ ,\ \boldsymbol{V}_r \in \mathbb{R}^{\mathrm{N}\times q_1}\ ,\ \boldsymbol{z}_r \in \mathbb{R}^{q_1\times 1}\ ,\ q_1 \ll N\ . \tag{4.86}$$

By substituting Eq. (4.86) into (4.80) and then multiply the state equation by the transpose of a projection matrix $\boldsymbol{W}_r$, a reduced order model $q = 2q_1$ is obtained as:

$$\boldsymbol{M}_r\ddot{\boldsymbol{z}}_r + \boldsymbol{D}_r\dot{\boldsymbol{z}}_r + \boldsymbol{K}_r\boldsymbol{z}_r = \boldsymbol{G}_r i(t) \tag{4.87a}$$

$$\boldsymbol{y}(t) = \boldsymbol{L}_r\boldsymbol{z}_r(t) \tag{4.87b}$$

where

$\boldsymbol{M}_r = \boldsymbol{W_r}^T(\boldsymbol{M}\boldsymbol{V}_r)$, $\boldsymbol{D}_r = \boldsymbol{W_r}^T(\boldsymbol{D}\boldsymbol{V}_r)$, $\boldsymbol{K}_r = \boldsymbol{W_r}^T(\boldsymbol{K}\boldsymbol{V}_r)$,

$\boldsymbol{G}_r = \boldsymbol{W_r}^T\boldsymbol{G}$, $\boldsymbol{L}_r = \boldsymbol{L}\boldsymbol{V}_r$.

According to the theorems stated in [70]:

Theorem 1: If the matrix $\boldsymbol{V}_r$ is the basis of the input second-order Krylov subspace $\mathcal{K}_{q_1}(-\boldsymbol{K}^{-1}\boldsymbol{D}, -\boldsymbol{M}^{-1}\boldsymbol{D}, -\boldsymbol{K}^{-1}\boldsymbol{G})$ with rank q_1 and the matrix $\boldsymbol{W_r}$ is chosen such that matrix $\boldsymbol{W_r}^T\boldsymbol{K}\boldsymbol{V}_r$ is non-singular, then the first q_1 moments of the original and the reduced-order models match.

As remarked in Sec. 4.7, a particular case where $\boldsymbol{W}_r = \boldsymbol{V}_r$, with $\boldsymbol{V_r}^T\boldsymbol{V}_r = \mathbb{I}$ is called one-sided Krylov method. To generalize the application of theorem 1 to two-sided methods, theorem 2 is considered thus [76]:

Theorem 2: If the matrix $\boldsymbol{V}_r$ and $\boldsymbol{W}_r$ are the bases of the input and output second-order Krylov subspaces $\mathcal{K}_{q_1}(-\boldsymbol{K}^{-1}\boldsymbol{D}, -\boldsymbol{M}^{-1}\boldsymbol{D}, -\boldsymbol{K}^{-1}\boldsymbol{G})$ and $\mathcal{K}_{q_1}(-\boldsymbol{K}^{-T}\boldsymbol{D}^T, -\boldsymbol{K}^{-T}\boldsymbol{M}^T, -\boldsymbol{K}^{-T}\boldsymbol{G})$, both with rank q_1, then the first $2q_1$ of the original moment and reduced-order system match.

Numerical implementation of the second-order reduction schemes is performed by extending the Arnoldi algorithm 1 to find the basis for the second-order Krylov subspaces. Algorithm 4.2 [78] given below can be used to find an orthonormal basis $\boldsymbol{V}_r$ such that $\boldsymbol{V_r}^T\boldsymbol{V}_r = \mathbb{I}$ and the columns of the matrix $\boldsymbol{V}_r$ are the basis for the given subspaces.

Algorithm 4.3 (**Second-order Arnoldi algorithm**)

Input: $\boldsymbol{A_1 = -K^{-1}D}$, $\boldsymbol{A_2 = -K^{-1}M}$, $\boldsymbol{\bar{G} = -K^{-1}G}$

0. (a) Delete all linearly dependent starting vectors to get m_1 linearly dependent vectors.

   (b) Set $\boldsymbol{v_1 = \frac{g_1}{\|g_1\|_2}}$

   where $\boldsymbol{g_1}$ is the starting vector after deleting the dependent starting vectors and set $\mathbf{I}_1 = \mathbf{0}$ for $\mathbf{I}_1 \in \mathbb{R}^{N\times 1}$

1. For $i = 2, 3, \ldots \ldots,$ do

   (a) Calculate the next vector: If $i \leq m_1$ then set $\bar{\boldsymbol{v}}_i$ as the ith starting vector and $\bar{\boldsymbol{I}}_i = \mathbf{0}$. Otherwise, set

   $\bar{\boldsymbol{v}}_i = \boldsymbol{A_1 v}_{i-m_1} + \boldsymbol{A_2 I}_{i-m_1}$, $\qquad \bar{\boldsymbol{I}}_i = \boldsymbol{v}_{i-m_1}$

   (b) Orthogonalization: For $j = 1$ to $i - 1$ do,

   $\mathrm{h} = \bar{\boldsymbol{v}}_i^{\,T}\boldsymbol{v}_j$, $\bar{\boldsymbol{v}}_i \leftarrow \bar{\boldsymbol{v}}_i - \mathrm{h}\boldsymbol{v}_j$, $\qquad \bar{\boldsymbol{I}}_i \leftarrow \bar{\boldsymbol{I}}_i - \mathrm{h}\boldsymbol{I}_j$

   (c) Deflation: If $\bar{\boldsymbol{v}}_i \neq \mathbf{0}$ then go to (1d)

   Elseif $\bar{\boldsymbol{I}}_i \neq \mathbf{0}$ then $\boldsymbol{v}_i = \mathbf{0}$ and go to (1e)

   Else, $m_1 = m_1 - 1$ and go to (1a) but go to step (2) if $m_1 = 0$.

   (d) Normalization: $\boldsymbol{v}_i = \frac{\bar{\boldsymbol{v}}_i}{\|\bar{\boldsymbol{v}}_i\|_2}$ and $\boldsymbol{I}_i = \frac{\bar{\boldsymbol{I}}_i}{\|\bar{\boldsymbol{v}}_i\|_2}$

   (e) Increase i and go to step (1a).

Return: $\boldsymbol{V}_r = (\boldsymbol{v}_1, \ldots\ldots, \boldsymbol{v}_s)$

2. Delete the zero columns of the matrix $\boldsymbol{V}_r$ produced by the deflation process.

In practical implementation, it is remarked in step (1c) that the vectors is not compared with zero but with a positive small number ϵ. Therefore, in step (1c) $\bar{\boldsymbol{v}}_i = \mathbf{0}$ and $\bar{\boldsymbol{I}}_i = \mathbf{0}$ is substituted with $\|\bar{\boldsymbol{v}}_i\|_2 < \epsilon$ and $\|\bar{\boldsymbol{I}}_i\|_2 < \epsilon$. Similar

procedure can be used to find the basis of the output Krylov subspace $\mathcal{K}_{q_1}(-\boldsymbol{K}^{-T}\boldsymbol{D}^T, -\boldsymbol{K}^{-T}\boldsymbol{M}^T, -\boldsymbol{K}^{-T}\boldsymbol{L})$. With the computation of $\boldsymbol{V}_r$ and $\boldsymbol{W}_r$, the system matrices of the reduced-order model $\boldsymbol{M}_r$, $\boldsymbol{D}_r$, $\boldsymbol{K}_r$ and $\boldsymbol{G}_r$ can be computed. By solving Eq. (4.87a), the reduced states are determined and then the approximation of the output of the original states can be obtained by using Eq. (4.87b).

CHAPTER 5

ADVANCED SHEAR-LAG MODELS FOR COUPLED THERMO-VISCO-ELASTIC MODELLING OF PHOTOVOLTAIC LAMINATES

5.1 Introduction

In Chapter 3, an overview of general theory of isotropic linear thermoelasticity was presented and a review of the governing equations for linear thermoelasticity outlined. Considering that a photovoltaic laminate is composed of layers of Glass, EVA, Silicon and Backsheet with different thermal, electrical and mechanical properties, the mechanical response of the laminate during lamination would be reasonably estimated using coupled thermoelastic relations. Reference solution for coupled thermoelastic relations for photovoltaic module using a classical approach is presented in this chapter. This is followed by using thermo-mechanical derivations in Chapter 3 subject to relaxed Kirchhoff's theory to obtain the governing thermo-mechanical relations for photovoltaic module during lamination by assuming a zero thickness for the EVA layer and substitution of a shear-lag interface with time-temperature dependent behaviour estimated based on the viscoelastic models highlighted in Chapter 3. A semi-analytic approach is then used

to obtain the solutions of the resulting thermo-mechanical equations by first assuming a spatially uniform temperature within the laminate and then using a more realistic non-uniform temperature distributions to accurately assess the amount of the residual compressive stresses raised in the Silicon cells after lamination [97]. The procedure described in this chapter is first derived for a 2D geometry with a single solar cell and since a typical photovoltaic module contains more than one Silicon cell in which the residual thermoelastic stresses may vary from one position to the other, an extension of the current formulation is provided for 3D geometry containing four Silicon cells so that a comprehensive analysis of induced thermoelastic stresses during lamination can be performed.

5.2 Thermo-elastic stress analysis of a laminate with fully bonded interface

This formulation is based on a stack of photovoltaic laminate which layers are composed of glass, EVA, Silicon, EVA and Backsheet. All the interfaces between the layers are considered here as fully bonded. The cross-section of the PV is shown in Fig. 5.1. The stack is heated to a high temperature of 150 ^{0}C to allow bonding of the various layers and then cooled down to room temperature of 25 ^{0}C. Thus, the 5 layer module is subjected to a differential thermal load of -125 ^{0}C.

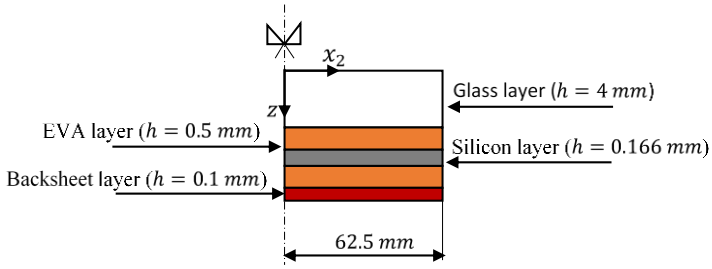

Figure 5.1: Cross-section of the PV module used for the stress analysis with perfectly bonded interfaces.

During lamination, the entire module is assumed to be at uniform temperature. Table 5.1 shows the material properties of the layers composing the module.

Table 5.1. Material properties of the layers composing the laminate.

	Glass layer	EVA layer	Silicon layer	Backsheet
Young's Modulus (MPa)	73×10^3	Viscoelastic	130×10^3	2.83×10^3
Coefficient of thermal expansion ($1/^o$C)	8×10^{-6}	2.7×10^{-4}	2.49×10^{-6}	5.04×10^{-5}
Poisson's ratio	0.23	0.35	0.28	0.40

Based on the Euler-Bernoulli's hypothesis of conservation of plane cross-sections, the longitudinal strain at an arbitrary position x_2 is given by [96]:

$$\varepsilon_{x_2,i} = \alpha_i \Delta T_i + \frac{\sigma_{x_2,i}}{E_i} = \varepsilon_0 + \Upsilon z \qquad \text{for } i = 1, 2, .., 5 \tag{5.1}$$

where ε_0 and Υ represent, respectively, the longitudinal strain and the beam curvature at $x_2 = 0$. In Eq. (5.1), E_i, α_i and ΔT_i are, respectively, the Young's modulus, coefficient of thermal expansion and change in temperature of a generic layer.

Eq. (5.1) allows the computation of the stresses σ_{x_2} at an arbitrary position along z:

$$\sigma_{x_2,i} = -E_i \alpha_i \Delta T_i + E_i \varepsilon_0 + E_i \Upsilon z \tag{5.2}$$

and the unknowns ε_0 and Υ can be determined by imposing the conditions of vanishing axial force and bending moment:

$$\sum_{i=1}^{n} \int_{z_i^{(1)}}^{z_i^{(2)}} \sigma_{x_2,i}\, \omega \, dz = 0 \tag{5.3a}$$

$$\sum_{i=1}^{n} \int_{z_i^{(1)}}^{z_i^{(2)}} \sigma_{x_2,i}\, \omega\, z dz = 0 \qquad (5.3b)$$

Where $z_i^{(1)}$ and $z_i^{(2)}$ are, respectively, the upper and lower interfaces of the ith layer, measured from the $x_2 - z$ plane, with thickness $h_i = z_i^{(2)} - z_i^{(1)}$, while ω denotes the out of plane thickness. By introducing Eq. (5.2) into (5.3), we obtain a set of equations in matrix form:

$$\begin{bmatrix} M_{11} & M_{12} \\ M_{21} & M_{22} \end{bmatrix} \begin{Bmatrix} \varepsilon_0 \\ \Upsilon \end{Bmatrix} = \begin{Bmatrix} V_1 \\ V_2 \end{Bmatrix} \qquad (5.4)$$

where the coefficients M_{11}, M_{12}, M_{21}, M_{22}, V_1 and V_2 are given by:

$$M_{11} = \sum_{i=1}^{n} \int_{z_i^{(1)}}^{z_i^{(2)}} E_i\, dz, \qquad (5.5a)$$

$$M_{12} = M_{21} = \sum_{i=1}^{n} \int_{z_i^{(1)}}^{z_i^{(2)}} E_i\, z dz, \qquad (5.5b)$$

$$M_{22} = \sum_{i=1}^{n} \int_{z_i^{(1)}}^{z_i^{(2)}} E_i\, z^2 dz, \qquad (5.5c)$$

$$V_1 = \sum_{i=1}^{n} \int_{z_i^{(1)}}^{z_i^{(2)}} E_i \alpha_i \Delta T_i\, dz,$$

(5.5d)

$$V_2 = \sum_{i=1}^{n} \int_{z_i^{(1)}}^{z_i^{(2)}} E_i \alpha_i \Delta T_i\, z dz$$

(5.5e)

Having computed ε_0 and Υ, stresses $\sigma_{x_2,i}$ and strains $\varepsilon_{x_2,i}$ can be determined at any point within the layers of the module.

5.3 2D Coupled thermomechanical shear-lag formulation

In this section, a coupled shear-lag model is proposed to estimate residual thermo-mechanical stresses in the module after lamination [97]. In this alternative structural model, relative displacements are admitted from one layer to the next, as the EVA layer is modelled as an adhesive with zero thickness (see Fig. 5.2). As compared to the simplified shear-lag theory proposed in [96], which does not account for the effect of normal peeling tractions in the shear-lag formulation and satisfies the rotational equilibrium only in an approximate way, the present formulation accounts for both peeling and shearing tractions.

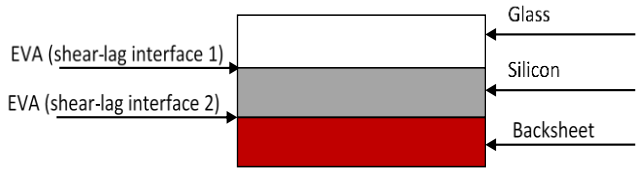

Figure 5.2: PV module cross-section for the shear-lag model.

For accurate estimation of the non-uniform temperature field during lamination, a formulation for the thermal system is first derived and using the thermal coupling, the solution for the thermal system is used as an input to obtain the mechanical response of the PV module.

5.3.1 Heat conduction problem

A model problem consisting of a Silicon cell embedded in a stack composed of glass, EVA and backsheet is considered as shown in Fig. 5.3. For an accurate heat conduction simulation of the lamination process and its subsequent stages, we consider a 3D heat equation of the form:

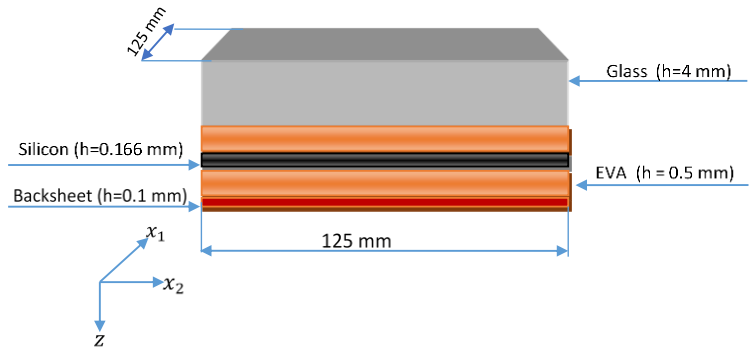

Figure 5.3: module geometry for the thermal analysis.

$$C\frac{\partial T}{\partial t} = \lambda_x \frac{\partial^2 T}{\partial {x_1}^2} + \lambda_y \frac{\partial^2 T}{\partial {x_2}^2} + \lambda_z \frac{\partial^2 T}{\partial z^2} + H \tag{5.6}$$

where $T\,(x_1, x_2, z, t)$ represents the unknown space- and time-dependent temperature profile; $C\,(x_1, x_2, z)$ is an equivalent volumetric heat capacity (J/m^{3}K), which is equal to an equivalent mass density multiplied by the equivalent specific heat capacity (C =$\rho \times c_p$), taking into account the composite structure of the laminate. The function $H\,(x_1, x_2, z, t)$ represents a heat source and, since there is no heat source in this problem, the term H can be dropped from Eq. (5.6). The coefficients $\lambda_{x_1}(x_1, x_2, z)$, $\lambda_{x_2}(x_1, x_2, z)$ and $\lambda_z(x_1, x_2, z)$ are the thermal conductivities in the x_1, x_2 and z directions, respectively. According to Fourier law, the heat flows in the x_1, x_2 and z direction can be related to the temperature gradients as follows:

$$\bar{q}_z = -\lambda_z \frac{\partial T}{\partial z} \tag{5.7a}$$

$$\bar{q}_x = -\lambda_{x_1} \frac{\partial T}{\partial x_1} \tag{5.7b}$$

$$\bar{q}_y = -\lambda_{x_2} \frac{\partial T}{\partial x_2} \tag{5.7c}$$

Substituting (5.7) into (5.6), we have:

$$C\frac{\partial T}{\partial t} = -\frac{\partial q_{x_1}}{\partial x_1} - \frac{\partial q_{x_2}}{\partial x_2} - \frac{\partial q_z}{\partial z} \tag{5.8}$$

Using now a finite difference (FD) discretization scheme defined by grid spacing Δx_i, Δy_j and Δz_k in the x_1-, x_2- and z-directions, respectively, with associated discretization indices i for $1 \leq i \leq l$, j for $1 \leq j \leq s$ and k for $1 \leq k \leq m$ (see Fig. 5.4), we can rephrase (5.8) as [16, 81]:

$$C_{i,j,k}\frac{dT_{i,j,k}}{dt} = \frac{q_{i-\frac{1}{2},j,k} - q_{i+\frac{1}{2},j,k}}{\Delta x_{1_i}} + \frac{q_{i,j-\frac{1}{2},k} - q_{i,j+\frac{1}{2},k}}{\Delta x_{2_j}} + \frac{q_{i,j,k-\frac{1}{2}} - q_{i,j,k+\frac{1}{2}}}{\Delta z_k} \tag{5.9}$$

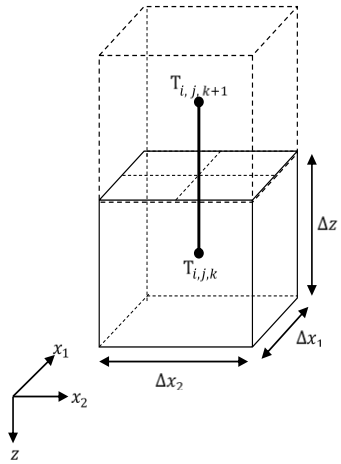

Figure 5.4: Finite difference discretization, reference system and grid spacing for a unit cell.

Multiplying Eq. (5.9) by the volume, $V_{i,j,k}$ of each cell in the FD discretization leads to:

$$C_{i,j,k}V_{i,j,k}\frac{\partial T_{i,j,k}}{\partial t} = \bar{Q}_{i-\frac{1}{2},j,k} - \bar{Q}_{i+\frac{1}{2},j,k} + \bar{Q}_{i,j-\frac{1}{2},k} - \bar{Q}_{i,j+\frac{1}{2},k} + \bar{Q}_{i,j,k-\frac{1}{2}} - \bar{Q}_{i,j,k+\frac{1}{2}} \tag{5.10}$$

where $\bar{Q}$ represents, consistently with energy conservation principles, the heat flow exchanged at mesh points, which can be further expressed as $\bar{Q} = K\Delta T$, where ΔT

is the temperature variation between two adjacent mesh points, and K is the corresponding thermal conductance. The latter is a function of the equivalent thermal conductivities of the grid points and on the laminate composition through its thickness, the width, and the size of the grid spacings, i.e. Δz_k, Δx_{2_j} and Δx_{1_i}. Since the volume of a cell is $V_{i,j,k} = \Delta x_{1_i} \Delta x_{2_j} \Delta z_k$, the equivalent thermal conductances can be computed according to [81]:

$$K_{i-\frac{1}{2},j,k} = \frac{\Delta x_{2_j} \Delta z_k}{\frac{\Delta x_{1_{i-1}}}{2\lambda_{i-1,j,k}} + \frac{\Delta x_{1_i}}{2\lambda_{i,j,k}} + R_{i-\frac{1}{2},j,k}}, \tag{5.11a}$$

$$K_{i+\frac{1}{2},j,k} = \frac{\Delta x_{2_j} \Delta z_k}{\frac{\Delta x_{1_{i+1}}}{2\lambda_{i+1,j,k}} + \frac{\Delta x_{1_i}}{2\lambda_{i,j,k}} + R_{i+\frac{1}{2},j,k}}, \tag{5.11b}$$

$$K_{i,j-\frac{1}{2},k} = \frac{\Delta x_{1_i} \Delta z_k}{\frac{\Delta x_{2_{j-1}}}{2\lambda_{i,j-1,k}} + \frac{\Delta x_{2_j}}{2\lambda_{i,j,k}} + R_{i,j-\frac{1}{2},k}}, \tag{5.11c}$$

$$K_{i,j+\frac{1}{2},k} = \frac{\Delta x_{1_i} \Delta z_k}{\frac{\Delta x_{2_{j+1}}}{2\lambda_{i,j+1,k}} + \frac{\Delta x_{2_j}}{2\lambda_{i,j,k}} + R_{i,j+\frac{1}{2},k}}, \tag{5.11d}$$

$$K_{i,j,k-\frac{1}{2}} = \frac{\Delta x_{1_i} \Delta x_{2_j}}{\frac{\Delta z_{k-1}}{2\lambda_{i,j,k-1}} + \frac{\Delta z_k}{2\lambda_{i,j,k}} + R_{i,j,k-\frac{1}{2},}}, \tag{5.11e}$$

$$K_{i,j,k+\frac{1}{2}} = \frac{\Delta x_{1_i} \Delta x_{2_j}}{\frac{\Delta z_{k+1}}{2\lambda_{i,j,k+1}} + \frac{\Delta z_k}{2\lambda_{i,j,k}} + R_{i,j,k+\frac{1}{2},}}, \tag{5.11f}$$

where the R terms are the interfacial resistances between adjacent cells. Since the laminate stack can be approximated as periodic in the x_1 and x_2 direction, those R terms in the x_1 and x_2 direction are vanishing, i.e.:

$$R_{i-\frac{1}{2},j,k} = R_{i+\frac{1}{2},j,k} = 0, \; R_{i,j-\frac{1}{2},k} = R_{i,j+\frac{1}{2},k} = 0 \tag{5.12}$$

It is also assumed that heat is absorbed from the upper and lower free sides of the laminate by natural convection. Therefore, a parallel thermal resistance configuration applies at the interface between the layers. If the thermal resistances R_g, R_E, R_s, and R_b represent, respectively, those of the glass, EVA, Silicon and backsheet resistances, then the thermal resistances at the interfaces can be computed as follows:

$$R_{int1} = \frac{1}{R_g} + \frac{1}{R_E}, \tag{5.13a}$$

$$R_{int2} = R_{int3} = \frac{1}{R_s} + \frac{1}{R_E}, \tag{5.13b}$$

$$R_{int4} = \frac{1}{R_b} + \frac{1}{R_E} \tag{5.13c}$$

The total heat flow converging to a cell (i, j, k) from the 6 adjacent cells is given by (see Fig. 5.4):

$$\bar{Q}_{i,j,k} = K_{i-\frac{1}{2},j,k}\left(T_{i-1,j,k} - T_{i,j,k}\right) + K_{i+\frac{1}{2},j,k}\left(T_{i+1,j,k} - T_{i,j,k}\right) + K_{i,j-\frac{1}{2},k}\left(T_{i,j-1,k} - T_{i,j,k}\right) + K_{i,j+\frac{1}{2},k}\left(T_{i,j+1,k} - T_{i,j,k}\right) + K_{i,j,k-\frac{1}{2}}\left(T_{i,j,k-1} - T_{i,j,k}\right) + K_{i,j,k+\frac{1}{2}}\left(T_{i,j,k+1} - T_{i,j,k}\right) \tag{5.14}$$

By considering that the materials of the layers composing the module are continuous along the x_1 and x_2 directions, $K_{i-\frac{1}{2},j,k} = K_{i+\frac{1}{2},j,k} = K_i$ and $K_{i-\frac{1}{2},j,k} = K_{i+\frac{1}{2},j,k} = K_j$, thus simplifying Eq. (5.14) as:

$$\bar{Q}_{i,j,k} = K_{i-\frac{1}{2},j,k}T_{i-1,j,k} + K_{i+\frac{1}{2},j,k}T_{i+1,j,k} + K_{i,j-\frac{1}{2},k}T_{i,j-1,k} + K_{i,j+\frac{1}{2},k}T_{i,j+1,k} + K_{i,j,k-\frac{1}{2}}T_{i,j,k-1} + K_{i,j,k+\frac{1}{2}}T_{i,j,k+1} - T_{i,j,k}\left(2K_i + 2K_j + K_{i,j,k-\frac{1}{2}} + K_{i,j,k+\frac{1}{2}}\right) \tag{5.15}$$

Substituting Eq. (5.15) into the overall heat equation (5.10), we have, for a single cell (see Fig. 5.4):

$$C_{i,j,k} V_{i,j,k} \frac{\Delta T_{i,j,k}}{\Delta t} = \bar{Q}_{i,j,k} \tag{5.16}$$

During module lamination, the stack is kept hot at 150 ºC for about 15 minutes during which the EVA partially melts and provides the sealing. Afterwards, it is cooled down to the ambient temperature in the cooling press and the EVA becomes solid. Considering that the press is large and made of a highly conductive material, this system can be modelled as a heat sink providing a uniform temperature. On this basis, the controlled volume to be analysed can be restricted to the laminate and the temperature at its top and at bottom sides can be set equal to the press temperature.

In a PV lamination process, homogeneous temperature enables a significant faster lamination process, as well as a more homogeneous cross-linking and sealing of the encapsulant. Hence it is assumed that the PV laminate attains a homogenous temperature of 150 ºC at every point in the module after heating. Therefore, the initial condition at time $t = 0$ is given as:

$$T(x_1, x_2, z, 0) = 150\ ℃, \quad 0 \le x_1 \le X,\ 0 \le x_2 \le Y,\ 0 \le z \le Z \tag{5.17}$$

5.3.2 Boundary conditions for thermal analysis

A constant temperature is imposed at the top $(z = 0)$ and bottom $(z = Z)$ sides of the laminate:

$$T(x_1, x_2, 0, t) = T(x_1, x_2, Z, t) = T_p \tag{5.18}$$

where T_p is the temperature of the press. Heat is absorbed only from the lateral sides of the laminate. Therefore, Robin (mixed) boundary conditions are imposed at the laminate sides to absorb heat away from the laminate, i.e., for t > 0:

$$\lambda \frac{\partial T(X,x_2,z,t)}{\partial x_1} + hT(X,x_2,z,t) = hT_p \quad (5.19a)$$

$$\lambda \frac{\partial T(0,x_2,z,t)}{\partial x_1} + hT(0,x_2,z,t) = -hT_p \quad (5.19b)$$

$$\lambda \frac{\partial T(x_1,Y,z,t)}{\partial x_2} + hT(x_1,Y,z,t) = hT_p \quad (5.19c)$$

$$\lambda \frac{\partial T(x_1,0,z,t)}{\partial x_2} + hT(x_1,0,z,t) = -hT_p \quad (5.19d)$$

h is the convection coefficient of the air in the cooling press.

To solve the thermal problem, a backward Euler implicit time integration scheme is employed. As described in details in chapter 4, a differential equation of the form:

$$\frac{\mathrm{d}y}{\mathrm{d}t} = f(t,y) \quad (5.20)$$

is integrated as

$$y(t_{k+1}) - y(t_k) \approx hf\big(t_{k+1}, y(t_{k+1})\big) \quad (5.21)$$

where $y(t_{k+1})$ and $y(t_k)$ denote the approximate solutions of the differential equation at $t = t_{k+1}$ and $t = t_k$, respectively. A total cooling period of 30 minutes is specified. The topmost (glass) and bottom (backsheet) layers maintain at a constant temperature of $25\,℃\,(298\,\mathrm{K})$ imposed by the air. Fig. 5.5 shows the temperature contour after 30 minutes of cooling in the $x_2 - z$ plane of the module.

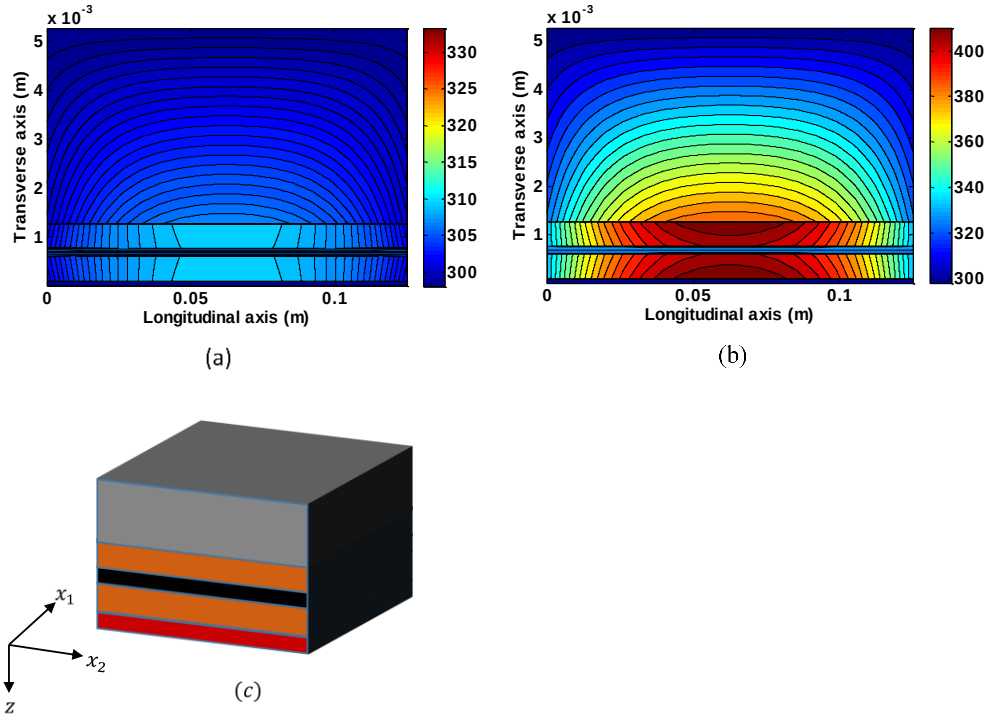

Figure 5.5: temperature contour (K) in the plane $x_2 - z$ of the PV laminate along the x_1 direction. (a) $x_1 = 0$ (at the boundary of the laminate); (b) $x_1 = 31.3$ mm (in the middle of the portion of the laminate); (c) Sketch of the laminate.

The solution of the heat equation shows that the temperature profile of the module is symmetric along the longitudinal axis, due to the same boundary conditions specified at the edges of the laminate. In the thickness direction, the degree of symmetry in the temperature variation is very high at the laminate boundary due to the same boundary constraints imposed at the top and bottom of the PV stack.

5.3.3 Shear-lag formulation for the encapsulant treated as a shear deformable zero thickness layer

As noted in the beginning of this chapter, relative displacements are admitted from one layer to the next with the EVA layer modelled as an adhesive with zero thickness (see Fig. 5.2). There are 3 real layers i.e., glass, Silicon, backsheet, and 2 shear-lag interfaces, a geometrical configuration which confers a computational advantage since the number of layers to be modelled are reduced with respect to a 5 layer module in reality. Each of the layer is modelled as a plate based on relaxed Kirchhoff's hypothesis [11, 97] in which the displacements in the 1 and 2 directions for a thin plate having axes x_1, x_2 and z are expressed as:

$$u_1 = -\frac{\partial w}{\partial x_1} z + U_1(x_1, x_2), \tag{5.22a}$$

$$u_2 = -\frac{\partial w}{\partial x_2} z + U_2(x_1, x_2) \tag{5.22b}$$

Where U_1 and U_2 represent the displacements in the middle plane and w is the deflection of the plate. Strains ε_1 and ε_2 are given by:

$$\varepsilon_1 = -z\frac{\partial^2 w}{\partial {x_1}^2} + \frac{\partial U_1}{\partial x_1} = \frac{1}{E}(\sigma_1 - \upsilon\sigma_2) + \alpha\Delta T \tag{5.23a}$$

$$\varepsilon_2 = -z\frac{\partial^2 w}{\partial {x_2}^2} + \frac{\partial U_2}{\partial x_2} = \frac{1}{E}(\sigma_2 - \upsilon\sigma_1) + \alpha\Delta T \tag{5.23b}$$

The product $\alpha\Delta T$ is the thermal strain in the layer due to cooling of the PV from 150 ℃ to the room temperature. Solving for stresses, we get:

$$\sigma_1 = \frac{E}{1-\upsilon^2}(\varepsilon_1 + \upsilon\varepsilon_2 - \alpha\Delta T(1+\upsilon)) = \frac{E}{1-\upsilon^2}\Big[-z\frac{\partial^2 w}{\partial {x_1}^2} + \frac{\partial U_1}{\partial x_1} - \upsilon z\frac{\partial^2 w}{\partial {x_2}^2} + \upsilon\frac{\partial U_2}{\partial x_2} - \alpha\Delta T(1+\upsilon)\Big] \tag{5.24a}$$

$$\sigma_2 = \frac{E}{1-\upsilon^2}[\varepsilon_2 + \upsilon\varepsilon_1 - \alpha\Delta T(1+\upsilon)] = \frac{E}{1-\upsilon^2}\left[-z\frac{\partial^2 w}{\partial {x_2}^2} + \frac{\partial U_2}{\partial x_2} - z\upsilon\frac{\partial^2 w}{\partial {x_1}^2} + \upsilon\frac{\partial U_1}{\partial x_1} - \alpha\Delta T(1+\upsilon)\right] \quad (5.24b)$$

If the strip has dimensions in x_2 much larger than in x_1, all the derivatives w.r.t. x_1 can be approximately neglected. Hence, σ_1 and σ_2 are respectively reduced to:

$$\sigma_1 = \frac{E\upsilon}{1-\upsilon^2}\left[-z\frac{\mathrm{d}^2 w}{\mathrm{d}{x_2}^2} + \frac{\mathrm{d}U_2}{\mathrm{d}x_2} - \alpha\Delta T\bar{\upsilon}\right] \quad (5.25a)$$

$$\sigma_2 = \frac{E}{1-\upsilon^2}\left[-z\frac{\mathrm{d}^2 w}{\mathrm{d}{x_2}^2} + \frac{\mathrm{d}U_2}{\mathrm{d}x_2} - \alpha\Delta T(1+\upsilon)\right] \quad (5.25b)$$

where $\bar{\upsilon} = \frac{(1+\upsilon)}{\upsilon}$.

The transverse strain ε_{zz} is given by:

$$\varepsilon_{zz} = \frac{\mathrm{d}w}{\mathrm{d}z} - \alpha\Delta T = 0 \quad (5.26)$$

Integrating Eq. (5.26) over the thickness z leads to:

$$w = W(x_2) + \alpha\Delta T z \quad (5.27)$$

where W is the mid-plate deflection.

By considering a differential element $\mathrm{d}x_1\mathrm{d}x_2\mathrm{d}z$ (as in Fig. 3.8), we can write equations for this differential element in equilibrium as:

$$\sum F_{x_1} = 0\ ,\ \sum F_{x_2} = 0\ ,\ \sum F_z = 0\ . \quad (5.28)$$

By neglecting body forces, the reduced equilibrium equations yield:

$$\frac{\mathrm{d}\sigma_2}{\mathrm{d}x_2} + \frac{\mathrm{d}\sigma_{z2}}{dz} = 0 \quad (5.29a)$$

$$\frac{\mathrm{d}\sigma_{2z}}{\mathrm{d}x_2} + \frac{\mathrm{d}\sigma_{zz}}{\mathrm{d}z} = 0 \quad (5.29b)$$

In case of the beam type plate, the boundary conditions required to solve the equilibrium equations are [11, 98]:

$$\sigma_{2z} = \sigma_{2z}(x_2, c)\ , \qquad \sigma_{zz} = \sigma_{zz}(x_2, c)\ , \qquad \text{at } z = \frac{h}{2} = c\ . \tag{5.30a}$$

$$\sigma_{2z} = \sigma_{2z}(x_2, -c)\ , \qquad \sigma_{zz} = \sigma_{zz}(x_2, -c)\ , \qquad \text{at } z = -\frac{h}{2} = -c\ . \tag{5.30b}$$

By integrating the reduced equilibrium equations w.r.t. z and applying the boundary conditions at $z = c$ and $z = -c$, we obtain:

$$\sigma_{2z} = \frac{E}{2(1-\upsilon^2)}\left[\frac{\mathrm{d}^3 w}{\mathrm{d}{x_2}^3}(z^2 - c^2) - 2\frac{\mathrm{d}^2 U_2}{\mathrm{d}{x_2}^2}(z - c)\right] + \sigma_{2z}(x_2, c) \tag{5.31a}$$

$$\sigma_{2z} = \frac{E}{2(1-\upsilon^2)}\left[\frac{\mathrm{d}^3 w}{\mathrm{d}{x_2}^3}(z^2 - c^2) - 2\frac{\mathrm{d}^2 U_2}{\mathrm{d}{x_2}^2}(z + c)\right] + \sigma_{2z}(x_2, -c) \tag{5.31b}$$

Adding Eq. (5.31a) and (5.31b) and simplifying, we get:

$$\sigma_{2z} = \frac{E}{2(1-\upsilon^2)}\frac{\mathrm{d}^3 w}{\mathrm{d}{x_2}^3}(z^2 - c^2) - \frac{E}{(1-\upsilon^2)}\frac{\mathrm{d}^2 U_2}{\mathrm{d}{x_2}^2}z + \frac{m}{2} \tag{5.32}$$

where $m = \sigma_{2z,c} + \sigma_{2z,-c}, \qquad \sigma_{2z,c} = \sigma_{2z}(x_2, c), \qquad \sigma_{2z,-c} = \sigma_{2z}(x_2, -c).$

Similarly, by substituting Eq. (5.32) into (5.29b) and integrating with the boundary conditions in Eq. (5.30):

$$\sigma_{zz} = \frac{E}{6(1-\upsilon^2)}\frac{\mathrm{d}^4 w}{\mathrm{d}{x_2}^4}(-z^3 + 3c^2 z - 2c^3) + \frac{E}{2(1-\upsilon^2)}\frac{\mathrm{d}^3 U_2}{\mathrm{d}{x_2}^3}(z^2 - c^2) - \frac{1}{2}\frac{\mathrm{d}m}{\mathrm{d}x_2}(z - c) + \sigma_{zz,c} \tag{5.33a}$$

$$\sigma_{zz} = \frac{E}{6(1-\upsilon^2)}\frac{\mathrm{d}^4 w}{\mathrm{d}{x_2}^4}(-z^3 + 3c^2 z + 2c^3) + \frac{E}{2(1-\upsilon^2)}\frac{\mathrm{d}^3 U_2}{\mathrm{d}{x_2}^3}(z^2 - c^2) - \frac{1}{2}\frac{\mathrm{d}m}{\mathrm{d}x_2}(z + c) + \sigma_{zz,-c} \tag{5.33b}$$

Adding Eq. (5.33a) and (5.33b) and simplifying, we get:

$$\sigma_{zz} = \frac{E}{6(1-\upsilon^2)}\frac{\mathrm{d}^4 w}{\mathrm{d}{x_2}^4}(-z^3 + 3c^2 z) + \frac{E}{2(1-\upsilon^2)}\frac{\mathrm{d}^3 U_2}{\mathrm{d}{x_2}^3}(z^2 - c^2) - \frac{1}{2}\frac{\mathrm{d}m}{\mathrm{d}x_2}z + \frac{p}{2} \tag{5.34}$$

where $p = \sigma_{zz,c} + \sigma_{zz,-c}$, $\sigma_{zz,c} = \sigma_{zz}(x_2, c)$, $\sigma_{zz,-c} = \sigma_{zz}(x_2, -c)$.

For a generic plate, the axial force, the shear force and the resultant bending moment (N, Q, M) are defined as:

$$N_i = \int_{-c}^{c} \sigma_i \, \mathrm{d}z \tag{5.35a}$$

$$M_i = \int_{-c}^{c} \sigma_i \, z \mathrm{d}z \tag{5.35b}$$

$$Q_i = \int_{-c}^{c} \sigma_{iz} \, \mathrm{d}z \qquad (\text{for } i = 1,2) \tag{5.35c}$$

Substituting for σ_i and σ_{iz} (for $i = 1, 2$) in the resultant equations, we have for a generic ply, the resultant force as:

$$\frac{N_1}{h} = \frac{Ev}{1-v^2}\left[\frac{\mathrm{d}U_2}{\mathrm{d}x_2} - \alpha \Delta T \bar{v}\right] \tag{5.36a}$$

$$\frac{N_2}{h} = \frac{E}{1-v^2}\left[\frac{\mathrm{d}U_2}{\mathrm{d}x_2} - \alpha \Delta T (1+v)\right] \tag{5.36b}$$

The moment resultant is given as:

$$M_1 = -\frac{Evh^3}{12(1-v^2)}\frac{\mathrm{d}^2 w}{\mathrm{d}{x_2}^2} = -\frac{EIv}{(1-v^2)}\frac{\mathrm{d}^2 w}{\mathrm{d}{x_2}^2}, \tag{5.37a}$$

$$M_2 = -\frac{Eh^3}{12(1-v^2)}\frac{\mathrm{d}^2 w}{\mathrm{d}{x_2}^2} = -\frac{EI}{(1-v^2)}\frac{\mathrm{d}^2 w}{\mathrm{d}{x_2}^2} \tag{5.37b}$$

Differentiating Eq. (5.27) twice and substituting into Eq. (5.37) we get:

$$M_1 = -\frac{Evh^3}{12(1-v^2)}\frac{\mathrm{d}^2 W}{\mathrm{d}{x_2}^2} = -\frac{EIv}{(1-v^2)}\frac{\mathrm{d}^2 W}{\mathrm{d}{x_2}^2}, \tag{5.38a}$$

$$M_2 = -\frac{Eh^3}{12(1-v^2)}\frac{\mathrm{d}^2 W}{\mathrm{d}{x_2}^2} = -\frac{EI}{(1-v^2)}\frac{\mathrm{d}^2 W}{\mathrm{d}{x_2}^2} \tag{5.38b}$$

Using Eq. (5.36) and (5.37), Eq. (5.24) for the normal stresses can be simplified as:

$$\sigma_i = \frac{N_i}{h} + \frac{M_i}{I} z \qquad (\text{for } i = 1, 2) \tag{5.39}$$

Evaluating Eq. (5.35c) for Q_2 gives:

$$Q_2 = -\frac{EI}{(1-\upsilon^2)}\frac{\mathrm{d}^3 W}{\mathrm{d}{x_2}^3} + mc, \tag{5.40a}$$

$$\frac{\mathrm{d}M_2}{\mathrm{d}x_2} + mc - Q_2 = 0 \tag{5.40b}$$

By subtracting Eq. (5.31b) from (5.31a) for the top and bottom of the plate and simplifying, we obtain:

$$\frac{Eh}{(1-\upsilon^2)}\frac{\mathrm{d}^2 U_2}{\mathrm{d}{x_2}^2} + \sigma_{2z}(x_2, c) - \sigma_{2z}(x_2, -c) = 0 \tag{5.41}$$

Taking $n = \sigma_{2z,c} - \sigma_{2z,-c}$ while noting that $\frac{Eh}{(1-\upsilon^2)}\frac{\mathrm{d}^2 U_2}{\mathrm{d}{x_2}^2} = \frac{dN_2}{dx_2}$ leads to:

$$\frac{\mathrm{d}N_2}{\mathrm{d}x_2} + n = 0 \tag{5.42}$$

By similarly subtracting Eq. (5.33b) from (5.33a) for the top and bottom of the plate and simplifying, we get:

$$-\frac{4Ec^3}{6(1-\upsilon^2)}\frac{\mathrm{d}^4 w}{\mathrm{d}{x_2}^4} + \frac{\mathrm{d}m}{\mathrm{d}x_2}c + \sigma_{zz,c} - \sigma_{zz,-c} = 0 \tag{5.43}$$

Taking $q = \sigma_{zz,c} - \sigma_{zz,-c}$ while noting that $-\frac{4Ec^3}{6(1-\upsilon^2)}\frac{\mathrm{d}^4 w}{\mathrm{d}{x_2}^4} + \frac{\mathrm{d}m}{\mathrm{d}x_2}c = \frac{\mathrm{d}Q_2}{\mathrm{d}x_2}$ leads to:

$$\frac{\mathrm{d}Q_2}{\mathrm{d}x_2} + q = 0 \tag{5.44}$$

The overall equilibrium equations for the beam type plate are now expressed as:

$$\frac{\mathrm{d}M_2}{\mathrm{d}x_2} + mc - Q_2 = 0, \tag{5.45a}$$

$$\frac{\mathrm{d}N_2}{\mathrm{d}x_2} + n = 0, \tag{5.45b}$$

$$\frac{\mathrm{d}Q_2}{\mathrm{d}x_2} + q = 0 \tag{5.45c}$$

Eq. (5.45a) and (5.45c) can be further combined to give:

$$\frac{\mathrm{d}^2 M_2}{\mathrm{d}{x_2}^2} + \frac{\mathrm{d}m}{\mathrm{d}x_2} c + q = 0 \tag{5.46}$$

In the sequel, σ_{zz} and σ_{2z} will henceforth be denoted respectively by σ and τ.

The rotation variable Ψ in the x_2 direction can be obtained from Eq. (5.22b)

$$\Psi = \frac{\mathrm{d}u_2}{\mathrm{d}z} = -\frac{\mathrm{d}w}{\mathrm{d}x_2} \tag{5.47}$$

By combining Eq. (5.27) and (5.47), we get:

$$\Psi = -\frac{\mathrm{d}W}{\mathrm{d}x_2} \tag{5.48}$$

5.4 Numerical Examples

For a 3 layer module as in Fig. 5.2 represented by a beam type plate, there are six equilibrium equations in total which are stated as:

$$\frac{\mathrm{d}^2 {M_2}^{(k)}}{\mathrm{d}{x_2}^2} + \frac{\mathrm{d}m^{(k)}}{\mathrm{d}x_2} c^{(k)} + q^{(k)} = 0, \tag{5.49a}$$

$$\frac{\mathrm{d}{N_2}^{(k)}}{\mathrm{d}x_2} + n^{(k)} = 0 \qquad \text{for } k = 1,2,3 \tag{5.49b}$$

where k is the number of layers.

The behaviour of the EVA interfaces modelled as deformable linear elastic springs is mathematically given as:

$${u_2}^{(i)} - {u_2}^{(i+1)} = \frac{\tau^{(i)}}{\mathrm{K_x}^{(i)}} \tag{5.50a}$$

$$w^{(i+1)} - w^{(i)} = \frac{\sigma^{(i)}}{\mathrm{K_y}^{(i)}} \qquad \text{for } i = 1, 2 \tag{5.50b}$$

where $\mathrm{K_x}^{(i)}$ and $\mathrm{K_y}^{(i)}$ are the longitudinal and transverse compliances at the interface i. In this work, we assume the same value for $\mathrm{K_x}^{(i)}$ and $\mathrm{K_y}^{(i)}$ which are given by:

$$\mathrm{K_x}^{(i)} = \mathrm{K_y}^{(i)} = \frac{E_E}{h_E}\omega \tag{5.51}$$

where E_E and h_E are the relaxation modulus and thickness of the EVA adhesive layer, and ω is the out of plane thickness.

Altogether there are 10 governing equations consisting of 6 equilibrium and 4 continuity equations. By substituting for the constitutive terms in these equations and further simplification, we have a system of 6 higher order ordinary differential equations which has to be solved to obtain the variables $U^{(k)}$, $W^{(k)}$ and their derivatives (for $k = 1,2,3$) while $\tau^{(i)}$ and $\sigma^{(i)}$ (for $i = 1, 2$) are calculated from the continuity equations, i.e., Eq. (5.50).

The solution of the problem can be achieved by converting the system of higher order ordinary differential equations to a system of first order ordinary differential equations which can then be solved to determine the stress distribution in the beam plate. For this case, we can write:

$$\frac{d\boldsymbol{v}(x_2)}{dx_2} = \boldsymbol{B}\boldsymbol{v}(x_2) + \boldsymbol{F} \tag{5.52}$$

$$\boldsymbol{v} = f(U_k, U_k', W_k, W_k', W_k'', W_k'''), \qquad \text{for } k = 1, 2, 3$$

$$\boldsymbol{F} = f\left(\mathrm{K_x}^{(i)}, \mathrm{K_y}^{(i)}, \Delta T,\ \alpha_k\right) = \text{constant}, \qquad \text{for } i = 1, 2$$

where $\boldsymbol{B}$ is an 18×18 sparse coefficient matrix which contains constant coefficients of the variables and their derivatives and $\boldsymbol{F}$ is 18×1 vector (see appendix **A**). The set of boundary conditions for this system of ODEs are (for $i = 1, 2$ and $k = 1, 2, 3$):

$$U_k = 0 \ , \ {Q_2}^{(k)} = 0, \ \tau^{(i)} = 0, \sigma^{(i)} = 0, \text{at } x_2 = 0 \tag{5.53a}$$

$${M_2}^{(k)} = 0, {N_2}^{(k)} = 0, \ \text{at} \ x_2 = L, \tag{5.53b}$$

5.4.1 Modelling viscoelasticity of the encapsulant and transient thermo-elastic analysis

To account for the visco-elastic behaviour of the EVA, the rheological model described in Chapter 3 based on fractional calculus is herein considered in which the constitutive equation of the simplest fractional element (also known as Scott-Blair element) is recalled as:

$$\sigma(t) = a \frac{\mathrm{d}^{\alpha} \varepsilon(t)}{\mathrm{d}t^{\alpha}} \qquad \alpha \in (0,1) \tag{5.54}$$

and the relaxation modulus assumes the power law form:

$$E(t) = a \frac{t^{-\alpha}}{\Gamma(1-\alpha)} \tag{5.55}$$

a has the SI unit of MPa s^{α} and its mechanical meaning varies with α from a stiffness ($\alpha = 0$) to a viscosity ($\alpha = 1$). Time t is measured in seconds.

As pointed out in Chapter 3, only two parameters (a and α) are required to model the viscoelastic behaviour of the EVA accurately and due to modification in the material microstructure of EVA at $\Delta T \sim 84$ ℃, two different correlations are used each for a and α to accurately fit the experimental data. Therefore, a total of four different correlations are required to predict the viscoelastic response of the EVA. By using the mathematical correlations (3.38) for the model fitting of a and α (see Fig. 3.6), the temperature-dependent values of a and α for EVA during lamination can be determined. Consequently, the temperature distribution history of the module computed during cooling after lamination can be used to evaluate the

temperature- and time-dependent properties of the EVA adhesive layer. After cooling of the PV laminate, the temperature of the layers varies along the longitudinal coordinate for each layer and along the transverse coordinate for the whole module. Thus, the interfacial compliance to be inserted in the shear lag constitutive equations now varies with temperature and time as well along the longitudinal axis of the module, which is a novelty with respect to standard shear lag theories that assume constant compliances. Hence, this leads to a non-homogeneous system of ordinary differential equations with time-dependent coefficients:

$$\frac{\mathrm{d}\boldsymbol{v}(x_2,t)}{\mathrm{d}x_2} = \boldsymbol{B}(x_2,t)\boldsymbol{v}(x_2,t) + \boldsymbol{F}(x_2,t) \tag{5.57}$$

where $\boldsymbol{F} = f\left(\mathrm{K_x}(x_2,t), \mathrm{K_y}(x_2,t), \Delta T(x_2,t), \alpha\right)$.

For non-uniform temperature simulations, a model with only the longitudinal compliance is considered. The compressive stresses in Silicon are computed at some relevant time intervals.

5.4.2 Numerical solution

An exact solution (as in Sec. 4.1) of the system of ordinary differential equations (5.57) can be achieved for the special case of a uniform temperature profile for the entire PV module after cooling. In the case of a non-uniform temperature analysis, the coefficients in the $\boldsymbol{B}$ matrix vary with time and space, so a numerical method is required. Specifically, for the non-uniform temperature case study, an integration scheme using a trapezium rule method (an average of forward and backward Euler method) is used as described in Sec. 4.5.2. To verify the accuracy of this numerical scheme for this analysis, a comparison was made between the exact solution of the uniform temperature analysis and the numerical solution using trapezium rule

method and a good agreement was achieved. The results of this comparison are shown in Sec. 5.7.

5.5 3D coupled thermo-visco-elastic shear-lag formulation

So far in the previous sections, a 2D formulation for thermo-visco-elastic stress analysis of a single Silicon solar cell has been developed leading to a quasi-static thermo-mechanical investigation of residual stresses in PV laminate. Typically, a PV module contains several Silicon cells which may experience stress fields varying from one position to the other due to interaction between mechanical, electrical and thermal fields in the laminate. On this basis therefore, prediction of stress field variations in the cells across the PV module deems important. And as mentioned earlier in Chapter 1, transient regimes which take place in accelerated environmental tests within climate chambers, or under operating conditions, have only marginally been investigated due to the inherent complexity related to the different thicknesses of the layers composing a PV module. In the sequel, a novel 3D coupled shear-lag formulation is developed to estimate residual stresses induced in Silicon cells during cooling after lamination. The prediction of stress distribution is enhanced by accounting for the viscoelastic response of the EVA encapsulant using an asymptotic model presented in [39]. A full dynamic analysis is proposed in this work to obtain an accurate estimate of the induced residual stresses during the lamination of the PV module.

5.5.1 3D shear-lag formulation for mechanical system

The model problem consists of 4 Silicon cells separated by a thin strip of EVA embedded in a stack composed of glass and Backsheet. The sectional view is as

shown in Fig. 5.6. The EVA layer is considered as an adhesive with zero thickness. The governing equations of linear elasticity for a solid in the absence of body forces consist of:

- Equilibrium equations:

$$\frac{\partial \sigma_1}{\partial x_1} + \frac{\partial \sigma_{12}}{\partial x_2} + \frac{\partial \sigma_{z1}}{\partial z} = \rho \frac{\partial^2 u_1}{\partial t^2} \tag{5.58a}$$

$$\frac{\partial \sigma_{12}}{\partial x_1} + \frac{\partial \sigma_2}{\partial x_2} + \frac{\partial \sigma_{z2}}{\partial z} = \rho \frac{\partial^2 u_2}{\partial t^2} \tag{5.58b}$$

$$\frac{\partial \sigma_{1z}}{\partial x_1} + \frac{\partial \sigma_{2z}}{\partial x_2} + \frac{\partial \sigma_{zz}}{\partial z} = \rho \frac{\partial^2 w}{\partial t^2} \tag{5.58c}$$

where σ_i (for $i = 1, 2 \; and \; z$), $\sigma_{iz} = \sigma_{zi}$ (for $i = 1, 2$), and $\sigma_{12} = \sigma_{21}$ are the axial stresses and shear stresses according to Fig. 3.8. σ_{zz} is the surface normal stress.

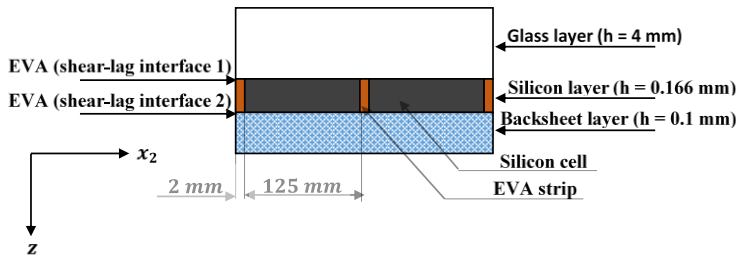

Figure 5.6. A sectional view of the PV module for stress analysis.

u_1, u_2 and w are, respectively, displacements in 1, 2 and z directions.

- Displacement relations, which according to relaxed Kirchhoff's hypothesis for a thin plate having axes x_1, x_2 and z, are given for the 1 and 2 directions respectively as:

$$u_1 = -\frac{\partial w}{\partial x_1} z + U_1 \tag{5.59a}$$

$$u_2 = -\frac{\partial w}{\partial x_2} z + U_2 \tag{5.59b}$$

where U_1 and U_2 are the longitudinal mid-plane displacements in the 1 and 2 directions.

- Plane stress constitutive equations of linear thermoelasticity [97]:

$$\sigma_1 = \frac{E}{1-\upsilon^2}\left[-z\frac{\partial^2 w}{\partial {x_1}^2} + \frac{\partial U_1}{\partial x_1} - \upsilon z\frac{\partial^2 w}{\partial {x_2}^2} + \upsilon\frac{\partial U_2}{\partial x_2} - \alpha\theta(1+\upsilon)\right] \tag{5.60a}$$

$$\sigma_2 = \frac{E}{1-\upsilon^2}\left[-z\frac{\partial^2 w}{\partial {x_2}^2} + \frac{\partial U_2}{\partial x_2} - \upsilon z\frac{\partial^2 w}{\partial {x_1}^2} + \upsilon\frac{\partial U_1}{\partial x_1} - \alpha\theta(1+\upsilon)\right] \tag{5.60b}$$

$$\sigma_{12} = \frac{E}{2(1+\upsilon)}\left[-2z\frac{\partial^2 w}{\partial x_1 \partial x_2} + U_{1,2} + U_{2,1}\right] \tag{5.60b}$$

where $\theta(x_1, x_2, z, t)$ is the excess temperature distribution of the plate.

By integrating the Eq. (5.58c) over the plate thickness with surface loads $\sigma_{zz,c}$ and $\sigma_{zz,-c}$ imposed at the upper and lower parts of the plate, we have:

$$a_{1,1} + a_{2,2} + [\sigma_{zz}]_{-c}^{c} = \rho\frac{\partial^2 \overline{w}}{\partial t^2} \tag{5.61}$$

where $a_i = \int_{-c}^{c} \sigma_{iz}\,\mathrm{d}z$, $\overline{w} = \int_{-c}^{c} w\,\mathrm{d}z$, for $i = 1, 2$

c is half of the plate's thickness.

Integrating Eq. (5.58a) and (5.58b) over the plate thickness with surface loads $\sigma_{zi,c}$ and $\sigma_{zi,-c}$, imposed at the upper and lower parts of the plate, we get:

$$g_{1,1} + e_{,2} + n_1 = \rho\frac{\partial^2 \hat{u}_1}{\partial t^2} \tag{5.62a}$$

$$e_{,1} + g_{2,2} + n_2 = \rho\frac{\partial^2 \hat{u}_2}{\partial t^2} \tag{5.62b}$$

where $g_i = \int_{-c}^{c} \sigma_i \, dz$, $\hat{u}_i = \int_{-c}^{c} u_i \, dz$ and $e = \int_{-c}^{c} \sigma_{12} \, dz$ $n_i = \sigma_{zi,c} - \sigma_{zi,-c}$ for $i = 1, 2$

Multiplying Eqs. (5.58a) and (5.58b) by z and Integrating over the plate thickness, we obtain:

$$b_{1,1} + d_{,2} - f_1 + cm_1 = \rho \frac{\partial^2 \bar{u}_1}{\partial t^2} \tag{5.63a}$$

$$d_{,1} + b_{2,2} - f_2 + cm_2 = \rho \frac{\partial^2 \bar{u}_2}{\partial t^2} \tag{5.63b}$$

where

$b_i = \int_{-c}^{c} \sigma_i \, z dz$, $f_i = \int_{-c}^{c} \sigma_{zi} \, dz$,

$\bar{u}_i = \int_{-c}^{c} u_i z \, dz$, $d = \int_{-c}^{c} \sigma_{12} \, z dz$

$m_i = \sigma_{zi,c} + \sigma_{zi,-c}$ for $i = 1, 2$

Note: $f_i = a_i$

By substituting the constitutive Eq. (5.60) into Eq. (5.62) and evaluating we get:

$$\left[U_{1,11} + \upsilon U_{2,21}\right] + \frac{(1-\upsilon)}{2}\left[U_{1,22} + U_{2,12}\right] - B\rho h \frac{\partial^2 U_1}{\partial t^2} + Bn_1 = 0 \tag{5.64a}$$

$$\left[U_{2,22} + \upsilon U_{1,12}\right] + \frac{(1-\upsilon)}{2}\left[U_{1,21} + U_{2,11}\right] - B\rho h \frac{\partial^2 U_2}{\partial t^2} + Bn_2 = 0 \tag{5.64b}$$

where $B = \frac{1-\upsilon^2}{Eh}$ and $h = 2c$

Simplifying Eq. (5.64) by ignoring mixed differential terms since it is considered small with respect to $U_{1,11}$, $U_{1,22}$, $U_{2,11}$ and $U_{2,22}$, we obtain:

$$U_{1,11} + \frac{(1-\upsilon)}{2} U_{1,22} - B\rho h \frac{\partial^2 U_1}{\partial t^2} + Bn_1 = 0 \tag{5.65a}$$

$$U_{2,22} + \frac{(1-v)}{2} U_{2,11} - B\rho h \frac{\partial^2 U_2}{\partial t^2} + Bn_2 = 0 \tag{5.65b}$$

Differentiating Eq. (5.63a) w.r.t. x_1 and (5.63b) w.r.t. x_2, we get:

$$b_{1,11} + d_{,21} - f_{1,1} + cm_{1,1} = -\rho I \frac{\partial^2 w_{,11}}{\partial t^2} \tag{5.66a}$$

$$d_{,12} + b_{2,22} - f_{2,2} + cm_{2,2} = -\rho I \frac{\partial^2 w_{,22}}{\partial t^2} \tag{5.66b}$$

Adding Eq. (5.66a) and (5.66b) together, we get:

$$b_{1,11} + d_{,21} + d_{,12} + b_{2,22} - (f_{1,1} + f_{2,2}) + c\left(m_{1,1} + m_{2,2}\right) = -\rho I\left(\frac{\partial^2 w_{,11}}{\partial t^2} + \frac{\partial^2 w_{,22}}{\partial t^2}\right) \tag{5.67}$$

Since $f_i = a_i$ from Eq. (5.61), we can write:

$$f_{1,1} + f_{2,2} = \rho h \frac{\partial^2 w}{\partial t^2} - [\sigma_{zz}]_{-c}^{c} \tag{5.68}$$

Therefore, Eq. (5.67) can be rewritten as:

$$b_{1,11} + d_{,21} + d_{,12} + b_{2,22} + c\left(m_{1,1} + m_{2,2}\right) + [\sigma_{zz}]_{-c}^{c} = \rho h \frac{\partial^2 w}{\partial t^2} - \rho I\left(\frac{\partial^2 w_{,11}}{\partial t^2} + \frac{\partial^2 w_{,22}}{\partial t^2}\right) \tag{5.69}$$

Since $I = \frac{2c^3}{3}$ is small as compared to $h = 2c$, we can neglect the $\frac{\partial^2 w_{,ii}}{\partial t^2}\,(i = 1, 2)$ so that Eq. (5.69) reduces to:

$$b_{1,11} + d_{,21} + d_{,12} + b_{2,22} + c\left(m_{1,1} + m_{2,2}\right) - \rho h \frac{\partial^2 w}{\partial t^2} = -[\sigma_{zz}]_{-c}^{c} \tag{5.70}$$

Evaluating b_1, b_2 and d using Eq. (5.63a) and Eq. (5.63b), we obtain:

$$b_1 = \frac{EI}{1-v^2}\left[-w_{,11} - vw_{,22} - \alpha(1+v)T\right] \tag{5.71}$$

$$b_2 = \frac{EI}{1-v^2}\left[-vw_{,11} - w_{,22} - \alpha(1+v)T\right] \tag{5.72}$$

$$d = -\frac{EI}{(1+v)}w_{,12} \tag{5.73}$$

where $\theta = T(x_1, x_2, t)z$ assuming linear temperature variation along the plate's transverse direction. Differentiating Eqs. (5.71–5.73) in accordance with the Eq. (5.70) and substituting, we get:

$$w_{,1111} + 2w_{,2211} + w_{,2222} + \alpha(1+v)\left(T_{,11} + T_{,22}\right) + D\rho h\frac{\partial^2 w}{\partial t^2} = D\left[[\sigma_{zz}]_{-c}^{c} + c\left(m_{1,1} + m_{2,2}\right)\right] \tag{5.74}$$

where $D = \frac{1-v^2}{EI}$

Eq. (5.74) can be rewritten as:

$$\nabla^4 w + \alpha(1+v)\nabla^2 T + D\rho h\frac{\partial^2 w}{\partial t^2} = D\left[p + c\left(m_{1,1} + m_{2,2}\right)\right] \tag{5.75}$$

where $\nabla^4 w = w_{,1111} + 2w_{,2211} + w_{,2222}$, $p = [\sigma_{zz}]_{-c}^{c}$.

5.5.2 Formulation for the thermal problem

The general heat conduction equation for the plate neglecting the mechanical coupling and the heat source term is given as:

$$\lambda\nabla^2\theta - \rho C\frac{\partial\theta}{\partial t} = 0 \tag{5.76}$$

where $\nabla^2\theta = \frac{\partial^2\theta}{\partial {x_1}^2} + \frac{\partial^2\theta}{\partial {x_2}^2} + \frac{\partial^2\theta}{\partial z^2}$

C is the specific heat per unit mass and λ is the thermal conductivity of the plate. Substituting for $\theta = T(x_1, x_2, t)z$ in Eq. (5.76) and separating the derivative in the thickness direction from the longitudinal directions gives:

$$\lambda\nabla^2(Tz) + \lambda_z \frac{\partial^2\theta}{\partial z^2} - \rho C \frac{\partial(Tz)}{\partial t} = 0 \tag{5.77}$$

where λ_z is the thermal conductivity in the z direction.

Multiplying Eq. (5.77) by z and integrating over the plate thickness leads to:

$$\lambda\nabla\left(\frac{\partial T}{\partial x_1} + \frac{\partial T}{\partial x_2}\right) I + \lambda_z \int_{-c}^{c} \frac{\partial^2\theta}{\partial z^2} z\mathrm{d}z - \rho C I \frac{\partial T}{\partial t} = 0 \tag{5.78}$$

Evaluating the integral term of Eq. (5.78),

$$\int_{-c}^{c} \lambda_z \frac{\partial^2\theta}{\partial z^2} z\mathrm{d}z = \lambda_z z \frac{\partial\theta}{\partial z}\Big|_{-c}^{c} - \int_{-c}^{c} \lambda_z \frac{\partial\theta}{\partial z}\mathrm{d}z \tag{5.79}$$

Let $q_1 = \lambda_z \frac{\partial\theta}{\partial z}\Big|_c$ and $q_2 = \lambda_z \frac{\partial\theta}{\partial z}\Big|_{-c}$

where q_1 and q_2 are the change in heat flow at upper and lower part for a generic layer. Therefore, the heat equation (5.78) becomes:

$$\lambda\nabla\left(\frac{\partial T}{\partial x_1} + \frac{\partial T}{\partial x_2}\right) I + c(q_1 + q_2) - \lambda_z h T - \rho C I \frac{\partial T}{\partial t} = 0 \tag{5.80}$$

where $h = 2c$

Dividing Eq. (5.80) by I gives:

$$\lambda\nabla^2 T - \frac{\lambda_z h T}{I} - \rho C \frac{\partial T}{\partial t} = -\frac{c}{I}(q_1 + q_2) \tag{5.81}$$

where $\nabla^2 T = \frac{\partial^2 T}{\partial {x_1}^2} + \frac{\partial^2 T}{\partial {x_2}^2}$

For a generic layer n, the overall governing equations to be solved for the plate are:

$$\nabla^4 w^{(n)} + \eta_1{}^{(n)}\nabla^2 T^{(n)} + \eta_2{}^{(n)}\frac{\partial^2 w^{(n)}}{\partial t^2} - \eta_3{}^{(n)}\left[p^{(n)} + c^{(n)}\left(m_{1,1}{}^{(n)} + m_{2,2}{}^{(n)}\right)\right] = 0 \quad (5.82a)$$

$$U_{1,11}{}^{(n)} + \mu_1{}^{(n)}U_{1,22}{}^{(n)} - \mu_2{}^{(n)}\frac{\partial^2 U_1{}^{(n)}}{\partial t^2} + \mu_3{}^{(n)}n_1{}^{(n)} = 0 \quad (5.82b)$$

$$U_{2,22}{}^{(n)} + \mu_1{}^{(n)}U_{2,11}{}^{(n)} - \mu_2{}^{(n)}\frac{\partial^2 U_2{}^{(n)}}{\partial t^2} + \mu_3{}^{(n)}n_2{}^{(n)} = 0 \quad (5.82c)$$

$$\lambda^{(n)}\nabla^2 T^{(n)} - \xi_1{}^{(n)}T^{(n)} - \xi_2{}^{(n)}\frac{\partial \mathrm{T}^{(n)}}{\partial t} + \xi_3{}^{(n)}\left(q_1{}^{(n)} + q_2{}^{(n)}\right) = 0 \quad (5.82d)$$

where

$\eta_1{}^{(n)} = \alpha^{(n)}(1 + v^n)$, $\eta_2{}^{(n)} = D^{(n)}\rho^{(n)}h^{(n)}$, $\eta_3{}^{(n)} = D^{(n)}$,

$\mu_1{}^{(n)} = \frac{(1-v^{(n)})}{2}$, $\mu_2{}^{(n)} = B^{(n)}\rho^{(n)}h^{(n)}$, $\mu_3{}^{(n)} = B^{(n)}$,

$\xi_1{}^{(n)} = \frac{\lambda_z{}^{(n)}h^{(n)}}{\mathrm{I}^{(n)}}$, $\xi_2{}^{(n)} = \rho^{(n)}C^{(n)}$, $\xi_3{}^{(n)} = \frac{\mathrm{c}^{(n)}}{\mathrm{I}^{(n)}}$.

5.5.3 Continuity relations

At the interface of the laminate are shear stresses σ_{1z}, σ_{2z} and peeling stresses σ_{zz} for the mechanical field while there is heat flow q for the thermal field. These interfacial loads which affect thermomechanical stress distribution of the PV laminate are governed by the relations:

$$w^{(i+1)} - w^{(i)} = \frac{\sigma_{zz}{}^{(i)}}{\mathrm{K_y}^{(i)}} \quad (5.83a)$$

$$u_1{}^{(i)} - u_1{}^{(i+1)} = \frac{\sigma_{1z}{}^{(i)}}{\mathrm{K_x}^{(i)}} \quad (5.83b)$$

$$u_2{}^{(i)} - u_2{}^{(i+1)} = \frac{\sigma_{2z}{}^{(i)}}{\mathrm{K_x}^{(i)}} \quad (5.83c)$$

$$\theta^{(i+1)} - \theta^{(i)} = \frac{q_i}{K_z{}^{(i)}} \tag{5.83d}$$

where $\mathrm{K_y}^{(i)}$, $\mathrm{K_x}^{(i)}$ and $K_z{}^{(i)}$ are, respectively, the transverse interfacial compliance, longitudinal interfacial compliance and thermal conductance in the thickness direction at the interface i. These interfacial parameters are evaluated according to:

$$\mathrm{K_x} = \mathrm{K_y} = \frac{\mathrm{E_e}}{\mathrm{h_e}} \tag{5.84a}$$

$$K_z{}^{(i)} = \frac{c_i}{\frac{h_{i+1}}{2\lambda_{i+1}} + \frac{h_i}{2\lambda_i} + R_{i,}} \tag{5.84b}$$

where $\mathrm{E_e}$ and $\mathrm{h_e}$ are the relaxation modulus and thickness of the EVA at the interface i. The term R denotes the thermal resistance at the interface between two layers.

5.6 Asymptotic viscoelastic model for the encapsulant

The isotropic linear viscoelastic model described in Sec. 3.2 is considered here for the estimation of EVA viscoelastic behaviour. It will be recalled that the equivalent shear relaxation modulus for the evaluation of EVA properties in the PV laminate is given as:

$$G_{visc} = G\left[\mu_0 + \sum_{i=1}^{N} \mu_i \, \Delta h^i(\Delta t)\right] \tag{5.85}$$

where $\Delta h^i = \frac{\lambda_i}{\Delta \mathrm{t}}\left[1 - \exp^{-\left(\frac{\Delta \mathrm{t}}{\lambda_i}\right)}\right]$

And the equivalent modulus $\mathrm{E_e}$ of the EVA is now evaluated according to:

$$\mathrm{E_e} = 2(1+v)G_{visc} \tag{5.86}$$

The relaxation parameters G_i and λ_i to evaluate G_{visc} are extracted from Table 3.1. To obtain a good approximate, seven Maxwell arms are chosen from the fourth arm to the fourteenth arm according to Table 5.2:

Table 5.2. Parameters from uniaxial relaxation test extracted from Table 3.1.

Maxwell arm	λ_i	G_i[MPa]
G_∞		$G_\infty = 0.02$
4	10^0	11
6	10^2	4
8	10^4	1.4
10	10^6	0.8
12	10^8	0.7
14	10^{10}	0.8

Using the G_i and λ_i data from Table 5.2, the instantaneous shear relaxation modulus $G(t=0)$ according to Eq. (3.16) is:

$$G(t=0) = 0.02 + 11 + 4 + 1.4 + 0.8. + 0.7 + 0.8 = 18.72$$

By dividing G_i $(i = 0, 1, \ldots\ldots, 6)$ by G, the parameters μ_i are obtained according to Eq. (3.16) and are presented in Table 5.3. The relaxation parameters in Tables 5.2 and 5.3 can be substituted into Eq. (5.85) to obtain G_{visc} and in turn $\mathrm{E_e}$ can be determined.

Table 5.3. Secondary relaxation parameters.

i	μ_i
0	0.002
1	0.59
2	0.21
3	0.075
4	0.043
5	0.037
6	0.043

5.7 Numerical implementation

An example of a laboratory test module consisting of a stack of glass, 4 Silicon solar cells (2×2 pieces separated by a thin EVA strip) and backsheet layers (see Fig. 5.6). The material properties of the layers composing the module are indicated in Table 5.1. The temperature of the topmost glass and bottom backsheet layers are fixed at the press temperature which is assumed to decrease during cooling of the laminate according to the exponential (cooling) function in Eq. (5.96). The cooling function is obtained by fitting the cooling data during lamination as presented in [2]. Consequently, this problem is defined by a total of 18 equations consisting of 10 equilibrium equations (9 for mechanical system and 1 for thermal system) and 8 compatibility equations at the interface. The load intensities for the three layers are derived according to Appendix **B.3**.

With respect to Eq. (5.59), Eq. (5.83) can be rewritten in terms of mid-plane displacements and deflections of the layers which in turn can be used to express the relations for surface loads p, n and m (see Appendix **B.3**). Consequently, in

accordance with Eq. (5.82), the overall equilibrium equations for the layers in the PV laminate are expressed as:

Layer 1

$$\nabla^4 w^{(1)} + \eta_2{}^{(1)} \frac{\partial^2 w^{(1)}}{\partial t^2} - \eta_{3(1)} \mathrm{K_y}{}^{(1)} \left(w^{(1)} - w^{(2)}\right) - \eta_{3(1)} \left[-c_1{}^2 K_{x1} \nabla^2 w^{(1)} - c_2 c_1 K_{x1} \nabla^2 w^{(2)} + K_{x1} c_1 \left(U_{1,1}{}^{(1)} - U_{1,1}{}^{(2)}\right) + K_{x1} c_1 \left(U_{2,2}{}^{(1)} - U_{2,2}{}^{(2)}\right)\right] = 0 \tag{5.87a}$$

$$U_{1,11}{}^{(1)} + \mu_1{}^{(1)} U_{1,22}{}^{(1)} - \mu_2{}^{(1)} \frac{\partial^2 U_1{}^{(1)}}{\partial t^2} + \mu_3{}^{(1)} K_{x1} \left(c_1 w_{,1}{}^{(1)} + c_2 w_{,1}{}^{(2)} + U_1{}^{(2)} - U_1{}^{(1)}\right) = 0 \tag{5.87b}$$

$$U_{2,22}{}^{(1)} + \mu_1{}^{(1)} U_{2,11}{}^{(1)} - \mu_2{}^{(1)} \frac{\partial^2 U_2{}^{(1)}}{\partial t^2} + \mu_3{}^{(1)} K_{x1} \left(c_1 w_{,2}{}^{(1)} + c_2 w_{,2}{}^{(2)} + U_2{}^{(2)} - U_2{}^{(1)}\right) = 0 \tag{5.87c}$$

Layer 2

$$\nabla^4 w^{(2)} + \eta_1{}^{(2)} \nabla^2 T^{(2)} + \eta_2{}^{(2)} \frac{\partial^2 w^{(2)}}{\partial t^2} + \eta_{3(2)} \mathrm{K_y}{}^{(2)} w^{(1)} - \left(\eta_{3(2)} \mathrm{K_y}{}^{(1)} + \eta_{3(2)} \mathrm{K_y}{}^{(2)}\right) w^{(2)} + \eta_{3(2)} \mathrm{K_{y,i,j}}{}^{(2)} w^{(3)} - \eta_{3(2)} \left[-c_2 c_1 K_{x1} \nabla^2 w^{(1)} - c_2 c_3 K_{x2} \nabla^2 w^{(3)} - \left(c_2{}^2 K_{x1} + c_2{}^2 K_{x2}\right) \nabla^2 w^{(2)} + K_{x1} c_2 \left(U_{1,1}{}^{(1)} - U_{1,1}{}^{(2)}\right) + K_{x2} c_2 \left(U_{1,1}{}^{(2)} - U_{1,1}{}^{(3)}\right) + K_{x1} c_2 \left(U_{2,2}{}^{(1)} - U_{2,2}{}^{(2)}\right) + K_{x2} c_2 \left(U_{2,2}{}^{(2)} - U_{2,2}{}^{(3)}\right)\right] = 0 \tag{5.88a}$$

$$U_{1,11}{}^{(2)} + \mu_1{}^{(2)} U_{1,22}{}^{(2)} - \mu_2{}^{(2)} \frac{\partial^2 U_1{}^{(2)}}{\partial t^2} + \mu_3{}^{(2)} K_{x1} \left(-c_1 w_{,1}{}^{(1)} - c_2 w_{,1}{}^{(2)} + U_1{}^{(1)} - U_1{}^{(2)}\right) + \mu_3{}^{(2)} K_{x2} \left(c_2 w_{,1}{}^{(2)} + c_3 w_{,1}{}^{(3)} + U_1{}^{(3)} - U_1{}^{(2)}\right) = 0 \tag{5.88b}$$

$$U_{2,22}{}^{(2)} + \mu_1{}^{(2)} U_{2,11}{}^{(2)} - \mu_2{}^{(2)} \frac{\partial^2 U_2{}^{(2)}}{\partial t^2} + \mu_3{}^{(2)} K_{x1}\left(-c_1 w_{,2}{}^{(1)} - c_2 w_{,2}{}^{(2)} + U_2{}^{(1)} - U_2{}^{(2)}\right) + \mu_3{}^{(2)} K_{x2}\left(c_2 w_{,2}{}^{(2)} + c_3 w_{,2}{}^{(3)} + U_2{}^{(3)} - U_2{}^{(2)}\right) = 0 \quad (5.88c)$$

Layer 3

$$\nabla^4 w^{(3)} + \eta_2{}^{(3)} \frac{\partial^2 w^{(3)}}{\partial t^2} - \eta_{3(3)} \mathrm{K_y}{}^{(2)}\left(w^{(3)} - w^{(2)}\right) - \eta_{3(3)}\left[-c_3 c_2 K_{x2} \nabla^2 w^{(2)} - c_3{}^2 K_{x2} \nabla^2 w^{(3)} + K_{x2} c_3\left(U_{1,1}{}^{(2)} - U_{1,1}{}^{(3)}\right) + K_{x2} c_3\left(U_{2,2}{}^{(2)} - U_{2,2}{}^{(3)}\right)\right] = 0 \quad (5.89a)$$

$$U_{1,11}{}^{(3)} + \mu_1{}^{(3)} U_{1,22}{}^{(3)} - \mu_2{}^{(3)} \frac{\partial^2 U_1{}^{(3)}}{\partial t^2} + \mu_3{}^{(3)} K_{x2}\left(-c_2 w_{,1}{}^{(2)} - c_3 w_{,1}{}^{(3)} + U_1{}^{(2)} - U_1{}^{(3)}\right) = 0 \quad (5.89b)$$

$$U_{2,22}{}^{(3)} + \mu_1{}^{(3)} U_{2,11}{}^{(3)} - \mu_2{}^{(3)} \frac{\partial^2 U_2{}^{(3)}}{\partial t^2} + \mu_3{}^{(3)} K_{x2}\left(-c_2 w_{,2}{}^{(2)} - c_3 w_{,2}{}^{(3)} + U_2{}^{(2)} - U_2{}^{(3)}\right) = 0 \quad (5.89c)$$

where

$$\nabla^2 w^{(i)} = \frac{\partial^2 w^{(i)}}{\partial x_1{}^2} + \frac{\partial^2 w^{(i)}}{\partial x_2{}^2}, \qquad \nabla^4 w^{(i)} = \frac{\partial^4 w^{(i)}}{\partial x_1{}^4} + 2\frac{\partial^4 w^{(i)}}{\partial x_1{}^2 \partial x_2{}^2} + \frac{\partial^4 w^{(i)}}{\partial x_2{}^4} \quad (5.90)$$

for $i = 1,2,3$

It should be noted that $\nabla^2 T^{(1)} = \nabla^2 T^{(3)} = 0$ since temperature of the glass and backsheet layers are already determined according to the cooling function (5.96). Therefore, only the thermal equation for the Silicon layer remains to be solved. Accordingly, the thermal equation is evaluated by substituting for heat flow at the upper and lower interface of the Silicon layer to obtain:

$$\lambda^{(2)}\nabla^2 T^{(2)} - {\xi_1}^{(2)} T^{(2)} - {\xi_2}^{(2)} \frac{\partial \mathrm{T}^{(2)}}{\partial t} + {\xi_3}^{(2)}\left({K_z}^{(2)}\theta^{(3)} - {K_z}^{(2)} c^{(2)} T^{(2)}\right) +$$

$${\xi_3}^{(2)}\left({K_z}^{(1)}\theta^{(1)} - {K_z}^{(1)} c^{(2)} T^{(2)}\right) = 0 \qquad (5.91)$$

The temperature change in the glass and Backsheet layers are assumed to be equal to the press temperature i.e., $\theta^{(3)} = \theta^{(1)} = T_p(t)$. ${K_2}^{(1)}$ and ${K_2}^{(2)}$ are the thermal conductance at the lower and upper interfaces of the Silicon layer.

where T_p is the press temperature.

Therefore, a total of 10 equations have to be solved to obtain 10 unknowns namely $w^{(1)}$, $w^{(2)}$, $w^{(3)}$, ${U_1}^{(1)}$, ${U_1}^{(2)}$, ${U_1}^{(3)}$, ${U_2}^{(1)}$, ${U_2}^{(2)}$, ${U_2}^{(3)}$ and $T^{(2)}$.

5.7.1 Boundary conditions

The boundary condition for the mechanical system is a simply supported condition at all the edges of the laminate. Therefore, all displacements, moments and axial forces at the edges vanishes. This is mathematically expressed as:

$$w^{(i)}(x_1, x_2) = 0 \qquad \text{for } x_1 = 0, L_1 \text{ and } x_2 = 0, L_2 \qquad (5.92a)$$

$${u_2}^{(i)}(z, x_1, x_2) = 0 \qquad \text{for } x_1 = 0, L_1 \qquad (5.92b)$$

$${u_1}^{(i)}(z, x_1, x_2) = 0 \qquad \text{for } x_2 = 0, L_2 \qquad (5.92c)$$

$${M_1}^{(i)}(x_1, x_2) = 0 \qquad \text{for } x_2 = 0, L_2 \qquad (5.92d)$$

$${M_2}^{(i)}(x_1, x_2) = 0 \qquad \text{for } x_1 = 0, L_1 \qquad (5.92e)$$

$${N_1}^{(i)}(x_1, x_2) = 0 \qquad \text{for } x_1 = 0, L_1 \qquad (5.92f)$$

$${N_2}^{(i)}(x_1, x_2) = 0 \qquad \text{for } x_2 = 0, L_2 \qquad (5.92g)$$

The boundary conditions for the thermal system is expressed as:

$$\lambda \frac{\partial T(X,x_2,t)}{\partial x_1} + hT(X,x_2,t) = hT_p \quad (5.93a)$$

$$\lambda \frac{\partial T(0,x_2,t)}{\partial x_1} + hT(0,x_2,t) = -hT_p \quad (5.93b)$$

$$\lambda \frac{\partial T(x_1,Y,t)}{\partial x_2} + hT(x_1,Y,t) = hT_p \quad (5.93c)$$

$$\lambda \frac{\partial T(x_1,0,t)}{\partial x_2} + hT(x_1,0,t) = -hT_p \quad (5.93d)$$

5.7.2 Finite difference discretization

To obtain the solution for the system equations, a centred divided difference is used for space discretization of the system of coupled higher order PDEs. The procedure to obtain the finite difference weights of derivatives of functions has been discussed extensively in Chapter 3 and it is hereby noted that,

$$w_{,xxxx} = \frac{w_{i+2,j} - 4w_{i+1,j} + 6w_{i,j} - 4w_{i-1,j} + w_{i-2,j}}{\Delta x^4} \quad (5.94a)$$

$$w_{,xxyy} = \frac{w_{i+1,j+1} - 2w_{i+1,j} + w_{i+1,j-1} - 2w_{i,j+1} + 4w_{i,j} - 2w_{i,j-1} + w_{i-1,j+1} - 2w_{i-1,j} + w_{i-1,j-1}}{\Delta x^2 \Delta y^2} \quad (5.94b)$$

$$w_{,xx} = \frac{w_{i+1,j} - 2w_{i,j} + w_{i-1,j}}{\Delta x^2} \quad (5.94c)$$

A backward difference approximation is applied for the first derivative as:

$$w_{,x} = \frac{w_{i,j} - w_{i-1,j}}{\Delta x} \quad (5.94d)$$

There is material discontinuity in the Silicon layer due to the presence of the thin EVA strip between Silicon solar cells. On this basis, a non-uniform mesh size is adapted for the region of discontinuity. To obtain the finite difference formula of the differentials in this region, Lagrangian polynomials are used to estimate the finite difference weights by interpolation as shown in Table 3.4 (see Appendix **B**).

The compact system equations after finite difference discretization becomes:

$$\boldsymbol{M}_w \frac{\mathrm{d}^2\boldsymbol{w}}{\mathrm{d}t^2} + \boldsymbol{K}_w\boldsymbol{w} + \boldsymbol{K}_u\boldsymbol{U}_1 + \boldsymbol{K}_v\boldsymbol{U}_2 + \boldsymbol{C}_T\boldsymbol{T} = \boldsymbol{F}_1 i(t)$$

(5.95a)

$$\boldsymbol{M}_u \frac{\mathrm{d}^2\boldsymbol{U}_1}{\mathrm{d}t^2} + \bar{\boldsymbol{K}}_u\boldsymbol{U}_1 + \bar{\boldsymbol{K}}_{w1}\boldsymbol{w} = \boldsymbol{F}_2 i(t)$$

(5.95b)

$$\boldsymbol{M}_v \frac{\mathrm{d}^2\boldsymbol{U}_2}{\mathrm{d}t^2} + \bar{\boldsymbol{K}}_v\boldsymbol{U}_2 + \bar{\boldsymbol{K}}_{w2}\boldsymbol{w} = \boldsymbol{F}_3 i(t)$$

(5.95c)

$$\boldsymbol{S}\frac{\partial \boldsymbol{T}}{\partial t} + \boldsymbol{H}\boldsymbol{T} = \boldsymbol{F}_4 i(t)$$

(5.95d)

In Eq. (5.95), $i(t)$ is the cooling function which is obtained by exponential fitting of the cooling data during lamination as presented in [2]. The correlation for the fit in Fig. 5.7 is expressed mathematically as:

$$i(t) = a\exp^{(b\times t)} + c\exp^{(d\times t)}$$

(5.96)

where

$a = -227.8$, $b = -0.0004404$, $c = 227.8$, $d = -0.002476$.

For this analysis, it is assumed that the press temperature $T_p = i(t)$.

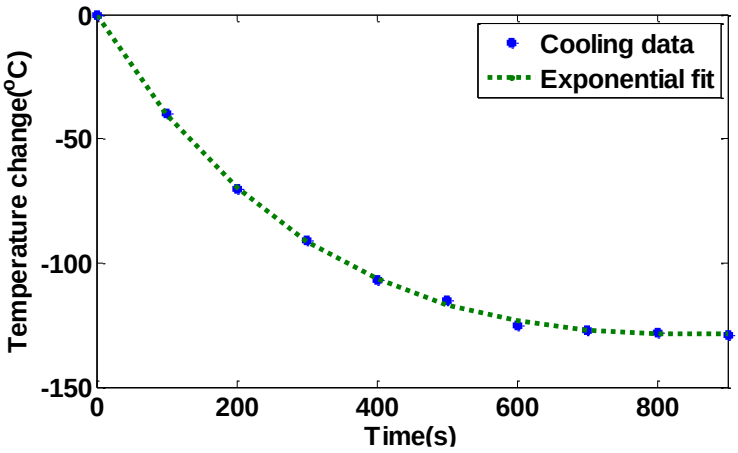

Figure 5.7. Exponential fit for the cooling data during lamination.

The global system matrix becomes:

$$\begin{bmatrix} \boldsymbol{M}_w & \mathbf{0} & \mathbf{0} & \mathbf{0} \\ \mathbf{0} & \boldsymbol{M}_u & \mathbf{0} & \mathbf{0} \\ \mathbf{0} & \mathbf{0} & \boldsymbol{M}_v & \mathbf{0} \\ \mathbf{0} & \mathbf{0} & \mathbf{0} & \mathbf{0} \end{bmatrix} \begin{Bmatrix} \ddot{\boldsymbol{w}} \\ \ddot{\boldsymbol{U}}_1 \\ \ddot{\boldsymbol{U}}_2 \\ \ddot{\boldsymbol{T}} \end{Bmatrix} + \begin{bmatrix} \mathbf{0} & \mathbf{0} & \mathbf{0} & \mathbf{0} \\ \mathbf{0} & \mathbf{0} & \mathbf{0} & \mathbf{0} \\ \mathbf{0} & \mathbf{0} & \mathbf{0} & \mathbf{0} \\ \mathbf{0} & \mathbf{0} & \mathbf{0} & \boldsymbol{S} \end{bmatrix} \begin{Bmatrix} \dot{\boldsymbol{w}} \\ \dot{\boldsymbol{U}}_1 \\ \dot{\boldsymbol{U}}_2 \\ \dot{\boldsymbol{T}} \end{Bmatrix} + \begin{bmatrix} \boldsymbol{K}_w & \boldsymbol{K}_u & \boldsymbol{K}_v & \boldsymbol{C}_T \\ \bar{\boldsymbol{K}}_{w1} & \boldsymbol{K}_{u1} & \mathbf{0} & \mathbf{0} \\ \bar{\boldsymbol{K}}_{w2} & \mathbf{0} & \boldsymbol{K}_{v1} & \mathbf{0} \\ \mathbf{0} & \mathbf{0} & \mathbf{0} & \boldsymbol{H} \end{bmatrix} \begin{Bmatrix} \boldsymbol{w} \\ \boldsymbol{U}_1 \\ \boldsymbol{U}_2 \\ \boldsymbol{T} \end{Bmatrix} = \begin{Bmatrix} \boldsymbol{F}_1 \\ \boldsymbol{F}_2 \\ \boldsymbol{F}_3 \\ \boldsymbol{F}_4 \end{Bmatrix} i(t) \tag{5.97}$$

5.7.3 Newmark time integration

Since there is no feedback coupling from the thermal system to the mechanical system in Eq. (5.97), the thermal system can be solved independently of the mechanical system and the predetermined temperature field can be used as an input to obtain the transient response of the mechanical system. Accordingly, Eq. (5.97) can be rewritten in a compact form as:

$$\begin{bmatrix} \boldsymbol{M}_1 & \boldsymbol{0} \\ \boldsymbol{0} & \boldsymbol{0} \end{bmatrix} \begin{Bmatrix} \ddot{\boldsymbol{\chi}} \\ \ddot{\boldsymbol{T}} \end{Bmatrix} + \begin{bmatrix} \boldsymbol{0} & \boldsymbol{0} \\ \boldsymbol{0} & \boldsymbol{S} \end{bmatrix} \begin{Bmatrix} \dot{\boldsymbol{\chi}} \\ \dot{\boldsymbol{T}} \end{Bmatrix} + \begin{bmatrix} \boldsymbol{K}_1 & \boldsymbol{C}_1 \\ \boldsymbol{0} & \mathbf{H} \end{bmatrix} \begin{Bmatrix} \boldsymbol{\chi} \\ \boldsymbol{T} \end{Bmatrix} = \begin{Bmatrix} \overline{\boldsymbol{F}}_1 \\ \boldsymbol{F}_4 \end{Bmatrix} i(t) \tag{5.98}$$

where

$$\boldsymbol{M}_1 = \begin{bmatrix} \boldsymbol{M_w} & \boldsymbol{0} & \boldsymbol{0} \\ \boldsymbol{0} & \boldsymbol{M_u} & \boldsymbol{0} \\ \boldsymbol{0} & \boldsymbol{0} & \boldsymbol{M_v} \end{bmatrix}, \boldsymbol{K}_1 = \begin{bmatrix} \boldsymbol{K_w} & \boldsymbol{K}_u & \boldsymbol{K}_v \\ \overline{\boldsymbol{K}}_{w1} & \boldsymbol{K}_{u1} & \boldsymbol{0} \\ \overline{\boldsymbol{K}}_{w2} & \boldsymbol{0} & \boldsymbol{K}_{v1} \end{bmatrix}, \boldsymbol{\chi} = \begin{Bmatrix} \boldsymbol{w} \\ \boldsymbol{U}_1 \\ \boldsymbol{U}_2 \end{Bmatrix}, \boldsymbol{C}_1 = \begin{Bmatrix} \boldsymbol{C}_T \\ \boldsymbol{0} \\ \boldsymbol{0} \end{Bmatrix},$$

$$\overline{\boldsymbol{F}}_1 = \begin{Bmatrix} \boldsymbol{F}_1 \\ \boldsymbol{F}_2 \\ \boldsymbol{F}_3 \end{Bmatrix}, \boldsymbol{M}_1,\ \boldsymbol{K}_1 \in \mathbb{R}^{\mathrm{N}_1 \times \mathrm{N}_1}, \boldsymbol{C}_1 \in \mathbb{R}^{\mathrm{N}_1 \times \mathrm{N}_T}, \mathrm{N}_1 = 3N .$$

To solve this system of coupled differential equations, general Newmark algorithm described in [82] is used. For approximation of variable $\boldsymbol{\chi}$ that occurs in second order at time t_{n+1},

$$\boldsymbol{\chi}_{n+1} = \boldsymbol{\chi}_n + \Delta t \dot{\boldsymbol{\chi}}_n + \tfrac{1}{2}\Delta t^2 \ddot{\boldsymbol{\chi}}_n + \tfrac{1}{2}\beta_2 \Delta t^2 \Delta \ddot{\boldsymbol{\chi}}_{n+1} \tag{5.99a}$$

$$\boldsymbol{\chi}_{n+1} = \boldsymbol{\chi}^p{}_{n+1} + \tfrac{1}{2}\beta_2 \Delta t^2 \Delta \ddot{\boldsymbol{\chi}}_{n+1} \tag{5.99b}$$

$\boldsymbol{\chi}^p$ denotes predetermined parameter.

The first-order time derivative $\dot{\boldsymbol{\chi}}$ is approximated at time t_{n+1} as:

$$\dot{\boldsymbol{\chi}}_{n+1} = \dot{\boldsymbol{\chi}}_n + \Delta t \ddot{\boldsymbol{\chi}}_n + \beta_1 \Delta t \Delta \ddot{\boldsymbol{\chi}}_{n+1} \tag{5.100a}$$

$$\dot{\boldsymbol{\chi}}_{n+1} = \dot{\boldsymbol{\chi}}^p{}_{n+1} + \beta_1 \Delta t \Delta \ddot{\boldsymbol{\chi}}_{n+1} \tag{5.100b}$$

Approximation of variable $\boldsymbol{T}$ that occurs in first order at time t_{n+1} gives:

$$\boldsymbol{T}_{n+1} = \boldsymbol{T}_n + \Delta t \dot{\boldsymbol{T}}_n + \vartheta \Delta t \Delta \dot{\boldsymbol{T}}_{n+1} \tag{5.101a}$$

$$\boldsymbol{T}_{n+1} = \boldsymbol{T}^p{}_{n+1} + \vartheta \Delta t \Delta \dot{\boldsymbol{T}}_{n+1} \tag{5.101b}$$

where

$$\Delta\ddot{\boldsymbol{\chi}}_{n+1} = \ddot{\boldsymbol{\chi}}_{n+1} - \ddot{\boldsymbol{\chi}}_n \tag{5.102a}$$

$$\Delta\dot{\boldsymbol{\chi}}_{n+1} = \dot{\boldsymbol{\chi}}_{n+1} - \dot{\boldsymbol{\chi}}_n \tag{5.102b}$$

$$\Delta\dot{\boldsymbol{T}}_{n+1} = \dot{\boldsymbol{T}}_{n+1} - \dot{\boldsymbol{T}}_n \tag{5.102c}$$

By substituting Eqs. (5.99–5.101) into Eq. (5.98), we obtain:

$$\boldsymbol{M}_1(\Delta\ddot{\boldsymbol{\chi}}_{n+1} + \ddot{\boldsymbol{\chi}}_n) + \boldsymbol{K}_1\left(\boldsymbol{\chi}^p{}_{n+1} + \frac{1}{2}\beta_2\Delta t^2\Delta\ddot{\boldsymbol{\chi}}_{n+1}\right) + \boldsymbol{C}_1\left(\boldsymbol{T}^p{}_{n+1} + \vartheta\Delta t\Delta\dot{\boldsymbol{T}}_{n+1}\right) = \overline{\boldsymbol{F}}_1 i(t) \tag{5.103a}$$

$$\boldsymbol{S}\left(\Delta\dot{\boldsymbol{T}}_{n+1} + \dot{\boldsymbol{T}}_n\right) + \boldsymbol{H}\left(\boldsymbol{T}^p{}_{n+1} + \vartheta\Delta t\Delta\dot{\boldsymbol{T}}_{n+1}\right) = \boldsymbol{F}_4 i(t) \tag{5.103b}$$

Eq. (5.103) can be rewritten by collecting like terms to get:

$$\underbrace{\left(\boldsymbol{M}_1 + \frac{1}{2}\beta_2\Delta t^2\boldsymbol{K}_1\right)}_{\overline{\boldsymbol{M}}_1}\Delta\ddot{\boldsymbol{\chi}}_{n+1} + \underbrace{\boldsymbol{C}_1\vartheta\Delta t}_{\overline{\boldsymbol{C}}_1}\Delta\dot{\boldsymbol{T}}_{n+1} = \underbrace{\overline{\boldsymbol{F}}_1 i(t) - \boldsymbol{M}_1\ddot{\boldsymbol{\chi}}_n - \boldsymbol{K}_1\boldsymbol{\chi}^p{}_{n+1} - \boldsymbol{C}_1\boldsymbol{T}^p{}_{n+1}}_{\boldsymbol{R}_1} \tag{5.104a}$$

$$\underbrace{(\boldsymbol{S} + \boldsymbol{H}\vartheta\Delta t)}_{\overline{\boldsymbol{S}}}\Delta\dot{\boldsymbol{T}}_{n+1} = \underbrace{\boldsymbol{F}_4 i(t) - \boldsymbol{S}\dot{\boldsymbol{T}}_n - \boldsymbol{H}\boldsymbol{T}^p{}_{n+1}}_{\boldsymbol{R}_2} \tag{5.104b}$$

$\Delta\dot{\boldsymbol{T}}_{n+1}$ determined from Eq. (5.104b) can be substituted into Eq. (5.104a) so that $\Delta\ddot{\boldsymbol{\chi}}_{n+1}$ is obtained from the following relation:

$$\overline{\boldsymbol{M}}_1\Delta\ddot{\boldsymbol{\chi}}_{n+1} = \boldsymbol{R}_1 - \overline{\boldsymbol{C}}_1\Delta\dot{\boldsymbol{T}}_{n+1} \tag{5.105}$$

To achieve unconditional numerical stability, the integration parameters ϑ, β_1, and β_2 are chosen as $\vartheta = 0.5$, $\beta_1 = 0.5$, $\beta_2 = 0.5$ and a time step $\Delta t = 1\text{s}$ is specified.

5.8 Numerical results

All mathematical formulations (for 2D and 3D) presented in the previous sections are implemented in MATLAB computational software. For the 2D case, the results are subdivided into uniform temperature case in which results for exact solution are computed and non-uniform temperature case in which results for numerical solution are presented. For results in the 3D category, numerical solutions for (axial, shear and peeling) stress distributions at different regions of the module are computed and observed transient stress evolution are also presented.

5.8.1 Uniform temperature across the PV module (2D case)

The module is considered to cool down inside the laminator from 150 °C to the room temperature (25 °C) in 30 minutes. At this final temperature, the EVA equivalent relaxation modulus $E(t)$ is calculated to be 6 MPa.

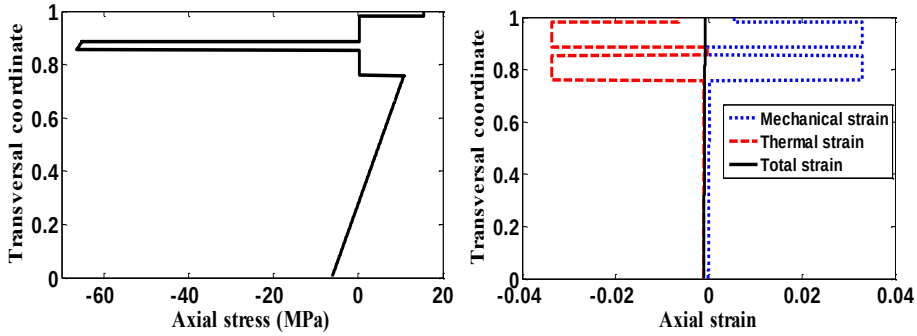

(a) (b)

Figure. 5.8 (a) Stress and (b) strain distributions for a perfect interface configuration of uniform temperature analysis.

In the case of perfectly bonded interfaces and EVA layers treated as continuum layers with their thicknesses, the axial stress and strain are plotted in Fig. 5.8. The Silicon layer results to be in a compressive stress state above 60 MPa. The thermal strain and the mechanical strain almost counteract each other, which makes the total strain to be almost zero in the entire module.

For the shear deformable interface configuration with 3 real layers and 2 shear-lag interfaces (glass-Silicon interface 1 and Silicon-backsheet interface 2), 2 models are examined thus:

(1) Shear deformable interfaces with longitudinal compliance only.

(2) Shear deformable interfaces with longitudinal and transverse compliances of equal magnitude.

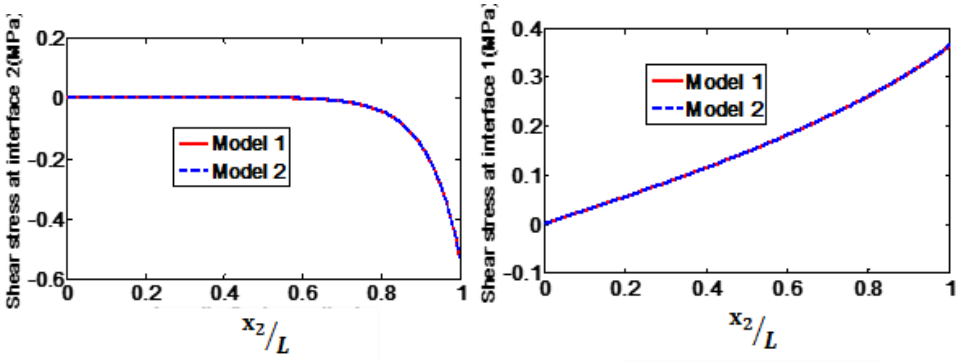

(a) (b)

Figure. 5.9 Shear stress at (a) interface 2 (b) interface 1 for a uniform temperature analysis.

It can be deduced from the results shown in Fig. 5.9 that the interfacial stress distribution for model 1 and model 2 are almost the same. This result is not unexpected, since isotropic adhesive layers at the interfaces for model 1 and model 2 (i.e., $K_x = K_y$) are assumed. The effect of the transverse compliance will

obviously be significant when an orthotropic adhesive (i.e. $K_x \neq K_y$) interface is considered.

The results of the interfacial stress distribution pinpoint that the magnitude of the shear stresses and the peeling stresses increases towards the edge of the laminate. Therefore, those points are critical locations for possible delamination. It is observed in Fig. 5.10 that the mean compressive stress in the silicon layer is reduced for the shear deformable interface configuration with respect to the perfect interface configuration, due to the finite compliance of the interfaces, which is a more realistic situation in practice.

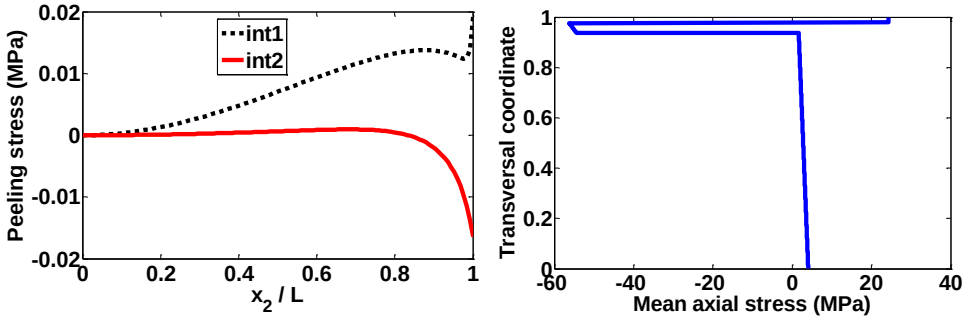

(a) (b)

Figure. 5.10 (a) Peeling stress along interfaces 1 and 2; (b) Silicon compressive stress for model 2.

5.8.2 Non-uniform temperature (2D case)

The stress formulation for this analysis involves a shear deformable interface with only longitudinal compliance, since the effect of the transverse compliance was already found to be negligible. The solution for this problem is achieved by using the trapezium rule method for time integration. As highlighted in Sec. 5.3.2, the accuracy of the numerical scheme is tested against the result from the exact solution

that can be determined for the uniform temperature boundary conditions. A very good agreement was found, see Fig. 5.11, proving the accuracy of the method.

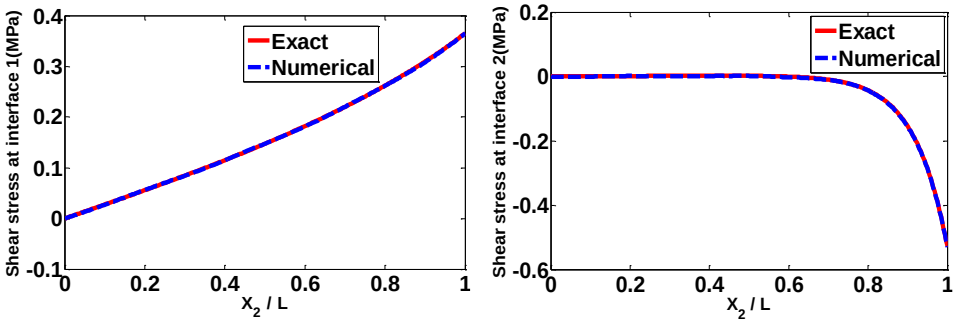

(a) (b)

Figure. 5.11 exact and numerical solution for uniform temperature analysis at (a) interface 1 (b) interface 2.

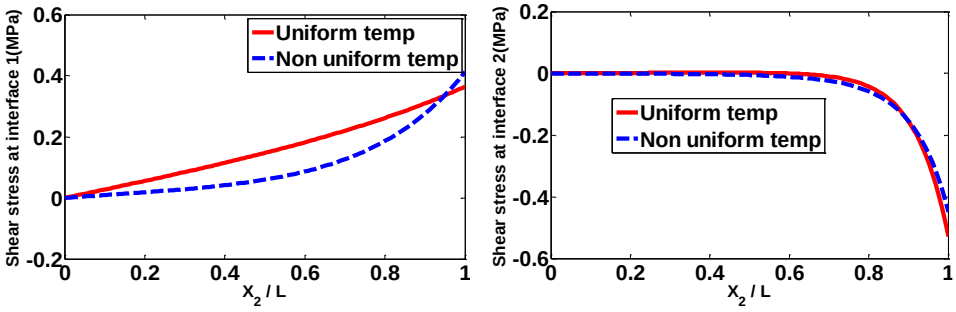

(a) (b)

Figure. 5.12 Shear stresses at: (a) interface 1, and (b) interface 2, after a cooling period of 30 minutes.

The numerical results for the non-uniform temperature analysis show that the magnitude of the interfacial stresses at the Glass-Silicon interface is reduced with respect to the uniform temperature analysis, as we move away from the core to the edge of the laminate. This may be attributed to the temperature variation from the core to the edge of the laminate, see Fig. 5.12(a). On the other hand, there is no

significant change in the stress distribution at the Silicon-backsheet interface, see Fig. 5.12(b).

Results in Fig. 5.13 show that the mean compressive stress in the Silicon cell increases along the longitudinal coordinate in the Silicon layer as the cooling time increases.

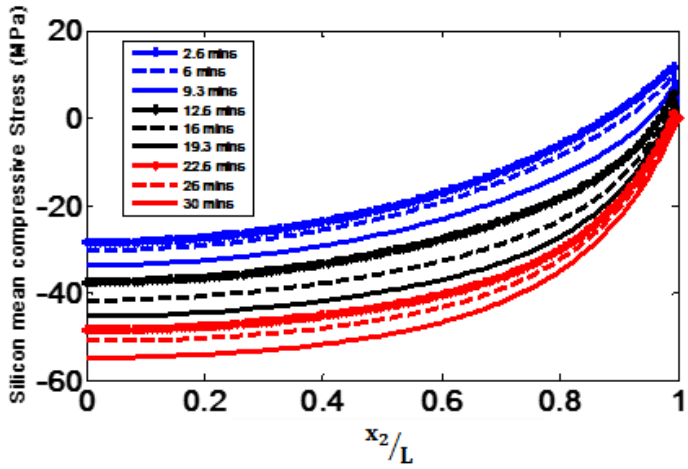

Figure. 5.13. Mean residual compresssive stresses in the Silicon layer vs. longitudinal coordinate, for different time intervals.

As shown in Fig. 5.14, the mean residual axial stress in the Silicon layer at the end of the lamination process after cooling is considerably lower by assuming a time-space-dependent temperature field instead of a uniform temperature across the whole module, i.e., about 45 MPa instead of about 60 MPa. A detailed comparison of numerical results for the different models is presented in Tables 5.4-5.6.

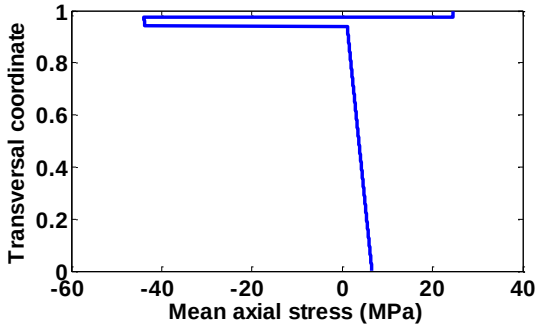

Figure. 5.14 Mean axial stress distribution in the module for non-uniform temperature analysis.

Table 5.4: mean axial stress in Silicon for different models and different thickness of Silicon cell.

Normalized Thickness	**Mean axial stress in Silicon (MPa)**		
	Uniform temperature		**Non-uniform temperature**
	Perfect interface	**Shear-lag**	**Shear-lag**
0.01	-66.452	-56.363	-44.005
0.10	-66.332	-56.184	-43.974
0.20	-66.212	-55.996	-43.938
0.30	-66.092	-55.817	-43.901
0.40	-65.973	-55.629	-43.865
0.50	-65.853	-55.450	-43.828
0.60	-65.733	-55.272	-43.792
0.70	-65.573	-55.084	-43.755
0.80	-65.453	-54.905	-43.719
0.90	-65.333	-54.717	-43.682
1.00	-65.213	-54.547	-43.648

Tabe 5.5: interlaminar stresses at the interface 1 between glass and Silicon for uniform and non-uniform temperatures.

Normalized length	**Interfacial stresses, interface 1 (MPa)**			
	Shear stresses		**Peeling stresses**	
	Uniform temperature	**Non uniform temperature**	**Uniform temperature**	**Non-uniform temperature**
0.00	0.00000	0.00000	0.00000	0.00000
0.10	0.00077	-0.00037	0.00285	0.00074
0.20	0.00145	-0.00090	0.00011	0.00117
0.30	0.00209	-0.00160	0.00024	-0.00301
0.40	0.00246	-0.00302	0.00042	-0.00561
0.50	0.00214	-0.00571	0.00064	-0.01248
0.60	-0.00025	-0.01153	0.00085	-0.02231
0.70	-0.01043	-0.02557	0.00094	-0.03551
0.80	-0.04275	-0.05874	0.00048	-0.06022
0.90	-0.16236	-0.16024	-0.00222	-0.09496
1.00	-0.52913	-0.45058	-0.01645	-0.13839

Table 5.6: Interlaminar stress distribution at the interface 2 between Silicon and backsheet for uniform and non-uniform temperatures.

Normalized length	**Interfacial stresses, interface 2 (MPa)**			
	Shear stresses		**Peeling stresses**	
	Uniform temperature	**Non uniform temperature**	**Uniform temperature**	**Non uniform temperature**
0.00	0.00000	0.00000	0.00000	0.00000
0.10	0.02870	0.00832	0.00034	-0.00052
0.20	0.05564	0.01579	0.00130	0.00047
0.30	0.08580	0.02502	0.00290	-0.00055
0.40	0.11500	0.03579	0.00480	0.00042
0.50	0.14866	0.05236	0.00713	-0.00067
0.60	0.18211	0.07454	0.00936	0.00053
0.70	0.22163	0.11093	0.01162	-0.00019
0.80	0.26196	0.16174	0.01322	-0.00128
0.90	0.31138	0.24590	0.01370	-0.00194
1.00	0.36520	0.36719	0.01919	-0.00378

5.8.3 Residual stress distributions (3D case)

Residual stresses at the end of lamination i.e., after 15 min of the simulation are examined to analyse the response of the coupled thermo-mechanical system. With interface 1 between Silicon and glass and the interface 2 between backsheet and Silicon, interfacial stresses in the longitudinal directions are shown in specific points in the plane. Peeling stresses along one of the longitudinal axes are also

evaluated. To obtain the normal stresses over the thickness in x_1 and x_2 directions, the PV module is divided into 4 regions as in Fig. 5.15a. To investigate the stress variation in the PV module, mean normal stresses are also computed over the laminate thickness for different points in the region 1 as shown in Fig. 5.15b since the stress condition of region 1 is the same for other regions due to the same boundary conditions imposed on all the sides.

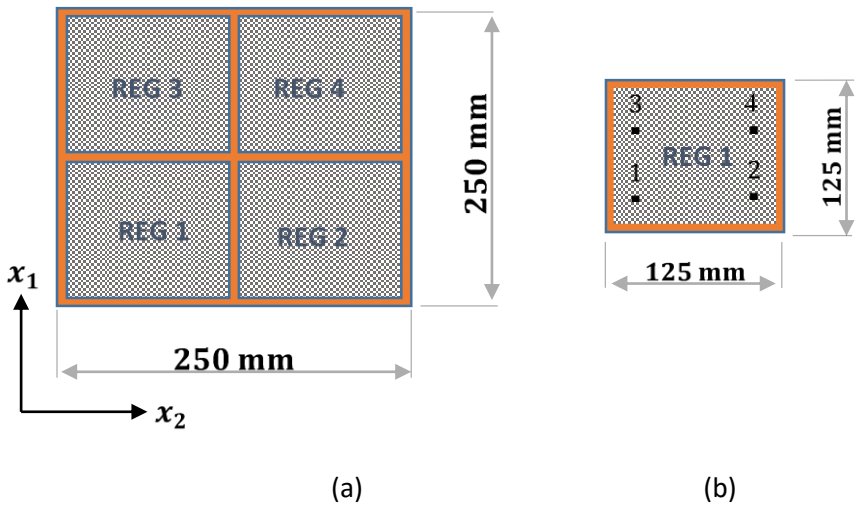

Figure 5.15. Regions indicating Silicon solar cells.

Figure 5.16 shows the interfacial stress 2 for interfaces 1 and 2 along the x_2 coordinate. A typical trend with a peak at the edges is observed due to stress concentrations. Specifically, a maximum of 0.4 MPa of the shear stress component 2 are obtained at the edges of the Silicon-backsheet interface while 0.1 MPa is attained at the edges of the Glass-Silicon interface. A similar trend characterizes the shear stress component 1 (see Fig. 5.17) since similar boundary conditions are imposed at the x_1 and x_2 edges of the laminate.

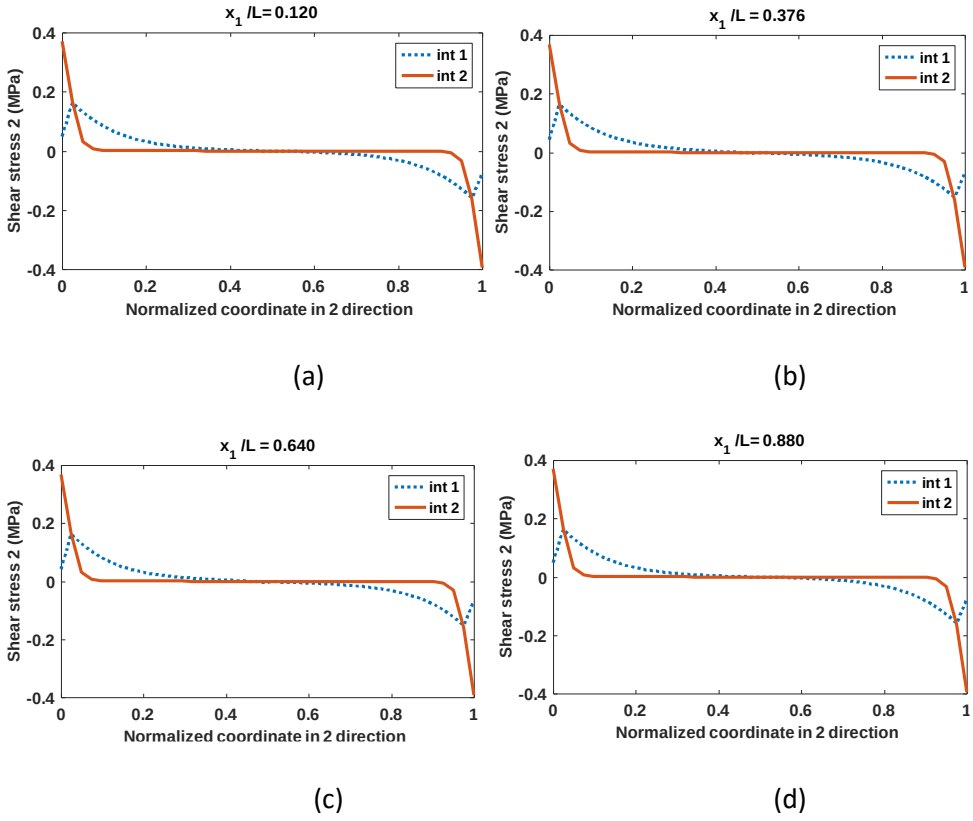

Figure 5.16. Shear stress 2 along the x_2 direction at specific points in x_1 direction.

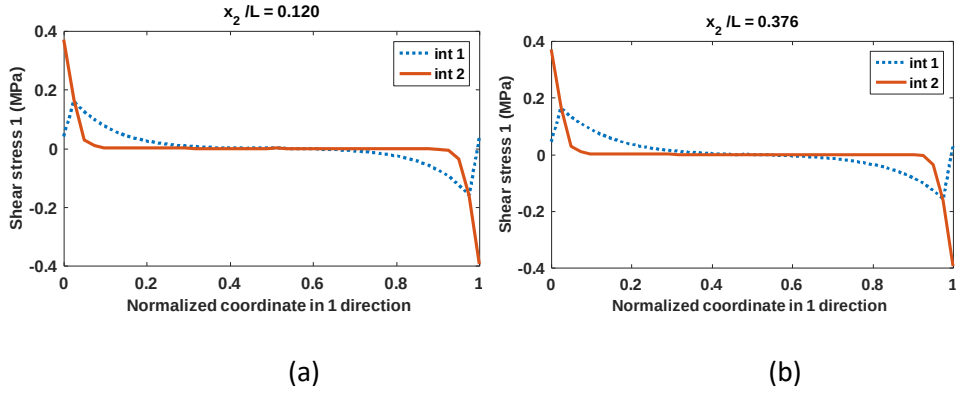

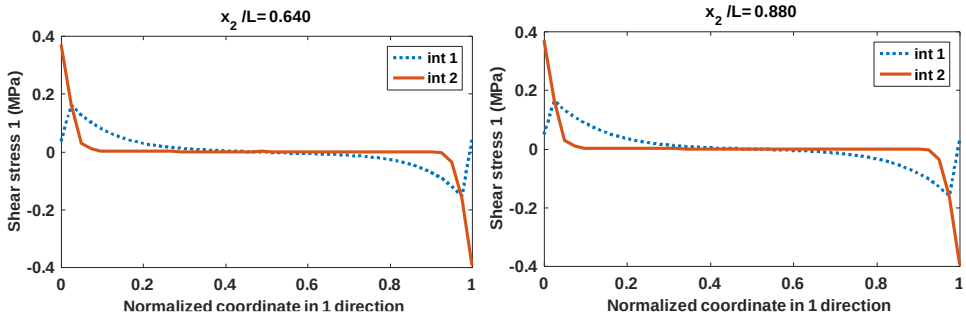

Figure 5.17. Shear stress 1 along the x_1 direction at specific points in x_2 direction.

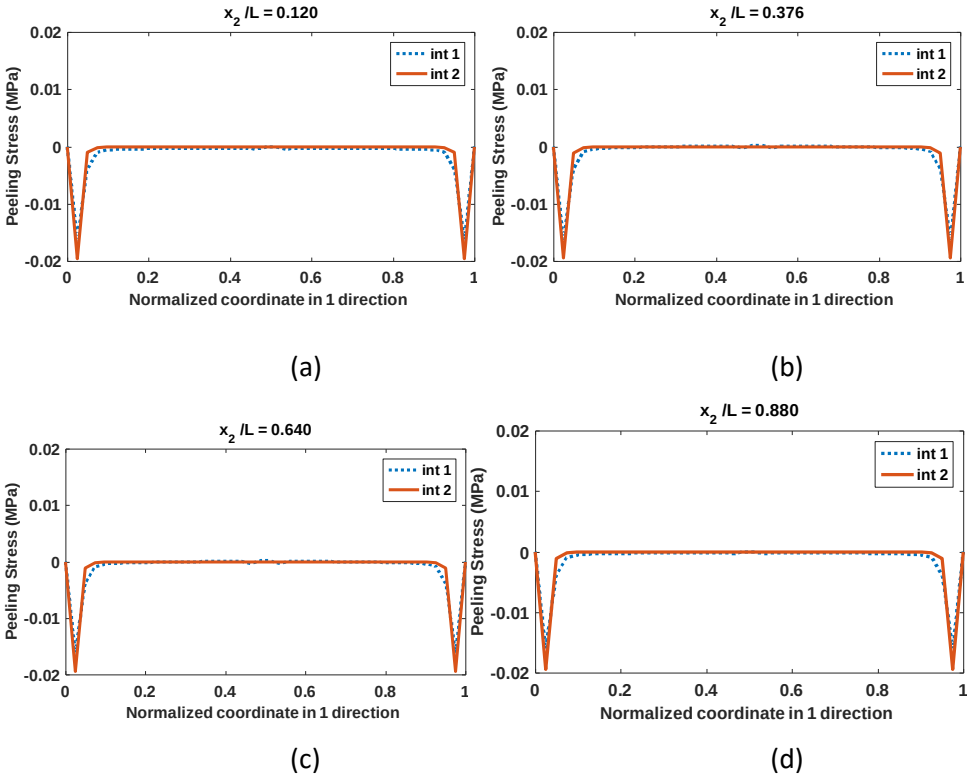

Figure 5.18. Peeling stresses along the x_2 direction.

The peeling stresses along the longitudinal axis in the x_1-direction is shown in Fig. 5.18. They are quite low in magnitude except at the edges, potential sites for delamination.

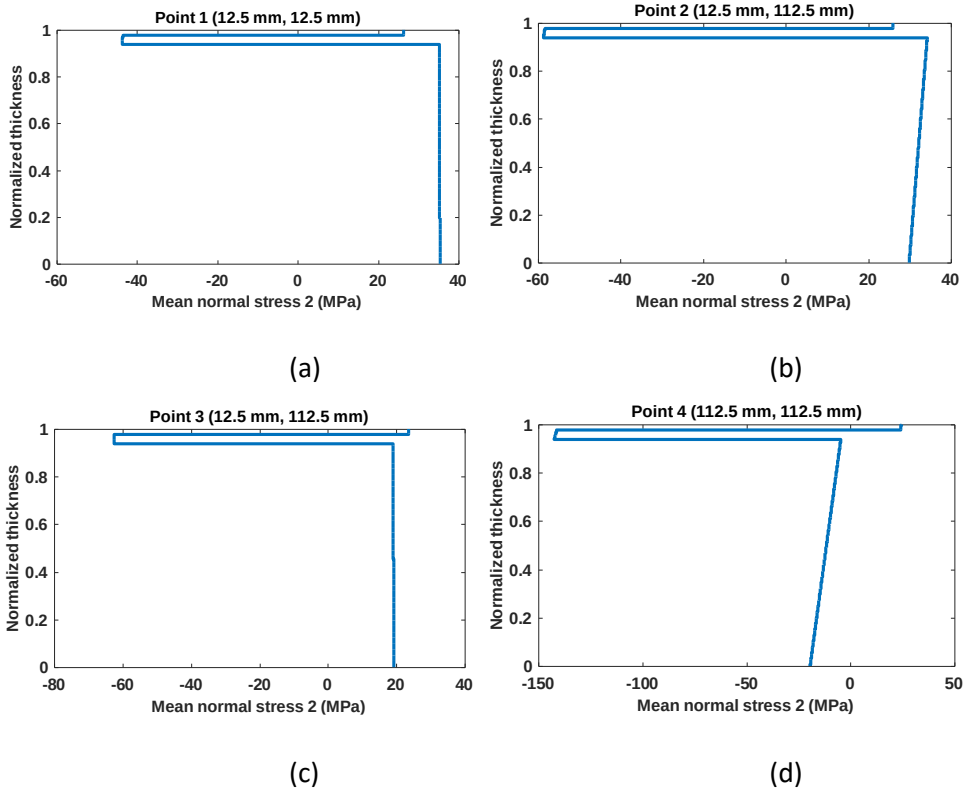

Figure 5.19. Mean axial stress 2 at specific regions in the PV laminate.

The mean normal stresses in the laminate are computed in accordance with Fig. (5.15). Figure 5.19 shows the computed normal stresses at different points in region 1 of the laminate and they clearly depend on the position in the Silicon cell. At the edges of the laminate (points 1-3), the Silicon layer experiences a compressive stress magnitude in the range of 40-65 MPa while at the mid-portion of the laminate (point 4), a compressive stress of about 140 MPa is obtained. The average normal stress averaged over the whole region 1 shows a peak of 60 MPa in compression

(see Fig. 5.20). This result corroborates the 2D uniform temperature analysis reported in [97].

The backsheet is generally in tension due to its low coefficient of thermal expansion and low bending moment while the glass is largely in tension due high thermal stresses in excess of mechanical stresses.

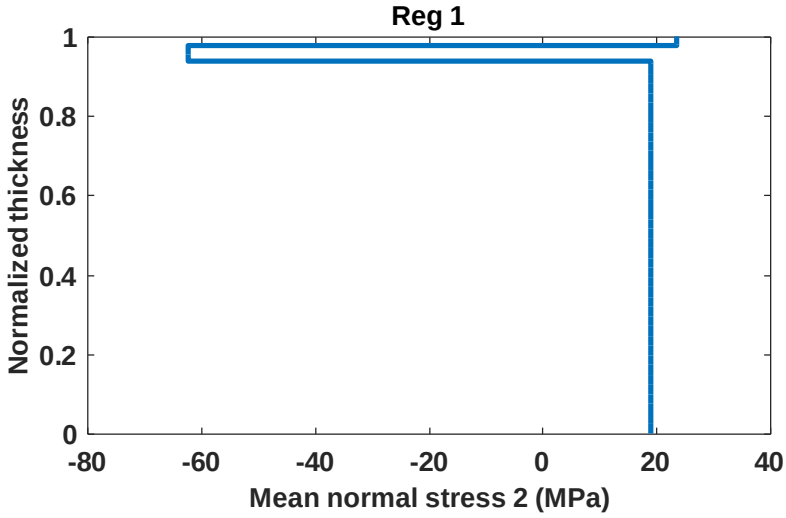

Figure 5.20. Normal stress component 2 averaged over the whole region 1 in the PV laminate.

The stress evolution profiles for the normal stress components in Silicon along the x_2-directions at the points specified in Fig. 5.15b are shown in Fig. (5.11) versus time. The transient stress response evolves exponentially similarly to the input cooling function $i(t)$. This observation highlights the importance of the choice of the cooling function that governs the transient regime of the coupled thermomechanical system.

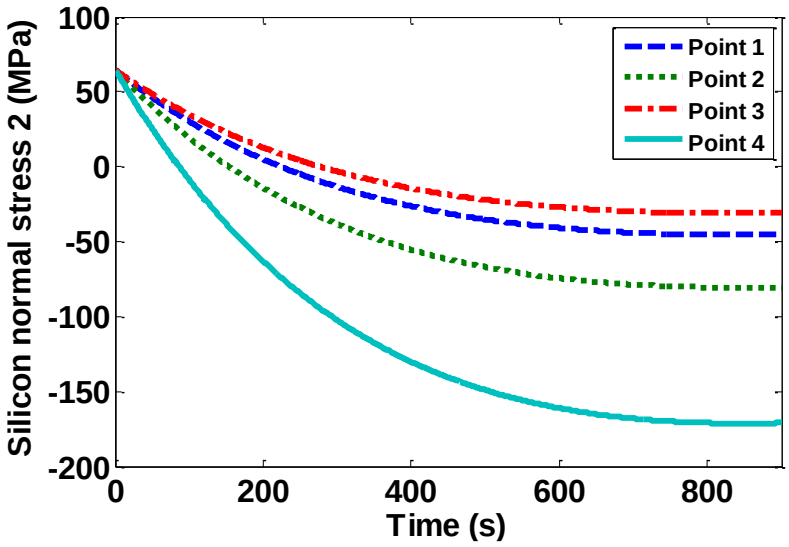

Figure 11. Stress component 2 evolution at specific regions in the laminate. The values at the last time step correspond to $t = 15$ minutes at the end of the cooling stage.

CHAPTER 6

MODEL ORDER REDUCTION OF STRUCTURAL MODELS FOR PHOTOVOLTAIC APPLICATIONS

6.1 Introduction

Modelling of physical systems may be a challenging task when it requires solving large sets of numerical equations. This is the case of photovoltaic (PV) systems which contain many PV modules, each module containing several silicon cells. The determination of the temperature and stress fields in the modules leads to large scale systems, which may be computationally expensive to solve. As demonstrated in chapter 5, discretization of the 3D coupled shear-lag system equations leads to more than 16,000 active (mechanical and thermal) degrees of freedom to be determined and to obtain a full solution of the discretized system becomes an expensive task. Model Order Reduction (MOR) techniques can be used to approximate the full system dynamics with a compact model that is much faster to solve. In this chapter, the techniques to reduce thermomechanical system equations for PV modules are described. Since it is believed that this is the first attempt to apply MOR techniques to reduce PV system equations, the procedure described here is implemented in two stages in order to examine, hierarchically, the

application of MOR techniques to PV system. The first stage describes the MOR approach to reduce a thermal (first-order) system of PV module during service while the second stage involves techniques to reduce large scale dynamic coupled thermomechanical (second-order) system equations for PV module during lamination.

Among the several available MOR approaches, in this work, a Proper Orthogonal Decomposition (POD) projection based approach together with Discrete Empirical Interpolation Method (DEIM) has been applied to the first-order thermal system, with a suitably modified formulation that is specifically designed for handling the nonlinear terms that are present in the equations governing the thermal behaviour of PV modules during service. The results show that the proposed DEIM technique is able to reduce significantly the system size, by retaining a full control on the accuracy of the solution. The second-order coupled thermomechanical system is efficiently reduced by using the second-order Krylov based method described in chapter 4. A detail comparison between state-space approach and the second-order Krylov method is herein presented. Due to the thermal coupling of the thermomechanical system, a structure preserving scheme is desired. Despite the fact that there is no standard approach in the literature for treating a second-order coupled system for structure preservation, a new structure preserving formulation for coupled system is proposed in this work and the results show good agreement with original system outputs.

6.2 Model order reduction of heat conduction problem in PV module

A 2D thermal model of a PV module is proposed here based on the work by Jones [79]. We consider a PV module containing 12 silicon cells embedded in a

composite made of glass, EVA, Silicon, EVA, backsheet and tedlar layers with the properties described in Table 6.1 [80]. Although solar cells are separated from each other by a small amount of EVA in their plane, in this work, a slightly simplified structure is considered by assuming all layers as uniform in the x and y directions, see Fig. 6.1. Further, it is considered that the y direction is infinite.

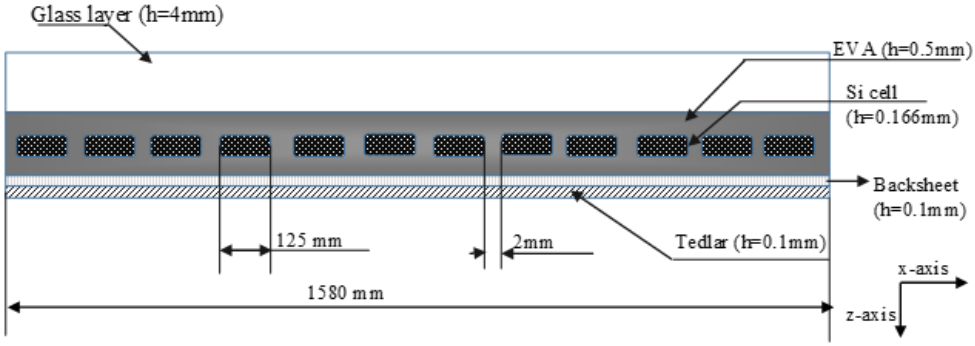

Figure 6.1. A sketch of a cross-section of a PV module, not in scale. For the actual value of the thicknesses, see the labels in the figure.

6.2.1 Formulation of the thermal problem and finite difference approximation

Under the above assumptions in Sec. 6.1, the following general 2D heat equation for the composite PV panel holds:

$$C\frac{\partial T}{\partial t} = \lambda_x \frac{\partial^2 T}{\partial x^2} + \lambda_z \frac{\partial^2 T}{\partial z^2} + H - G \qquad (6.1)$$

where $T\ (x, z, t)$ represents the space and time dependent temperature profile of the module. $C\ (x, z)$ is an equivalent volumetric heat capacity (J/m^{3}K), which is equal to an equivalent mass density times the equivalent specific heat capacity (C =$\rho . c_p$). The function $H\ (x, z, t)$ represents the heat losses by radiation and convection taking place at any place within the PV module, and $G(x, z, t)$ is the electrical

energy generated by the cell layer. The coefficients $\lambda_x(x,z)$ and $\lambda_z(x,z)$ are the thermal conductivities in the x and z directions respectively. According to Fourier's law of heat conduction, the heat flows in the x and z direction are related to these thermal conductivities by:

$$q_z = -\lambda_z \frac{\partial T}{\partial z} \quad , \quad q_x = -\lambda_x \frac{\partial T}{\partial x} \tag{6.2}$$

Substituting (6.2) into (6.1) gives:

$$C \frac{\partial T}{\partial t} = -\frac{\partial q_x}{\partial x} - \frac{\partial q_z}{\partial z} + H - G \tag{6.3}$$

Using now a finite difference (FD) discretization scheme defined by grid spacing Δx_i and Δz_j in the x and z-direction, respectively, with associated discretization indices i for $1 \leq i \leq l$ and j for $1 \leq j \leq s$ (see Fig. 6.2), Eq. (6.3) can be rephrased as:

$$C_{i,j} \frac{dT_{i,j}}{dt} = \frac{q_{i-\frac{1}{2},j} - q_{i+\frac{1}{2},j}}{\Delta x_i} + \frac{q_{i,j-\frac{1}{2}} - q_{i,j+\frac{1}{2}}}{\Delta z_j} + H_{i,j} - G_{i,j} \tag{6.4}$$

Table 6.1. Material properties of the layers of the PV module [80].

Layer	**Thickness** (mm)	**Thermal conductivity** (W/m^{o}K)	**Density** (Kg/m^3)	**Specific heat capacity** (J/Kg^{o}K)
Glass	4	1.8	3000	500
EVA	0.5	0.35	960	2090
PV Cells	0.166	148	2330	677
EVA	0.5	0.35	960	2090
Back contact	0.1	237	2700	900
Tedlar	0.1	0.2	1200	1250

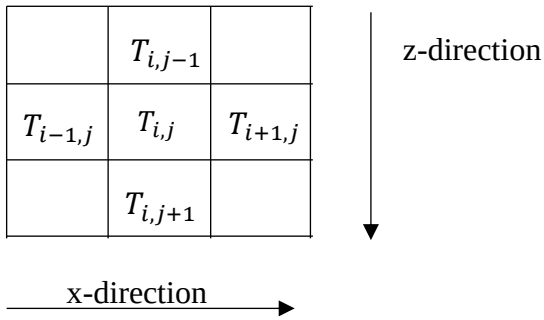

Figure 6.2. Finite difference discretization of the PV module in its plane.

where $q_{i-\frac{1}{2},j}$ and $q_{i+\frac{1}{2},j}$ are the heat flows through the left and right boundaries of element (i,j), and $q_{i,j-\frac{1}{2}}$ and $q_{i,j+\frac{1}{2}}$ are the heat flows through the upper and lower boundaries of the element in its plane. Multiplying (6.4) by the area $A_{i,j} = \Delta x_i \Delta z_j$of each grid element in the FD discretization leads to:

$$C_{i,j}A_{i,j}\frac{\partial T_{i,j}}{\partial t} = Q_{i-\frac{1}{2},j} - Q_{i+\frac{1}{2},j} + Q_{i,j-\frac{1}{2}} - Q_{i,j+\frac{1}{2}} + A_{i,j}H_{i,j} - A_{i,j}G_{i,j} \qquad (6.5)$$

where Q represents, consistently with energy conservation principles, the heat flow between adjacent cells, which can be further expressed as $Q = K\Delta T$ [80], where ΔT is the temperature change between the two cells, and K is the corresponding thermal conductance. The latter is a function of the equivalent thermal conductivities of the two cells and the width and length of the elements, i.e. Δz_j and Δx_i.

6.2.2 Thermal conductances and heat flows

The discretized thermal conductances $K_{i,j}$ (W/mK) provide information on the thermal coupling between the elements in the discretization of the PV module. Assuming perfect bonding at the various interfaces between the layers, the thermal conductance per unit length in the x-direction between cells $(i-1,j)$ and (i,j) is given by [16, 81]:

$$K_{i-\frac{1}{2},j} = \frac{\Delta z_j}{\Delta x_{i-1}/2\lambda_{x\,i-1,j} + \Delta x_i/2\lambda_{x\,i,j} + R_{i-\frac{1}{2},j}} \tag{6.6}$$

where R is the thermal resistance at the interface between the elements. Since in the present approximation, the PV layers are uniform in the x-direction, the thermal conductivity λ_x does not change in the x direction and we have $R_{i-\frac{1}{2},j} = 0$ and notation can be simplified as $\lambda_{x\,i-1,j} = \lambda_{x\,i,j} = \lambda_j$. This assumption is still reasonable for the silicon cell layer, since the cells are separated from each other by a small amount of EVA (2mm), much smaller than the lateral size of each silicon cell (125mm). Grid spacing Δx is also considered to be constant in the x direction. Therefore, Eq. (6.6) becomes:

$$K_{i-\frac{1}{2},j} = \frac{\Delta z_j}{\Delta x/2\lambda_j + \Delta x/2\lambda_j} = \lambda_j \frac{\Delta z_j}{\Delta x} \tag{6.7}$$

and $K_{i-\frac{1}{2},j} = K_{i+\frac{1}{2},j} = K_j$ due to material homogeneity in the x-direction.

In the z-direction,

$$K_{j-\frac{1}{2}} = \frac{\Delta x}{\Delta z_{j-1}/2\lambda_{z\,j-1} + \Delta z_j/2\lambda_{z\,j} + R_{j-\frac{1}{2}}} \tag{6.8}$$

$$K_{j+\frac{1}{2}} = \frac{\Delta x}{\Delta z_{j+1}/2\lambda_{z\,j+1} + \Delta z_j/2\lambda_{z\,j} + R_{j+\frac{1}{2}}}$$

and at the top and bottom boundary elements of the PV module, $(i, 1)$ and (i, s),

$$K_{\frac{1}{2}} = \frac{\Delta x}{\Delta z_1/2\lambda_{z\,1} + R_{\frac{1}{2}}} \tag{6.9}$$

$$K_{s-\frac{1}{2}} = \frac{\Delta x}{\Delta z_s/2\lambda_{z\,s} + R_{s-\frac{1}{2}}} \tag{6.10}$$

where $R_{\frac{1}{2}}$ and $R_{s-\frac{1}{2}}$ are the thermal resistances between the top and bottom elements and the free surfaces.

From Eq. (6.5), the heat flows through the left and the right boundaries of the element (i, j) are thus defined as:

$$Q_{i-\frac{1}{2},j} = K_j(T_{i-1,j} - T_{i,j}) \tag{6.11}$$

$$Q_{i+\frac{1}{2},j} = K_j(T_{i,j} - T_{i+1,j}) \tag{6.12}$$

whereas the heat flows through the lower and upper boundary of the element (i, j) are:

$$Q_{i,j-\frac{1}{2}} = K_{j-\frac{1}{2}}(T_{i,j-1} - T_{i,j}) \tag{6.13}$$

$$Q_{i,j+\frac{1}{2}} = K_{j+\frac{1}{2}}(T_{i,j} - T_{i,j+1}) \tag{6.14}$$

6.2.3 Boundary conditions

In this study, a constant (Dirichlet) temperature is applied to the right and left boundary of the module. Thus, the heat flow at the left and right boundary elements of the PV module $(1, j)$ and (l, j) are:

$$Q_{\frac{1}{2},j} = K_j(T_{b1} - T_{1,j}) \quad (6.15)$$

$$Q_{l-\frac{1}{2},j} = K_j(T_{l,j} - T_{b2}) \quad (6.16)$$

Where T_{b1} and T_{b2} are the fixed temperatures imposed at the right and left of the module. In all subsequent simulations, the boundary temperature value will set equal to 343 K and 313 K in order to simulate a distinct differential temperature profile from one end of the PV module to the other.

The heat flow at the top and bottom boundary elements of the PV module $(i, 1)$ and (i, s) are instead:

$$Q_{i,\frac{1}{2}} = K_{\frac{1}{2}}(T_{sky} - T_{i,1}) \quad (6.17)$$

$$Q_{i,s-\frac{1}{2}} = K_{s-\frac{1}{2}}(T_{i,s} - T_{sky}) \quad (6.18)$$

where T_{sky} is the temperature of the sky.

6.2.4 Heat loss

The heat loss, which varies through the layer thickness of the module, is given by the sum of the following contributions [79]:

$$H(x, z, t) = q_{lw}(x, z, t) + q_{sw}(x, z, t) + q_{conv}(x, z, t) \quad (6.19)$$

where the short wave, long wave and convection heat transfers are denoted by q_{sw}, q_{lw} and q_{conv} respectively.

The short wave radiation heat transfer of a body of area A is given by:

$$q_{sw} = A\alpha\Phi \quad (6.20)$$

where α and Φ are the absorptivity of the material and the total incident irradiance input to the module surface, respectively. The long wave radiation heat transfer is given by the Stefan Boltzmann law:

$$q_{lw} = \sigma \varepsilon T^4 \tag{6.21}$$

where σ is the Boltzmann's constant (5.607×10^{-8} $Js^{-1}m^{-2}K^{-4}$) and ε is the emissivity of the body. It is assumed that the net long wave exchange is negligible for the rear of the module. Thus, it is only necessary to calculate the long wave exchange from the surface of the module. The net long wave radiation exchange between two surfaces x and y is given by [79]:

$$q_{lw_{xy}} = A_x F_{xy}\left(L_x - L_y\right) = A_y F_{xy}(L_y - L_x) \tag{6.22}$$

Here L_x and L_y are long wave irradiance per unit area for surface x and y respectively which are given by:

$L_x = \sigma \varepsilon_x {T_x}^4$ and $L_y = \sigma\ \varepsilon_y {T_y}^4$

where F_{xy} is the view factor, a fraction of the radiation leaving surface x that reaches surface y.

A tilted module surface not overlooked by adjacent buildings at an angle θ from the horizontal has a view factor of $\frac{(1+\cos\theta)}{2}$ for the sky and $\frac{(1-\cos\theta)}{2}$ for the horizontal ground [79]. Thus, inserting the view factor coefficient for sky and ground into L_x leads to:

$$L_x = \sigma \frac{(1+\cos\theta)}{2} \varepsilon_{sky} {T_{sky}}^4 + \sigma \frac{(1-\cos\theta)}{2} \varepsilon_{ground} {T_{ground}}^4 \tag{6.23}$$

$$L_y = \sigma \varepsilon_{mod} T^4 \tag{6.24}$$

where ε_{mod} is the module emissivity.

Substituting Eqs. (6.23) and (6.24) into (6.22) produces:

$$q_{lw} = A\sigma\left(\frac{(1+\cos\theta)}{2}\varepsilon_{sky}{T_{sky}}^4 + \frac{(1-\cos\theta)}{2}\varepsilon_{ground}{T_{ground}}^4 - \varepsilon_{mod}T^4\right) \quad (6.25)$$

Further, $T_{sky} = T_{ambient} - \delta T$ for clear sky condition in which $\delta T = 20$K and $T_{sky} = T_{ambient}$ for overcast condition.

The convection heat transfer is related to the temperature gap between the upper part of the solar panel and the ambient [79]:

$$q_{conv} = -A\big(h_{c,forced} + h_{c,free}\big)(T - T_{ambient}) \quad (6.26)$$

where $h_{c,forced}$ and $h_{c,free}$ in W/m^2 K are the forced and free convection heat transfer coefficients which depend on the wind speed.

Collecting all the heat loss contributions together now leads to:

$$H_{i,j} = A_{i,j}[\alpha_{i,j}\Phi + \sigma\left(\frac{(1+\cos\theta)}{2}\varepsilon_{sky}{T_{sky}}^4 + \frac{(1-\cos\theta)}{2}\varepsilon_{ground}{T_{ground}}^4 - \varepsilon_{i,j}{T_{i,j}}^4\right) - \big(h_{c,forced} + h_{c,free}\big)\big({T_{i,j}}^4 - T_{ambient}\big)] \quad (6.27)$$

where $\alpha_{i,j}$ and $\varepsilon_{i,j}$ denote the absorptivity and emissivity coefficients of the discretized cells in the different layers.

6.2.5 Power generated by the PV Cell

The power generated by the PV cell at location (i,j) can be estimated as [79]:

$$G_{i,j} = C_{FF}\frac{E\ ln(\gamma E)}{T_{i,j}} \quad (6.28)$$

where C_{FF} is the fill factor model constant (1.22 K m^2) and $E(t)$ in W/m^2 is the incident irradiance input through the thickness of the PV module. The constant γ is equal to 10^6 m^2/W. It should be noted that the power generated by the discretized PV cells in (6.28) is non-zero only for the silicon cell layer.

The incident irradiance input into the system is obtained from experimental data [79]. To obtain a validated result of the reduced order model to be derived in Sec. 6.2, a minute by minute irradiance input obtained from the solar resource and meteorological assessment project website (http://www.nrel.gov/midc/kalaeloa_oahu/) will be used. The plots for irradiance for a period of 30 minutes are shown below in Fig. 6.3.

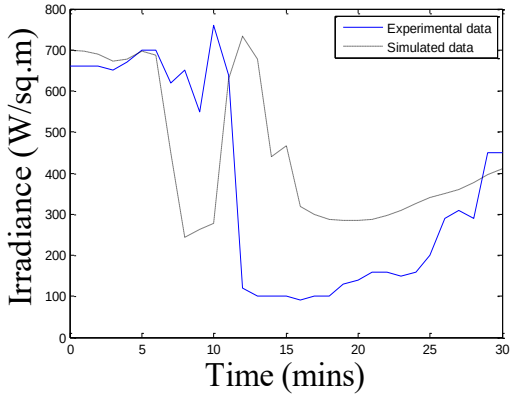

Figure 6.3. Experimental and simulated irradiance input (from 09:52-10:22, 11/01/2011)

6.2.6 System of nonlinear ODEs for the PV module

Considering all the relations established so far in Sec. 6.2, the discretized thermal equation (6.5) can be rewritten after substituting the corresponding expressions for Q, H and G as:

$$C_{i,j}A_{i,j}\frac{\partial T_{i,j}}{\partial t} - K_j T_{i+1,j} - K_j T_{i-1,j} + T_{i,j}\left(2K_j + K_{i,j+\frac{1}{2}} + K_{i,j-\frac{1}{2}}\right) - K_{j+\frac{1}{2}}T_{i,j+1} - K_{j-\frac{1}{2}}T_{i,j-1} - A_{i,j}[\alpha_{i,j}\Phi + \sigma\left(\frac{(1+\cos\theta)}{2}\varepsilon_{sky}{T_{sky}}^4 + \frac{(1-\cos\theta)}{2}\varepsilon_{ground}{T_{ground}}^4 - \varepsilon_{i,j}{T_{i,j}}^4\right) - \left(h_{c,forced} + h_{c,free}\right)\left(T_{i,j} - T_{ambient}\right)] = -A_{i,j}C_{FF}\frac{E\,ln(aE)}{T_{i,j}} \quad (6.29)$$

At the left and right boundaries of the PV module, $Q_{i-\frac{1}{2},j}$ and $Q_{i+\frac{1}{2},j}$ from (6.5) are replaced by $Q_{\frac{1}{2},j}$ and $Q_{l-\frac{1}{2},j}$ respectively from Eq. (6.15) and Eq. (6.16), while at the top and bottom boundaries of the PV module, $Q_{i,j-\frac{1}{2}}$ and $Q_{i,j+\frac{1}{2}}$ are replaced by $Q_{i,\frac{1}{2}}$ and $Q_{i,s-\frac{1}{2}}$ respectively from Eq. (6.17) and Eq. (6.18).

The discretized thermal equation (6.29) can finally be written in a compact matrix form:

$$\boldsymbol{CA}\frac{d\boldsymbol{T}(t)}{dt} = \bar{\boldsymbol{K}}\boldsymbol{T}(t) + \boldsymbol{AI}(\boldsymbol{T}(t), E(t)) \quad (6.30)$$

or, in explicit form, as

$$\frac{d\boldsymbol{T}(t)}{dt} = \underbrace{\boldsymbol{K}\boldsymbol{T}(t)}_{\text{linear term}} + \underbrace{\boldsymbol{F}(\boldsymbol{T}(t), E(t))}_{\text{Non-linear term}} \quad (6.31)$$

where $\boldsymbol{K} = (\boldsymbol{CA})^{-1}.(\bar{\boldsymbol{K}})$ and $\boldsymbol{F} = \boldsymbol{C}^{-1}\boldsymbol{I}$. The independent variable $t \in [0, h]$ denotes time, and $\boldsymbol{T}(t) = [T_1(t), \ldots., T_n(t)]^T \in \mathbb{R}^n$ is the unknown temperature vector for all the cells in the FD discretization, where we use a single subscript with *n* denoting the total number of nodes. $E(t)$ is the time-varying irradiance input to the system, the matrix $\boldsymbol{K} \in \mathbb{R}^{n\times n}$ contains constants and $\boldsymbol{F}(\boldsymbol{T}(t), E(t))$ is a nonlinear function evaluated at $\boldsymbol{T}(t)$ component-wise i.e.

$$\boldsymbol{F} = [F_1, \ldots., F_n]^T \quad (6.32)$$

6.2.7 Reference solution for the complete thermal system

Before applying the proposed model order reduction approach, a reference solution is derived for Eq. (6.31) by direct time discretization. A backward Euler finite difference scheme is selected to solve the thermal problem to avoid any convergence issues associated with explicit methods in terms of choice of time step. The numerical method is implemented in Matlab software. A uniform discretization of the module in the x-direction is adopted with l=361 grid points, while there are s=6 strips in the z-direction with different thicknesses so that $n = s \times l = 2166$. The solution of this problem is performed for n_s=186 time steps, each step representing 10 s of physical time. Figure 6.4(a) shows the temperature profile for node 741 in the silicon layer for all the 186 time steps. The temperature along the silicon layer vs. position at the last time step is shown in Fig. 6.4(b). As it can be seen, the transient regime is quite evident and the temperature in the silicon cell layers is significantly different from cell to cell.

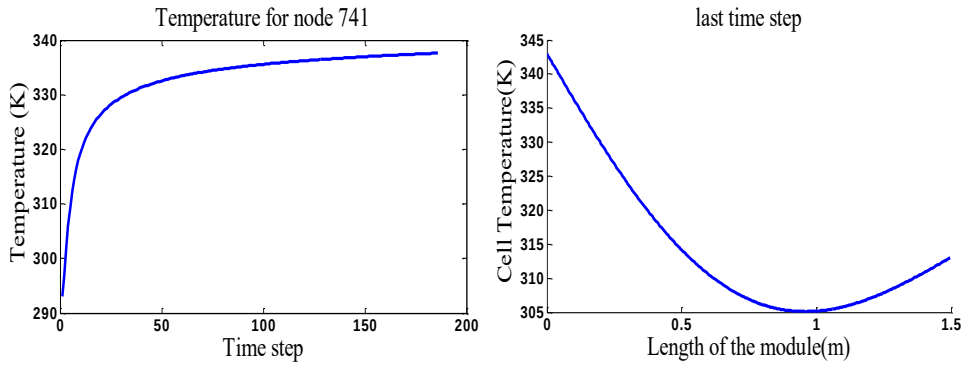

(a) (b)

Figure 6.4. Temperature profile of the full system for (a) a node within the silicon layer vs. time step and (b) along the silicon layer at the last time step of the simulation.

6.3 Model order reduction of thermal system via POD/DEIM

The direct numerical simulation of Eq. (6.31) may be quite demanding in terms of computing resources, especially in view of its extension to a full 3D geometry. For this reason, a MOR technique is investigated in this section, with the objective of approximating the large-scale system (6.31) with a lower order compact dynamical model, that is able however to preserve accuracy in its input/output transient response. The two key aspects of proposed MOR approach are: i) a massive reduction in the degrees of freedom (states), and ii) an accurate representation of the nonlinear terms that influence the heat exchange of the structure. These two aspects are analysed in detail subsequently.

6.3.1 System projection

The reduction in the degrees of freedom is here performed through a standard projection approach. The vector $\boldsymbol{T}$ collecting all n cell temperatures is approximated as a linear superposition of a small number of k "basis vectors", which span a reduced order subspace. More precisely, lets consider the representation $\boldsymbol{T} \approx \boldsymbol{V}_k \widetilde{\boldsymbol{T}}$ **,** where $\widetilde{\boldsymbol{T}} \in \mathbb{R}^k$ is a reduced temperature vector collecting the coefficients of $\boldsymbol{T}$ into a reduced basis, defined by the columns of matrix $\boldsymbol{V}_k \in \mathbb{R}^{n\times k}$**.** An orthonormal basis is considered, so that $\boldsymbol{V}_k{}^{\boldsymbol{T}}\boldsymbol{V}_k = \mathbb{I} \in \mathbb{R}^{k\times k}$ $(k \ll n)$ with $\mathbb{I}$ an identity matrix. Introducing the above reduced expression for $\boldsymbol{T}$ into (6.31), we have:

$$\boldsymbol{V}_k \frac{d\widetilde{\boldsymbol{T}}(t)}{dt} \approx \boldsymbol{K}\boldsymbol{V}_k\widetilde{\boldsymbol{T}}(t) + \boldsymbol{F}(\boldsymbol{V}_k\widetilde{\boldsymbol{T}}(t), E(t)) \tag{6.33}$$

Projecting now these equations onto the subspace generated by $\boldsymbol{V}_k$ leads to:

$$\frac{d\widetilde{\boldsymbol{T}}(t)}{dt} \approx \underbrace{\boldsymbol{V}_k{}^T\boldsymbol{K}\boldsymbol{V}_k}\,\widetilde{\boldsymbol{T}}(t) + \boldsymbol{V}_k{}^T\boldsymbol{F}(\boldsymbol{V}_k\widetilde{\boldsymbol{T}}(t), E(t))$$

with $\boldsymbol{V}_k{}^T \boldsymbol{K} \boldsymbol{V}_k = \widetilde{\boldsymbol{K}}$ and where $\widetilde{\boldsymbol{K}} \in \mathbb{R}^{k \times k}$

The reduced form of the thermal equation (6.31) reads:

$$\frac{d\widetilde{\boldsymbol{T}}(t)}{dt} = \widetilde{\boldsymbol{K}}\widetilde{\boldsymbol{T}}(t) + \boldsymbol{V}_k{}^T \boldsymbol{F}\left(\boldsymbol{V}_k \widetilde{\boldsymbol{T}}(t),\ E(t)\right) \tag{6.34}$$

The above system represents a reduced order model, since its main variables are the coefficients of a reduced basis. In order to determine $\boldsymbol{V}_k$, a Proper Orthogonal Decomposition (POD) is considered, which extracts the basis vectors from the actual transient solution of the full system by means of a truncated singular value decomposition. In particular, a collection of n_s snapshots $\boldsymbol{T}(t_h)$ is performed which is obtained from the full solution of the system at discrete time steps of size h in the following snapshot matrix:

$$\boldsymbol{S} = [\boldsymbol{T}(t_1), \ldots\ldots, \boldsymbol{T}(t_{ns})] \tag{6.35}$$

and the POD algorithm is applied as follows:

Algorithm 6.1

INPUT: $\boldsymbol{S} = [\boldsymbol{T}(t_1), \ldots\ldots, \boldsymbol{T}(t_{ns})] \subset \mathbb{R}^{n \times ns}$

OUTPUT: $\boldsymbol{V}_k = [\boldsymbol{v_1}, \ldots\ldots, v_k] \in \mathbb{R}^{\boldsymbol{n} \times \boldsymbol{k}}$

1. Form the shapshot matrix $\boldsymbol{S} = \{\boldsymbol{T}(t_1), \ldots\ldots, \boldsymbol{T}(t_{ns})\}$
2. Perform the singular value decomposition $\boldsymbol{T} = \boldsymbol{V}\boldsymbol{\Sigma}\boldsymbol{W}^T$ to produce orthogonal matrices $\boldsymbol{V} = [\boldsymbol{v_1}, \ldots\ldots, \boldsymbol{v_r}] \in \mathbb{R}^{\boldsymbol{n} \times \boldsymbol{r}}$ and $\boldsymbol{W} = [\boldsymbol{w}_1, \ldots\ldots \boldsymbol{w}_r] \in \mathbb{R}^{n_s \times r}$ and diagonal matrix $\boldsymbol{\Sigma} = \text{diag}\,(\sigma_1, \ldots\ldots, \sigma_r) \in \mathbb{R}^{\boldsymbol{r} \times \boldsymbol{r}}$ where r is the rank of $\boldsymbol{S}$.
3. Set a threshold to pick the k highest modes from the diagonal matrix $\boldsymbol{\Sigma}$
4. Pick the columns in matrix $\boldsymbol{V}$ which correspond to the modes selected in 3 to generate the POD basis $\boldsymbol{V}_k = [\boldsymbol{v}_1, \ldots\ldots, \boldsymbol{v}_k] \in \mathbb{R}^{n \times k}$

Note that in the present case we choose $n_s = 186$, as the total number of time steps in the full solution. The choice of n_s should be carefully considered since it can strongly influence the accuracy of the approximation and the computational cost, as shown later.

6.3.2 Discrete Empirical Interpolation Method (DEIM)

System (6.34) is a reduced order model, but the evaluation of the nonlinear term still requires the mapping $\boldsymbol{V}_k$ to the full-size space. The DEIM approach is used here to further approximate the nonlinear terms, thus reducing the computational cost associated with the simulation of the reduced model. According to [54], the nonlinear term of (6.34) can be written in the form:

$$\boldsymbol{N}(\widetilde{\boldsymbol{T}}) = \underbrace{\boldsymbol{V_k}^T}_{k\times n}\underbrace{\boldsymbol{F}\big(\boldsymbol{V_k}\widetilde{\boldsymbol{T}}(t), E(t)\big)}_{n\times 1} \tag{6.36}$$

and define the nonlinear term as:

$$\boldsymbol{f}(t) = \boldsymbol{F}\big(\boldsymbol{V_k}\widetilde{\boldsymbol{T}}(t), E(t)\big) \tag{6.37}$$

The basic idea is to approximate $\boldsymbol{f}(t)$ by projecting it onto the subspace spanned by a suitable set of $m \ll n$ basis vectors $\mathbf{u}_1, \ldots, \mathbf{u}_m$ via

$$\boldsymbol{f}(t) \approx \mathbf{U}\mathbf{c}(\mathrm{t}) \tag{6.38}$$

where $\mathbf{U} = [\mathbf{u}_1, \ldots, \mathbf{u}_m] \in \mathbb{R}^{n\times m}$. The corresponding coefficient vector $\mathbf{c}(\mathrm{t})$ is determined by selecting m significant rows from the overdetermined system (6.38). This can be achieved by considering the mapping matrix:

$$\mathbf{P} = [\mathbf{e}_{\varrho_1}, \ldots, \mathbf{e}_{\varrho_m}] \in \mathbb{R}^{n\times m} \tag{6.39}$$

Where $\mathbf{e}_{\varrho_i} = [0, \ldots, 0, 1, 0, \ldots, 0]^{\boldsymbol{T}} \in \mathbb{R}^n$ is the ϱ_ith column of the identity matrix $\mathbb{I} \in \mathbb{R}^{n \times n}$ for $i = 1, \ldots, m$. The coefficient $\mathbf{c}(t)$ can thus be determined by inverting system:

$$\mathbf{P}^{\mathbf{T}}\boldsymbol{f}(t) = (\mathbf{P}^{\mathbf{T}}\mathbf{U})\mathbf{c}(t) \tag{6.40}$$

Provided $\mathbf{P}^{\mathbf{T}}\mathbf{U}$ is non-singular, the final approximation of (6.38) is:

$$\boldsymbol{f}(t) \approx \mathbf{U}\mathbf{c}(t) = \mathbf{U}(\mathbf{P}^{\mathbf{T}}\mathbf{U})^{-\mathbf{1}}\mathbf{P}^{\mathbf{T}}\boldsymbol{f}(t) \tag{6.41}$$

Since $\boldsymbol{f}(t) = \boldsymbol{F}\big(\boldsymbol{V_k}\widetilde{\boldsymbol{T}}(t), E(t)\big)$, Eq. (6.41) can thus be written as:

$$\boldsymbol{F}\big(\boldsymbol{V_k}\widetilde{\boldsymbol{T}}(t), E(t)\big) \approx \mathbf{U}(\mathbf{P}^{\mathbf{T}}\mathbf{U})^{-\mathbf{1}}\mathbf{P}^{\mathbf{T}}\boldsymbol{F}\big(\boldsymbol{V_k}\widetilde{\boldsymbol{T}}(t), E(t)\big) \tag{6.42}$$

Eq. (6.42) ensures that the nonlinear function $\boldsymbol{F}$ is evaluated for the full system and then interpolated by matrix $\mathbf{P}$, an operation which still shows the dependence of the reduced system on the complete system size. To avoid this dependence, DEIM interpolates the input vector of the nonlinear function $\boldsymbol{F}$ and then evaluates $\boldsymbol{F}$ component-wise at its interpolated input vector. Based on this, (6.42) can be written as:

$$\boldsymbol{F}\big(\boldsymbol{V_k}\widetilde{\boldsymbol{T}}(t)E(t)\big) \approx \mathbf{U}(\mathbf{P}^{\mathbf{T}}\mathbf{U})^{-\mathbf{1}}\widetilde{\boldsymbol{F}}\big(\mathbf{P}^{\mathbf{T}}\boldsymbol{V_k}\widetilde{\boldsymbol{T}}(t), E(t)\big) \tag{6.43}$$

Where $\widetilde{\boldsymbol{F}}$ denotes the selected components of $\boldsymbol{F}$.This approximation is particularly effective when the full nonlinear function $\boldsymbol{F}$ is evaluated independently for each component of its vector argument, as in present FD formulation. The nonlinear term in Eq. (6.36) can now be represented as:

$$\boldsymbol{N}\big(\widetilde{\boldsymbol{T}}(t)\big) = \underbrace{\boldsymbol{V_k}^{T}\mathbf{U}(\mathbf{P}^{\mathbf{T}}\mathbf{U})^{-\mathbf{1}}}_{k \times m}\ \underbrace{\widetilde{\boldsymbol{F}}\big(\mathbf{P}^{\mathbf{T}}\boldsymbol{V_k}\widetilde{\boldsymbol{T}}(t), E(t)\big)}_{m \times 1} \tag{6.44}$$

Now, to evaluate $\boldsymbol{N}\big(\widetilde{\boldsymbol{T}}\big)$ in (6.44), we must specify the projection basis $[\mathbf{u}_1, \ldots, \mathbf{u}_m]$ and the interpolation indices$[\boldsymbol{\varrho}_1, \ldots, \boldsymbol{\varrho}_m]$. We can obtain the basis $[\mathbf{u}_1, \ldots, \mathbf{u}_m]$ by applying the above described POD scheme to the matrix collecting the nonlinear snapshots $\boldsymbol{F} = \{F\big(\boldsymbol{T}(t_1)\big), \ldots, F\big(\boldsymbol{T}(t_{ns})\big)\}$ resulting from a direct evaluation of the nonlinear function of the full system at different time steps, and then using the

DEIM algorithm described in [66]. The following implementation is used to iteratively construct the basis vectors and the set of interpolation indices.

Algorithm 6.2

INPUT: $\{\boldsymbol{u_i}\}_{i=1}^{m} \subset \mathbb{R}^n$ linearly independent

OUTPUT: $\vec{\boldsymbol{\varrho}} = [\,\boldsymbol{\varrho}_1, \ldots., \boldsymbol{\varrho}_m] \in \mathbb{R}^m$

1. $[|\boldsymbol{\rho}|, \boldsymbol{\varrho_1}] = \mathbf{max}\{|\mathbf{u}_1|\}$
2. $\mathbf{U} = |\mathbf{u}_1|$, $\mathbf{P} = \left[\mathbf{e}_{\boldsymbol{\varrho_1}}\right]$, $\vec{\boldsymbol{\varrho}} = [\,\boldsymbol{\varrho_1}]$
3. **for** $i = 2$ to m do
4. Solve $(\mathbf{P^T U})\mathbf{c} = \mathbf{P^T}\boldsymbol{u_i}$ for $\mathbf{c}$
5. $\mathbf{r} = \boldsymbol{u_i} - \mathbf{Uc}$
6. $[|\boldsymbol{\rho}|, \boldsymbol{\varrho_i}] = \mathbf{max}\{|\mathbf{r}|\}$
7. $\mathbf{U} \leftarrow [\mathbf{U}\ \boldsymbol{u_i}]$, $\mathbf{P} = \left[\mathbf{P}\ \mathbf{e}_{\boldsymbol{\varrho_i}}\right]$, $\vec{\boldsymbol{\varrho}} = \begin{bmatrix} \vec{\varrho} \\ \boldsymbol{\varrho_i} \end{bmatrix}$

end for

6.3.3 Modification of DEIM formulation

To control the accuracy of the reduced system more efficiently, it is noticed that: i) there are two nonlinear terms with different characteristics in the thermal formulation of the PV module, and that ii) these two terms influence different layers of the PV module. In fact, since it is assumed that the net long wave exchange for the rear of the module is negligible (see Sec. 6.1.4), the heat loss term in the thermal system formulation has most impact on the surface of the PV module. On the other hand, the power output is generated only by the silicon cell (third layer). On this note, the DEIM operation is here performed separately for the two

nonlinear terms using two different sets of snapshots. Accordingly, Eq. (6.43) is respectively expressed for the two nonlinear terms in the reduced system as:

$$\boldsymbol{F_1}\left(\boldsymbol{V_k}\widetilde{\boldsymbol{T}}(t), E(t)\right) \approx \mathbf{U_1}(\mathbf{P_1}^{\mathbf{T}}\mathbf{U_1})^{-1}\widetilde{\boldsymbol{F}}_{\mathbf{1}}\left(\mathbf{P_1}^{\mathbf{T}}\boldsymbol{V_k}\widetilde{\boldsymbol{T}}(t), E(t)\right) \tag{6.45}$$

$$\boldsymbol{F_2}\left(\boldsymbol{V_k}\widetilde{\boldsymbol{T}}(t), E(t)\right) \approx \mathbf{U_2}(\mathbf{P_2}^{\mathbf{T}}\mathbf{U_2})^{-1}\widetilde{\boldsymbol{F}}_{\mathbf{2}}\left(\mathbf{P_2}^{\mathbf{T}}\boldsymbol{V_k}\widetilde{\boldsymbol{T}}(t), E(t)\right) \tag{6.46}$$

Finally, the nonlinear term in (6.36) can now be represented as:

$$\boldsymbol{N}(\widetilde{\boldsymbol{T}}) = \underbrace{\boldsymbol{V_k}^{T}\mathbf{U_1}(\mathbf{P_1}^{\mathbf{T}}\mathbf{U_1})^{-1}}_{k\times m_1}\underbrace{\widetilde{\boldsymbol{F}}_{\mathbf{1}}\left(\mathbf{P_1}^{\mathbf{T}}\boldsymbol{V_k}\widetilde{\boldsymbol{T}}(t)E(t)\right)}_{m_1\times 1} + \underbrace{\boldsymbol{V_k}^{T}\mathbf{U_2}(\mathbf{P_2}^{\mathbf{T}}\mathbf{U_2})^{-1}}_{k\times m_2}\underbrace{\widetilde{\boldsymbol{F}}_{\mathbf{2}}\left(\mathbf{P_2}^{\mathbf{T}}\boldsymbol{V_k}\widetilde{\boldsymbol{T}}(t), E(t)\right)}_{m_2\times 1} \tag{6.47}$$

With this modification, the interpolation of the nonlinear terms can be handled independently, enabling a finer control on reduced system complexity and efficiency.

6.4 Numerical results of thermal system modelling

In this section, the accuracy of the proposed reduced modelling scheme is assessed by comparing the responses of the compact model and the original system. In particular, investigation of the convergence of the reduced system is performed as a function of the three parameters that measure its complexity, namely the size k of the reduced basis used in the state-space (linear) projection, and the two orders m_1, m_2 of the nonlinear interpolations.

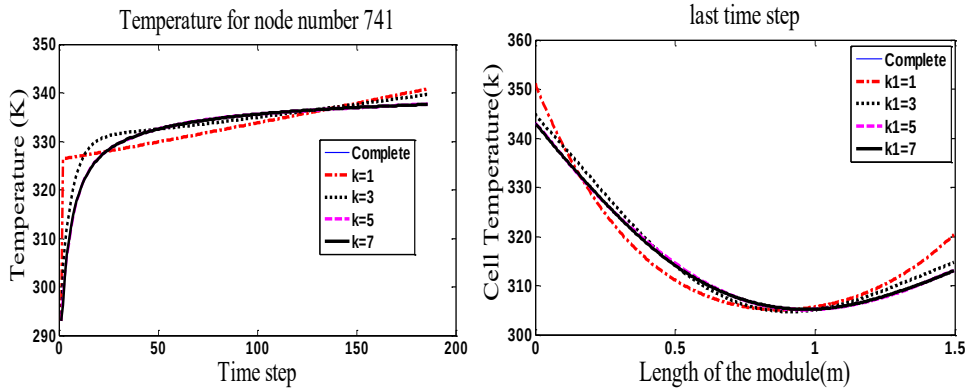

(a) (b)

Figure 6.5. Convergence of reduced solution to the full solution with increasing order of k and fixed interpolation points $m_1=m_2=3$ for (a) a specific point in the silicon layer, and (b) for the entire silicon layer.

As shown in Fig. 6.5, the cell temperatures at the last time step of the iterative solution of the full system and of the reduced system are in fair good agreement by increasing the order k of the reduced system. As the order of the reduced system increases from k=1 to k=7, the approximation of the reduced system approaches the exact value of the complete system. At k=7, the reduced system approximation fits well the complete system such that further increasing the order of the reduced system does not change the result significantly.

It is noticed that the number of snapshots n_s used to construct the compact model also affects its convergence to the full solution. Convergence is achieved more efficiently using a high number of samples in the snapshots matrix $\boldsymbol{S}$ than using a small number of samples. The plots in Fig. 6.6 illustrate the convergence of the reduced solution using 185, 100, 70 and 40 snapshots while fixing the order of k = 7 and interpolation order $m_1=m_2=5$.

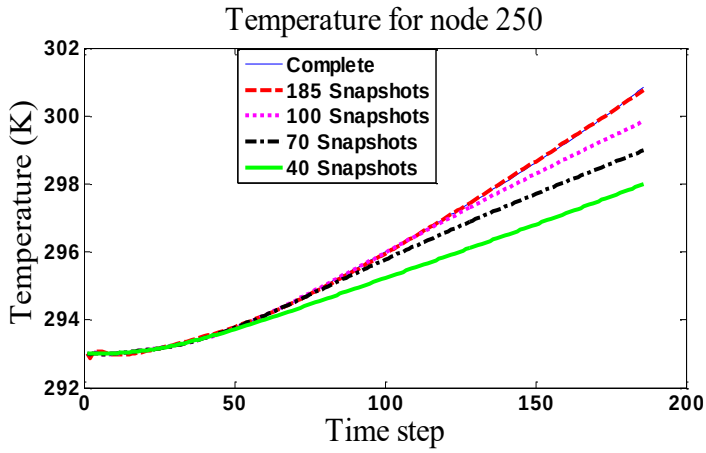

Figure 6.6. Convergence of the reduced solution by increasing the number of snapshots for order of basis k=7 and interpolation points with m_1=m_2 = 5.

6.4.1 Validation of the reduced model using simulated irradiance data

In this section, investigation of the sensitivity of the reduced model to the input irradiance signal is performed. To this end, the reduced model is first constructed based on snapshots derived from experimental irradiance data, see Fig. 6.3. Then, simulated irradiance data is used to excite the model, and the corresponding response is compared to the full system response computed by direct time discretization. The irradiance data for this validation was carefully selected to have different environmental characteristics with the identification experimental data. On this basis, a day is chosen in autumn of November, 2011 with average air temperature of 22^{o}C and average wind speed of 3 m/s. It is verified that the reduced model approximates the full system to a reasonable degree of accuracy also under this different excitation, as shown in Fig. 6.7.

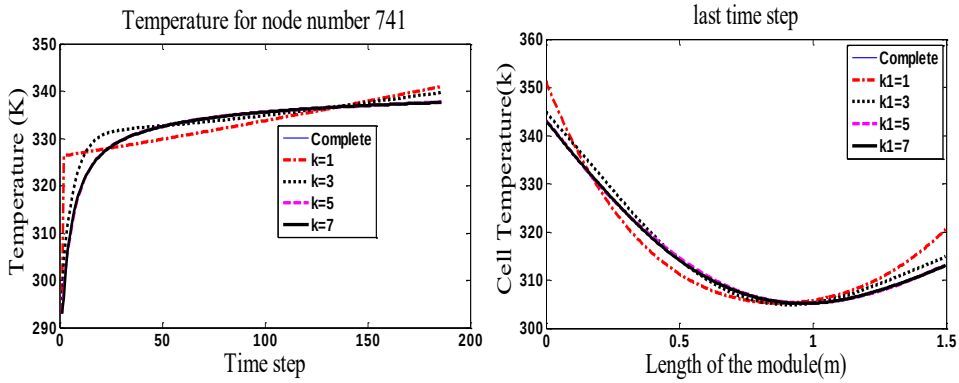

(a) (b)

Figure 6.7. Convergence of reduced solution to the full solution with increasing order of k and fixed interpolation points m_1=m_2 = 3 for (a) a specific point in the silicon layer, and (b) for the entire silicon layer.

6.4.2 Error Analysis

To demonstrate the efficiency and accuracy of the nonlinear order reduction, an error plot is deemed necessary to observe the convergence of the responses by varying the interpolation points m_1, m_2 and the dynamical order k. To do this, the normalized error $\varepsilon(k, m_1, m_2)$ is computed as:

$$\varepsilon = \frac{\|\boldsymbol{T}-\tilde{\boldsymbol{T}}\|_2}{\|\boldsymbol{T}\|_2} \tag{6.48}$$

where the norm is defined either in time domain by fixing the cell location, or in the space domain by fixing time step.

In order to observe the rate of convergence of the reduced system as its dynamical order k is increased with a fixed number of interpolation points m_1=m_2=m, the error at specific time steps representative of the beginning, middle and end of simulation

is now computed. A time variation error plot is also obtained for a selected node in the PV module for all the time steps. The results are shown in Fig. 6.8.

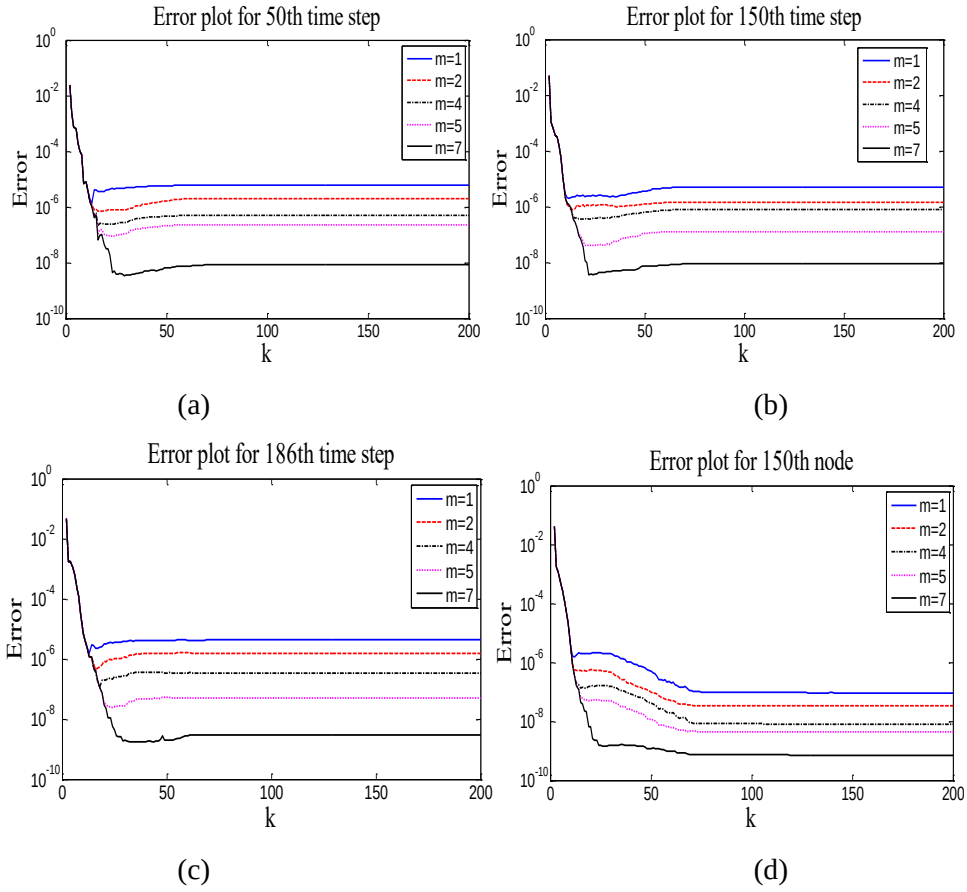

Figure 6.8. Error plot for the topmost layer for fixed $m_1=m_2=m$ at (a) 50th time step (b) 150th time step (c) 186th time step, and for (d) node number 150 in the discretized module for all 186 time steps.

A clear lower error bound can be observed from the error plots, which is an indication that the reduced system response converges, as the order of the system is increased, only to the extent allowed by the representation of the nonlinear terms. It should be generally noted that the error obtained by using only one interpolation

point (i.e. an equivalent of a linear system) is in the range of 10^{-5} to 10^{-6}, an indication that the nonlinearity in the system is not at all strong. Increasing the number of interpolation points further shifts the error bound from 10^{-5} to less than 10^{-8} which confirms the excellent suitability of the DEIM algorithm for this thermal modelling task.

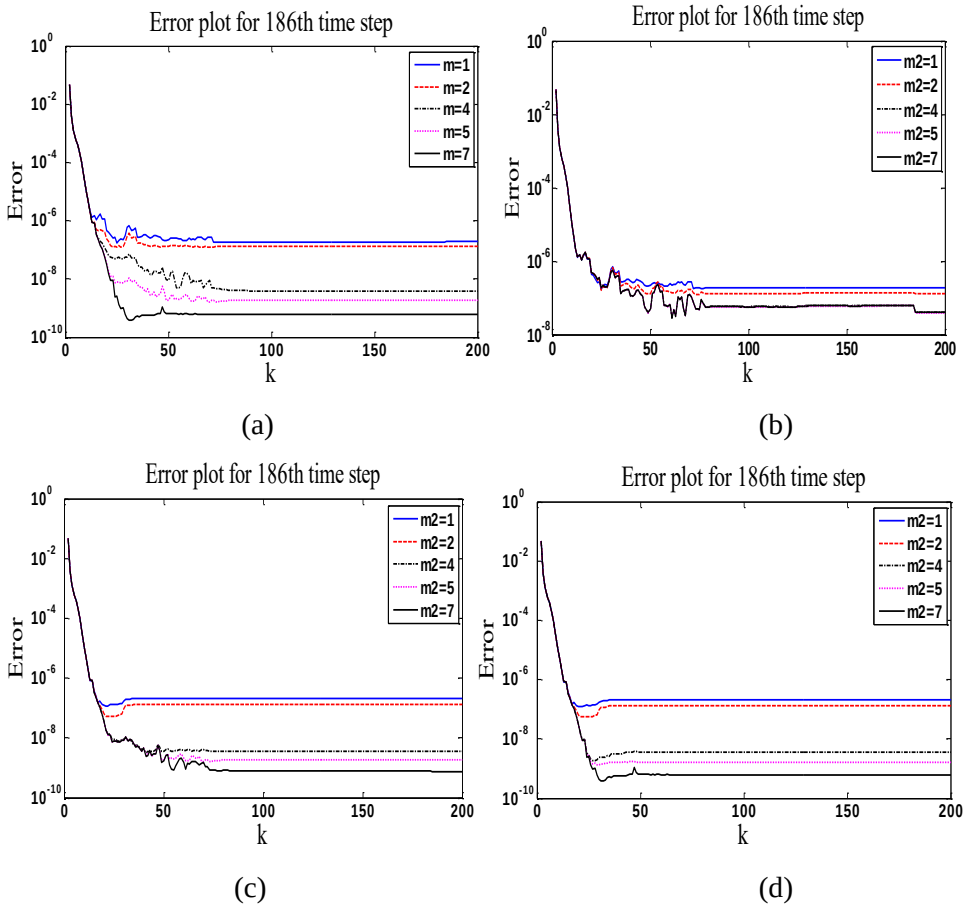

Figure 6.9. Error plot for the third layer for (a) $m_1=m_2=m$ (b) $m_1=1$ (c) $m_1=5$ (d) $m_1=7$.

In order to verify the improved efficiency that can be achieved by using different interpolation points for the two nonlinear terms, as against using the same interpolation order for the two nonlinear terms, various numerical experiments are performed by independently varying m_1 *and* m_2. The results are shown in Fig. 6.9.

The plots shown in Fig. 6.9 confirm that by independently varying m_1 *and* m_2, a better control of the accuracy of the reduced model can be achieved. In Fig. 6.9a where the same interpolation order is used for the two nonlinear terms, the reduced model becomes efficient as order k is increased above 50 when the lower bound error becomes more stable. By varying m_1 *and* m_2 independently, the stability of the lower error bound is attained with a smaller order k . It can be clearly observed in Fig. 6.9b-6.9d that there is a reduction in the lower bound error from less than 10^{-6} to less than 10^{-8} as m_1 is increased from 1 to 7 while m_2 is varied for each fixed m_1. Furthermore with independent variation of m_1 *and* m_2, a lower order k (< 50) of the linear subspace projection is required to attain a stable error bound. This observation proves that, a better approximation of the full system can be achieved by independent variation of the interpolation of the nonlinear terms.

6.4.3 Computation time

Finally, the advantages of proposed MOR technique is emphasized by reporting the runtime required for the various simulations on the same commodity laptop. A transient analysis of the full system requires 61.40 seconds. Based on available snapshots, the construction of the reduced model via the proposed POD/DEIM requires as few as 0.86 seconds, whereas the transient simulation of the reduced model (k=7 and $m_1=m_2=3$) takes only 1.40 seconds. Excluding model setup and construction, the overall speedup is almost 44X. Considering that the proposed

model is a quite simplified and 2D structure, more dramatic speedup is expected when applying this process to a full 3D geometry.

6.5 Model order reduction of coupled thermo-mechanical photovoltaic systems

The problem description entails a PV module containing 4 Silicon cells sandwiched between glass and Backsheet layers while the encapsulant EVA is represented by a zero thickness shear-lag interface as illustrated in chapter 5 (see Fig. 5.6). Discretization of the system equations leads to numerous mechanical and thermal degrees of freedom. Although the full system solution, using a Matlab solver, is presented in chapter 5, it is worthy to note that computation of these degrees of freedom is an expensive computational task. And taking into consideration that a centred finite difference scheme is used for the space discretization of the system with an error order $\mathcal{O}(h^2)$ where h is the mesh size, computation of the full solution with many degrees of freedom can introduce significant errors in final result. On this basis, a reduction scheme is desired, where the full system can be approximated with few degrees of freedom with a good control of the system accuracy. Given that the state equation representing the thermomechanical PV system is of coupled type, there is no standard approach in the literature for the treatment of second order system of this nature for structure preservation and some proposed methods are subject of current research in advanced model order reduction. Therefore, the procedure described in this section provides a means to make a detail comparison between the classical state-space approach for general first-order system and the recently introduced second-order reduction method in [76]. Finally, a proposed approach for structure preservation of the coupled second-order system is herein presented and it is shown that this approach can reduce satisfactorily coupled thermomechanical equations of the PV system.

6.5.1 Classical state-space approach (first-order system)

The original system formulation is recalled here according to Eq. (5.97). We are interested to output the displacements for the Silicon layer.

$$\begin{bmatrix} \boldsymbol{M_w} & \mathbf{0} & \mathbf{0} & \mathbf{0} \\ \mathbf{0} & \boldsymbol{M_u} & \mathbf{0} & \mathbf{0} \\ \mathbf{0} & \mathbf{0} & \boldsymbol{M_v} & \mathbf{0} \\ \mathbf{0} & \mathbf{0} & \mathbf{0} & \mathbf{0} \end{bmatrix} \begin{Bmatrix} \ddot{\mathbf{W}} \\ \ddot{\mathbf{U}} \\ \ddot{\mathbf{V}} \\ \ddot{\mathbf{T}} \end{Bmatrix} + \begin{bmatrix} \mathbf{0} & \mathbf{0} & \mathbf{0} & \mathbf{0} \\ \mathbf{0} & \mathbf{0} & \mathbf{0} & \mathbf{0} \\ \mathbf{0} & \mathbf{0} & \mathbf{0} & \mathbf{0} \\ \mathbf{0} & \mathbf{0} & \mathbf{0} & \boldsymbol{S} \end{bmatrix} \begin{Bmatrix} \dot{\mathbf{W}} \\ \dot{\mathbf{U}} \\ \dot{\mathbf{V}} \\ \dot{\mathbf{T}} \end{Bmatrix} + \begin{bmatrix} \boldsymbol{K}_w & \boldsymbol{K}_u & \boldsymbol{K}_v & \boldsymbol{C}_T \\ \bar{\boldsymbol{K}}_{w1} & \boldsymbol{K}_{u1} & \mathbf{0} & \mathbf{0} \\ \bar{\boldsymbol{K}}_{w2} & \mathbf{0} & \boldsymbol{K}_{v1} & \mathbf{0} \\ \mathbf{0} & \mathbf{0} & \mathbf{0} & \boldsymbol{H} \end{bmatrix} \begin{Bmatrix} \mathbf{W} \\ \mathbf{U} \\ \mathbf{V} \\ \mathbf{T} \end{Bmatrix} = \begin{Bmatrix} \boldsymbol{F}_1 \\ \boldsymbol{F}_2 \\ \boldsymbol{F}_3 \\ \boldsymbol{F}_4 \end{Bmatrix} i(t) \tag{6.49}$$

In Eq. (5.97), $\boldsymbol{U}_1$ and $\boldsymbol{U}_2$ are replaced with $\mathbf{U}$ and $\mathbf{V}$ respectively in Eq. (6.49) for convenience of notation.

$\mathbf{W},\ \mathbf{U},\ \mathbf{V}, \in \mathbb{R}^{\mathrm{N}\times 1}$, $\mathbf{T} \in \mathbb{R}^{\mathrm{N}_T\times 1}$, $\boldsymbol{F}_1,\ \boldsymbol{F}_2,\ \boldsymbol{F}_3, \in \mathbb{R}^{N\times 1}$, $\boldsymbol{F}_4, \in \mathbb{R}^{\mathrm{N}_T\times 1}$,

$\boldsymbol{M}_w,\ \boldsymbol{M}_u,\ \boldsymbol{M}_v,\ \boldsymbol{K}_w, \boldsymbol{K}_u,\ \boldsymbol{K}_v,\ \boldsymbol{K}_{u1},\ \boldsymbol{K}_{v1},\ \bar{\boldsymbol{K}}_{w1},\ \bar{\boldsymbol{K}}_{w2},\ \in \mathbb{R}^{\mathrm{N}\times\mathrm{N}}$,

$\boldsymbol{C}_T \in \mathbb{R}^{\mathrm{N}\times\mathrm{N}_T}$, $\boldsymbol{H},\ \boldsymbol{S} \in \mathbb{R}^{\mathrm{N}_T\times\mathrm{N}_T}$.

and the compact form according to Eq. (5.98) is recalled as:

$$\begin{bmatrix} \boldsymbol{M}_1 & \mathbf{0} \\ \mathbf{0} & \mathbf{0} \end{bmatrix} \begin{Bmatrix} \ddot{\boldsymbol{\chi}} \\ \ddot{\boldsymbol{T}} \end{Bmatrix} + \begin{bmatrix} \mathbf{0} & \mathbf{0} \\ \mathbf{0} & \boldsymbol{S} \end{bmatrix} \begin{Bmatrix} \dot{\boldsymbol{\chi}} \\ \dot{\boldsymbol{T}} \end{Bmatrix} + \begin{bmatrix} \boldsymbol{K}_1 & \bar{\boldsymbol{C}}_T \\ \mathbf{0} & \mathbf{H} \end{bmatrix} \begin{Bmatrix} \boldsymbol{\chi} \\ \boldsymbol{T} \end{Bmatrix} = \begin{Bmatrix} \bar{\boldsymbol{F}}_1 \\ \boldsymbol{F}_4 \end{Bmatrix} i(t) \tag{6.50}$$

where

$$\boldsymbol{M}_1 = \begin{bmatrix} \boldsymbol{M_w} & \mathbf{0} & \mathbf{0} \\ \mathbf{0} & \boldsymbol{M_u} & \mathbf{0} \\ \mathbf{0} & \mathbf{0} & \boldsymbol{M_v} \end{bmatrix}, \boldsymbol{K}_1 = \begin{bmatrix} \boldsymbol{K_w} & \boldsymbol{K}_u & \boldsymbol{K}_v \\ \bar{\boldsymbol{K}}_{w1} & \boldsymbol{K}_{u1} & \mathbf{0} \\ \bar{\boldsymbol{K}}_{w2} & \mathbf{0} & \boldsymbol{K}_{v1} \end{bmatrix}, \bar{\boldsymbol{C}}_T = \begin{Bmatrix} \boldsymbol{C}_T \\ \mathbf{0} \\ \mathbf{0} \end{Bmatrix}, \bar{\boldsymbol{F}}_1 = \begin{Bmatrix} \boldsymbol{F}_1 \\ \boldsymbol{F}_2 \\ \boldsymbol{F}_3 \end{Bmatrix}$$

$\boldsymbol{M}_1,\ \boldsymbol{K}_1 \in \mathbb{R}^{\mathrm{N}_1\times\mathrm{N}_1}$, $\bar{\boldsymbol{C}}_T \in \mathbb{R}^{\mathrm{N}_1\times\mathrm{N}_T}$, $\mathrm{N}_1 = 3\mathrm{N}$.

For this investigation, we use a discretization mesh with $\mathrm{N}_1 = 14400$ and $\mathrm{N}_T = 1600$.

$i(t)$ is the given the input function recalled from Eq. (5.96) as:

$$i(t) = a\exp^{(b\times t)} + c\exp^{(d\times t)}$$

where

$a = -227.8, \quad b = -0.0004404, \qquad c = 227.8, \qquad d = -0.002476.$

The state-space representation of the system Eq. (6.50) is written in first-order form as:

$$\boldsymbol{E}\dot{\boldsymbol{\Phi}} = \boldsymbol{A}\boldsymbol{\Phi} + \boldsymbol{b}i(t) \tag{6.51}$$

where

$$\boldsymbol{E} = \begin{bmatrix} \boldsymbol{I} & \mathbf{0} & \mathbf{0} \\ \mathbf{0} & \boldsymbol{M}_1 & \mathbf{0} \\ \mathbf{0} & \mathbf{0} & \boldsymbol{S} \end{bmatrix}, \mathbf{A} = \begin{bmatrix} \mathbf{0} & \boldsymbol{I} & \mathbf{0} \\ -\boldsymbol{K}_1 & \mathbf{0} & -\overline{\boldsymbol{C}}_T \\ \mathbf{0} & \mathbf{0} & -\boldsymbol{H} \end{bmatrix}, \boldsymbol{\Phi} = \begin{bmatrix} \boldsymbol{\chi} \\ \dot{\boldsymbol{\chi}} \\ \mathbf{T} \end{bmatrix}, \boldsymbol{b} = \begin{bmatrix} \mathbf{0} \\ \overline{\boldsymbol{F}}_1 \\ \boldsymbol{F}_4 \end{bmatrix}.$$

$\mathbf{E}, \boldsymbol{A}, \in \mathbb{R}^{(2\mathrm{N}_1+\mathrm{N}_T)\times(2\mathrm{N}_1+\mathrm{N}_T)}$, $\boldsymbol{\Phi}, \boldsymbol{b} \in \mathbb{R}^{(2\mathrm{N}_1+\mathrm{N}_T)\times 1}$.

If a projection matrix of the state-space Eq. (6.51) is defined by $\boldsymbol{V}_1 = (\boldsymbol{v}_1, \ldots\ldots, \boldsymbol{v}_r)$, the reduced version of Eq. (6.51) can be obtained (as in Sec. 4.7.3) by applying the mapping $\boldsymbol{\Phi} = \boldsymbol{V}_1\boldsymbol{\Phi}_r$ to the system Eq. (6.51) and the state equation multiplied by the transpose of the projection matrix $\boldsymbol{V}_1$. Accordingly, we get:

$$\boldsymbol{V}_1{}^T\mathbf{E}\boldsymbol{V}_1\dot{\boldsymbol{\Phi}}_r = \boldsymbol{V}_1{}^T\boldsymbol{A}\boldsymbol{V}_1\boldsymbol{\Phi}_r + \boldsymbol{V}_1{}^T\boldsymbol{b}i(t) \tag{6.52}$$

$\boldsymbol{V}_1 \in \mathbb{R}^{(2\mathrm{N}_1+\mathrm{N}_T)\times r}, \qquad \boldsymbol{\Phi}_r \in \mathbb{R}^{r\times 1}, \qquad$ with $\quad r < 2\mathrm{N}_1 + \mathrm{N}_T$

$\boldsymbol{\Phi}_r$ is the reduced state variable. The reduced state equation of order r can now be written as:

$$\boldsymbol{E}_r\dot{\boldsymbol{\Phi}}_r = \boldsymbol{A}_r\boldsymbol{\Phi}_r + \boldsymbol{b}_r i(t) \tag{6.53a}$$

where

$$\boldsymbol{E}_r = \boldsymbol{V}_1{}^T \boldsymbol{E}\boldsymbol{V}_1,\ \boldsymbol{A}_r = \boldsymbol{V}_1{}^T \boldsymbol{A}\boldsymbol{V}_1\ ,\ \boldsymbol{b}_r = \boldsymbol{V}_1{}^T \boldsymbol{b},$$

$$\boldsymbol{E}_r, \boldsymbol{A}_r \in \mathbb{R}^{r\times r},\ \boldsymbol{b}_r \in \mathbb{R}^{r\times 1}.$$

The task now is to determine the projection matrix $\boldsymbol{V}_1$ which can be constructed with the POD method as described in section 6.2 since the full system solution has been obtained in chapter 5. The efficiency of the POD scheme for reduction of thermal system equations has been established in section 6.2. So, the method is hereby extended to coupled thermomechanical system. In this case, the snapshots collection consists of augmented vectors of displacement, velocity and temperature at discrete times t_i. Mathematically,

$$\boldsymbol{S} = [\begin{bmatrix}\boldsymbol{\chi}\\ \dot{\boldsymbol{\chi}}\\ \mathbf{T}\end{bmatrix}_1 , \dots . , \begin{bmatrix}\boldsymbol{\chi}\\ \dot{\boldsymbol{\chi}}\\ \mathbf{T}\end{bmatrix}_{ns}] \tag{6.54}$$

By performing SVD on the snapshot matrix $\boldsymbol{S}$, the dominant modes can be selected as the basis of the projection matrix $\boldsymbol{V}_1$. With $\boldsymbol{V}_1$ computed, the reduced system matrices $\boldsymbol{E}_r$, $\boldsymbol{A}_r$ and the vector $\boldsymbol{b}_r$ in Eq. (6.53) can be evaluated. Consequently, Eq. (6.53) is now solved for the approximate system output variable $\boldsymbol{y}$ by using modified Euler method as presented in chapter 4. The result are analysed in Sec. 6.5.

6.5.2 Second-order based reduction by projection

It is noted that the reduction of the coupled system by state-space representation described above does not preserve the second order structure of the global system Eq. (6.50). To preserve the second order structure of the global system, Eq. (6.50) is rewritten in another compact form as:

$$\boldsymbol{M}\ddot{\boldsymbol{u}} + \boldsymbol{D}\dot{\boldsymbol{u}} + \boldsymbol{K}\boldsymbol{u} = \boldsymbol{F}i(t) \tag{6.55}$$

$\boldsymbol{M}, \boldsymbol{D}, \boldsymbol{K} \in \mathbb{R}^{(\mathrm{N}_1+\mathrm{N}_T)\times(\mathrm{N}_1+\mathrm{N}_T)}$, $\boldsymbol{F}, \boldsymbol{u} \in \mathbb{R}^{(\mathrm{N}_1+\mathrm{N}_T)\times 1}$,

where

$$\boldsymbol{M} = \begin{bmatrix} \boldsymbol{M}_1 & \mathbf{0} \\ \mathbf{0} & \mathbf{0} \end{bmatrix},\ \boldsymbol{D} = \begin{bmatrix} \mathbf{0} & \mathbf{0} \\ \mathbf{0} & \boldsymbol{S} \end{bmatrix},\ \boldsymbol{K} = \begin{bmatrix} \boldsymbol{K}_1 & \overline{\boldsymbol{C}}_T \\ \mathbf{0} & \mathbf{H} \end{bmatrix},\ \boldsymbol{F} = \begin{Bmatrix} \overline{\boldsymbol{F}}_1 \\ \boldsymbol{F}_4 \end{Bmatrix},\ \boldsymbol{u} = \begin{Bmatrix} \boldsymbol{\chi} \\ \mathbf{T} \end{Bmatrix}.$$

If a projection matrix is defined as $\boldsymbol{V}_2 = \left(\mathbf{v}_1, \ldots\ldots, \mathbf{v}_\mathrm{q}\right)$ with $q \ll (\mathrm{N}_1 + \mathrm{N}_T)$, the reduced state vector $\boldsymbol{u}_q$ can be constrained to the column space of $\boldsymbol{V}_2$ to obtain an approximation of the system state $\boldsymbol{u}$ as:

$$\boldsymbol{u} = \boldsymbol{V}_2\boldsymbol{u}_q,\ \boldsymbol{V}_2 \in \mathbb{R}^{(\mathrm{N}_1+\mathrm{N}_T)\times q},\ \ \boldsymbol{u}_q \in \mathbb{R}^{q\times 1}. \tag{6.56}$$

By mapping the reduced states onto the projection matrix $\boldsymbol{V}_2$ and multiplying by the transpose of the projection matrix $\boldsymbol{W}$ as for one-sided Krylov method i.e., $\boldsymbol{W} = \boldsymbol{V}_2$, the reduced system of order q is obtained thus:

$$\boldsymbol{M}_q\ddot{\boldsymbol{u}}_q + \boldsymbol{D}_q\dot{\boldsymbol{u}}_q + \boldsymbol{K}_q\boldsymbol{u}_q = \boldsymbol{F}_q i(t) \tag{6.57}$$

$$\boldsymbol{M}_q, \boldsymbol{D}_q, \boldsymbol{K}_q \in \mathbb{R}^{q\times q},\quad \boldsymbol{F}_q \in \mathbb{R}^{q\times 1}$$

where

$$\boldsymbol{M}_q = \boldsymbol{V}_2{}^T(\boldsymbol{M}\boldsymbol{V}_2),\ \boldsymbol{D}_q = \boldsymbol{V}_2{}^T(\boldsymbol{D}\boldsymbol{V}_2),\ \boldsymbol{K}_q = \boldsymbol{V}_2{}^T(\boldsymbol{K}\boldsymbol{V}_2),\ \boldsymbol{F}_q = \boldsymbol{V}_2{}^T\boldsymbol{F}.$$

To determine the projection matrix $\boldsymbol{V}_2$, two approaches are considered in this work namely a POD based approach and second order Krylov based approach. The efficiency of the POD technique has been established in Sec. 6.2 and since the full system solution has been performed in chapter 5, it is possible to collect a sample snapshots of the system full solution at discrete times t_i and apply Algorithm 6.1 to extract the bases which span the column space of the projection matrix $\boldsymbol{V}_2$. In this case, the snapshots are collected as augmented vectors of displacement and thermal degrees of freedom at discrete times t_i:

$$\boldsymbol{S} = [\begin{bmatrix}\boldsymbol{\chi}\\ \boldsymbol{T}\end{bmatrix}_1, \ldots., \begin{bmatrix}\boldsymbol{\chi}\\ \boldsymbol{T}\end{bmatrix}_{ns}], \tag{6.58}$$

ns is the number of snapshots and for efficient computation of the projection matrix, ns should be sufficient. Consequently, the reduced system matrices is obtained according to Eq. (6.57) and approximation of the system output is computed as reported in Sec. 6.5.

An alternative approach to obtaining the second order projection matrix $\boldsymbol{V}_2$ is to consider theorem 1 stated in chapter 4; if the matrix $\boldsymbol{V}_2$ is the basis of the second-order input Krylov subspace $\mathcal{K}_q(-\boldsymbol{K}^{-1}\boldsymbol{D}, -\boldsymbol{K}^{-1}\boldsymbol{M}, -\boldsymbol{K}^{-1}\boldsymbol{F})$ and a projection matrix $\boldsymbol{W}$ is chosen such that $\boldsymbol{W}^T\boldsymbol{V}_2 = \mathbb{I}$, the first q moments of the original and reduced models match. The columns of the matrix $\boldsymbol{V}_2$ which are the basis of second-order Krylov subspace $\mathcal{K}_q(-\boldsymbol{K}^{-1}\boldsymbol{D}, -\boldsymbol{K}^{-1}\boldsymbol{M}, -\boldsymbol{K}^{-1}\boldsymbol{F})$ are orthonormal i.e., ${\boldsymbol{V}_2}^T\boldsymbol{V}_2 = \mathbb{I}$, and can be obtained by implementing modified Gram Schmidt algorithm described in [71] where it is assumed that in each iteration step an orthogonal vector exists. Otherwise, the algorithm is terminated and the number of iteration q is reduced. Computing the inverse of matrix $\boldsymbol{K}$ which is quite large can be computationally expensive by direct inverse procedure. By performing LU decomposition of $\boldsymbol{K}$ and solving a system of linear equations, the recursive procedure becomes efficient computationally than using a direct inverse procedure.

To improve the system output approximation, a rational interpolation of the second-order Krylov subspace at $s_v = 0, 1, \ldots, k$ is considered so that few moments can be matched at different expansion points s_v and the projection matrix is generated as a union of multiple second-order Krylov subspaces. Instead of a local error approximation of the system outputs, this procedure will allow the approximation error to spread across the various expansion points. According to [71], this implies that second-order Krylov matrices $\boldsymbol{K}$, and $\boldsymbol{D}$ are substituted, respectively, with $\boldsymbol{K} + s_v\boldsymbol{D} + {s_v}^2\boldsymbol{M}$ and $\boldsymbol{D} + 2s_v\boldsymbol{M}$. Although this increases the

computational cost of this reduction scheme but a better and more stable approximation is obtained as discussed later in Sec. 6.5. The modified Gram Schmidt scheme for rational interpolation of second-order Krylov subspace is presented in Algorithm 6.4:

Algorithm 6.4 (Modified Gram Schmidt for second-order rational Arnoldi iteration)

Input: matrices $\boldsymbol{K}$, $\boldsymbol{D}$, $\boldsymbol{M}$, $\boldsymbol{F}$, vector of repeated expansion points $\mathcal{S}$.

Solve $-(\boldsymbol{K} + s_0\boldsymbol{D} + {s_0}^2\boldsymbol{M})\mathbf{b}_1 = \boldsymbol{F}$

1. Set $\mathbf{v}_1 = \frac{\mathbf{b}_1}{\|\mathbf{b}_1\|_2}$ and $\mathbf{I}_1 = \mathbf{0}$
2. **for** $i = 2, 3, \ldots\ldots,$ **do**
   a. Calculate the next vector
   if $s_{i+1} = s_i$ **then**
   solve $-(\boldsymbol{K} + s_i\boldsymbol{D} + {s_i}^2\boldsymbol{M})\bar{\mathbf{v}}_\mathrm{i} = (\boldsymbol{D} + 2s_i\boldsymbol{M})\mathbf{v}_{\mathrm{i}-1} + \boldsymbol{M}\mathbf{I}_{\mathrm{i}-1}$ $\hat{\mathbf{I}}_\mathrm{i} = \mathbf{v}_{\mathrm{i}-1}$
   else
   solve $-(\boldsymbol{K} + s_i\boldsymbol{D} + {s_i}^2\boldsymbol{M})\bar{\mathbf{v}}_\mathrm{i} = \boldsymbol{F}$ $\hat{\mathbf{I}}_\mathrm{i} = \mathbf{v}_{\mathrm{i}-1}$
   end if
   b. Orthogonalization: For $j = 1$ to $i - 1$ do:
   $h = \bar{\mathbf{v}}_\mathrm{i}^{\,T}\mathbf{v}_j$
   $\bar{\mathbf{v}}_\mathrm{i} = \bar{\mathbf{v}}_\mathrm{i} - h\mathbf{v}_j$ $\hat{\mathbf{I}}_\mathrm{i} = \hat{\mathbf{I}}_\mathrm{i} - j\mathbf{I}_\mathrm{i}$

c. Normalization: if the vector $\|\bar{\mathbf{v}}_i\|_2 < \epsilon$ break the loop. Otherwise, the ith column of the projection matrices are:

$$\mathbf{v}_i = \frac{\bar{\mathbf{v}}_\mathrm{i}}{\|\bar{\mathbf{v}}_\mathrm{i}\|_2} \qquad \mathbf{I}_i = \frac{\hat{\mathbf{I}}_\mathrm{i}}{\|\bar{\mathbf{v}}_\mathrm{i}\|_2}$$

3. **end for**
4. **Output** $\boldsymbol{V}_2 = (\mathbf{v}_1, \ldots\ldots, \mathbf{v}_\mathrm{q})$

In step 3b of algorithm 6.4 to get sufficient orthogonality, the orthogonalization is iterated twice due to loss of linear independence as the iteration progresses. ϵ is a small positive number denoting the limit below which linear dependence of successive vectors is critical and sufficient orthogonality is not guaranteed. After implementing Algorithm 6.4 to obtain $\boldsymbol{V}_2$, the reduced system matrices are computed according to Eq. (6.59) and consequently, a solution of the reduced equation is performed by using Newmark algorithm described in chapter 4. Again, the results for the reduced system output for this formulation are discussed in Sec. 6.5.

6.5.3 Structure-preserving reduced-order for coupled second-order system

The reduced-order formulation in Sec. 6.5.2 preserves only the second-order structure of the global system equation but not the individual structure of the mechanical and thermal system. it is noted here that the mechanical system equation is undamped i.e., damping matrix is zero and the system oscillates at its natural resonant frequency, so a reduced-order of the global system with a damping matrix $\boldsymbol{D}$ (as performed in Sec. 6.4.2) can introduce some undesirable effects into the system dynamics of the reduced-order model which may eventually impair the stability of the reduced system. This is indeed the reason why rational Krylov method is applied in Sec. 6.4.2 as there is quick loss of orthogonality as the iteration proceeds for different expansion points so that only few stable moments are

matched at each point. Hence the need for a structure-preserving approach to reduce the coupled system. Structure-preserving techniques for coupled state-space systems have been discussed extensively in [99, 100]. The basic idea involves applying basic Arnoldi algorithm for standard state-space Krylov subspace of the global system to generate projection bases separately for the individual systems. To achieve this, the global projection matrix, say $\widetilde{\boldsymbol{V}}$, is partitioned into sub-blocks of row size of each sub-system as:

$$\widetilde{\boldsymbol{V}} = \begin{bmatrix} \overline{\boldsymbol{V}}_1 \\ \overline{\boldsymbol{V}}_2 \end{bmatrix} \tag{6.59}$$

By using the sub-blocks $\overline{\boldsymbol{V}}_i$ to build a block diagonal reduction matrices,

$$\overline{\boldsymbol{V}} = \begin{bmatrix} \overline{\boldsymbol{V}}_1 & \boldsymbol{0} \\ \boldsymbol{0} & \overline{\boldsymbol{V}}_2 \end{bmatrix} \tag{6.60}$$

a structure-preserving reduced-order system can be obtained as:

$$\boldsymbol{M}_r \ddot{\boldsymbol{\chi}}_r + \boldsymbol{K}_r \boldsymbol{\chi}_r + \boldsymbol{C}_r \boldsymbol{T}_r = \boldsymbol{F}_{1r} i(t) \tag{6.61a}$$

$$\boldsymbol{S}_r \dot{\boldsymbol{T}}_r + \boldsymbol{H}_r \boldsymbol{T}_r = \boldsymbol{F}_{4r} i(t) \tag{6.61b}$$

where

$$\boldsymbol{M}_r = \overline{\boldsymbol{V}}_1{}^T \boldsymbol{M}_1 \overline{\boldsymbol{V}}_1 \,,\ \boldsymbol{K}_r = \overline{\boldsymbol{V}}_1{}^T \boldsymbol{K}_1 \overline{\boldsymbol{V}}_1 \,,\ \boldsymbol{C}_r = \overline{\boldsymbol{V}}_1{}^T \overline{\boldsymbol{C}}_T \overline{\boldsymbol{V}}_2 \,,\ \boldsymbol{\chi}_r = \overline{\boldsymbol{V}}_1 \boldsymbol{\chi} \,,$$

$$\boldsymbol{S}_r = \overline{\boldsymbol{V}}_2{}^T \boldsymbol{S} \overline{\boldsymbol{V}}_2 \,,\ \boldsymbol{H}_r = \overline{\boldsymbol{V}}_2{}^T \boldsymbol{H} \overline{\boldsymbol{V}}_2 \,,\ \boldsymbol{F}_{4r} = \overline{\boldsymbol{V}}_2{}^T \boldsymbol{F}_4 \,,\ \boldsymbol{T} = \overline{\boldsymbol{V}}_2 \boldsymbol{T}_r \,.$$

To generate a linearly dependent columns for the sub-blocks $\overline{\boldsymbol{V}}_i$ as there is loss of independence after partitioning of $\widetilde{\boldsymbol{V}}$ into sub-blocks $\overline{\boldsymbol{V}}_i$, a re-orthogonalization of $\overline{\boldsymbol{V}}_i$ is required to remove every possible linear dependence. This can be achieved by performing a singular value decomposition (SVD) on the blocks separately based on which the dominant modes can be selected as bases of the projection matrices for individual sub-systems. The drawback of this structure-preserving

approach is that the calculation of the projection matrices of the sub-system requires solving systems with the entire coupled system's coefficient matrix. So this approach is expensive in some sense, at least, to the extent of the computation of the projection basis of the original coupled system.

As a way to circumvent this computational cost, it is remarked that while the undamped mechanical system equation is coupled to the thermal system, there is no feedback coupling from the mechanical to the thermal system i.e., one-sided coupling. Therefore, the thermal system can be reduced independently using any of the general MOR techniques for state-space system and then use the transient solution of the reduced temperature state as an input to the mechanical system to obtain the unknown displacement degrees of freedom. Let the reduced thermal system be represented as:

$$\boldsymbol{S}_t\dot{\boldsymbol{T}}_t + \boldsymbol{H}_t\boldsymbol{T}_t = \boldsymbol{F}_{4t}i(t) \tag{6.62}$$

where

$\boldsymbol{S}_t = {\boldsymbol{V}_t}^T\boldsymbol{S}\boldsymbol{V}_t$, $\boldsymbol{H}_t = {\boldsymbol{V}_t}^T\boldsymbol{H}\boldsymbol{V}_t$, $\boldsymbol{F}_{4t} = {\boldsymbol{V}_t}^T\boldsymbol{F}_4$, $\boldsymbol{T} = \boldsymbol{V}_t\boldsymbol{T}_t$,

$\boldsymbol{V}_t \in \mathbb{R}^{\mathrm{N}_T \times q1}$, $\boldsymbol{T}_t \in \mathbb{R}^{q1\times 1}$, $\boldsymbol{S}_t, \boldsymbol{H}_t \in \mathbb{R}^{q1\times q1}$.

By considering a first-order Krylov subspace $\mathcal{K}_q(-\boldsymbol{H}^{-1}\boldsymbol{S},\ -\boldsymbol{H}^{-1}\boldsymbol{F}_4)$, the projection basis $\boldsymbol{V}_t$ for the thermal system can be obtained by using the basic Arnoldi scheme as described in chapter 4. This is followed by applying the mapping $\boldsymbol{T} = \boldsymbol{V}_t\boldsymbol{T}_t$ and then projection according to Eq. (6.62) and by solving Eq. (6.62) using the modified Euler method, the reduced temperature states $\boldsymbol{T}_t$ can be determined at various time steps. Figure 6.10 shows the error plot for the reduced thermal system at the beginning (100th time step) and last time (900th time step) steps and it can be seen that the thermal system is reduced efficiently to the tune of 10^{-13} relative error and a stable error bound is attained with a reduced order as

small as 10. This realization is used as a clue in the optimal selection of reduced temperature states for the thermal coupling term in the undamped mechanical system.

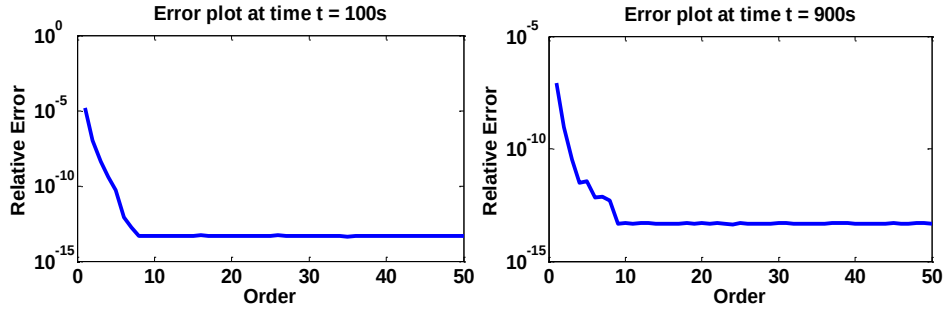

Figure 6.10 Error plot for reduced-order thermal system at times 100 and 900 seconds.

Let us define the projection matrix for the thermally coupled mechanical system as $\boldsymbol{V}_m = (\mathbf{v}_1, \ldots\ldots, \mathbf{v}_\mathrm{q})$ which can be used as a change-of-coordinate basis for the displacement degrees of freedom as $\boldsymbol{\chi} = \boldsymbol{V}_m \boldsymbol{\chi}_r$ to produce the reduced-order coupled system after projection:

$$\boldsymbol{M}_r \ddot{\boldsymbol{\chi}}_r + \boldsymbol{K}_r \boldsymbol{\chi}_r + \boldsymbol{C}_r \boldsymbol{T}_r = \boldsymbol{F}_r i(t) \tag{6.63}$$

where

$$\boldsymbol{M}_r = {\boldsymbol{V}_m}^T \boldsymbol{M}_1 \boldsymbol{V}_m,\ \boldsymbol{K}_r = {\boldsymbol{V}_m}^T \boldsymbol{K}_1 \boldsymbol{V}_m,\ \boldsymbol{C}_r = {\boldsymbol{V}_m}^T \boldsymbol{C}_1 \boldsymbol{V}_t,\ \boldsymbol{F}_r = {\boldsymbol{V}_m}^T \boldsymbol{F}_1\ .$$

To obtain the projection matrix for the mechanical system $\boldsymbol{V}_m$, the first-order equivalent of the global system is recalled as:

$$\boldsymbol{E}\dot{\boldsymbol{\Phi}} = \boldsymbol{A}\boldsymbol{\Phi} + \boldsymbol{b} i(t) \tag{6.64}$$

where matrices $\boldsymbol{E}$, $\boldsymbol{A}$ and vector $\boldsymbol{b}$ are as defined in Eq. (6.51).

The moment and the input Krylov subspace for the first-order system (6.64) are defined as:

$$\boldsymbol{m}_i = \boldsymbol{c}^T(\boldsymbol{A}^{-1}\boldsymbol{E})^i\boldsymbol{A}^{-1}\boldsymbol{b}\mathbf{b}\ ,\ \mathcal{K}_r(\boldsymbol{A}^{-1}\boldsymbol{E}, \boldsymbol{A}^{-1}\boldsymbol{b})\ ,\quad i = 0, 1, \ldots. \tag{6.65}$$

By using a block inverse procedure, It is noted that:

$$\boldsymbol{A}^{-1} = \begin{bmatrix} \mathbf{0} & \boldsymbol{I} & \mathbf{0} \\ -\boldsymbol{K}_1 & \mathbf{0} & -\overline{\boldsymbol{C}}_T \\ \mathbf{0} & \mathbf{0} & -\boldsymbol{H} \end{bmatrix}^{-1} = \begin{bmatrix} \mathbf{0} & -\boldsymbol{K}_1{}^{-1} & \boldsymbol{K}_1{}^{-1}\overline{\boldsymbol{C}}_T\boldsymbol{H}^{-1} \\ \boldsymbol{I} & \mathbf{0} & \mathbf{0} \\ \mathbf{0} & \mathbf{0} & -\boldsymbol{H}^{-1} \end{bmatrix} \tag{6.66}$$

With this realization, the moment for the first-order system is expressed as:

$$\boldsymbol{m}_i = \boldsymbol{c}^T\left(\begin{bmatrix} \mathbf{0} & -\boldsymbol{K}_1{}^{-1}\boldsymbol{M}_1 & \boldsymbol{K}_1{}^{-1}\overline{\boldsymbol{C}}_T\boldsymbol{H}^{-1}\boldsymbol{S} \\ \boldsymbol{I} & \mathbf{0} & \mathbf{0} \\ \mathbf{0} & \mathbf{0} & -\boldsymbol{H}^{-1}\boldsymbol{S} \end{bmatrix}\right)^i \begin{bmatrix} -\boldsymbol{K}_1{}^{-1}\overline{\boldsymbol{F}}_1 + \boldsymbol{K}_1{}^{-1}\overline{\boldsymbol{C}}_T\boldsymbol{H}^{-1}\boldsymbol{F}_4 \\ \mathbf{0} \\ -\boldsymbol{H}^{-1}\boldsymbol{F}_4 \end{bmatrix} \tag{6.67}$$

With respect to Eq. (6.67), the Krylov subspace for the thermal and the coupled mechanical system are $\mathcal{K}_{r1}(-\boldsymbol{H}^{-1}\boldsymbol{S}, -\boldsymbol{H}^{-1}\boldsymbol{F}_4)$ and $\mathcal{K}_{r2}\left(-\boldsymbol{K}_1{}^{-1}\boldsymbol{M}_1, \boldsymbol{K}_1{}^{-1}\overline{\boldsymbol{C}}_T\boldsymbol{H}^{-1}\boldsymbol{S}, -\boldsymbol{K}_1{}^{-1}\overline{\boldsymbol{F}}_1 + \boldsymbol{K}_1{}^{-1}\overline{\boldsymbol{C}}_T\boldsymbol{H}^{-1}\boldsymbol{F}_4\right)$. It is evident that $\mathcal{K}_{r1}(-\boldsymbol{H}^{-1}\boldsymbol{S}, -\boldsymbol{H}^{-1}\boldsymbol{F}_4)$ exactly corresponds to the Krylov subspace for the uncoupled thermal system (6.49) while $\mathcal{K}_{r2}\left(-\boldsymbol{K}_1{}^{-1}\boldsymbol{M}_1, \boldsymbol{K}_1{}^{-1}\overline{\boldsymbol{C}}_T\boldsymbol{H}^{-1}\boldsymbol{S}, -\boldsymbol{K}_1{}^{-1}\overline{\boldsymbol{F}}_1 + \boldsymbol{K}_1{}^{-1}\overline{\boldsymbol{C}}_T\boldsymbol{H}^{-1}\boldsymbol{F}_4\right)$ is considered as the equivalent input Krylov subspace for the undamped mechanical system. More appropriately, let us denote the Krylov subspace for the thermal and coupled mechanical systems as $\mathcal{K}_{r1}(\boldsymbol{G}, \boldsymbol{b}_2)$ and $\mathcal{K}_{r2}\left(\widetilde{\boldsymbol{A}}, \boldsymbol{Y}, \boldsymbol{b}_1\right)$ with

$$\widetilde{\boldsymbol{A}} = -\boldsymbol{K}_1{}^{-1}\boldsymbol{M}_1,\quad \boldsymbol{Y} = \boldsymbol{K}_1{}^{-1}\overline{\boldsymbol{C}}_T\boldsymbol{H}^{-1}\boldsymbol{S},\quad \boldsymbol{b}_1 = -\boldsymbol{K}_1{}^{-1}\overline{\boldsymbol{F}}_1 + \boldsymbol{K}_1{}^{-1}\overline{\boldsymbol{C}}_T\boldsymbol{H}^{-1}\boldsymbol{F}_4$$

$$\boldsymbol{G} = -\boldsymbol{H}^{-1}\boldsymbol{S},\quad \boldsymbol{b}_2 = -\boldsymbol{H}^{-1}\boldsymbol{F}_4$$

At this point, it is remarked that the input second-order Krylov subspace for moment matching about zero for an uncoupled, undamped mechanical system

(6.68) with input vector $\boldsymbol{F}_1$ is $\mathcal{K}_{q2}\left(\boldsymbol{0}, -\boldsymbol{K_1}^{-1}\boldsymbol{M}_1, -\boldsymbol{K_1}^{-1}\boldsymbol{F}_1\right)$ which results in the following projection matrix [83]:

$$\boldsymbol{M}_1\ddot{\boldsymbol{\chi}} + \boldsymbol{K}_1\boldsymbol{\chi} = \boldsymbol{F}_1 i(t) \tag{6.68}$$

$$\text{colspan}(\boldsymbol{V}_x) = \text{colspan}\left\{-\boldsymbol{K_1}^{-1}\boldsymbol{F}_1, \boldsymbol{0}, -\boldsymbol{K_1}^{-1}\boldsymbol{M}_1\boldsymbol{K_1}^{-1}\boldsymbol{F}_1, \boldsymbol{0}, \dots\right\} = \mathcal{K}_{q2}\left(-\boldsymbol{K_1}^{-1}\boldsymbol{M}_1, -\boldsymbol{K_1}^{-1}\boldsymbol{F}_1\right) \tag{6.69}$$

Eq. (6.69) implies that the basic blocks of the Krylov subspace corresponding to odd numbers are zero. Indeed, this fact is clear by stating the moment for the undamped mechanical system as:

$$\boldsymbol{m}_i = [\boldsymbol{L} \quad \boldsymbol{0}]\left(\begin{bmatrix}\boldsymbol{0} & \boldsymbol{I}\\ -\boldsymbol{K}_1 & \boldsymbol{0}\end{bmatrix}^{-1}\begin{bmatrix}\boldsymbol{I} & \boldsymbol{0}\\ \boldsymbol{0} & \boldsymbol{M}_1\end{bmatrix}\right)^{\boldsymbol{i}}\begin{bmatrix}\boldsymbol{0} & \boldsymbol{I}\\ -\boldsymbol{K}_1 & \boldsymbol{0}\end{bmatrix}^{-1}\begin{bmatrix}\boldsymbol{0}\\ \boldsymbol{F}_1\end{bmatrix} \qquad i = 0, 1, \dots \tag{6.70a}$$

$$\boldsymbol{m}_i = [\boldsymbol{L} \quad \boldsymbol{0}]\begin{bmatrix}\boldsymbol{0} & -\boldsymbol{K_1}^{-1}\boldsymbol{M}_1\\ \boldsymbol{I} & \boldsymbol{0}\end{bmatrix}^{\boldsymbol{i}}\begin{bmatrix}-\boldsymbol{K_1}^{-1}\boldsymbol{F}_1\\ \boldsymbol{0}\end{bmatrix} \tag{6.70b}$$

It is clear from Eq. (6.70b) that the odd moments $\boldsymbol{m}_i$ are zeros. Therefore, the basis of the Krylov subspace $\mathcal{K}_{q2}\left(-\boldsymbol{K_1}^{-1}\boldsymbol{M}_1, -\boldsymbol{K_1}^{-1}\boldsymbol{F}_1\right)$ constitute the columns of the projection matrix $\boldsymbol{V}_x$ which are orthonormal. With this idea noted, moment expansion of thermal Krylov subspace $\mathcal{K}_{r1}(\boldsymbol{G}, \boldsymbol{b}_2)$ and coupled second-order Krylov subspace $\mathcal{K}_{r2}\left(\widetilde{\boldsymbol{A}}, \boldsymbol{Y}, \boldsymbol{b}_1\right)$ in accordance with (6.67) about zero yields matrices $\boldsymbol{V}_s$ and $\boldsymbol{V}_n$ respectively for $i = 0, 1, \dots$

$$colspan(\boldsymbol{V}_n) = colspan\{\boldsymbol{b}_1, \boldsymbol{Y}\boldsymbol{b}_2, \widetilde{\boldsymbol{A}}\boldsymbol{b}_1 + \boldsymbol{Y}\boldsymbol{G}\boldsymbol{b}_2, \widetilde{\boldsymbol{A}}\boldsymbol{Y}\boldsymbol{b}_2 + \boldsymbol{Y}\boldsymbol{G}^2\boldsymbol{b}_2, \widetilde{\boldsymbol{A}}^2\boldsymbol{b}_1 + \widetilde{\boldsymbol{A}}\boldsymbol{Y}\boldsymbol{G}\boldsymbol{b}_2 + \boldsymbol{Y}\boldsymbol{G}^3\boldsymbol{b}_2, \dots\} \tag{6.71a}$$

$$\text{colspan}(\boldsymbol{V}_s) = \text{colspan}\{\boldsymbol{b}_2, \boldsymbol{G}\boldsymbol{b}_2, \boldsymbol{G}^2\boldsymbol{b}_2, \boldsymbol{G}^3\boldsymbol{b}_2, \dots\} \tag{6.71b}$$

From Eq. (6.71), our objective is to extract the so called coupled moments that grows in the expansion with the starting vectors $\boldsymbol{b}_1$ and $\boldsymbol{b}_2$ since the mechanical system is coupled with the thermal system. It is observed that the odd moments of $colspan(\boldsymbol{V}_n)$ grows in the moment expansion with only $\boldsymbol{b}_2$, the starting vector for the thermal system, so these moments can be neglected. In addition, it is noted that the even moments of $colspan(\boldsymbol{V}_n)$ appears to grow with the odd moments of $colspan(\boldsymbol{V}_s)$ while the odd moments of $colspan(\boldsymbol{V}_n)$ grows with the even moments of $colspan(\boldsymbol{V}_s)$. Note that $\boldsymbol{b}_1 = -{\boldsymbol{K}_1}^{-1}\overline{\boldsymbol{F}}_1 - {\boldsymbol{K}_1}^{-1}\overline{\boldsymbol{C}}_T\boldsymbol{b}_2$, so the starting vector $\boldsymbol{b}_1$ constitutes a coupled moment since it depends on $\boldsymbol{b}_2$. On this basis, we can pick the even (coupled) moments of $colspan(\boldsymbol{V}_n)$ and the odd moments of $colspan(\boldsymbol{V}_s)$ to form a new coupled Krylov subspaces $\mathcal{K}_{r2}\left(\widetilde{\boldsymbol{A}}, \boldsymbol{Y}, \boldsymbol{b}_1\right)$ and $\mathcal{K}_{r1}(\boldsymbol{G}^2, \boldsymbol{G}\boldsymbol{b}_2)$ with a new projection matrix $\boldsymbol{V}_m$ defined as:

$$colspan(\boldsymbol{V}_m) = colspan\left\{\boldsymbol{b}_1, \widetilde{\boldsymbol{A}}\boldsymbol{b}_1 + \boldsymbol{Y}\boldsymbol{G}\boldsymbol{b}_2, \widetilde{\boldsymbol{A}}^2\boldsymbol{b}_1 + \widetilde{\boldsymbol{A}}\boldsymbol{Y}\boldsymbol{G}\boldsymbol{b}_2 + \boldsymbol{Y}\boldsymbol{G}^3\boldsymbol{b}_2, \ldots\right\} \quad (6.72)$$

In (6.72), the coupled term of $\mathcal{K}_{r2}\left(\widetilde{\boldsymbol{A}}, \boldsymbol{Y}, \boldsymbol{b}_1\right)$ is $\boldsymbol{Y}$ and it is recursively iterated with $\mathcal{K}_{r1}(\boldsymbol{G}^2, \boldsymbol{G}\boldsymbol{b}_2)$. $\boldsymbol{V}_m$ constitutes a column space where the coupled undamped system state evolves. The next task is numerical computation of $\boldsymbol{V}_m$ and this can be achieved with the modified Arnoldi algorithm for coupled second-order system developed in Algorithm 6.5. Numerical issues associated with the construction of the projection basis $\boldsymbol{V}_m$ is constituted by the computation of the inverse of $\boldsymbol{K}_1$ and $\boldsymbol{H}$ which is expensive by direct inverse approach. By performing LU decomposition of $\boldsymbol{K}_1$ and $\boldsymbol{H}$ and solving a system of linear equations, the recursive procedure becomes efficient computationally than using a direct inverse procedure. Since the coupled moments are not picked successively from the moment expansion of the Krylov subspace of the global system, there is possibility of weak linear independence in the Arnoldi iteration, so a re-orthogonalization is applied through singular value decomposition (SVD) based on which singular values are

retained for the system projection. In Algorithm 6.5, the modified Arnoldi algorithm for the coupled second-order Krylov subspace is outlined.

Algorithm 6.5 (**Coupled second-order Arnoldi algorithm**)

Input: matrices $\widetilde{\boldsymbol{A}}, \boldsymbol{Y}, \boldsymbol{G}, \boldsymbol{b}_1, \boldsymbol{b}_2$, dimension of Krylov subspace q_2

1. Set $\tilde{\mathbf{v}}_1 = \frac{\boldsymbol{b}_1}{\|\boldsymbol{b}_1\|_2}$ $\bar{\mathbf{v}}_1 = \frac{\boldsymbol{G}\boldsymbol{b}_2}{\|\boldsymbol{G}\boldsymbol{b}_2\|_2}$
2. **for** $k = 1, 2, \ldots\ldots, q_2$ **do**
   a. $\boldsymbol{u}_1 = \widetilde{\boldsymbol{A}}\tilde{\mathbf{v}}_k + \boldsymbol{Y}\bar{\mathbf{v}}_{\mathrm{k}}$; $\boldsymbol{u}_2 = \boldsymbol{G}^2\bar{\mathbf{v}}_{\mathrm{k}}$

   Orthogonalization

   b. **for** $j = 1, \ldots, k$ **do**

   $h_1 = \tilde{\mathbf{v}}_j{}^T \boldsymbol{u}_1$; $h_2 = \bar{\mathbf{v}}_j{}^T \boldsymbol{u}_2$

   $\boldsymbol{u}_1 \leftarrow \boldsymbol{u}_1 - h_1\tilde{\mathbf{v}}_j$; $\boldsymbol{u}_2 \leftarrow \boldsymbol{u}_2 - h_2\bar{\mathbf{v}}_j$

   end for

   c. Normalization: if the vector $\|\boldsymbol{u}_1\|_2 < \epsilon$ break the loop. Otherwise, the ith column of the projection matrices are:

$\tilde{\mathbf{v}}_{k+1} = \frac{\boldsymbol{u}_1}{\|\boldsymbol{u}_1\|_2}$ $\bar{\mathbf{v}}_{k+1} = \frac{\boldsymbol{u}_2}{\|\boldsymbol{u}_2\|_2}$

end for

3. **output** $\widetilde{\boldsymbol{V}}_m = \left(\tilde{\mathbf{v}}_1, \ldots, \tilde{\mathbf{v}}_{\mathrm{q2}}\right)$
4. **compute** SVD $\widetilde{\boldsymbol{V}}_m \approx \boldsymbol{U}_q \boldsymbol{\Sigma}_q \boldsymbol{V}_q{}^T$ and pick $q \ll \mathrm{N}_1$ singular values
5. **return** $\boldsymbol{V}_m = \left(\mathbf{v}_1, \ldots, \mathbf{v}_{\mathrm{q}}\right)$

Finally, computation of the reduced system matrices $\boldsymbol{M}_r$, $\boldsymbol{K}_r$, $\boldsymbol{C}_r$ and $\boldsymbol{F}_r$ can be performed according to Eq. (6.63). The solution of the reduced-order model is

obtained based on Newmark time integration scheme and the results are analysed in details in Sec. 6.6.

6.6 Numerical results

The system configuration considered here is shown in Fig. 5.6. A total of 15 min or 900 sec of cooling is specified for the PV system after the system had been raised to a homogeneous temperature of $150℃$. We are mainly interested in the thermomechanical response of the Silicon layer, so the displacements of the second layer are output for the reduced system. Model results for various formulations are analysed and discussed in this section based on the relative error between the original system outputs (displacements) and the reduced order outputs as well as the computational time required to obtain the reduced system solutions. The results are divided into three categories namely, state-space model, second-order based model and coupled second-order structure preserving model. In the sequel, the error plots and displacement plots for the original and reduced system are presented. Plots of displacements are presented in accordance with Fig. 5.15. In the displacement plots V_1 is the projection matrix of the global system except in section 6.5.3 where V_1 represents the projection matrix of the coupled mechanical system while V_2 represents the projection matrix of the thermal system. w, U and V denote deflection and mid-plane displacements of the layers in the x_1 and x_2 directions respectively.

6.6.1 State-space model

Figure 6.11 (a–c) shows the error plots for the three displacement variables at times representative of the beginning, middle and end of the simulation. The efficiency of the POD scheme for the state-space representation of the thermomechanical system is observed. In Fig. 6.11 (d), the reduced-order output displacements at node

2885 in the Silicon layer show good approximation as the relative error of about 10^{-6} is attained for V displacement while less than 10^{-8} error is achieved for w and U displacements. It is evident from the error plots that the system dynamic response is characterized by low inertial forces since the error attained with order 1 is about 10^{-4} for V, w and U displacements. In order words, the thermomechanical system response of the PV module is largely quasi-static.

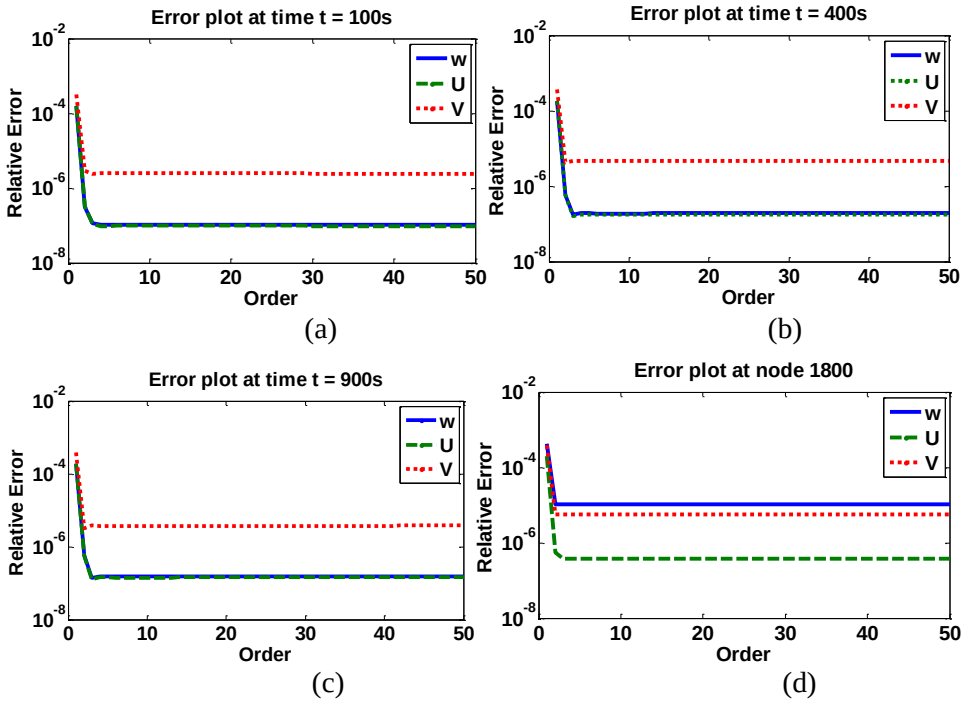

Figure 6.11 Error plots for reduced-order State-space model at times (a) 100 sec (b) 400 sec (c) 900 sec and node (d) 1800.

A stable error bound is attained for all the displacement outputs in time and space domain with order 5. To ensure low computational cost, the POD scheme is applied to the state-space representation of the system by collecting few snapshots (about 10) which strongly characterize the system dynamic response. Specifically, the first 10 snapshots of the full system solution are collected for the POD scheme and as

remarked in Sec. 6.3, the collection of more snapshots may improve the result by ensuring that the POD modes are better approximated and in turn improve the reduced system outputs. However, observations from numerical experiments indicate that collection of too many snapshots may lead to high computational cost of the POD scheme and poor approximation of the POD modes which may strongly impair the accuracy and stability of the reduced system solution. In essence, only necessary snapshots which ensure accuracy and numerical stability of the reduced system at low computational cost are collected.

Displacement versus normalized longitudinal direction plots at the last time step for the Silicon layer are output for the reduced-order solution as shown in Fig. 6.12 and it is observed that the complete solution is well approximated by the reduced solution with order as low as 3.

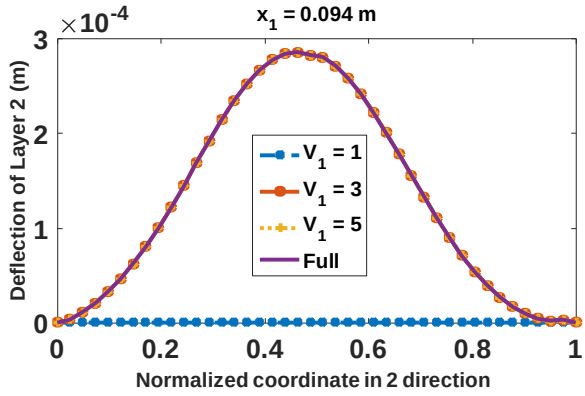

(a)

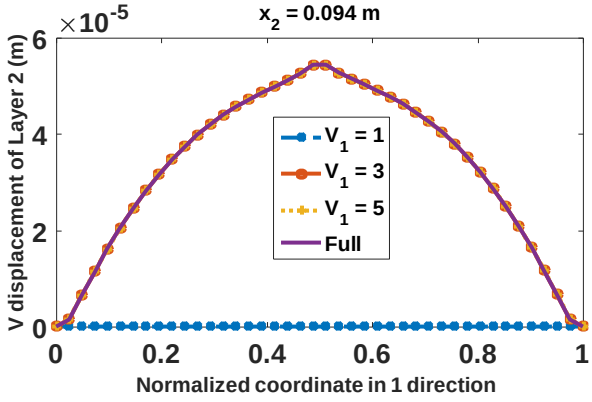

(b)

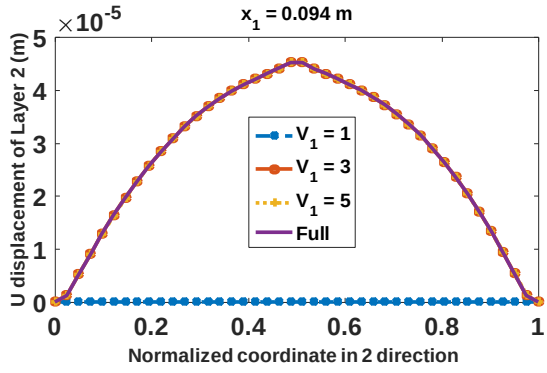

(c)

Figure 6.12 (a) w (b) V (c) U Displacement variables for the reduced solution and full solution.

6.6.2 Second-order preserving model

To preserve the second-order structure of the global system, a second-order based reduction is implemented and the results are shown in Figs. (6.13 – 6.16). Two different approaches are considered, a POD based approach and a rational second-order Krylov method. The requirement for collection of snapshots for the second-order POD method is as described in Sec. 6.6.1 except that the snapshots in this

case consist of augmented vectors of displacement and temperature at discrete times. As shown in Fig. 6.13, a good approximation of the system output is obtained with a relative error magnitude of 10^{-6} for the V displacement and more than 10^{-7} for w and U displacement variables in time and space domains. In case of the second-order POD scheme, a stable error bound is attained with less than order 5 at the last time step. These results confirm the suitability of the POD scheme for preservation of the second-order structure of the coupled thermomechanical system.

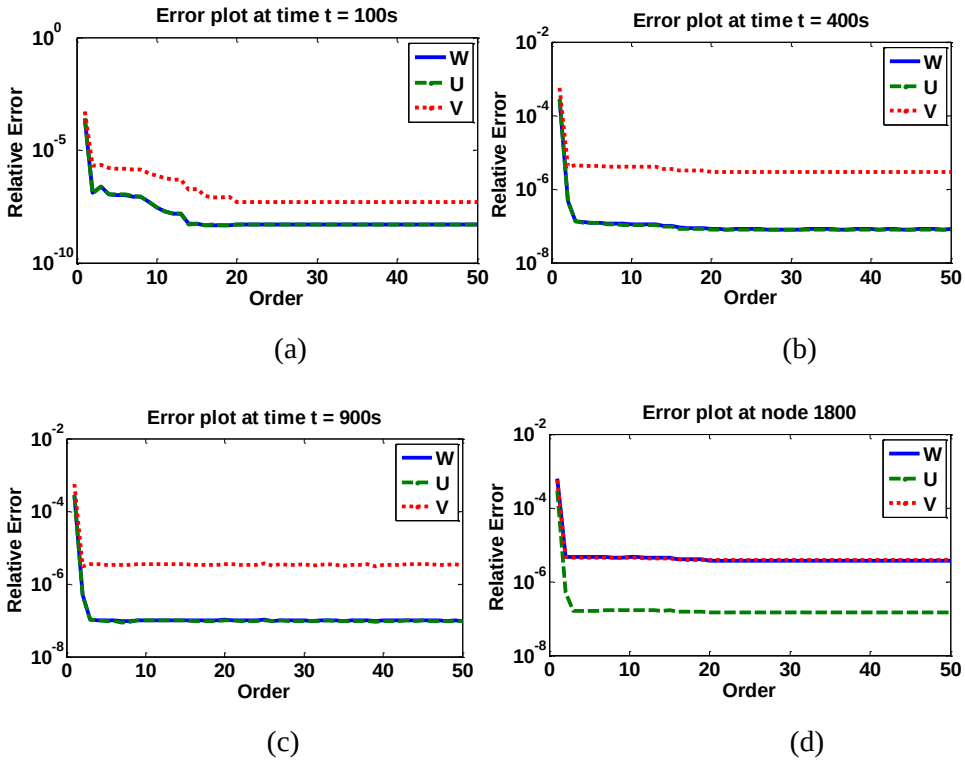

Figure 6.13 Error plots for POD-based second-order preserving reduced-order system at times (a) 100 sec (b) 400 sec (c) 900 sec and node (d) 1800.

A good approximation of the system outputs is obtained as shown in Fig. 6.14 with reduced order 3. This outcome supports the previously remarked statement that the

coupled mechanical system is of very low inertial such that the system dynamic response is very close to a quasi-static case.

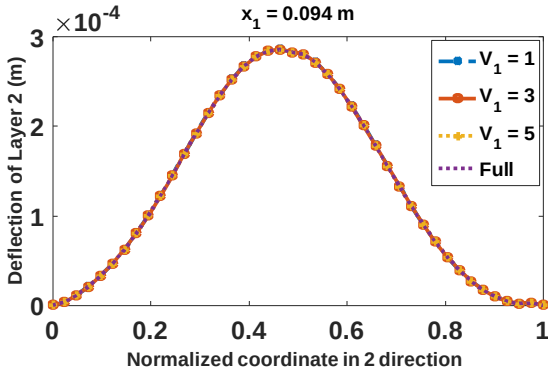

(a)

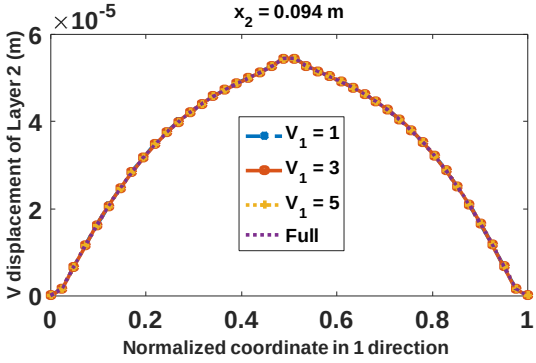

(b)

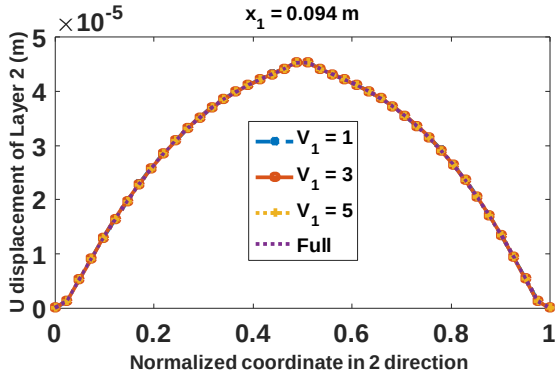

(c)

Figure 6.14 (a) w (b) V (c) U Displacement variables for the POD second-order preserving reduced solution and full solution.

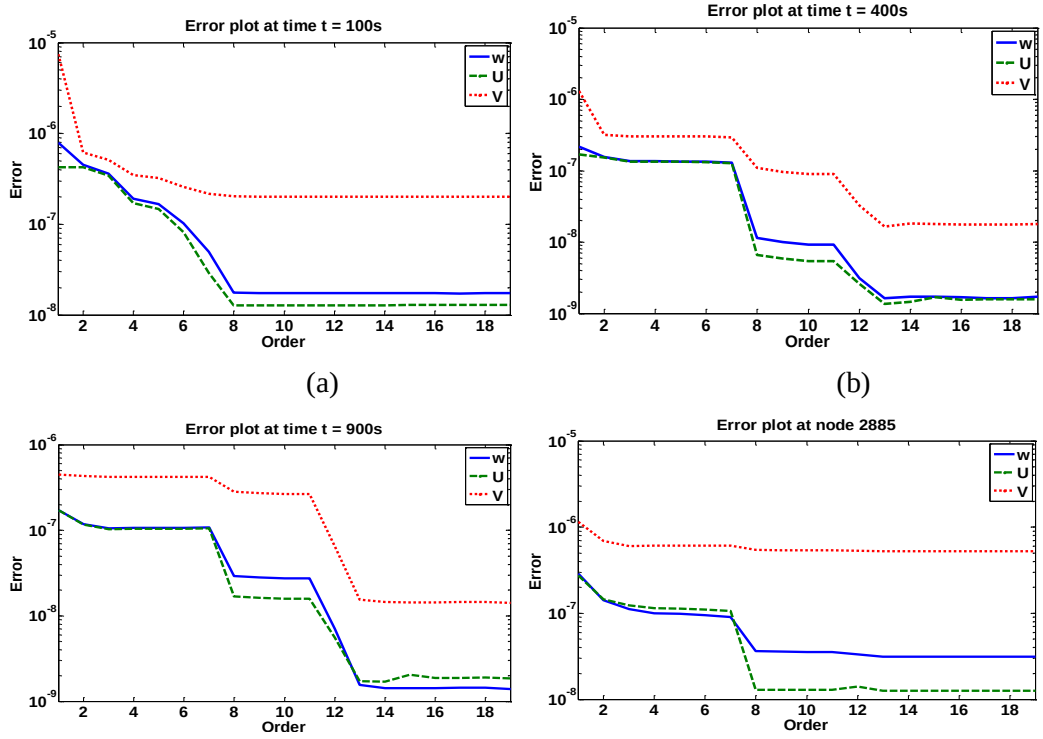

(a) (b)

(c) (d)

Figure 6.15 Error plots for Krylov-based second-order preserving reduced-order system at times (a) 100 sec (b) 400 sec (c) 900 sec and node (d) 2885.

An alternative second-order model is also considered based on rational Krylov method. Four expansion points (0, 0.01, 0.02, 0.03) are chosen to enhance the system outputs as it is observed that expansion about 0 leads to quick loss of orthogonality as the iteration proceeds. Few moments are matched at each expansion point such that the error is spread across the expansion points. This ensures more stable and reduced model outputs with better accuracy as shown in Figs. 6.15-6.16. In the time domain, an error of about 10^{-9} is achieved for w and U displacements while an error magnitude of about 10^{-8} is achieved for V displacement. In the space domain, an error magnitude of about 10^{-8} is achieved for w and U displacements while an absolute error magnitude of more than 10^{-6} is achieved for V displacement. With a reduced order of 3, a good system output approximation is achieved for the displacement variables (see Fig. 6.16).

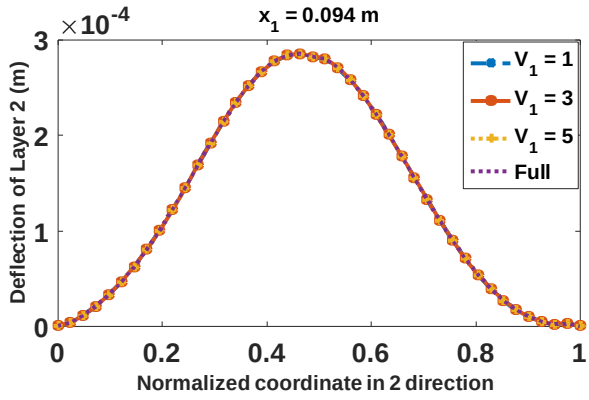

(a)

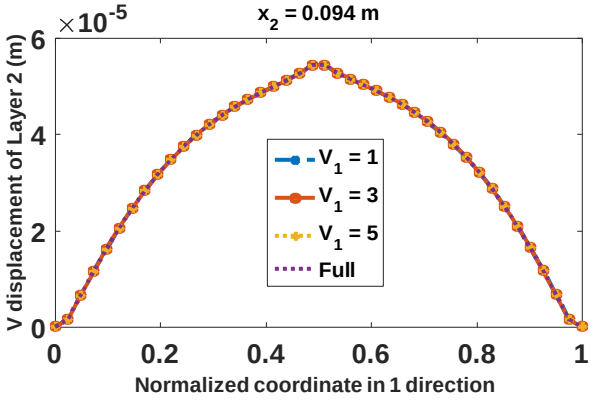

(b)

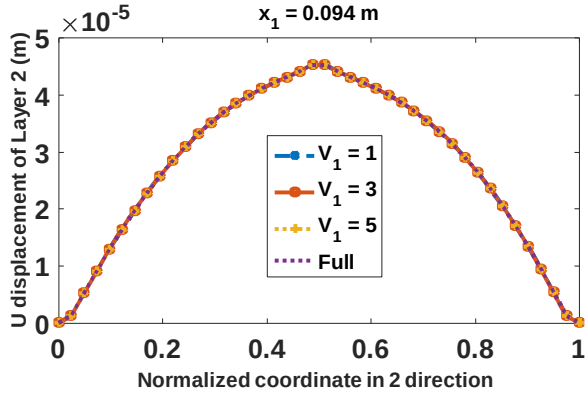

(c)

Figure 6.16 (a) w (b) V (c) U Displacement variables for the Krylov second-order preserving reduced solution and full solution.

6.6.3 Coupled second-order structure preserving model

As the second-order reduced model could not preserve the coupled structure of the global system, a new coupled structure preserving model is proposed. This approach ensures that the individual systems are reduced independently with more

flexibility in the choice of order of reduction for each sub-system. While the uncoupled thermal system is well reduced by applying basic Krylov method as shown in Fig. 6.10, a new structure preserving formulation is applied to the mechanical system with the order of the thermal system fixed at 10 and the results show good approximation of original system outputs (see Figs. 6.17–6.18).

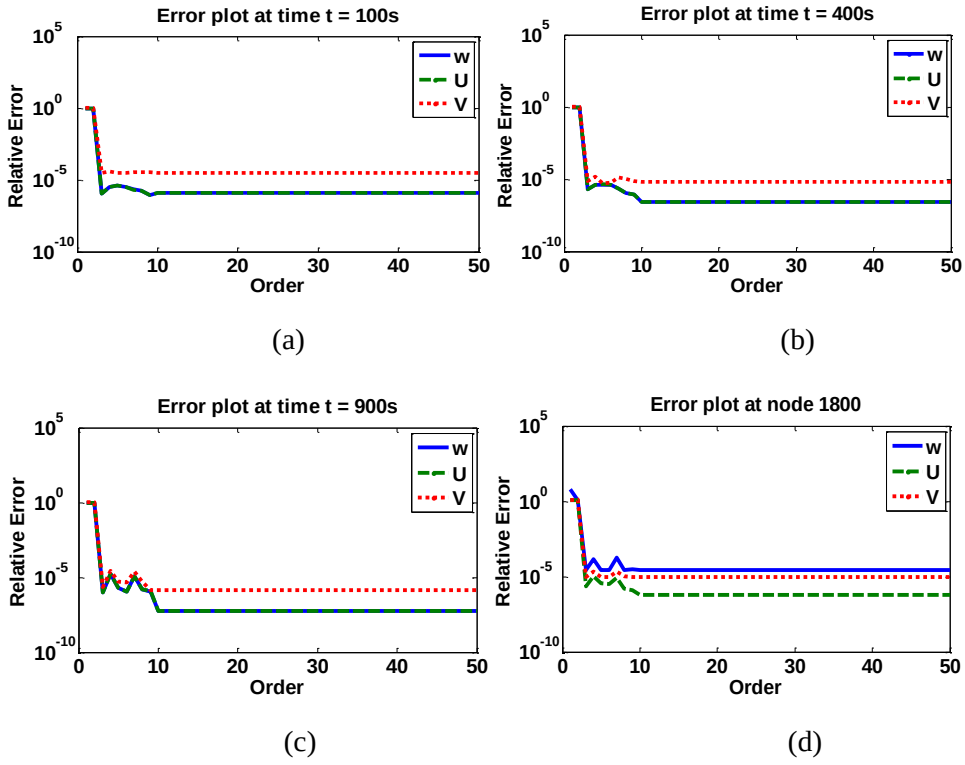

Figure 6.17 Error plots for Krylov-based coupled second-order structure preserving reduced-order system at times (a) 100 sec (b) 400 sec (c) 900 sec and node (d) 1800 for thermal order $V_2 = 10$.

In the time and space domain, an error magnitude of about 10^{-8} is achieved respectively for w and U displacements while V displacement output is reduced to

the tune of 10^{-7} relative error. It is remarked from Fig. 6.17-6.18 that the coupled mechanical system attains a stable error bound at a reduced order of about 10.

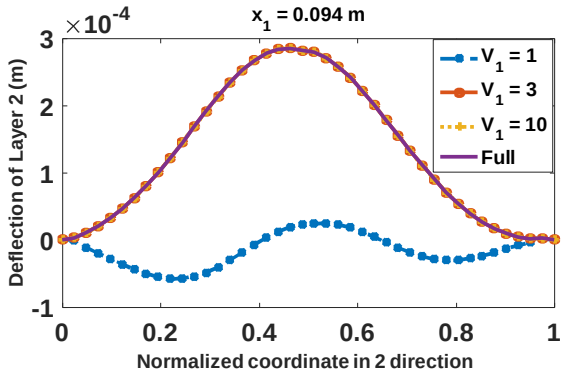

(a)

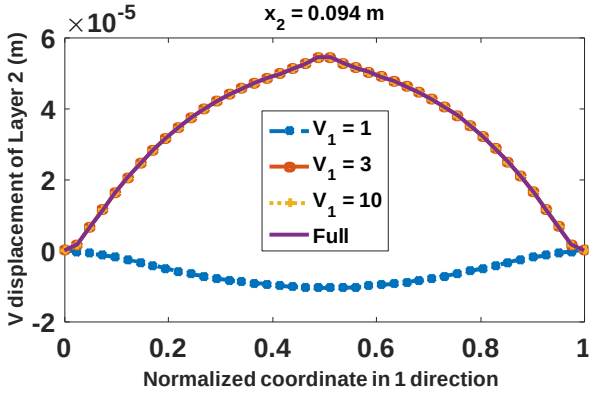

(b)

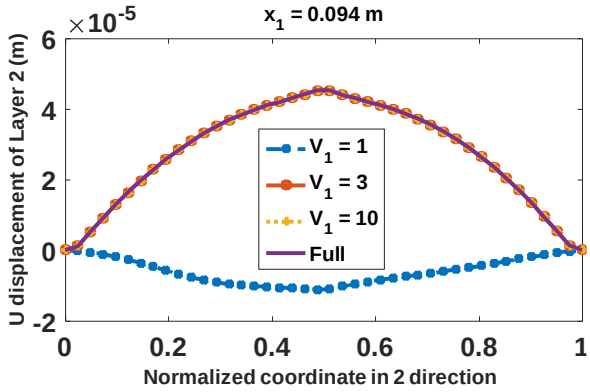

(c)

Figure 6.18 (a) w (b) V (c) U Displacement variables for the Krylov coupled second-order structure preserving reduced solution and full solution for thermal order $V_2 = 10$.

With reduced model of order of 3, the displacement outputs of the reduced-order model adequately approximate the outputs of the original system.

6.6.4 Computation time for the reduced models

Finally the computational time for the various models is reported in Table 6.1. This comparison is important to highlight the significant gain in computational cost of the reduced solutions. It is evident from Table 6.1 that there is a huge computational gain in the solution of the reduced solution. This gain will be a great advantage in situation where repeated simulations are required as the input function only needs be changed to investigate the system response.

Table 6.1. Computational time for solution of reduced models and full solution.

Model	Order	Computational time
Coupled second-order structure preserving reduction	$V_1 = 3$ $V_2 = 10$	0.522 sec
	$V_1 = 5$ $V_2 = 10$	0.851 sec
Second-order preserving reduction	$V_1 = 3$	0.420 sec
	$V_1 = 5$	0.50 sec
State-space reduction	$V_1 = 4$	0.681 sec
	$V_1 = 5$	1.024 sec
Full solution	16000	838 sec

6.6.5 Validation of the coupled second-order structure preserving model

The proposed structure preserving model is validated by using another input function (6.73) to excite the thermo-mechanical system. The new cooling function is plotted against time as shown in Fig. 6.19.

$$i(t) = 25 + (0 - 25)\exp^{(0.002t)} \tag{6.73}$$

In the error plots for the validated model in Fig. 6.20, order of the thermal system is fixed at 10 and order of the mechanical system is varied up to 50. It is observed that the reduced-order model derived using the coupled second-order Krylov approach satisfactorily approximates the original system outputs to the tune of 10^{-7} relative error in time and space domains. It is evident that a stable error bound occurs at a reduced model of an order of 10, the thermal system order. In Fig. 6.21,

it is shown that validated system outputs is well approximated by the reduced solution with order of 5 which shows efficiency of the proposed coupled second-order Krylov approach for reduction of coupled thermo-mechanical systems.

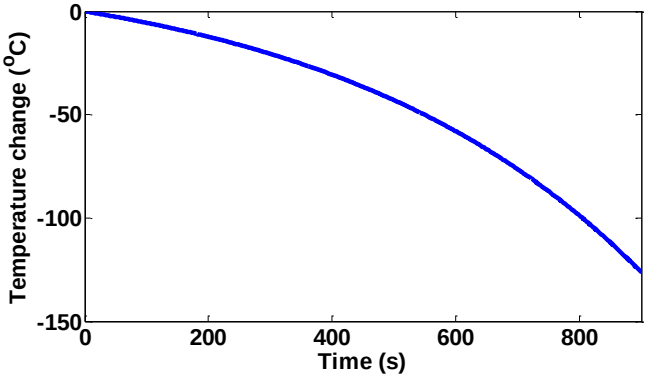

Figure 6.19. Input function for validation of coupled structure preserving model.

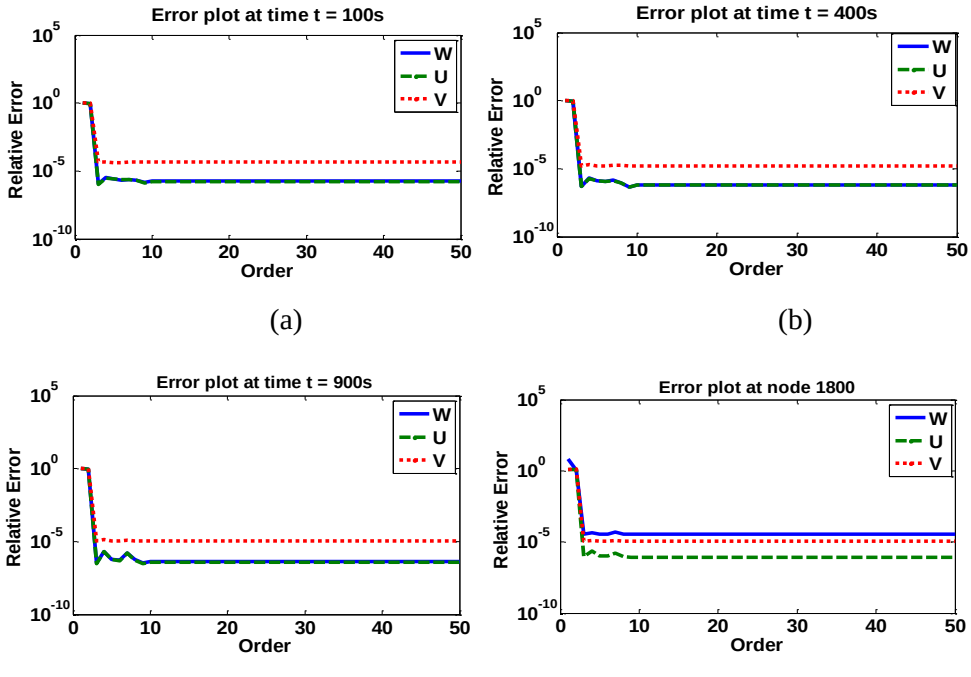

Figure 6.20 Error plots for validation of Krylov-based coupled second-order structure preserving reduced-order model at times (a) 100 sec (b) 400 sec (c) 900 sec and node (d) 1800 for thermal order $V_2 = 5$.

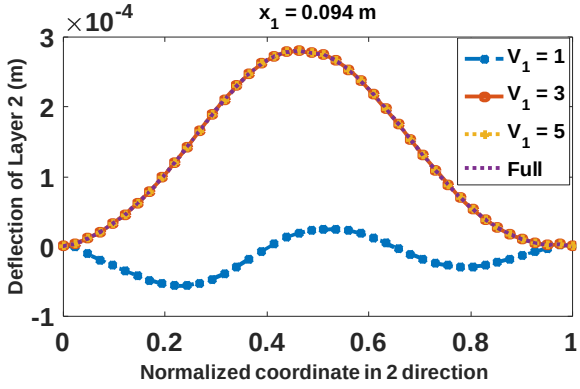

(a)

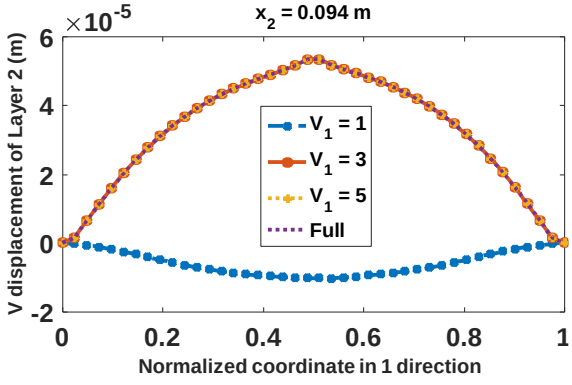

(b)

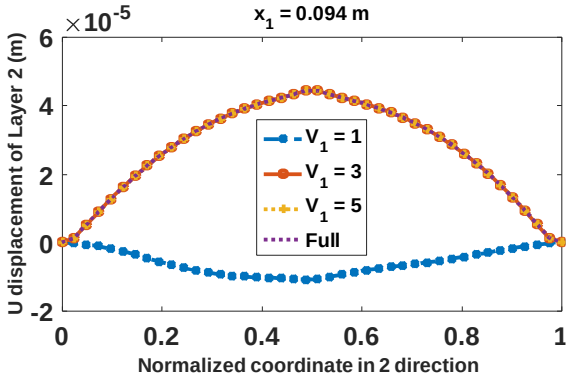

(c)

Figure 6.21 (a) w (b) V (c) U Displacement variables for validated model of the coupled second-order structure preserving reduced solution and full solution for thermal order $V_2 = 5$.

CHAPTER 7

CONCLUSIONS

Advanced beam formulations (2D and 3D) based on shear-lag theory are presented and implemented in this work with the aim to investigate thermo-mechanical stress distribution inside a PV module during lamination. With respect to the 2D case, a detailed analysis is conducted by comparing a spatially uniform temperature distribution dependent on time and a non-uniform temperature distribution obtained by numerically solving the heat conduction equation in space and time. A semi-analytic approach is proposed in this work by taking into account the viscoelastic behaviour of the EVA layer, based on fractional calculus considerations. The predictions of this shear-lag model have been compared with another classical structural model where the EVA layer is considered as a continuum, as in linear elastic finite element analyses of PV laminates. The results of the stress analysis show that Silicon is subjected to a residual mean compressive stress of about 60 MPa if uniform temperature is considered. On the other hand, if a non-uniform temperature distribution is accounted for in the analysis, as it happens during the simulation of the transient heat conduction regime, the stress field reduces to 40 MPa after lamination.

To further refine the present semi-analytical predictions, an extension to 3D coupled thermo-visco-elastic shear-lag model is considered in which a laboratory

test PV module of geometric size 250×250 mm with 4 Silicon cells is used for this analysis. Viscoelastic properties of EVA is taken into account to enhance the residual stress prediction and this is achieved by using an asymptotic viscoelastic model which is stable for small and large time steps of strain increments. The result of the investigation shows that the PV module experiences small magnitude of interfacial stresses at the laminate edges while at the mid-portion, magnitude of the interfacial stresses are negligible. Examination of the mean axial residual stresses at different regions in the laminate shows that the Silicon cells experience compressive stress state of higher magnitude at the laminate centre with respect to the laminate edges. The backsheet and the glass layers are largely in tension. Study of the transient stress evolution indicates that the transient response of the coupled system imitate the cooling function during lamination, an observation which highlights the importance of the cooling function.

As the numerical solution of the 3D coupled shear-lag model is characterized by many degrees of freedom after finite difference discretization with a high computational cost, model order reduction is considered to circumvent this hurdle. To hierarchically examine the suitability of model order reduction to PV systems, a formulation for heat conduction within a 2D photovoltaic system is first derived and a numerical solution based on a finite difference scheme is implemented. POD/DEIM order reduction technique with a modified formulation is identified as suitable and efficient to reduce the thermal system through a combination of linear subspace projection and interpolation of nonlinear terms. It is shown that the heat conduction of a PV system discretized into 2166 nodes along the module span is successfully reduced to a compact model with dynamical order k=7, based on interpolation with only $m_1=m_2=3$ points. Investigation shows that the efficiency and accuracy of the numerical solution can be fine- tuned by carefully selecting a different interpolation order for individual nonlinear terms and from the validation

results, it is concluded that the reduced solution is not very sensitive to the input function as it approximates well the simulated irradiance data much the same way as the experimental irradiance data used in the construction of the compact model.

Having established a suitable order reduction for a thermal system of PV module during service, the efficient POD technique is extended to model order reduction of the proposed 3D coupled thermo-mechanical model. Due to the coupled second-order structure of the system equation, 3 difference model order reduction procedures are examined. The classical state-space approach, a first-order based method is implemented using a POD technique to derive the projection basis and the results of reduced system outputs show good approximation of the original system outputs with a reduced system order of 10 and relative error of 10^{-7} attained. A second-order based approach is also considered to preserve the second-order structure of the global system. This procedure is investigated by implementing 2 different techniques, a POD based method and a second-order Krylov based method. It is shown that the POD technique is also suitable to preserve the second-order structure of the global system with good accuracy of the reduced system approximation of the original system outputs to the tune of above 10^{-7} error and with reduced system order of 5. The second-order Krylov based method on the other hand is implemented based on rational second-order Krylov method in order to obtain improved reduced system outputs. A good approximation of the original system outputs is obtained with reduced system order of 3 and a relative error of about 10^{-9} is achieved. Finally, a new coupled second-order Krylov based formulation is proposed to preserve the coupled second-order structure of the thermo-mechanical system and to allow for more control in the choice of the order of individual system. To obtain a stable reduced order model with a reasonable degree of accuracy, the projection basis of the coupled Krylov subspaces is derived based on a combination of modified Gram-Schmidt algorithm

for second-order system and singular value decomposition method (SVD). With a fixed order of 10 for the thermal system, the outputs of the reduced mechanical system approximate well the original system outputs to the tune of 10^{-8} error and with reduced system order of 10. An important observation in the reduction of the coupled thermo-mechanical system shows that the mechanical system response during lamination is close to a quasi-static case as a system with reduced order of 1 leads to fairly satisfactory approximation of the original system outputs with relative error of about 10^{-4}. Finally, the coupled second-order Krylov model is validated by using another input function and it is shown that the reduced solution of the validated model approximates well the outputs of the full model, thus confirming the efficiency of the proposed coupled second-order Krylov method.

It is believed that the current coupled formulation which is derived based on shear-lag theory and discretization by finite difference method can be improved upon by considering a formulation based on finite element method using shell theory that takes into account the rotational degrees of freedom of the system. In addition, finite element models enjoy widespread use in structural engineering with discretization in space leading to high dimensional system of ODEs whose transient analysis takes much computational effort. Therefore, application of model order reduction to produce a compact representation of the system with low dimension but accurate approximation of the large-scale system is desirable. In the case of PV module where coupling between many fields is well established, advanced model order reduction techniques are available for structure preservation of the reduced model which can guarantee better control in the analysis of the system response. Consequently, this procedure can offer opportunity to investigate failures such as thermomechanically induced degradation phenomena examples of which are delamination and fracture of Silicon solar cell in photovoltaic laminates. The computational requirements of such simulation can efficiently be economized

by using model order reduction techniques and in particular, computational complexities associated with phenomena such as crack propagation and fatigue degradation which are often characterized by fine mesh of the area of discontinuity and repeated application of load can be effectively minimized.

REFERENCES

[1] B. Metz, O. Davidson, P. Bosch, R. Dave and L. M. (editors). Climate change 2007: Working group III: Mitigation of climate change. Tech. rep., IPCC (Intergovernmental panel on climate change), 2007.

[2] U. Eitner, Thermomechanics of photovoltaic modules, Ph.D thesis, Centre for Engineering Sciences, Martin Luther University of Halle-Wittenberg (2011).

[3] M. Paggi, I. Berardone, A. Infuso, M. Corrado, Fatigue degradation and electric recovery in Silicon solar cells embedded in photovoltaic modules, Scientific Reports 4 (2014) 4506 doi:10.1038/srep04506.

[4] M. Köntges, I. Kunze, S. Kajari-Schröder, X. Breitenmoser, B. Bjrneklett. The risk of power loss in crystalline silicon based photovoltaic modules due to microcracks, Sol. Energy Mater. Sol. Cells, 95 (2011), 1131-1137.

[5] M. Paggi, M. Corrado, M.A. Rodriguez., A multi-physics and multiscale numerical approach to microcracking and power-loss in photovoltaic modules. Composite Structures 2013; **95**: 630-638.

[6] Eitner, U., Köntges, M., and Brendel, R. Use of digital image correlation technique to determine thermomechanical deformations in photovoltaic laminates: measurements and accuracy. Solar Energy Mater. Solar Cells, 94 (2010), 1346-1351.

[7] M. Paggi, M. Corrado, M.A. Rodriguez. A multi-physics and multi-scale numerical approach to microcracking and power-loss in photovoltaic modules. Compos Structure 95 (2013), 630-638.

[8] A. Sapora, M. Paggi, A coupled cohesive zone model for transient analysis of thermoelastic interface debonding, Computational Mechanics, 53 (2014), 845-857.

[9] Y. Leea, A. Andrew, B. Taya, Finite Element Thermal Analysis of a Solar Photovoltaic Module, Energy Procedia 15 (2012), 413-420.

[10] M. Paggi, A. Sapora, Numerical Modelling of Microcracking in PV Modules induced by Thermo-mechanical loads, Energy Procedia 38 (2013), 506-515.

[11] Y. Wen, C. Basaran., An analytical model for thermal stress analysis of multi-layered microeloctronic packaging. Mechanics of Materials 2004; **36**: 369-385.

[12] U. Eitner, S. Kajari-Schröder, M. Köntges, H. Altenbach, Thermal Stress and Strain of Solar Cells in Photovoltaic Modules, Advanced Structured Materials Vol. 15, 2011, 453-468.

[13] E. Suhir, D. Shangguan, L. Bechou, Predicted thermal stresses in a trimaterial assembly with application to silicon based photovoltaic module, Journal of Applied Mechanics, (2013), Vol. 80, 1-10.

[14] M. Tahani, A. Nosier, Free edge stress analysis of general cross-ply composite laminates under extension and thermal loading, Composite Structures 60 (2003) 91-103.

[15] Y. Wen, C. Basaran, Thermomechanical stress analysis of multilayered electronic packaging, Journal of Applied Mechanics, (2003), Vol. 80, 134-138.

[16] S.O. Ojo, S. Grivet-Talocia, M. Paggi, Model order reduction applied to heat conduction in photovoltaic modules, Composite Structures 119 (2015), 477-486.

[17] I. Tobias, C. del Canizo and J. Alonso. Handbook of Photovoltaic Science and Engineering, chap. Crystalline Silicon Solar Cells and Modules, 255-306. Wiley, 2003.

[18] Handbook for Solar Photovoltaic systems. http://www.bca.gov.sg/publications/others/handbook_for_solar_pv_systems.pdf

[19] S. Ranjan, S. Balaji, Rocco A. Panella, B. Erik Ydstie, Silicon solar cell production, Computers and Chemical Engineering 35 (2011), 1439-1453.

[20] J. Pern, Module Encapsulation materials, Processing and Testing, APP international PV reliability workshop, 2008.

[21] R. F. M. Lange, Y. Luo, R. Polo, J. Zahnd, The lamination of (multi) crystalline and thin film based photovoltaic modules, Progress in photovoltaics: Research and applications (2010), Wiley InterScience (www.interscience.wiley.com). DOI: 10.1002/pip.993, 1-6.

[22] Y.S. Tsuo, T.H. Wang, and T.F. Ciszek, Crystalline-Silicon Solar Cells for the 21st Century, conference paper: Electrochemical Society Annual Meeting (1999), NREL/CP-590-26513, 3-5.

[23] S. W. Gluntz, R. Preu, D. Biro, Crystalline silicon solar cells – state – of – Art and Future Development, Comprehensive Renewable Energy, ISBN: 978-08-087873-7 (2012), 6-10.

[24] M. T. Zarmai, N.N. Ekere, C.F. Oduoza, E. H. Amalu, A review of interconnection technologies for improved crystalline silicon solar cell photovoltaic module assembly, Applied Energy 154 (2015), 173-182.

[25] R. Kopecek , T. Buck , A. Kränzl , J. Libal , K. Peter, A. Schneider , P. Sánchez-Friera , I. Röver, K. Wambach, E. Wefringhaus, P. Fath, Module interconnection with alternate p- and n-type Silicon solar cells, http://isc-konstanz.de/fileadmin/deutsch/dokumente/publikationen/DRESDEN-KOPECEK_et_al..pdf.

[26] U. Blieske, T. Doege, P. Gayout, M. Neander, D. Neumann and A. Prat. Light-trapping in solar modules using extra-white textured glass. In: Proceedings of 3rd World Conference on Photovoltaic Energy Conversion, 2003, 188-191.

[27] G. Helsch, J. Deubener, Compatibility of antireflective coatings on glass for solar applications with photocatalytic properties, Solar Energy 86 (2012), 831-836.

[28] M.Paggi, A. Sapora, An accurate thermos-viscoelastic rheological model for ethylene vinyl acetate based on fractional calculus. International journal of photoenergy 2015, 1-17.

[29] M. Di Paola, F. Pinnola, M. Zingales, A discrete mechanical model of fractional hereditary materials, Meccanica 2013, **48**: 1573-1586.

[30] M. Di Paola, A. Pirrotta, A. Valenza, Visco-elastic behavior through fractional calculus: An easier method for best fitting experimental results, Mechanics of Materials 2011, 43: 799-806.

[31] R. Taylor, Finite Element Analysis Program Theory Manual (version 8.3), University of Berkeley, California (2011), 74-80.

[32] M. Kempe. Design criteria for photovoltaic back-sheet and front-sheet materials. Photovoltaics International, vol. 2: 2008, 100-104.

[33] G. Jorgensen, K. Terwilliger, J. DelCueto, S. Glick, M. Kempe, J. Pankow, F. Pern and T. McMahon. Moisture transport, adhesion, and corrosion protection of

PV module packaging materials. Solar Energy Materials and Solar Cells, vol. 90(16): 2006, 2739-2775,

[34] D. C. Jordan, S. R. Kurtz Photovoltaic Degradation Rates - An Analytical Review, Progress in Photovoltaics: Research and Applications (2011), 1-5.

[35] A. Kaisare, Reliability challenges for solar modules, InterPACK tutorial (2011), 28-57.

[36] M. Köntges, S. Kurtz, C. Packard, U. Jahn, K. A. Berger, K. Kato, T. Friesen, H. Liu, M. Van Iseghem, Performance and reliability of photovoltaic systems, Subtask 3.2: Review of failures of photovoltaic modules, IEA PVPS Task 13 External final report IEA-PVPS (2014), 4-20.

[37] S. Ling Ho, A numerical analysis of penny-shaped delaminations in an encapsulated silicon module, Electronic Components and Technology Conference (ECTC), 2011 IEEE 61st, 1115-1121

[38] S. Kaplanis, E. Kaplani (2011). Energy performance and degradation over 20 years performance of BP c-Si PV modules: Simulation Modelling Practice and Theory, Vol. 19, 1201-1211.

[39] O. C. Zienkiewicz, R. L. Taylor, The Finite Element Method, fifth edition Vol. 2, Butterworth-Heinemann (2000), 38-46.

[40] A. S. Wineman and K. R. Rajagopal. Mechanical Response of Polymers: An Introduction, Cambridge University Press, 2000.

[41] M. Pander, S. Dietrich, S.-H. Schulze, U. Eitner, M. Ebert, Thermo-mechanical assessment of solar cell displacement with respect to the viscoelastic behaviour of the encapsulant, In Proc. 12th International Conference on Thermal, Mechanical and Multi-Physics Simulation and Experiments in Microelectronics and Microsystems (EuroSimE), 2011, 1-6.

[42] F. Mainardi, Fractional Calculus and Waves in Linear Viscoelasticity: An Introduction to Mathematical Models. London: Imperial College Press, 2010.

[43] C. Basaran, Y. Wen, Influence of interfacial compliance on thermomechanical stresses in multilayered microelectronic packaging, IEEE transactions on advanced packaging 2006; **26**: 666-673.

[44] S. Abdolmajid Yousefsani, M. Tahani, An analytical investigation on thermomechanical stress analysis of adhesively bonded joints undergoing heat conduction, Arch Appl Mech 2014, **84**: 67-79.

[45] S. Timoshenko, Analysis of Bi-metal thermostats, J. Optic. Soc. Am. 1925, vol. 11, 233-255.

[46] B. A. Boley, R. B. Testa, Thermal stresses in composite beams, International journal of solid and structures 1969, 5, 1153-1169.

[47] D. Chen, S. Cheng, T. D. Gerdhart, Thermal stresses in laminated beams, J. Thermal Stresses 1982, Vol. 5, 67-84.

[48] P. B. Grimado, Interlamina thermoelastic stresses in layered beams, J. Thermal stresses 1978, vol. 1, 75-86.

[49] T. Hayashi, Analytical study of interlaminar shear stresses in a laminate composite plate, Trans. Jpn. Soc. Aeron. & Space Sci. 10 (17) 1967, 43-48.

[50] A. Y. Kuo, Thermal stresses at the edge of a bimetallic thermostat, ASME J. Appl. Mech. 1989, 56, 585-589.

[51] J. M. Souza, Boundary conditions in the finite difference methods, Sec~ao de Engenharia Mecanica. Instituto Militar de Engenharia, Brasil, 23-33. www.cimec.org.ar/ojs/index.php/mc/.../2607.

[52] A. C. Antoulas, Approximation of Large-Scale Dynamical Systems. Society for Industrial and Applied Mathematics, Philadelphia, PA, USA, 2005.

[53] Peter Benner, Michael Hinze, and E Jan W Ter Maten. Model reduction for circuit simulation, Lecture Notes in Electrical Engineering, vol. 74, Springer, 2010.

[54] S.X.D Tan and L. He. Advanced Model Order Reduction Techniques in VLSI Design. Cambridge University Press, New York, 2007.

[55] W.H.A. Schilders, H.A. Van Der Vorst, and J. Rommes. Model order reduction: theory, research aspects and applications. Springer Verlag, 2008.

[56] A. Odabasioglu, M. Celik, and L. T. Pileggi, "PRIMA: passive reduced-order interconnect macromodeling algorithm," IEEE Trans. on Computer-Aided Design of Integrated Circuits and Systems, Vol. 17, no. 8, 1998, 645-654.

[57] W.E. Arnoldi. The principle of minimized iterations in the solution of the matrix eigenvalue problem. Quart. Appl. Math, 9(1): 1951, 17-29.

[58] C. Lanczos. An iteration method for the solution of the eigenvalue problem of linear differential and integral operators1. Journal of Research of the National Bureau of Standards, 45(4), 1950.

[59] B. Moore. Principal component analysis in linear systems: Controllability, observability, and model reduction. Automatic Control, IEEE Transac- tions on, 26(1): 1981, 17-32.

[60] K. Glover. All optimal hankel-norm approximations of linear multivari- able systems and their l—inf error bounds. International Journal of Control, 39(6): 1984, 1115-1193.

[61] K. Willcox and J. Peraire. "Balanced model reduction via the proper orthogonal decomposition." AIAA journal, vol. 40, no. 11 (2002): 2323-2330.

[62] B. Bond, Z. Mahmood, Y. Li, R. Sredojevic, A. Megretski, V. Stojanovic, Y. Avniel, and L. Daniel, "Compact modeling of nonlinear analog circuits using system identification via semidefinite programming and incremental stability

certification," IEEE Trans. on CAD of Integrated Circuits and Systems, vol. 29, no. 8, 2010, 1149-1162.

[63] J. R. Phillips, "Projection-based approaches for model reduction of weakly nonlinear, time-varying systems," IEEE Trans. Comput.-Aided Design Integr. Circuits Syst., vol. 22, no. 2, 2003, 171-187.

[64] M. Rewienski and J. White, "A trajectory piecewise-linear approach to model order reduction and fast simulation of nonlinear circuits and micro-machined devices," IEEE Trans. Comput.-Aided Design Integr. Circuits Syst., vol. 22, no. 2, 2003, 155-170.

[65] Astolfi, A., "Model Reduction by Moment Matching for Linear and Nonlinear Systems," Automatic Control, IEEE Transactions on, vol.55, no.10, 2010, 2321-2336.

[66] S. Chaturantabut, D. Sorensen, Nonlinear Model Reduction via Discrete Empirical Interpolation**,** SIAM J. SCI. COMPUT, Vol. 32, No. 5 (2010), 2737-2764.

[67] P. Benner, E. S. Quintana Orti, and G. Quintana Ort´ı. Efficient Numerical Algorithms for Balanced Stochastic Truncation. Int. J. Appl. Math. Comp. Sci., 11(5): 2001, 1123-1150.

[68] A. J. Laub, M. T. Heath, C. C. Paige, and R. C. Ward. Computation of System Balancing Transformations and Other Applications of Simultaneous Diagonalization Algorithms. IEEE Trans. on Automatic Control, AC-32(2): 1987, 115-122.

[69] M. G. Safonov and R. Y. Chiang. A Schur Method for Balanced Truncation Model Reduction. IEEE Trans. Aut. Control, 34(7): 1989, 729-733.

[70] B. Salimbahrami, B. Lohmann, Order reduction of large scale second-order systems using Krylov subspace methods, Linear Algebra and its Applications 415 (2006), 385-405.

[71] B. Lohmann, B. Salimbahrami, Structure preserving reduction of large second order models by moment matching, Proc. Appl. Math. Mech. 4 (1) (2004), 672-673.

[72] Z. Bai, Krylov subspace techniques for reduced-order modelling of large-scale dynamical systems, Applied Numerical Mathematics 43 (2002), 9-44.

[73] A. Charest, M. S. Nakhla, and R. Achar. Delay extracted stable rational approximations for tabulated networks with periodic reflections. IEEE Microwave and Wireless Components Letters, 19(12): 2009, 768-770.

[74] S. Grivet-Talocia. Packagemacromodeling via time-domain vector fitting. IEEE Microwave and Wireless Components Letters, 13(11): 2003, 472-474.

[75] S. Grivet-Talocia, B. Gustavsen, Passive Macromodeling: Theory and Applications, John Wiley & Sons Inc (2014).

[76] B. Salimbahrami and B. Lohmann. Order Reduction of Large Scale Second Order Systems Using Krylov Subspace Methods. Accepted for publication in Linear Algebra and its Appl., 2003.

[77] B. Lohmann and B. Salimbahrami. Reduction of Second Order Systems using Second Order Krylov subspaces. In IFAC world congress, Prag, Czech Rep., 2005.

[78] B. Salimbahrami, Structure preserving order reduction of large scale second order models, PhD Thesis, Technischen Universität München, 2005.

[79] A. Jones C. Underwood, A Thermal Model for Photovoltaic Systems, Solar Energy Vol. 70, No. 4 (2001), 349-359.

[80] S. Armstrong, W. Hurley, A Thermal Model for Photovoltaic Panels under Varying Atmospheric Conditions, Applied Thermal Engineering 30 (2010), 1488-1495.

[81] T. Blomberg, Heat Conduction in Two and Three Dimensions: Computer Modelling Of Building Physics Applications, Report TVBH-1008, Department of Building Physics, Lund University, Sweden (1996), 5-13.

[82] O. C. Zienkiewicz, R. L. Taylor, The Finite Element Method, fifth edition Vol. 1, Butterworth-Heinemann (2000), 493-572.

[83] R. Eid, B. Salimbahrami, B. Lohmann, Parametric Order Reduction of Proportionally Damped Second Order Systems, Technical Reports on Automatic Control, Vol. TRAC-1, 2006, 1-11.

[84] Wilson, E. L., "Dynamic Response by Step-By-Step Matrix Analysis", Proceedings, Symposium On The Use of Computers in Civil Engineering, Labortorio Nacional de Engenharia Civil, Lisbon, Portugal, (1962).

[85] Wilson, E. L., I. Farhoomand and K. J. Bathe, "Nonlinear Dynamic Analysis of Complex Structures", Earthquake Engineering and Structural Dynamics, 1, 1973, 241-252.

[86] Hughes, Thomas, "The Finite Element Method - Linear Static and Dynamic Finite Element Analysis", Prentice Hall, Inc., (1987).

[87] J. S. Han, E. B. Rudnyi, J. G. Korvink. "Efficient optimization of transient dynamic problems in MEMS devices using model order reduction." Journal of Micromechanics and Microengineering 2005, Vol. 15, N 4, 822-832.

[88] L. Del Tin, R. Gaddi, E. B. Rudnyi, A. Greiner, J. G. Korvink, "Compact modeling of RF-MEMS resonators by means of model order reduction", submitted to Journal of Micromechanics and Microengineering, 2006.

[89] T. Bechtold, Model order reduction of Electro-thermal MEMS, Doctorate thesis, Albert-Ludwigs University of Freiburg, 2005.

[90] P. Heres and W. Schilders. Model order reduction of interconnect structures in Fasterix. Technical note, Philips Research, 2003.

[91] R. Ionutiu and J. Rommes. Circuit synthesis of reduced order models. Technical note NXP-TN-2008/00316, NXP Semiconductors, 2009.

[92] R. Ionutiu and J. Rommes. SparseRC: sparsity preserving model reduction for RC circuits with many terminals. CASA-Report 11-05, Eindhoven University of Technology, 2011.

[93] A. Odabasioglu, M. Celik, and Pileggi L.T. PRIMA: Passive reduced-order interconnect macromodeling algorithm. IEEE Transactions on Computer-Aided Design of Integrated Circuits and Systems, 8: 1998, 645-654.

[94] R.F. Milsom, RF simulation of passive ics using Fasterix. Report rp3506, Philips Electronics, 1996.

[95] L. M. Silveira, M. Kamon, and J. White. Efficient Reduced-Order Modeling of Frequency-Dependent Coupling Inductances associated with 3-D Interconnect Structures. In Proc. 32nd Design Automation Conf., San Francisco, CA, 1995, 376-380.

[96] A. Carpinteri, M. Paggi., Thermo-elastic mismatch in non-homogeneous beams. J. Eng. Math. 2008; **61**: 371-384.

[97] S. O. Ojo, M. Paggi, A thermo-visco-elastic shear-lag model for the prediction of residual stresses in photovoltaic modules after lamination, Composite Structures, 136 (2016), 481-492.

[98] Y. Wen, Thermomechanical analysis of multilayered microelectronics packaging: Modelling and tesing, PhD thesis, University at Buffalo, State University of New York, 2003, 75-95.

[99] A. Lutowska, Model Order Reduction for Coupled Systems using Low-rank Approximations, PhD Thesis, Technische Universiteit Eindhoven, 2012, pp. 53 – 117.

[100] R. W. Freund, Recent Advances in Structure-Preserving Model Order Reduction, https://www.math.ucdavis.edu/~freund/freund10.pdf

[101] A. Faes, H. Li, F. Galliano, C. Ballif, L. Perret-Aebi, Lamination process and encapsulation materials for glass–glass PV module design, Photovoltaics International Vol. 27, 2015, 1-9.

[102] R.R. Craig Jr. Coupling of substructures for dynamic analysis: an overview. In Proceedings of the 41st AIAA/ASME/ASCE/AHS/ASC Structures, Structural Dynamics, and Materials Conference, Atlanta, USA, 2000.

[103] D. de Klerk, D.J. Rixen, and S.N. Voormeeren. General framework for dynamics substructuring: history, review, and classification of techniques. AIAA Journal, 46(5): 2008, 1169-1181.

[104] J.W.S. Rayleigh. The theory of sound. Dover Publications, New York, 1945.

[105] E.L. Wilson, M.-W. Yuan, and J.M. Dickens. Dynamic analysis by direct superposition of Ritz vectors. Earthquake Engineering & Structural Dynamics, 10(6): 1982, 813-821.

[106] Y. Fu, Non-linear analysis of laminated plates and shells with damage, WIT press, UK, 2013.

APPENDIX

APPENDIX A.

A.1 Elements of $\boldsymbol{v}$ vector

The vector of unknowns $\boldsymbol{v}$ in Eqs. (5.52) and (5.57) is defined as:

$$\boldsymbol{v} = [U_1\ U_1'\ U_2\ U_2'\ U_3\ U_3'\ W_1\ W_1'\ W_1''\ W_1'''\ W_2\ W_2'\ W_2''\ W_2'''\ W_3\ W_3'\ W_3''\ W_3''']^T$$

A.2 Coefficients of B matrix

The matrix operator $\boldsymbol{B}$ entering Eqs. (5.52) and (5.56) is given by:

$$\boldsymbol{B}$$

$$= \begin{bmatrix}
0 & 1 & 0 & 0 & 0 & 0 & 0 & 0 & 0 & 0 & 0 & 0 & 0 & 0 & 0 & 0 & 0 & 0 \\
\kappa_1 & 0 & \kappa_2 & 0 & 0 & 0 & 0 & \kappa_3 & 0 & 0 & 0 & \kappa_4 & 0 & 0 & 0 & 0 & 0 & 0 \\
0 & 0 & 0 & 1 & 0 & 0 & 0 & 0 & 0 & 0 & 0 & 0 & 0 & 0 & 0 & 0 & 0 & 0 \\
\xi_1 & 0 & \xi_2 & 0 & \xi_3 & 0 & 0 & \xi_4 & 0 & 0 & 0 & \xi_5 & 0 & 0 & 0 & \xi_6 & 0 & 0 \\
0 & 0 & 0 & 0 & 0 & 1 & 0 & 0 & 0 & 0 & 0 & 0 & 0 & 0 & 0 & 0 & 0 & 0 \\
0 & 0 & \varrho_2 & 0 & \varrho_3 & 0 & 0 & 0 & 0 & 0 & 0 & \varrho_5 & 0 & 0 & 0 & \varrho_6 & 0 & 0 \\
0 & 0 & 0 & 0 & 0 & 0 & 0 & 1 & 0 & 0 & 0 & 0 & 0 & 0 & 0 & 0 & 0 & 0 \\
0 & 0 & 0 & 0 & 0 & 0 & 0 & 0 & 1 & 0 & 0 & 0 & 0 & 0 & 0 & 0 & 0 & 0 \\
0 & 0 & 0 & 0 & 0 & 0 & 0 & 0 & 0 & 1 & 0 & 0 & 0 & 0 & 0 & 0 & 0 & 0 \\
\lambda_7 & \lambda_1 & \lambda_8 & \lambda_2 & 0 & 0 & \lambda_5 & \lambda_9 & \lambda_3 & 0 & \lambda_6 & \lambda_{10} & \lambda_4 & 0 & 0 & 0 & 0 & 0 \\
0 & 0 & 0 & 0 & 0 & 0 & 0 & 0 & 0 & 0 & 0 & 1 & 0 & 0 & 0 & 0 & 0 & 0 \\
0 & 0 & 0 & 0 & 0 & 0 & 0 & 0 & 0 & 0 & 0 & 0 & 1 & 0 & 0 & 0 & 0 & 0 \\
0 & 0 & 0 & 0 & 0 & 0 & 0 & 0 & 0 & 0 & 0 & 0 & 0 & 1 & 0 & 0 & 0 & 0 \\
\gamma_{10} & \gamma_1 & \gamma_{11} & \gamma_2 & \gamma_{12} & \gamma_3 & \gamma_7 & \gamma_{13} & \gamma_4 & 0 & \gamma_8 & \gamma_{14} & \gamma_5 & 0 & \gamma_9 & \gamma_{15} & \gamma_6 & 0 \\
0 & 0 & 0 & 0 & 0 & 0 & 0 & 0 & 0 & 0 & 0 & 0 & 0 & 0 & 0 & 1 & 0 & 0 \\
0 & 0 & 0 & 0 & 0 & 0 & 0 & 0 & 0 & 0 & 0 & 0 & 0 & 0 & 0 & 0 & 1 & 0 \\
0 & 0 & 0 & 0 & 0 & 0 & 0 & 0 & 0 & 0 & 0 & 0 & 0 & 0 & 0 & 0 & 0 & 1 \\
0 & 0 & \delta_7 & \delta_1 & \delta_8 & \delta_2 & 0 & 0 & 0 & 0 & \delta_5 & \delta_9 & \delta_3 & 0 & \delta_6 & \delta_{10} & \delta_4 & 0
\end{bmatrix}$$

where the entries of the $\boldsymbol{B}$ matrix are defined as:

$$\Lambda_i = -\frac{(1-{\nu_i}^2)}{E_i h_i},$$

$$\Upsilon_i = \frac{(1-{\nu_i}^2)}{E_i I_i}, \quad i = 1, 2, 3$$

$$\kappa_1 = -\Lambda_1 \mathrm{K_{x1}}, \ \kappa_2 = \Lambda_1 \mathrm{K_{x1}}, \quad \kappa_3 = \Lambda_1 \mathrm{K_{x1} c_1}, \ \kappa_4 = \Lambda_1 \mathrm{K_{x1} c_2},$$

$$\xi_1 = \Lambda_2 \mathrm{K_{x1}}, \qquad \xi_2 = -\Lambda_2 (\mathrm{K_{x1}} + \mathrm{K_{x2}}), \qquad \xi_3 = \Lambda_2 \mathrm{K_{x2}},$$

$$\xi_4 = -\Lambda_2 \mathrm{K_{x1} c_1}, \qquad \xi_5 = \Lambda_2 \mathrm{c_2} (\mathrm{K_{x1}} - \mathrm{K_{x2}}), \qquad \xi_6 = \Lambda_2 \mathrm{K_{x2} c_3},$$

$$\varrho_1 = \Lambda_3 \mathrm{K_{x2}}, \quad \varrho_2 = -\Lambda_3 \mathrm{K_{x2}}, \ \varrho_3 = -\Lambda_3 \mathrm{K_{x2} c_2}, \ \varrho_4 = -\Lambda_3 \mathrm{K_{x2} c_3},$$

$$\lambda_1 = \Upsilon_1 \mathrm{K_{x1} c_1}, \ \lambda_2 = -\Upsilon_1 \mathrm{K_{x1} c_1}, \ \lambda_3 = -\Upsilon_1 \mathrm{K_{x1} {c_1}^2}, \ \lambda_4 = -\Upsilon_1 \mathrm{K_{x1} c_1 c_2},$$

$$\lambda_5 = \Upsilon_1 \mathrm{K_{y1}}, \quad \lambda_6 = -\Upsilon_1 \mathrm{K_{y1}}, \quad \lambda_7 = \frac{\Upsilon_1 \mathrm{c_1}}{\mathrm{K_{x1}}} \frac{\partial \mathrm{K_{x1}}}{\partial x_2}, \qquad \lambda_8 = -\frac{\Upsilon_1 \mathrm{c_1}}{\mathrm{K_{x1}}} \frac{\partial \mathrm{K_{x1}}}{\partial x_2},$$

$$\lambda_9 = -\frac{\Upsilon_1 {c_1}^2}{K_{x1}}\frac{\partial K_{x1}}{\partial x_2}, \qquad \lambda_{10} = -\frac{\Upsilon_1 c_1 c_2}{K_{x1}}\frac{\partial K_{x1}}{\partial x_2}.$$

$$\gamma_1 = \Upsilon_2 K_{x1} c_2,\ \gamma_2 = \Upsilon_2 c_2 (K_{x2} - K_{x1}),\ \gamma_3 = -\Upsilon_2 K_{x2} c_2,\ \gamma_4 = -\Upsilon_2 K_{x1} c_1 c_2,$$

$$\gamma_5 = -\Upsilon_2 {c_2}^2 (K_{x2} + K_{x1}), \qquad \gamma_6 = -\Upsilon_2 K_{x2} c_3 c_2, \qquad \gamma_7 = -\Upsilon_2 K_{y1},$$

$$\gamma_8 = \Upsilon_2 (K_{y1} + K_{y2}), \qquad \gamma_9 = -\Upsilon_2 K_{y2}, \qquad \gamma_{10} = \frac{\Upsilon_2 c_2}{K_{x1}}\frac{\partial K_{x1}}{\partial x_2},$$

$$\gamma_{11} = \Upsilon_2 c_2 \left(\frac{1}{K_{x2}}\frac{\partial K_{x2}}{\partial x_2} - \frac{1}{K_{x1}}\frac{\partial K_{x1}}{\partial x_2}\right),\ \gamma_{12} = -\frac{\Upsilon_2 c_2}{K_{x2}}\frac{\partial K_{x2}}{\partial x_2}, \qquad \gamma_{13} = -\frac{\Upsilon_2 c_1 c_2}{K_{x1}}\frac{\partial K_{x1}}{\partial x_2},$$

$$\gamma_{14} = -\Upsilon_2 {c_2}^2 \left(\frac{1}{K_{x2}}\frac{\partial K_{x2}}{\partial x_2} + \frac{1}{K_{x1}}\frac{\partial K_{x1}}{\partial x_2}\right), \qquad \gamma_{15} = -\frac{\Upsilon_2 c_3 c_2}{K_{x2}}\frac{\partial K_{x2}}{\partial x_2}.$$

$$\delta_1 = \Upsilon_3 K_{x2} c_3, \quad \delta_2 = -\Upsilon_3 K_{x2} c_3, \quad \delta_3 = -\Upsilon_3 K_{x2} c_3 c_2, \quad \delta_4 = -\Upsilon_3 K_{x2} {c_3}^2$$

$$\delta_5 = -\Upsilon_3 K_{y2}, \quad \delta_6 = \Upsilon_3 K_{y2}, \qquad \delta_7 = \frac{\Upsilon_1 c_1}{K_{x1}}\frac{\partial K_{x1}}{\partial x_2}, \qquad \delta_8 = -\frac{\Upsilon_1 c_1}{K_{x1}}\frac{\partial K_{x1}}{\partial x_2}$$

$$\delta_9 = -\frac{\Upsilon_1 {c_1}^2}{K_{x1}}\frac{\partial K_{x1}}{\partial x_2}, \qquad \delta_{10} = -\frac{\Upsilon_1 c_1 c_2}{K_{x1}}\frac{\partial K_{x1}}{\partial x_2}.$$

A.3 Coefficients of F vector

$$\boldsymbol{F} = \begin{Bmatrix} 0 \\ 0 \\ 0 \\ 0 \\ 0 \\ 0 \\ 0 \\ 0 \\ 0 \\ \lambda_{11} \\ 0 \\ 0 \\ 0 \\ \gamma_{16} \\ 0 \\ 0 \\ 0 \\ \delta_{11} \end{Bmatrix}$$

where the entries of the $\boldsymbol{F}$ vector are defined as:

$\lambda_{11} = \Upsilon_1 \mathrm{K_{y1}}(\Delta T_2 \alpha_2 \mathrm{c_2} + \Delta T_1 \alpha_1 \mathrm{c_1})$,

$\gamma_{16} = -\Upsilon_2 \left[\mathrm{K_{y1}} \Delta T_1 \alpha_1 \mathrm{c_1} + \Delta T_2 \alpha_2 \mathrm{c_2} \left(\mathrm{K_{y1}} - \mathrm{K_{y2}}\right) - \mathrm{K_{y2}} \Delta T_3 \alpha_3 \mathrm{c_3}\right]$,

$\delta_{11} = \Upsilon_1 \mathrm{K_{y1}}(\Delta T_2 \alpha_2 \mathrm{c_2} + \Delta T_1 \alpha_1 \mathrm{c_1})$.

APPENDIX B.

B.1 Fourth derivative approximation for non-uniform finite difference

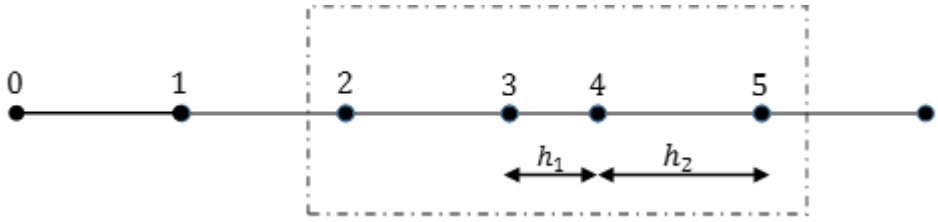

Figure B.1 points with non-uniform grid spacing.

Let $r = \frac{h_1}{h_2}$.

To evaluate the fourth derivative at point 2 (in Fig. B.1) for a five point stencil and centred divided difference approximation, the fourth order polynomial is considered:

$$P_4(x_2) = \sum_{j=0}^{4} F(x_j) l_j(x) \qquad \text{(B.1)}$$

with grid spacing,

$x_0 = x - 2h_2,$ $x_1 = x - h_2,$ $x_2 = x,$

$x_3 = x + h_2,$ $x_4 = x + (1 + r)h_2,$

And the Lagrange polynomials $l_j(x)$ are expressed as:

$$l_0(x) = \frac{x - x_1}{x_0 - x_1}\frac{x - x_2}{x_0 - x_2}\frac{x - x_3}{x_0 - x_3}\frac{x - x_4}{x_0 - x_4}$$

$$l_1(x) = \frac{x - x_0}{x_1 - x_0}\frac{x - x_2}{x_1 - x_2}\frac{x - x_3}{x_1 - x_3}\frac{x - x_4}{x_1 - x_4}$$

$$l_2(x) = \frac{x - x_0}{x_2 - x_0}\frac{x - x_1}{x_2 - x_1}\frac{x - x_3}{x_2 - x_3}\frac{x - x_4}{x_2 - x_4}$$

$$l_3(x) = \frac{x - x_0}{x_3 - x_0}\frac{x - x_1}{x_3 - x_1}\frac{x - x_2}{x_3 - x_2}\frac{x - x_4}{x_3 - x_4}$$

$$l_4(x) = \frac{x - x_0}{x_4 - x_0}\frac{x - x_1}{x_4 - x_1}\frac{x - x_2}{x_4 - x_2}\frac{x - x_3}{x_4 - x_3}$$

By differentiating Eq. (B.1) four times, we have:

$$P_4(x_2)^{\text{iv}} = \sum_{j=0}^{4} F(x_j) l_j(x)^{\text{iv}} \tag{B.2}$$

where

$$l_0(x)^{\text{iv}} = \frac{24}{6(3+r){h_2}^4}, \qquad l_1(x)^{\text{iv}} = -\frac{24}{2(2+r){h_2}^4}, \qquad l_2(x)^{\text{iv}} = \frac{24}{2(1+r){h_2}^4},$$

$$l_3(x)^{\text{iv}} = -\frac{24}{6r{h_2}^4}, \qquad l_4(x)^{\text{iv}} = \frac{24}{r(3+r)(2+r)(1+r){h_2}^4}$$

Eq. (B.2) can now be expressed as:

$$P_4(x_2)^{\text{iv}} = \frac{24}{6(3+r){h_2}^4}F(x_0) - \frac{24}{2(2+r){h_2}^4}F(x_1) + \frac{24}{2(1+r){h_2}^4}F(x_2) - \frac{24}{6r{h_2}^4}F(x_3) + \frac{24}{r(3+r)(2+r)(1+r){h_2}^4}F(x_4) \tag{B.3}$$

By rationalizing Eq. (B.3), we obtain:

$$P_4(x_2)^{\text{iv}} = \frac{4r(2+r)(1+r)}{s_1}F(x_0) - \frac{12r(3+r)(1+r)}{s_1}F(x_1) + \frac{12r(3+r)(2+r)}{s_1}F(x_2) - \frac{4r(3+r)\left(r^2+3r+2\right)}{s_1}F(x_3) + \frac{24}{s_1}F(x_4) \tag{B.4}$$

where $s_1 = r(3+r)(2+r)(1+r){h_2}^4$

Similar procedure can be used to obtain the fourth derivative approximation of points $3, 4, 5$.

B.2 Second derivative approximation for non-uniform finite difference

To evaluate the formula for second derivative of point 3 based on three point stencil and centred divided difference approximation, a second order polynomial is considered:

$$P_2(x_3) = \sum_{j=2}^{4} F(x_j) l_j(x) \tag{B.5}$$

with grid spacing,

$x_2 = x - h_2$, $x_3 = x$, $x_4 = x + rh_2$.

and

$$l_2(x) = \frac{x - x_3}{x_2 - x_3} \frac{x - x_4}{x_2 - x_4}$$

$$l_3(x) = \frac{x - x_2}{x_3 - x_2} \frac{x - x_4}{x_3 - x_4}$$

$$l_4(x) = \frac{x - x_2}{x_4 - x_2} \frac{x - x_3}{x_4 - x_3}$$

By differentiating Eq. (B.5) twice, we have:

$$P_2(x_3)'' = \sum_{j=2}^{2} F(x_j) l_j(x)'' \tag{B.6}$$

where

$l_2(x)'' = \frac{2}{(1+r){h_2}^2}$, $l_3(x)'' = -\frac{2}{r{h_2}^2}$, $l_2(x)'' = \frac{2}{r(1+r){h_2}^2}$.

Eq. (B.6) can now be expressed as:

$$P_2(x_3)s'' = \frac{2}{(1+r){h_2}^2}F(x_2) - \frac{2}{r{h_2}^2}F(x_3) + \frac{2}{r(1+r){h_2}^2}F(x_4) \quad \text{(B.7)}$$

By rationalizing (B.7), we get:

$$P_2(x_3)'' = \frac{2r}{s_2}F(x_2) - \frac{2(1+r)}{s_2}F(x_3) + \frac{2}{s_2}F(x_4) \quad \text{(B.8)}$$

where $s_2 = r(1+r){h_2}^2$

This procedure can be repeated to obtain the second derivative approximation of point 4.

B.3 Surface loads

Interfacial stresses are derived based on the following formulations:

Interface 1

$$\sigma_{z1}{}^{(1)} = \mathrm{K_x}\left(u_1{}^{(1)} - u_1{}^{(2)}\right) = \mathrm{K_x}\left(-c_1 w_{,1}{}^{(1)} - c_2 w_{,1}{}^{(2)} + U_1{}^{(1)} - U_1{}^{(2)}\right) \quad \text{(B.9a)}$$

$$\sigma_{z2}{}^{(1)} = \mathrm{K_x}\left(u_2{}^{(1)} - u_2{}^{(2)}\right) = \mathrm{K_x}\left(-c_1 w_{,2}{}^{(1)} - c_2 w_{,2}{}^{(2)} + U_2{}^{(1)} - U_2{}^{(2)}\right) \quad \text{(B.9b)}$$

$$\sigma_{zz}{}^{(1)} = \mathrm{K_y}\left(w^{(2)} - w^{(1)}\right) \quad \text{(B.9c)}$$

Interface 2

$$\sigma_{z1}{}^{(2)} = \mathrm{K_x}\left(u_1{}^{(2)} - u_1{}^{(3)}\right) = \mathrm{K_x}\left(-c_1 w_{,1}{}^{(2)} - c_2 w_{,1}{}^{(3)} + U_1{}^{(2)} - U_1{}^{(3)}\right)$$
(B.10a)

$$\sigma_{z2}{}^{(2)} = \mathrm{K_x}\left(u_2{}^{(2)} - u_2{}^{(3)}\right) = \mathrm{K_x}\left(-c_1 w_{,2}{}^{(2)} - c_2 w_{,2}{}^{(3)} + U_2{}^{(2)} - U_2{}^{(3)}\right)$$
(B.10b)

$$\sigma_{zz}{}^{(2)} = \mathrm{K_y}\left(w^{(3)} - w^{(2)}\right) \quad \text{(B.10c)}$$

With respect to Eqs. (B.9) and (B.10), the surface loads are specified as follows:

$$n_1^{(1)} = -\sigma_{1z}^{(1)} = \mathrm{K_x}\left(c_1 w_{,1}^{(1)} + c_2 w_{,1}^{(2)} - U_1^{(1)} + U_1^{(2)}\right) \quad \text{(B.11a)}$$

$$n_1^{(2)} = \sigma_{1z}^{(1)} - \sigma_{1z}^{(2)} = \mathrm{K_x}\left(-c_1 w_{,1}^{(1)} - c_2 w_{,1}^{(2)} + U_1^{(1)} - U_1^{(2)}\right) + \mathrm{K_x}\left(c_1 w_{,1}^{(2)} + c_2 w_{,1}^{(3)} - U_1^{(2)} + U_1^{(3)}\right) \quad \text{(B.11b)}$$

$$n_1^{(3)} = \sigma_{1z}^{(2)} = \mathrm{K_x}\left(-c_1 w_{,1}^{(2)} - c_2 w_{,1}^{(3)} + U_1^{(2)} - U_1^{(3)}\right) \quad \text{(B.11c)}$$

$$n_2^{(1)} = -\sigma_{2z}^{(1)} = \mathrm{K_x}\left(c_1 w_{,2}^{(1)} + c_2 w_{,2}^{(2)} - U_2^{(1)} + U_2^{(2)}\right) \quad \text{(B.12a)}$$

$$n_2^{(2)} = \sigma_{2z}^{(1)} - \sigma_{2z}^{(2)} = \mathrm{K_x}\left(-c_1 w_{,2}^{(1)} - c_2 w_{,2}^{(2)} + U_2^{(1)} - U_2^{(2)}\right) + \mathrm{K_x}\left(c_1 w_{,2}^{(2)} + c_2 w_{,2}^{(3)} - U_2^{(2)} + U_2^{(3)}\right) \quad \text{(B.12b)}$$

$$n_2^{(3)} = \sigma_{2z}^{(2)} = \mathrm{K_x}\left(-c_1 w_{,2}^{(2)} - c_2 w_{,2}^{(3)} + U_2^{(2)} - U_2^{(3)}\right) \quad \text{(B.12c)}$$

$$m_1^{(1)} = \sigma_{z1}^{(1)} = \mathrm{K_x}\left(-c_1 w_{,1}^{(1)} - c_2 w_{,1}^{(2)} + U_1^{(1)} - U_1^{(2)}\right) \quad \text{(B.13a)}$$

$$m_1^{(2)} = \sigma_{z1}^{(1)} + \sigma_{z1}^{(2)} = \mathrm{K_x}\left(-c_1 w_{,1}^{(1)} - c_2 w_{,1}^{(2)} + U_1^{(1)} - U_1^{(2)}\right) + \mathrm{K_x}\left(-c_1 w_{,1}^{(2)} - c_2 w_{,1}^{(3)} + U_1^{(2)} - U_1^{(3)}\right) \quad \text{(B.13b)}$$

$$m_1^{(3)} = \sigma_{z1}^{(2)} = \mathrm{K_x}\left(-c_1 w_{,1}^{(2)} - c_2 w_{,1}^{(3)} + U_1^{(2)} - U_1^{(3)}\right) \quad \text{(B.13c)}$$

$$m_2^{(1)} = \sigma_{z2}^{(1)} = \mathrm{K_x}\left(-c_1 w_{,2}^{(1)} - c_2 w_{,2}^{(2)} + U_2^{(1)} - U_2^{(2)}\right) \quad \text{(B.14a)}$$

$$m_2^{(2)} = \sigma_{z2}^{(1)} + \sigma_{z2}^{(2)} = \mathrm{K_x}\left(-c_1 w_{,2}^{(1)} - c_2 w_{,2}^{(2)} + U_2^{(1)} - U_2^{(2)}\right) + \mathrm{K_x}\left(-c_1 w_{,2}^{(2)} - c_2 w_{,2}^{(3)} + U_2^{(2)} - U_2^{(3)}\right) \quad \text{(B.14b)}$$

$$m_2^{(3)} = \sigma_{z2}^{(2)} = \mathrm{K_x}\left(-c_1 w_{,2}^{(2)} - c_2 w_{,2}^{(3)} + U_2^{(2)} - U_2^{(3)}\right) \quad \text{(B.14c)}$$

$$p^{(1)} = -{\sigma_{zz}}^{(1)} = \mathrm{K_y}\left(w^{(2)} - w^{(3)}\right) \tag{B.15a}$$

$$p^{(2)} = {\sigma_{zz}}^{(1)} - {\sigma_{zz}}^{(2)} = \mathrm{K_y}\left(w^{(2)} - w^{(1)}\right) - \mathrm{K_y}\left(w^{(2)} - w^{(3)}\right) \tag{B.15b}$$

$$p^{(3)} = {\sigma_{zz}}^{(2)} = \mathrm{K_y}\left(w^{(3)} - w^{(2)}\right) \tag{B.15c}$$